UNIVERSITY OF SOUTHAMPTON

FACULTY OF ENGINEERING, SCIENCE & MATHEMATICS

OPTOELECTRONICS RESEARCH CENTRE

Development and Applications of UV Written Waveguides

Ian James Grayston Sparrow

Submitted for the degree of Doctor of Philosophy

September 2005

UNIVERSITY OF SOUTHAMPTON

ABSTRACT

Optoelectronics Research Centre

Doctor of Philosophy

Development and Applications of UV Written Waveguides.

Ian James Grayston Sparrow

This thesis presents a description of the development of structures suitable for the technique of Direct UV Writing and demonstrates applications for which the resultant waveguiding devices may be used.

Broadly speaking, the thesis may be divided into two sections. Firstly the development of a PECVD deposition process for the fabrication of multiple thin silica films on planar substrates is described. The photosensitive properties of these layers are investigated by UV writing to produce waveguides and Bragg gratings. Single mode waveguides with a propagation loss of $1.27 \pm 0.09 \text{dBcm}^{-1}$ at 1560nm and Bragg gratings with a refractive index perturbation of approximately 4×10^{-4} are produced.

The later stages of the thesis present several applications of the direct UV writing process and of devices fabricated by the technique. Firstly, direct grating writing is used as a waveguide analysis technique to measure the effects of thermal annealing on UV written structures in PECVD and FHD fabricated samples. Following this, the use of UV written devices as refractive index sensors is shown using the detection of phase transitions in water and a liquid crystal as examples. The detection of supercooling in water is demonstrated and identification of the supercool state is found to be straightforward. Building on these results, the first tunable planar Bragg grating using a liquid crystal layer is fabricated and experimentally demonstrated. An electrically controlled tuning range of 35GHz is recorded.

一期一会

One meeting, one chance

Acknowledgements

There are of course many people to whom thanks are due for the help that they provided me with over the course of my PhD.

Many thanks are due to Professor Peter Smith for his extensive advice and ceaseless supply of suggestions from the outset. Thanks are also due to Greg Emmerson, Corin Gawith, Denis Guilhot, Sam Watts, Richard Williams and Rafiq Adikan, who have all played a part in getting me to the stage where I could complete a thesis. Particular thanks go to Corin and Greg for, amongst other things, having the patience to (repeatedly) answer my questions and for making the UV system do what it should. For their assistance, I would also like to thank Malgosia Kaczmarek and Andriy Dyadyusha.

I am also very grateful to Dave Sager, Ed Weatherby and Mark Lessey for their unique blend of help, advice and humour which made life considerably easier and more bearable than it would otherwise have been.

Finally, I also wish to express my gratitude to my family who despite events over the last few years have always been a source of support. For resisting the urge to ask me "How's it going?" I am truly grateful!

Once again, Thank you.

Ian

Contents

Chapter 1

Introduction

When describing the field of integrated optics or planar waveguides to someone without a background in the field it is often convenient to draw comparisons with optical fibres. Whilst public awareness of the existence of optical fibres as the backbone of modern telecommunications systems is relatively high, familiarity with the concept of optical manipulation using integrated optics is very low. Conversely, from the field of microelectronics the phrase *integrated circuit* has entered popular culture and goes hand in hand with the consumer electronics that we all take for granted in everyday life.

As everyday life in western society becomes ever more dependent on 'high tech' devices the role of optics as a whole will become more apparent to the users of these components. In the last decade the use of compact discs and DVDs, both of which are optically based technologies, has become so common as to be taken for granted. Just as CDs and DVDs replaced their forerunners which included the vinyl record, the cassette tape and the floppy disk, so too will other optical technologies increasingly replace older technologies that were previously considered to set the standard in their fields.

In addition to the markets for consumer technology a vast range of technological markets are exploiting the continuing development of optical technologies. Telecommunications systems seek to use higher bit rates and wider wavelength ranges, med-

ical systems require rapid, low cost technologies to diagnose disorders with the minimum of patient discomfort, security systems must have means of detecting the presence of people, pathogens or dangerous technology. These are all examples of markets that are increasingly developing and using optical components as replacements for legacy systems.

The driving force behind this development is performance and, of course, cost. One means of addressing both of these goals is through the integration of multiple functionalities onto a single device. For example, a multi-wavelength optical communication system may require multiplexers, modulators and switches. These can be taken as individual components and concatenated to provide the required functionality. Alternatively, if the individual functions can be integrated into one package and use a single technology base then total production costs can be lowered and performance (e.g. optical loss) improved whilst at the same time making the end product smaller.

The concept of integrated optics was introduced in 1969 when Miller proposed the development of "laser beam circuitry" [1]. It was shown that in principle resonators, couplers and other functions could be realised in a single device through the use of embedded dielectric waveguides. Since that time the optical component market has grown significantly and the use of integrated devices becomes increasingly attractive. The laser beam circuits proposed by Miller are now referred to as planar lightwave circuits (PLC), planar waveguides and also commonly by the somewhat ambiguous term, waveguide.

Many fabrication techniques used in the production of integrated optical components were in fact developed for the microelectronics industry. Both integrated circuits and integrated optics require highly toleranced, well characterised structures made from a range of materials. Thus the development of microelectronics, which became of commercial significance before integrated optics, provided many standard tools allowing high quality optical components to be developed.

A vast range of components may be included in the general category of integrated optics. These include lasers, amplifiers, multiplexers, filters, sensors, modulators

and switches all of which can be fabricated in planar geometries. A similarly wide variety of techniques exist for the development of this range of functions. In general terms the goal behind the development of all of these device types is to allow more and more functions to included onto a single device for the reduction of cost and improvement of performance. One of the big limitations of integration is in the compatibility of processing methods. For example, processing temperatures for one device type can damage previously developed structures restricting the level of integration of the two device styles. Therefore, development of new fabrication techniques provides alternative routes towards higher levels of integration and higher functionality. This thesis is based on the development of one such technique for producing integrated optics, specifically optical waveguides defined by the technique of UV writing.

Of particular interest here, is the creation of optical waveguides in silica. Owing to the widespread use of silica optical fibres for transmission of light, it is often convenient to use similar materials when designing planar components to interface with the fibres. Therefore a large amount of work relating to integrated optics is silica based. Increasingly, alternative materials are being used which allow the production of more compact devices through the use of additional materials with higher refractive index [2]. Nonetheless, silica based components continue to see strong development and the purpose of the work presented in this thesis was to develop both fabrication techniques and applications of the devices.

1.1 Context

All of the research activity presented here was performed in the context of a wider range of developments of at the Optoelectronics Research Centre. Prior work within the author's research group has included the development of a Flame Hydrolysis Deposition system and a Direct UV Writing facility [3, 4]. Using the deposition system production processes were developed to produce planar waveguide samples specifically designed to be used with the UV writing equipment to define waveguiding devices. These projects provided the first demonstration of the Direct Grat-

ing Writing technique where simultaneous definition of a Bragg grating and optical waveguides without the need for additional device specific hardware such as phase masks. Subsequent extension of this work applied the UV writing method to rare earth doped samples fabricated with the same deposition system [5]. This work demonstrated how the combined techniques enable the production and integration of planar waveguide lasers and Bragg gratings through a single process route.

To complement the prior work, this thesis takes two approaches towards furthering the development of UV defined integrated optical components. Firstly, an alternative deposition technique (Plasma Enhanced Chemical Vapour Deposition) was used to produce planar substrates designed for the use of the UV writing techniques developed within the group. Additionally applications of UV defined devices as well as of the UV writing process itself have been demonstrated. In addition to devices fabricated by plasma enhanced chemical vapour deposition (PECVD) commercially produced samples, fabricated by flame hydrolysis deposition (FHD), have also been utilised. From the local perspective, this work has extended the technology base that may be used in the development of UV written waveguides. Within the wider context of integrated optics, the work has shown the use UV writing as an analysis tool, demonstrated specific applications of UV written devices and provided the first experimental demonstration of a particular integrated planar component.

In conjunction with the work that is discussed in the following chapters a range of additional, linked work was undertaken which is omitted from this thesis as it is not closely related to the main goals of the PhD. This involved the design and development of an improved wafer mount and heater for the in-house flame hydrolysis deposition equipment as well as fabrication of samples using this equipment. Thus a good grounding in the principles and use of the two silica fabrication techniques relevant to this thesis has been gained throughout the presented work.

1.2 Presentation Structure

Many of the principles behind the work presented in subsequent chapters are intrinsically linked and discussion of one naturally tends to draw upon topics relevant to other areas. Therefore, prior to the presentation of any practical work the appropriate background to all associated topics is provided in the early stages of this thesis. For clarity these topics are divided into chapters concerned with each of the broad categories. Initially, the basic theoretical considerations of optical waveguides and Bragg gratings is presented. These principles form the basis of the operation of all the waveguiding devices produced as part of this work and so a basic understanding was required in order to make appropriate steps in the development of devices and appreciate their performance and characteristics.

Chapters 3 and 4 are closely related but are treated separately for clarity. The UV writing process and its relative merits are first introduced in conjunction with other waveguide definition processes. Direct grating writing, an extension of direct UV writing is then discussed and the properties of the technique pertinent to the work of the subsequent chapters are provided. Chapter 4 then provides the more general background behind the processing steps that are required in order to fabricate the layers of material necessary for the formation of the waveguides by any of the techniques discussed in the preceding chapter.

The final provision of the necessary background is in chapter 5 where the phenomenon and principles of photosensitivity in silica are introduced. All of the waveguides produced in this work have been the result of the material photosensitive response and although it is a complex topic an appreciation of the fundamentals of the subject is beneficial.

Having introduced the appropriate background, chapter 6 details how a PECVD deposition process was developed to produce samples for UV writing. The development of this process is described and the successful production of the required 'three layer' structures is discussed. Building on this development, chapter 7 presents the results of UV writing into the deposited samples and how the resultant waveguides were characterised. Propagation loss, numerical aperture, waveguide effective in-

dex, birefringence and the effects of variation of UV exposure are all discussed.

The applications of UV written waveguides are the topics of chapters 8, 9 and 10. The former demonstrates the use of the direct grating writing technique as a tool to analyse the behaviour of UV defined structures over time or when subject to a range of environmental conditions. Using thermal annealing as an example, the characteristics of waveguides written into both PECVD and FHD substrates were monitored and their behaviour compared. Such work can provide not only the waveguide characteristics but also give insight into the material behaviour and its photosensitive response. The application of directly written waveguides as devices is demonstrated in chapters 9 and 10. Firstly the use of such devices as sensors is presented both theoretically and experimentally. Their use has been demonstrated by the detection of phase transitions between physical states in water and a liquid crystal. When studying the phase transitions of water it was found straightforward to identify the transitions between gas, liquid, solid and supercool states. Identification of the supercool state has previously required careful measurement techniques often involving human intervention and so the results represent a simplification of an existing measurement technique. Phase changes in a nematic liquid crystal make an interesting contrast with those of water. In the case of water, phase changes are accompanied by very obvious transitions between gas, solid or liquid. The transition from a liquid crystal to a liquid is from one fluid state to another. Nonetheless this change can be clearly identified, demonstrating the power of such sensor devices to provide insight into very small changes in the molecular order of such substances.

The final application that is presented is that of an electronically tunable filter. The results represent the first practical realisation of this style of filter. The overclad layer of a planar Bragg grating was replaced with a nematic liquid crystal. Using an applied electric field the wavelength response of the device was tuned and centre wavelength shifts of up to 35GHz were achieved. Applications of such a device are briefly discussed along with several routes that have been identified to improve the tunability.

There is, of course, considerable scope for further development of the work that has been carried out during the course of the PhD. Process refinement and additional

characterisation of UV defined structures will no doubt lead to further opportunities for applications of the resultant devices. Even with the process unchanged from its current state there are many avenues of fruitful investigation that remain open. Some of these future possibilities are outlined in chapter 11 and initial work to investigate these properties is, where relevant, covered.

1.3 References

[1] S.E. Miller. "Integrated Optics: An Introduction". *The Bell System Technical Journal*, 48(7):2059–2069, 1969.

[2] A.Sugita, M.Kotoku, and Y.Inoue. "Hybrid Integrated Photonics Devices and Planar Lightwave Circuits Technology". *Proceedings of 12th European Conference on Integrated Optics, Grenoble*, (WeP1):22–25, 2005.

[3] S.P. Watts. "Flame Hydrolysis Deposition of Photosensitive Silicate Layers Suitable for the Definition of Waveguiding Structures through Direct Ultraviolet Writing". *PhD Thesis*, 2002. University of Southampton.

[4] G.D. Emmerson. "Novel Direct UV Written Devices". *PhD Thesis*, 2003. University of Southampton.

[5] D.A.Guilhot. "UV-written devices in rare-earth doped silica-on-silicon grown by FHD". *PhD Thesis*, 2004. University of Southampton.

Chapter 2

Introduction to Waveguide and Bragg Grating Theory

2.1 Introduction

The nature of the work presented in this thesis is such that the emphasis is primarily on experimental results and their subsequent analysis. Whilst the field of UV defined planar waveguides has to date not been well developed the principles which underly their performance are well understood. In the fabrication, characterisation and subsequent development of the devices discussed in subsequent chapters an appreciation of the theory which is the foundation of this work was required. The following sections provide an overview of the principles behind optical waveguides and Bragg gratings and introduces the methods used to model the characteristics of these structures. A wide range of literature is available to provide guidance in this field but the approach used draws heavily on just a few ([1,2,3]).

Throughout this chapter step index waveguides are used to simplify the analysis of both waveguides and Bragg gratings. The UV written waveguides that form the basis of the experimental work of this thesis will not be step index and will have geometries differing somewhat from the idealised structures used here. Nonetheless the subsequent sections allow insight into the fundamental properties of waveguides

and gratings and also provide an excellent means of determining expected performance of the devices discussed in subsequent chapters.

2.2 Principles of Optical Waveguides

A waveguide is a structure that confines and directs wave propagation. Here, in particular, electromagnetic waves are of interest, more specifically, those at optical frequencies. To introduce waveguide theory consideration will first be given to light incident upon an interface between two materials before the approach is extended to a planar slab guide and then onto modelling methods for more specialised structures.

2.2.1 Plane Interfaces

Reflection and refraction are commonly observed phenomena and the interaction of light with a plane surface has long been known, through experimental observation, to obey what is known as Snell's law. This states that the angle of reflection and refraction of an incident electromagnetic wave are related by

$$n_1 sin\theta_1 = n_2 sin\theta_2 \tag{2.1}$$

where θ_1 and θ_2 are the angles of incidence and refraction respectively, n_1 and n_2 are the refractive indices of the materials either side of the boundary as shown in figure 2.1.

For the case $n_1 > n_2$, when the angle of incidence is given by $\theta_1 = sin^{-1}(n_2/n_1)$, the angle of refraction is $\pi/2$ and the refracted wave travels along the interface between the materials. This value of θ_1 is known as the critical angle and any angle greater than this results in no transmitted wave and all power incident on the surface is reflected in a process known as total internal reflection. For the case where $n_1 < n_2$ the angle of refraction can never equal $\pi/2$ and total internal reflection is not possible.

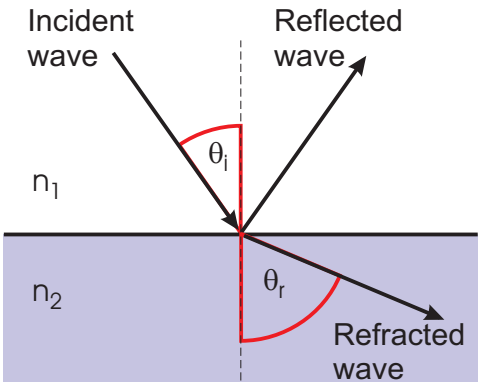

Figure 2.1: Refraction and reflection at a plane interface.

2.2.2 The Slab Waveguide

To gain insight into the properties of optical waveguides the relatively simple case of the symmetric slab waveguide is analysed. Whilst being a rather simplified case this approach has the advantage that optical propagation can be solved analytically rather than requiring computationally intensive numerical methods. Additionally this analysis of the slab waveguide introduces the principles which are required for an understanding of the channel waveguides that are relevant to this thesis.

For the purposes of this analysis the slab waveguide shall be defined as a planar layer, which shall be referred to as the core, of refractive index n_1, of thickness d, extending uniformly in the y and z planes as shown in figure 2.2. For $|x| > \frac{d}{2}$) the core is covered entirely by material of refractive index n_2, where $n_2 < n_1$.

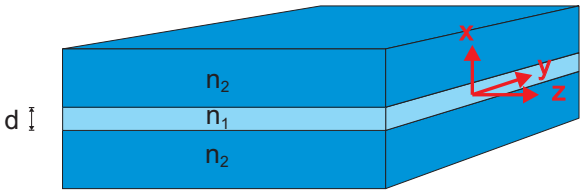

Figure 2.2: The structure of the symmetric slab waveguide.

Maxwell's equations for isotropic, linear, non-conducting and non magnetic media provide

$$\nabla \times \boldsymbol{\mathcal{E}} = -\mu_0 \frac{\partial \boldsymbol{\mathcal{H}}}{\partial t} \tag{2.2}$$

$$\nabla \times \boldsymbol{\mathcal{H}} = \epsilon_0 n^2 \frac{\partial \boldsymbol{\mathcal{E}}}{\partial t} \tag{2.3}$$

$$\epsilon_0 \nabla \cdot (n^2 \boldsymbol{\mathcal{E}}) = 0 \tag{2.4}$$

$$\nabla \cdot \boldsymbol{\mathcal{H}} = 0 \tag{2.5}$$

where $\boldsymbol{\mathcal{E}}$ and $\boldsymbol{\mathcal{H}}$ are the electric field and magnetic field vectors respectively. ϵ_0 is the permittivity of free space and μ_0 is the permeability of free space. The refractive index of the medium in which the light propagates is given by n.

The electric and magnetic fields can be analysed to provide the vectorial wave equation for the medium in which they propagate. Initially, looking at the electric field and taking the curl of 2.2 gives

$$\nabla \times (\nabla \times \boldsymbol{\mathcal{E}}) = -\mu_0 \frac{\partial}{\partial t} (\nabla \times \boldsymbol{\mathcal{H}}) \tag{2.6}$$

Then using 2.3 and rewriting the left hand side provides

$$\nabla(\nabla \cdot \boldsymbol{\mathcal{E}}) - \nabla^2 \boldsymbol{\mathcal{E}} = -\epsilon_0 \mu_0 n^2 \frac{\partial^2 \boldsymbol{\mathcal{E}}}{\partial t^2} \tag{2.7}$$

Since 2.4 can be rewritten as

$$\epsilon_0 \nabla \cdot (n^2 \boldsymbol{\mathcal{E}}) = \epsilon_0 [\nabla n^2 \cdot \boldsymbol{\mathcal{E}} + n^2 \nabla \cdot \boldsymbol{\mathcal{E}}] \tag{2.8}$$

we have

$$\nabla \cdot \boldsymbol{\mathcal{E}} = -\frac{\nabla n^2 \cdot \boldsymbol{\mathcal{E}}}{n^2} \tag{2.9}$$

which can be inserted into 2.7 to obtain

$$\nabla^2 \boldsymbol{\mathcal{E}} + \nabla \left[\frac{\nabla n^2 \cdot \boldsymbol{\mathcal{E}}}{n^2} \right] - \epsilon_0 \mu_0 n^2 \frac{\partial^2 \boldsymbol{\mathcal{E}}}{\partial t^2} = 0 \tag{2.10}$$

This is the wave equation for the electric field propagating through a refractive index n. The materials of the slab waveguide have already been specified as uniform so for light in the core or cladding the second term of the full vector wave equation (2.10) equates to zero leaving

$$\nabla^2 \boldsymbol{\mathcal{E}} - \epsilon_0 \mu_0 n^2 \frac{\partial^2 \boldsymbol{\mathcal{E}}}{\partial t^2} = 0 \tag{2.11}$$

Applying a similar procedure for the magnetic field using equations 2.3, 2.5 and 2.2 the equivalent wave equation is reached

$$\nabla^2 \boldsymbol{\mathcal{H}} - \epsilon_0 \mu_0 n^2 \frac{\partial^2 \boldsymbol{\mathcal{H}}}{\partial t^2} = 0 \tag{2.12}$$

By defining the light propagation direction to be parallel to the z axis and recognising that the refractive index varies only in the x direction, these wave equations have solutions

$$\mathcal{E}_j = E_j(x) e^{i(\omega t - \beta z)} \tag{2.13}$$

$$\mathcal{H}_j = H_j(x) e^{i(\omega t - \beta z)} \tag{2.14}$$

for $j = x, y, z$. In these equations β is known as the propagation constant and ω is the angular frequency of the oscillation.

Thus there are two similar solutions for electric and magnetic fields that can propagate through the slab structure of figure 2.2. These solutions are referred to as the modes of the waveguide and are field distributions that are supported by the system that can propagate such that the transverse field distribution (described by $E_j(x)$ and $H_j(x)$) is constant.

Inserting these solutions back into equations 2.2 and 2.3 and separating the x, y and z components reveals that the physical interpretation of the two equations is one mode with its electric field oscillating in the y-plane and the other with its magnetic field oscillating in the y-plane. These two solutions are responsible for what are commonly referred to as TE (transverse electric) and TM (transverse magnetic) modes and can be reduced to a second order differential equation which describes them. Examining the TE modes the electric field is described by

$$\frac{d^2 E_y}{dx^2} + \left[k_0^2 n^2 - \beta^2\right] E_y = 0 \tag{2.15}$$

where n describes the refractive index structure which only varies in the x direction. k_0, referred to as the freespace wavenumber, is given by $\omega(\epsilon_0 \mu_0)^{\frac{1}{2}}$. Recalling the symmetry of the planar slab and that the core layer of thickness d, centred at $x = 0$ and applying boundary conditions at the core-clad interface allows further reduction of the problem. Within the core layer

$$\frac{d^2 E_y}{dx^2} + \left[k_0^2 n_1^2 - \beta^2\right] E_y = 0 \qquad |x| < \frac{d}{2} \tag{2.16}$$

and in the cladding

$$\frac{d^2E_y}{dx^2} + \left[k_0^2 n_2^2 - \beta^2\right] E_y = 0 \qquad |x| > \frac{d}{2} \tag{2.17}$$

Recognising that 2.16 and 2.17 are of the form

$$\frac{d^2y}{dx^2} + Ay = 0 \tag{2.18}$$

suggests solutions of the form

$$y = Be^{c_1 x} + De^{-c_1 x} \qquad A < 0 \tag{2.19}$$

$$y = Dcos(c_2 x) + Esin(c_2 x) \qquad A > 0 \tag{2.20}$$

where A, B, c_1, c_2, D and E are constants. From the definition of a mode and simple consideration of snell's law, guided modes will conform to a solution of the form of 2.20 and will be mostly confined to the core layer. Therefore,

$$\beta^2 < k_0^2 n_1^2 \tag{2.21}$$

and in the cladding

$$\beta^2 > k_0^2 n_2^2 \tag{2.22}$$

Therefore, in order for guided modes to exist

$$n_2^2 < \frac{\beta^2}{k_0^2} < n_1^2 \tag{2.23}$$

showing that the waveguide core layer must have a higher refractive index core layer than cladding layers. This is a general condition for a mode to be guided and is equivalent to the requirement for total internal reflection as discussed earlier.

Further detail is obtained by applying the requirement for continuity at the boundary between the core and cladding layers. Both E_y and its derivative with respect to x must be continuous at the interface. Symmetry requirements allow additional reduction of the problem as the field within the core must be symmetric or antisymmetric about $x = 0$. The symmetric solutions may be described by

$$E_y(x) = \begin{cases} Acos(\kappa x) & |x| < -\frac{d}{2} \\ Ce^{-\gamma|x|} & |x| > \frac{d}{2} \end{cases} \tag{2.24}$$

and antisymmetric by

$$E_y(x) = \begin{cases} Bsin(\kappa x) & |x| < -\frac{d}{2} \\ \frac{x}{|x|} De^{-\gamma|x|} & |x| > \frac{d}{2} \end{cases} \tag{2.25}$$

where the substitutions $\kappa^2 = k_0^2 n_1^2 - \beta^2$ and $\gamma^2 = \beta^2 - k_0^2 n_2^2$ have been used. Application of the boundary conditions leads to

$$\frac{\kappa d}{2} tan\left(\frac{\kappa d}{2}\right) = \frac{\gamma d}{2} \tag{2.26}$$

and

$$\frac{-\kappa d}{2} cot\left(\frac{\kappa d}{2}\right) = \frac{\gamma d}{2} \tag{2.27}$$

for the symmetric and antisymmetric modes respectively. These two equations describe the modes supported by the slab waveguide.

2.2.2.1 Normalised Parameters

It is frequently more convenient to rewrite the equations describing waveguide modes in terms of dimensionless variables. The 'V number' or dimensionless waveguide parameter is given by

$$V = k_0 d (n_1^2 - n_2^2)^{\frac{1}{2}} \tag{2.28}$$

Similarly, the dimensionless propagation constant is written, for later use, as

$$b = \frac{\beta^2/k_0^2 - n_2^2}{n_1^2 - n_2^2} \tag{2.29}$$

Making use of V, equations 2.26 and 2.27 can be rearranged, providing

$$\frac{\kappa d}{2} tan\left(\frac{\kappa d}{2}\right) = \left(\frac{V^2}{4} - \frac{\kappa^2 d^2}{4}\right)^{\frac{1}{2}} \quad \text{Symmetric Modes} \tag{2.30}$$

$$\frac{-\kappa d}{2} cot\left(\frac{\kappa d}{2}\right) = \left(\frac{V^2}{4} - \frac{\kappa^2 d^2}{4}\right)^{\frac{1}{2}} \quad \text{Antisymmetric Modes} \tag{2.31}$$

The right hand sides of each equation are equal and consequently both left hand sides and the right hand side may all be plotted on the same axes. Such a graphical solution is shown in figure 2.3. The two circular segments (red) correspond to plots of

the right hand side of the equations, by inspection of the equations it can be seen that they represent circles of radius $V/2$, thus each plotted circular segment is an example of a different V numbered waveguide. The points at which the circular plots intersect with the tan and cot functions represent the guided modes of the waveguide. The smaller radius curve is equivalent to $V = \pi$ and so for $0 < V < \pi$ only one mode is guided and the structure is described as single mode. The larger radius segment ($V = 10$) intersects at four points showing that a symmetrical planar slab guide will support four modes (two symmetric and two antisymmetric) when V=10.

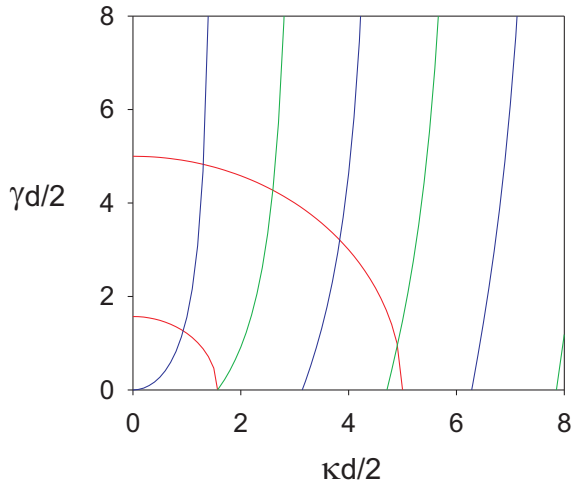

Figure 2.3: Graphical solution for guided modes of a symmetric planar slab waveguide. Blue lines represent symmetric modes, green describes antisymmetric.

It is generally true for a waveguide that the larger V the more modes are supported. From equation 2.28 it can be easily seen that larger core thicknesses and larger index differences $\Delta n = n_1 - n_2$ the larger the V number will be and the more modes that will be guided.

The above process shows how the TE guided modes of the symmetrical planar slab waveguide may be determined. To find the TM modes a similar process is used, however as this provides no additional insight and is well documented in the literature it is not covered here.

2.2.3 The Marcatili Method

In general the properties of channel waveguides cannot be analytically evaluated without turning to numerical methods or making simplifying assumptions. Various methods of differing complexity and flexibility are possible but owing to its straightforward application the method selected to model simple channel waveguides was that of Marcatili. Whilst somewhat less flexible than some available alternatives the approach is found to give good agreement with other more complex techniques.

Several analytical approximations for the analysis of waveguides have been developed as well as highly powerful numerical techniques [4]. The Marcatili method described here and the slightly more refined approximations known as Kumar's method and the effective index method are restricted to rectangular cross section waveguides. Numerical approaches such as finite element analysis (FEM) or the beam propagation method (BPM) are somewhat less simple to implement but allow analysis of complex structures. In the UV writing work of this thesis the exact refractive index profile of the waveguides is unknown and as such, any method used would be relying only on predictions of the waveguide index structure. UV written waveguides can reasonably be expected to have a graded index structure and so, strictly speaking, any analysis should use a numerical technique to take this into account. However, as the waveguide devices that are being produced are intended to propagate only the fundamental mode the benefits of more rigourous modelling become limited.

Figure 2.4 shows a comparison of transverse mode profiles for waveguides with step and gaussian refractive index profiles as shown. The mode shapes have been calculated using a commercial BPM software package and the comparison shows the similarity in fundamental mode shape despite the difference in refractive index profile. Thus, although the precise refractive index profile of a UV defined waveguide is unknown, a waveguide model which assumes a step index profile will provide a very good approximation to the actual waveguide behaviour. Although the difference in effective index of these two examples (1.4×10^{-3}) is not insignificant, given the necessary assumptions on practical index structure and the requirements for single

mode propagation, it was decided that the simplicity but relatively high accuracy of the Marcatili method make it the most attractive technique for the purposes of modelling the simple structures described in this thesis.

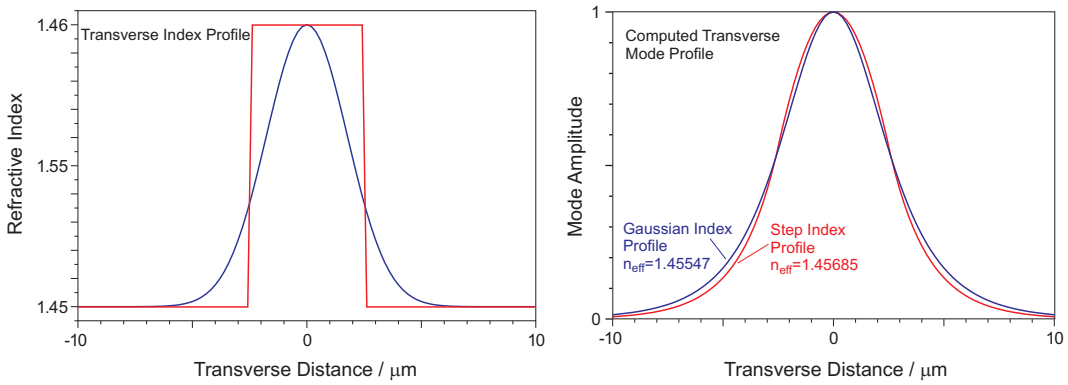

Figure 2.4: Comparison of transverse fundamental mode profiles of step index channel waveguide and gaussian index profile fibre determined at 1550nm using BPM software.

The Marcatili method [5] is a simple method to approximate the effective refractive index of a channel waveguide. The model treats the waveguide core as having a rectangular cross section of refractive index n_1, with cladding on each side of the core of refractive indices n_2, n_3, n_4 and n_5 as shown in figure 2.5. Modelled structures are therefore treated as having step index changes. This is not considered to be a realistic model of the UV defined waveguides of this work but nonetheless the application of this model provides insight into the behaviour and expectations of the fabricated devices. The method is based on the assumption that for a well guided

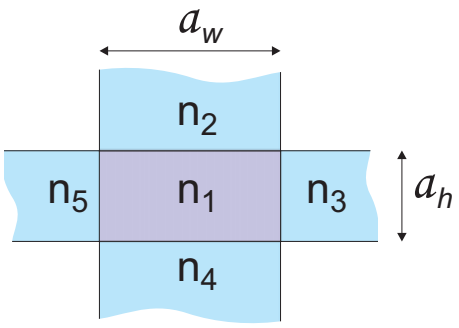

Figure 2.5: The refractive index structure used for the Marcatili method.

mode the field is mostly confined to the core with an exponentially decaying field in the regions 2,3,4 and 5. The unshaded corner regions of the structure of figure 2.5 are assumed to have small enough fields that they can be neglected without significant error being introduced to the calculations. This simplifies the analysis as the requirement to match the fields across the boundaries of the cladding regions is removed. To approximately analyse the modes of the waveguide the structure is treated as two independent slab waveguides in the horizontal (regions n_5, n_1 and n_3) and vertical (regions n_2, n_1 and n_4) directions. Propagation constants may be determined through the use of the appropriate boundary conditions between the core (region n_1) and the surrounding cladding regions. The waveguide effective index can then be determined through calculation of the propagation constant k_z in the direction of propagation. It can be shown [5]

$$k_z = (k_1^2 - k_x^2 - k_y^2)^{\frac{1}{2}} \tag{2.32}$$

$$n_{\text{eff}} = \frac{k_z \lambda}{2\pi} \tag{2.33}$$

where k_x and k_y are the transverse propagation constants in the x and y planes respectively. k_v (v=1,2,$\cdots$5) represents the propagation constant of a plane wave in a region of refractive index n_v.

Through the assumptions of the model the propagation constants can be determined as

$$k_x = \frac{p\pi}{a_w}\left(1 + \frac{A_3 + A_5}{\pi a_w}\right)^{-1} \tag{2.34}$$

$$k_y = \frac{q\pi}{a_h}\left(1 + \frac{n_2^2 A_2 + n_4^2 A_4}{\pi n_1^2 a_h}\right)^{-1} \tag{2.35}$$

Where p and q are used to indicate the number of extrema of the sinusoidal field components within the waveguide core. The values of A are provided by

$$A_{2,3,4,5} = \frac{\lambda}{2(n_1^2 - n_{2,3,4,5,)}^2)^{\frac{1}{2}}} \tag{2.36}$$

In the application of this model the waveguides are assumed to be sufficiently symmetrical to avoid distinguishing between TE and TM polarisations.

Figure 2.6 plots the normalised propagation constant b against the V number for a square cross section channel waveguide calculated using the Marcatili method with $n_2 = n_1/1.05$ and $n_2 = n_3 = n_4 = n_5$. Three TE guided modes are shown, the fundamental ($p = 1, q = 1$) and two higher orders ($p = 2, q = 1$ and $p = 2, q = 2$). Such a plot conveniently displays the propagation constants of the different order modes for a given waveguide structure.

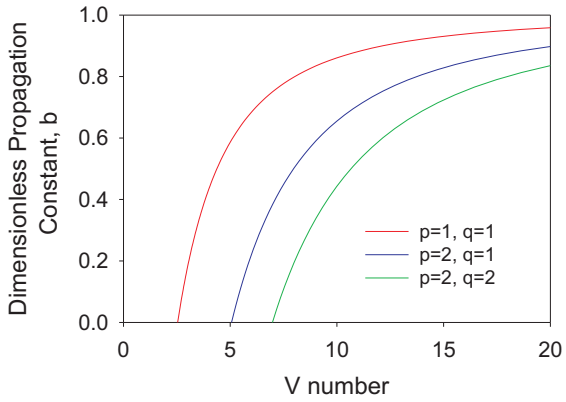

Figure 2.6: Variation of propagation constant with V number as calculated by the Marcatili method.

2.3 Principles of Bragg Gratings

Bragg gratings play a significant role in the applications of UV written waveguides that are presented in the following chapters. In order to interpret the optical behaviour of these structures some knowledge of the underlying principles is required. Extensive reviews of the properties and performance of Bragg gratings are available and those of [2] and [6] provide more detail than the overview provided here and are also used as the foundation of the subsequent discussion.

The majority of Bragg gratings produced today are based in optical fibre and often referred to as fibre Bragg gratings (FBG). Usually defined into a pre-existing waveguiding core most Bragg gratings differ slightly to those defined by the direct UV writing technique that forms the basis of all work in this thesis. The direct writing

approach creates both the optical waveguide and the Bragg grating simultaneously but the analysis of such gratings is the same as that used for FBGs, about which the vast majority of available literature is written.

In the most simple configuration, a Bragg grating is an optical wavelength filter created by the periodic modulation of the effective index of a waveguide. This modulation is most commonly achieved by variation of the refractive index or the physical dimensions of the waveguiding core. At each change of refractive index a reflection of the propagating light occurs. The repeated modulation of the refractive index results in multiple reflections of the forward travelling light. The period of index modulation relative to the wavelength of the light determines the relative phase of all the reflected signals. At a particular wavelength, known as the Bragg wavelength, all reflected signals are in phase and add constructively and a back reflected signal centred about the Bragg wavelength is observed. Reflected contributions from light at other wavelengths does not add constructively and are cancelled out and as a result these wavelengths are transmitted through the grating.

More complex configurations than that described above can be fabricated. The period and amplitude of the index modulation can be controlled along the length of the grating to shape the wavelength response. Additionally the grating planes can be tilted so that they are not perpendicular to the direction of propagation, resulting in light being coupled into the waveguide cladding.

In addition to Bragg gratings, another common class of gratings used in the field of fibre optic components is that of long period or transmission gratings. Such gratings do not provide the reflective response of a Bragg grating but couple selected modes into the fibre or waveguide cladding. Thus transmission dips are observed in a long period grating spectrum but such structures are not used in reflection. This subset of gratings is not discussed further here as it does not play a role in any work presented. However owing to their significant role in evanescent field sensing it is noted that long period gratings play a strong role in optical sensing technology and as such are an alternative to the devices discussed in chapter 9.

2.3.1 Bragg Grating Performance

The following discussion is restricted to uniform Bragg gratings where the grating planes are perpendicular to the direction of wave propagation in the waveguide. The analysis is based on the use of single mode, step index optical fibres which although not identical in structure to the waveguides developed in this thesis, still allows the key principles to be understood. As mentioned earlier the actual refractive index profile of the waveguides fabricated in this thesis is not exactly known, however the assumption is made that in the single mode waveguides of interest here the profile of the fundamental mode is not significantly different to that of an etched rib channel waveguide or a single mode fibre.

Using the principles of energy and momentum conservation the centre wavelength reflected by a uniform Bragg grating (subsequently referred to as the Bragg wavelength) can be determined. For energy to be conserved there can be no change in frequency as a result of reflections at grating planes. For conservation of momentum the sum of the incident wavevector k_i and the grating wavevector K must equal the wavevector of the reflected wave k_r

$$k_i + K = k_r \tag{2.37}$$

When the Bragg condition is satisfied $k_r = -k_i$ and so 2.37 can be rewritten as

$$\frac{2\pi}{\lambda} n_{\text{eff}} + \frac{2\pi}{\Lambda} = -\frac{2\pi}{\lambda} n_{\text{eff}} \tag{2.38}$$

which in turn simplifies to the equation relating the Bragg wavelength, effective index and grating period

$$\lambda_B = 2 n_{\text{eff}} \Lambda \tag{2.39}$$

where λ_B is the Bragg wavelength, Λ is the grating period and n_{eff} is the effective waveguide index.

This simple relation does not provide any information on the bandwidth of the filter response or the strength of the reflection. A common means of predicting this information is the use of coupled mode theory which is found to allow straightforward and accurate modelling of uniform as well as more highly structured gratings. The

results of applying this theory are applied here as the derivation and application to Bragg gratings is discussed in many other topical reviews [6,7].

When the direction of forward propagation is along the z axis, the refractive index profile, $n(z)$, along the Bragg grating can be described by

$$\delta n_{\text{eff}}(z) = \overline{\delta n_{\text{eff}}}(z)\,[1 + cos(Kz)] \tag{2.40}$$

where $\overline{\delta n_{\text{eff}}}$ is the refractive index perturbation averaged over a grating period.

Based on this description, it can be shown that the variation of reflectivity of a grating is given by [6]

$$r = \frac{sinh^2(L\sqrt{\kappa^2 - \hat{\sigma}^2})}{cosh^2(L\sqrt{\kappa^2 - \hat{\sigma}^2}) - \frac{\hat{\sigma}^2}{\kappa^2}} \tag{2.41}$$

where L provides the length of the grating and κ and $\hat{\sigma}$ are coupling coefficients. More specifically,

$$\kappa = \frac{\pi\overline{\delta n_{\text{eff}}}}{\lambda} \tag{2.42}$$

$$\hat{\sigma} = \delta + \sigma \tag{2.43}$$

where

$$\sigma = \frac{2\pi\overline{\delta n_{\text{eff}}}}{\lambda} \tag{2.44}$$

and

$$\delta = 2\pi n_{\text{eff}}\left(\frac{1}{\lambda} - \frac{1}{\lambda_D}\right) \tag{2.45}$$

The detuning, δ, is obtained from the difference between propagating wavelengths, λ, and the design wavelength, $\lambda_D \equiv 2n_{\text{eff}}\Lambda$ for an infinitesimally weak grating.

Equation 2.41 allows the maximum reflectivity to be calculated as

$$r_{max} = tanh^2(\kappa L) \tag{2.46}$$

and determined to occur at

$$\lambda_{max} = \left(1 + \frac{\overline{\delta n_{\text{eff}}}}{n_{\text{eff}}}\right)\lambda_D \tag{2.47}$$

Examples of grating reflectivity are plotted in figure 2.7 where spectra for a range of values of κL are shown. In these spectra the grating length was held constant and the coupling constant varied through the magnitude of the refractive index modulation

forming the grating. Clearly, higher reflectivity is obtained when the amplitude of the refractive index modulation is increased. It is also apparent the the bandwidth of the response is dependent on the grating parameters.

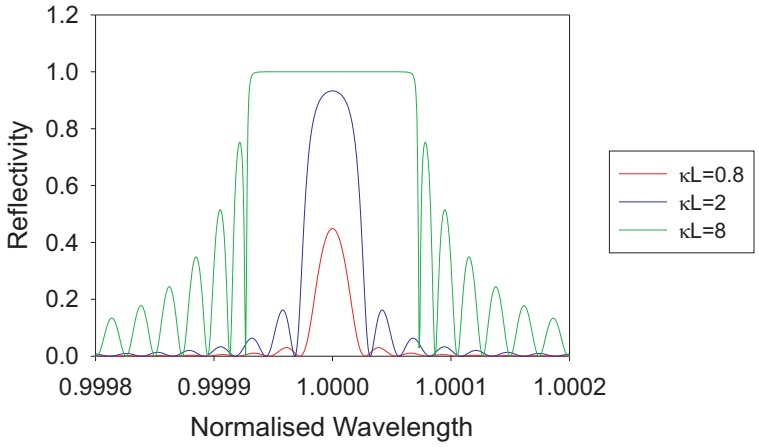

Figure 2.7: Reflection spectra plotted against normalised wavelength for uniform Bragg gratings with κL=0.8,2 and 8 corresponding to a constant length structure with average refractive index increase of 2×10^{-5} , 5×10^{-5} and 1.9×10^{-4} respectively.

A convenient measurement of the bandwidth of the grating response can be taken from the two zeros either side of the maximum reflectivity peak and is commonly expressed as

$$\frac{\Delta\lambda_0}{\lambda} = \frac{\overline{\delta n_{\text{eff}}}}{n_{\text{eff}}}\sqrt{1+\left(\frac{\lambda_D}{\overline{\delta n_{\text{eff}}}L}\right)^2} \tag{2.48}$$

Thus the bandwidth is dependent on both the refractive index modulation and the grating length. For a fixed length grating an example of the variation of bandwidth is shown in figure 2.8. When plotted on logarithmic axes there are two clear regimes of bandwidth dependency on modulation. At low index perturbations the bandwidth shows very low dependence on index modulation. Indeed, for $\overline{\delta n_{\text{eff}}} \ll \frac{\lambda_D}{L}$ the right hand side of equation 2.48 reduces to

$$\frac{\lambda_D}{n_{\text{eff}}L} \tag{2.49}$$

showing that the bandwidth is limited by the grating length. This regime is commonly referred to as the weak grating limit.

In contrast, strong gratings ($\overline{\delta n_{\text{eff}}} \gg \frac{\lambda_D}{L}$) the modulation reduces to

$$\frac{\overline{\delta n_{\text{eff}}}}{n_{\text{eff}}} \tag{2.50}$$

where any dependency on the grating length has been lost. In this limit light close to the Bragg wavelength does not penetrate the full length of the grating and the reflectivity tends towards 100%. Such reflection spectra will be similar to the response shown in figure 2.7 for κL=8.

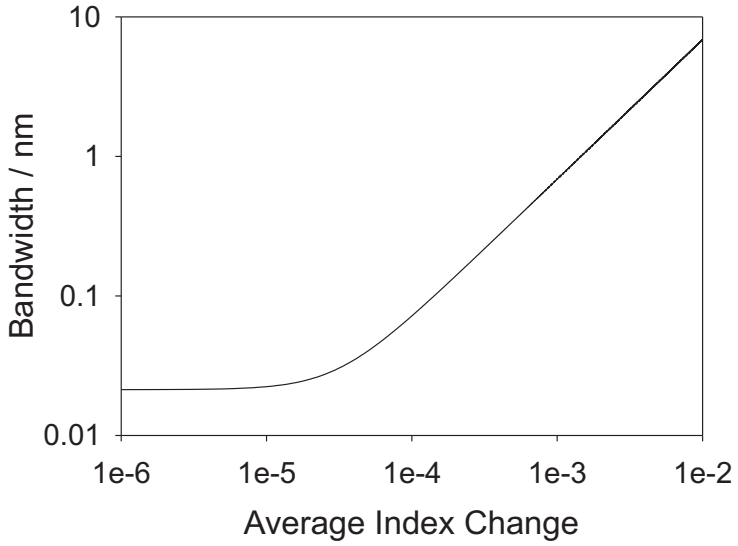

Figure 2.8: Variation of grating bandwidth with average index change of a uniform Bragg grating.

2.4 Summary

The basic properties of optical waveguides and Bragg gratings have been discussed to provide a basic description of the effects of some of the various design parameters. Particular attention was paid to the symmetric slab waveguide and uniform Bragg grating as examples of the two optical structures relevant to the work presented in subsequent chapters. The Marcatili method as a model for channel waveguides was introduced as a means of calculating effective modal indices for any chosen refractive index structure. Whilst the presented discussion is far from comprehensive

the topics that have been covered have been chosen in the context of the following chapters and the results and analysis presented therein.

2.5 References

[1] A.Ghatak and K.Thyagarajan. *Introduction to Fiber Optics*. Cambridge University Press, 1998.

[2] A.Othonos and K.Kalli. *Fiber Bragg Gratings. Fundamentals and Applications in Telecommunications and Sensing*. Artech House, 1999.

[3] R.Kashyap. *Fiber Bragg Gratings*. Academic Press, 1999.

[4] K.Okamoto. *Fundamentals of Optical Waveguides*. Academic Press, 1992.

[5] E.A.J.Marcatili. "Dielectric Rectangular Waveguide and Directional Coupler for Integrated Optics". *The Bell System Technical Journal*, 48(7):2071–2012, 1969.

[6] T.Erdogan. "Fiber Grating Spectra". *IEEE Journal of Lightwave Technology*, 15(8):1277–1294, 1997.

[7] D.K.W.Lam and B.K.Garside. "Characterization of single-mode optical fiber filters". *Applied Optics*, 20(3):440–445, 1981.

Chapter 3

Waveguide and Bragg Grating Definition Techniques

3.1 Introduction

The previous chapter provided a definition and brief analysis of optical waveguides. Now, attention is turned to methods of creating such structures *i.e.* waveguide cores surrounded by cladding on all sides. Waveguides may be defined in a variety of materials and are routinely fabricated in crystals, glasses and polymers. Here silica is the material of interest and as such, the discussion is biased significantly towards techniques used in silica. The methods presented are in some cases applicable to other materials but the overlap between these media and silica is not discussed. Similarly, techniques of forming the silica used in waveguide formation are not discussed here as this is the topic of chapter 4.

Relatively speaking, direct UV writing is a recent development in the definition of planar waveguides. Therefore, to provide a historical perspective and a basis for comparison more established methods of waveguide definition are introduced.

Direct UV writing is then introduced and some of its advantages over the more 'traditional' techniques described. The particular extension to the direct writing technique upon which the work in this thesis relies heavily is the process of Direct

Grating Writing (DGW). This technique, developed and first demonstrated by previous members of the author's research group allows the simultaneous definition of waveguides and Bragg gratings within a planar substrate. The process is flexible and applicable to a wide range of devices such as those discussed in the subsequent chapters.

To introduce the two related topics of waveguide and grating definition the chapter is divided into two. Initially the subject of channel waveguide definition is discussed with particular reference to the common technique of photolithography and then detail on the use of direct UV writing is provided.

Methods of fabricating Bragg gratings are predominantly fibre based and as such the appropriate background detail has a heavy fibre bias. After discussing common fibre Bragg grating manufacture techniques the extension to the production of planar Bragg gratings is described. In this way the UV exposure techniques pertinent to all devices produced in this thesis are fully explained.

3.2 Channel Waveguide Definition Techniques

Generally speaking there are two routes towards creating the refractive index structure required to form a channel waveguide. Materials of different refractive index can be deposited or bonded to one another or an external influence can be used to cause localised changes to the refractive index of a pre-made substrate. Of the latter group of techniques perhaps the most notable are ion implantation or ion diffusion.

The most prevalent technique of defining waveguides in planar light circuits is the use of etching and photolithography. The process is shown in diagrammatic form in figure 3.1. A continuous layer of the material required for the waveguide core is deposited onto a layer of the required underclad material (figure 3.1a). This substrate is covered in a thin layer of photoresist by spin coating. The resist layer is then exposed to UV light through a specially designed mask such that the regions where a waveguide core is required are exposed to UV (figure 3.1b, c). The exposure causes cross linking of the polymer structure such that a developing step can

be used to wash away the unexposed resist leaving the substrate patterned with an etch resistant layer (figure 3.1d). Thus after developing the treated substrate may be etched (for example by reactive ion etching) to remove the areas of the core material that were exposed through the mask (figure 3.1e). Remaining photoresist is removed through a solvent cleaning process. The resultant structure is a raised profile of waveguide core over an undercladding layer (figure 3.1f). This rib structure may be left in this state such that air acts as the overclad layer. Typically however, to isolate the structure from external influences an additional overclad layer is deposited over the rib structure to produce a fully buried waveguide device (figure 3.1g). Photolithography and etching is a well proven technique for the mass production of planar waveguide devices but it does have its limitations. Ultimately the smallest structure that can be defined is determined by the quality of the mask manufacture and the UV exposure. Current capabilities allow rectangular cross section waveguides of the order of a few hundred nanometres to be defined and etched [1]. The etch stage to remove the unwanted regions of core layer requires a well controlled and characterised process. Avoidance of waveguide sidewall roughness and symmetry of the cross section requires care during fabrication to avoid waveguides with high loss, high birefringence or undesirable mode shapes. Other difficulties relate to the final overclad deposition process where it is possible for voids in the overclad to occur in the vicinity of small features such as the intersection of two planes (*e.g.* where rib waveguide meets underclad).

3.2.1 UV Writing

Chapter 5 discusses the phenomenon of photosensitivity in doped silica. In the meantime it is sufficient to mention that on exposure to UV light in the region of 244nm certain silica compositions display an increase in their refractive index. This can be exploited through UV writing to produce optical waveguides. Restricting the areas of silica that are exposed by the use of a mask can allow features with dimensions suitable for single mode optical propagation. Here, the emphasis is on the use of UV writing into silica but a range of glasses and polymers have also been shown to be suitable for UV definition processes.

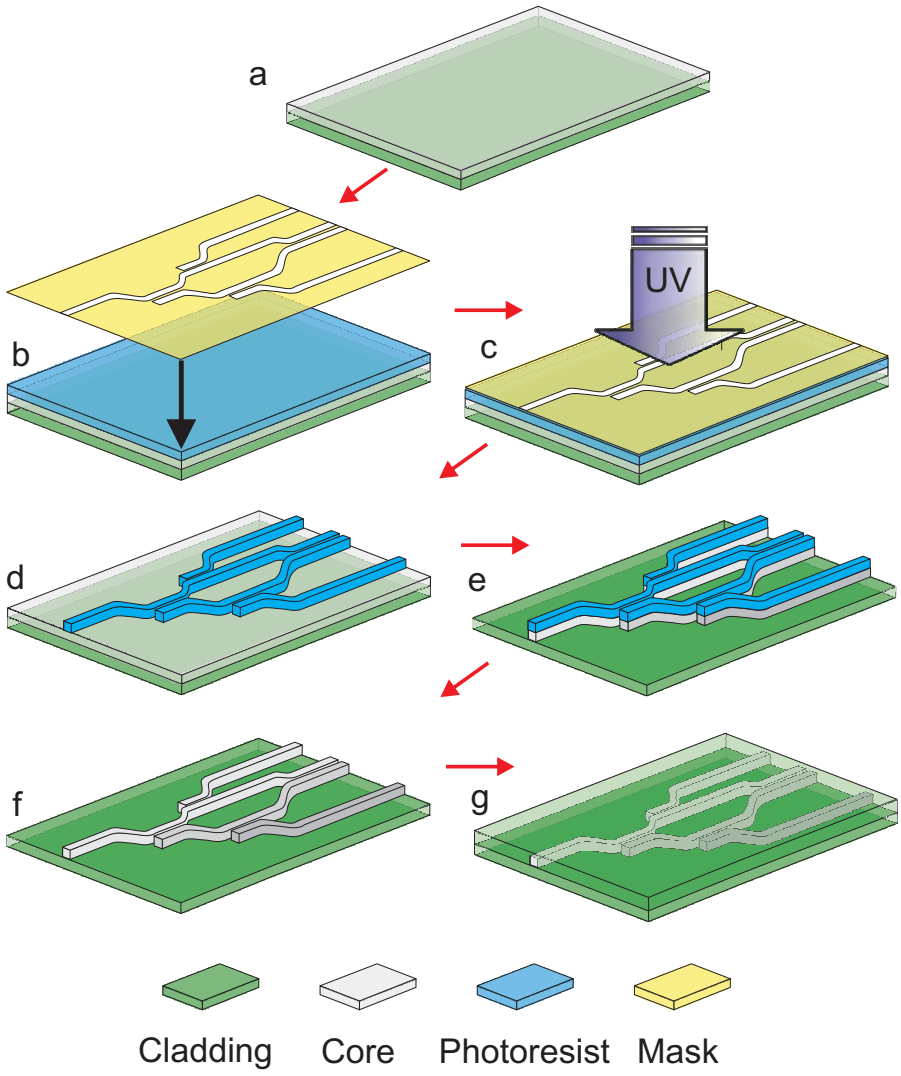

Figure 3.1: Schematic representation of the key stages in the production of buried etched waveguides. Individual steps are described in the text.

Such fabrication methods offer few advantages over the etched waveguide equivalents as mask design is still required prior to device manufacture and the opportunity to use core and cladding of different compositions is lost. However, a particular class of UV writing, that of Direct UV writing, offers several notable advantages that are exploited in this thesis.

3.2.2 Direct UV Writing

In contrast to the photolithography based etched waveguide, direct UV writing uses a single stage process to define waveguides into a previously fabricated sample. No addition or removal of material occurs during the direct write process and no masks are required to define the waveguiding structure that is desired.

Like the more general case of 'ordinary' UV writing, the technique utilises the photosensitivity of doped silica to generate a localised refractive index change and thereby define an optical waveguide. Rather than using a wide area exposure that is restricted using a mask, direct writing uses a focussed optical exposure such that the dimensions of the UV induced structure are determined by the focussed spot size (typically a few microns in diameter). Although the direct writing technique was used as early as 1974 to produce single mode waveguides in polymer [2] it was not well developed until the work by Svalgaard [3] exploited the photosensitivity of doped silica for the definition of a variety of single mode waveguiding devices.

Figure 3.2 shows the simple principles behind direct UV writing. A prefabricated, photosensitive sample with no inherent waveguiding structures is translated in two dimensions beneath the focussed UV beam. Straight waveguides of arbitrary length and direction can be defined as well as curves of any selected radius. The effective limit on the size of device that can be produced is determined by the maximum distance offered by the translation stages in use and the size of substrate that may be fabricated.

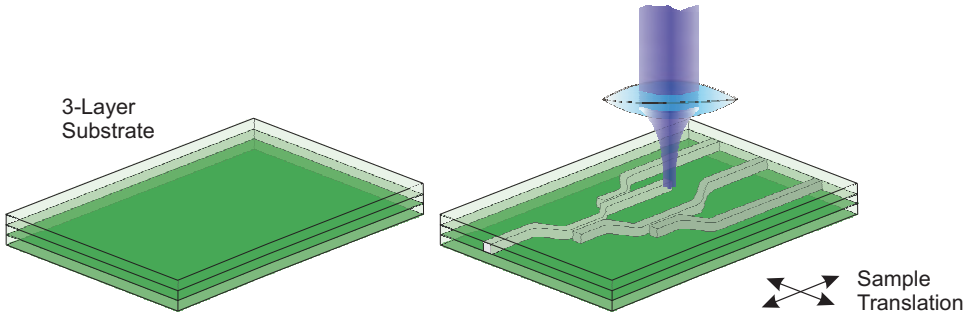

Figure 3.2: Single beam direct UV writing.

3.2.2.1 Fluence

Up to the point at which UV induced refractive index change saturates, the longer and more intense the UV exposure is, the greater the resultant refractive index change will be. This allows control over not just the layout of waveguides but also the strength of the mode confinement within the guide. To quantify the exposure used for UV writing, the concept of fluence is introduced. Fluence is a measure of the energy delivered to the sample and is dependent on both the UV power and the translation speed. The fluence, F, measured in units of kJcm^{-2} is expressed as

$$F = \frac{I_{UV} \times a}{v_{translation}} \tag{3.1}$$

where I_{UV} is the average power density of the writing spot (KWcm^{-2}), a is the spot diameter (cm) and $v_{translation}$ is the translation speed (cms^{-1}).

3.2.2.2 Substrates for UV Writing

A term that is frequently used in the context of direct UV writing is that of the index-matched three-layer sample. This, as the name suggests is a sample which has been fabricated to provide three (or more) layers of silica on a substrate (most commonly silicon) such that each layer has the same or very similar refractive index. More specifically the layers are designed such that the central core layer is photosensitive whilst the outer two cladding layers are not. Upon exposure to UV the core layer undergoes a refractive index increase whilst the cladding layers remain unchanged. When the UV exposure takes the form of a translating focussed spot the end result is a buried waveguide.

3.2.2.3 Waveguide Layout

Translation of the sample relative to the UV beam is performed under computer control such that the required layout is defined in software and loaded into the stage control system. The software used for the work in this thesis was G-code, a standard language commonly used in the control of CNC (computerised numerical control)

milling machines. Using this language, linear translation speeds and distances in the x and y directions may be simply described allowing waveguides in any direction to be defined. Curved waveguides are not used in the work presented in the following chapters but are easily generated through the definition of multiple short straight sections of incrementally varying directions.

3.2.3 Advantages and Disadvantages of Direct UV Writing

As a technique direct UV writing provides a straightforward route towards rapid prototyping of waveguiding devices. Once suitable three layer substrates are available all layout work is carried out entirely in software before the UV exposure is performed. Additionally, as the core layer is covered by cladding layers no clean room precautions are required during the writing process. Simple cleanliness requirements must be observed to ensure no gross level of contamination is present on the sample surface but this is found to be a simple precaution experimentally.

Complex or large devices can require long fabrication times as each waveguide segment must be written one after the other rather than in the 'parallel' fashion allowed by photolithography. The refractive index contrast of silica UV written structures has been demonstrated to be as high as 2×10^{-2} [4] but are more commonly of the order of 1×10^{-3} or lower.

It must also be remembered that in direct UV writing, the minimum feature size that may be defined is determined by the focus spot size and the resolution and accuracy of the translation stages. In the photolithographic case, limitations are imposed by the quality of the mask production and the reliability of the exposure stage.

For the purposes of comparison a summary of these key features of Direct UV writing are compared with the photolithographic equivalent in table 3.1. In a very general sense UV writing is well suited to the production of small to medium volumes where rapid development, design flexibility and low initial investment (i.e. no photolithographic masks) are a priority. For medium to volume production, the ability to simultaneously fabricate multiple devices with high repeatability makes photolitho-

graphic methods more appealing

Feature	**Direct UV Writing**	**Photolithography**
Cleanliness Requirement	Low	High
Available Index Contrast	Low-Medium	Low-High
Production Cost:		
Low Volumes	Low	High
High Volumes	Medium-High	Low
Production Time:		
Low Volumes	Low	High
High Volumes	High	Low

Table 3.1: Comparison of key features of direct UV writing and photolithographic production.

3.3 Bragg Grating Definition Techniques

The introduction to photosensitivity in silica (chapter 5) describes the first, non-intentional fabrication of a fibre Bragg grating by Hill and co-workers [5]. A standing wave caused by the reflections from the fibre ends caused the 488nm signal to induce a periodic refractive index change in the fibre core. This first example produced a narrowband reflection centred at the writing wavelength. Since that time the definition of grating structures has been heavily developed with several techniques providing the means to produce gratings operating at any wavelength with arbitrary wavelength profiles

To place the planar Bragg grating fabrication process into context a summary of key developments of the prior work based in fibres is necessary. Whilst some specific references to notable work are provided here more thorough overviews are provided in both [6] and [7].

3.3.1 Fibre Bragg Gratings

Applications of the so-called self written gratings observed by Hill are limited as they provide a narrow response (∼200MHz) centred at the writing wavelength. This limits the gratings to operate at wavelengths where a sufficient photosensitive response occurs. It was not until the development of a side-writing technique over a decade later that it became possible to define gratings over a wider range.

Using a 244nm source an interferometer was arranged by simply splitting and recombining the laser beam at an angle as shown in figure 3.3 [8].

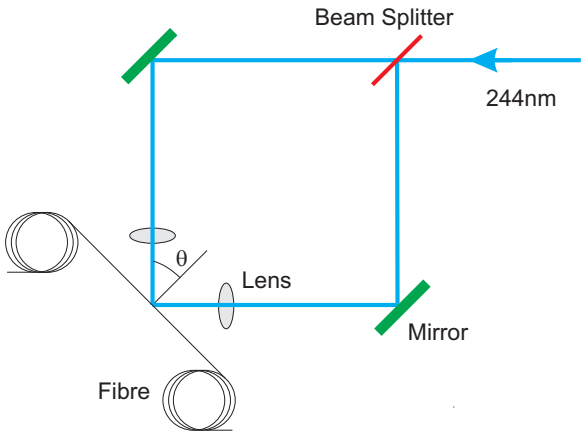

Figure 3.3: Interferometer used for side exposure of fibres in the production of Bragg gratings.

The recombination of the two beams after splitting generates an interference pattern the period of which is determined by the angle of intersection of the two beams such that the period of the intensity variation Λ is

$$\Lambda = \frac{\lambda_{UV}}{2sin\theta} \tag{3.2}$$

where θ is the intersection angle as shown in figure 3.3 and λ_{UV} is the wavelength of the writing beams. The Bragg wavelength is therefore determined by the angle of intersection and not just the writing wavelength. Manipulation of the beam profiles using cylindrical lenses allows the size of the focussed interference pattern to be controlled and thus the grating length determined. Whilst dramatically improving the flexibility of the writing technique the method demands high levels of stability

in the temporal and spatial beam characteristics as well as the requirement for the minimisation of mechanical vibrations or air currents through the interferometer. Any variation in the interference pattern can significantly reduce the grating quality through reduction of the contrast of the grating planes.

3.3.1.1 Phase Masks

An alternative to splitting the laser beam to create an interferometer is the use of phase masks. These are diffractive elements which give rise to a spatial modulation of the incident UV light. Masks are fabricated from silica plates and one surface is etched to provide a periodic relief structure acting as a diffraction grating. Typically such masks are designed to minimise the zeroth order diffracted light such that maximum incident light is transferred to the ±first orders. It is these diffracted orders which interfere with one another resulting in an periodic intensity variation of a period that is half that of the mask (figure 3.4). To inscribe a grating into a fibre the mask is positioned in close proximity to the fibre such that the interference pattern produces a corresponding refractive index modulation in the fibre core.

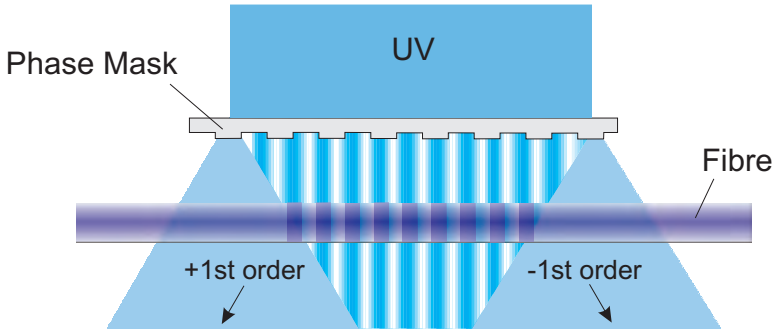

Figure 3.4: Definition of fibre Bragg grating using a phase mask.

Use of phase masks in this way alleviates the problems of mechanical vibration associated with free space interferometers such as that shown in figure 3.3. Additionally, as there is essentially only one optical path involved, requirements in the temporal coherence of the source can be relaxed. Spatial coherence of the beam can however be critical. As the fibre-mask distance increases, the diffracted beams which interfere

at the fibre core will originate from points on the mask more distant from each other resulting in a strong dependence on the spatial properties of the incident beam.

3.3.1.2 Point by Point Definition

Perhaps the most conceptually straightforward means of grating definition is the point by point technique. In this case the UV beam is incident upon a slit which is imaged onto the fibre core. A single pulse of the laser is used to write a single grating plane in the fibre core. Relative translation of the fibre to the slit allows multiple planes to be defined and a Bragg grating created. The technique is limited by the dimensions of the individual planes which can be too large to be of use for first order gratings at telecommunications wavelengths. Production times can also be very lengthy resulting in the need for careful control of thermal and stress effects in the fibre over time to avoid alteration of the effective period. This method does however provide a high level of control over the grating structure as apodisation and chirping are controlled simply by variation of the UV power and translation step size respectively.

3.3.2 Long and Highly Structured Gratings

Manipulation of beam profiles, careful mask design or variation of fibre strain during the writing process can allow the methods described above to be extended for the fabrication of apodised or multiple wavelength gratings. Often however, requirements for long and complex grating structures makes such techniques impractical. To overcome this issue, inscription methods based on constant period phase masks or interferometers have been developed. Formation of the complete grating structure is achieved through the combination of multiple sub-gratings each of which has their amplitude and phase controlled relative to other sub-gratings. An example of this, following the work of [9] is shown in figure 3.5.

The fibre is translated at a carefully controlled speed beneath the interference pattern (obtained via an interferometer or phase mask) whilst the UV laser is pulsed.

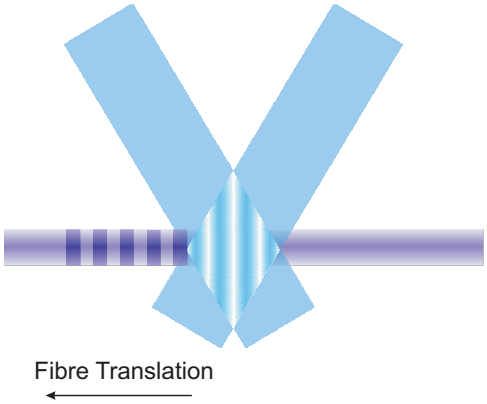

Figure 3.5: Side writing of fibre using multiple exposures for definition of long or complex Bragg gratings. UV beams are modulated at the correct rate relative to the translation speed. Note: Typically the interference pattern will contain 10s or 100s of periods, far more than shown here.

Short pulses (∼10ns) mean that the fibre is essentially stationary for each exposure. The laser is modulated such that each sub-grating is defined at the desired point in the fibre. In this way gratings can be formed by multiple concatenated exposures, have phase differences inserted between each sub-section or be apodised through variation of the writing power in each section.

An alternative approach, again using a uniform phase mask has been developed utilising translation of both the UV light source and either the phase mask or the fibre [10]. The relative speed of the light source to the phase mask (or fibre) determines the period of the index modulation that is inscribed into the fibre thus providing control over the Bragg wavelength of the resultant structure.

3.3.3 Planar Bragg Gratings

Suitably doped silica planar waveguides can have Bragg gratings inscribed using techniques very similar to those previously described for FBGs. Of these methods the use of application specific phase masks positioned directly over the substrate for UV exposure is most common.

Additionally owing to their more robust nature, planar based gratings can be de-

fined using surface relief. In this case the waveguide effective index is modulated by variation of the material through which light propagates (e.g. figure 3.6). Such structures can be challenging to fabricate and require very uniform etching to maintain the grating uniformity.

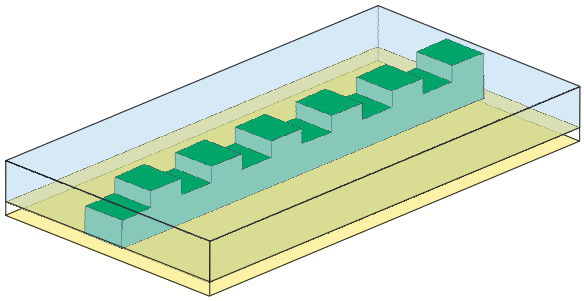

Figure 3.6: Example of buried relief grating. Alternative versions can use air as the 'overclad' layer or periodic variation of the overclad material to vary the effective index.

3.3.4 Direct Grating Writing

Direct Grating Writing (DGW) is a technique developed at the Optoelectronics Research Centre as a particularly flexible route towards the inscription of Bragg gratings into planar substrates. The technique is an extension of the direct UV writing process already described. The key difference between direct writing and DGW is that the latter uses two beams focussed onto the same spot rather than a single beam (figure 3.7). This arrangement can be used to define waveguiding structures in exactly the same way as the single beam arrangement but owing to the twin beam arrangement allows the additional benefit of Bragg grating definition. Where the two beams overlap an interference pattern occurs with a period determined by the angle between the beams, just as in the case of the free space interferometer of figure 3.3. This intensity profile is used in an analagous manner to define the refractive index profile of the waveguide. In a single process step both waveguides and Bragg gratings can be defined into one sample. Further, the Bragg grating is defined as a waveguiding element in a single step and not superimposed onto a predefined waveguide. A schematic diagram of the DGW equipment is shown in figure 3.8. In

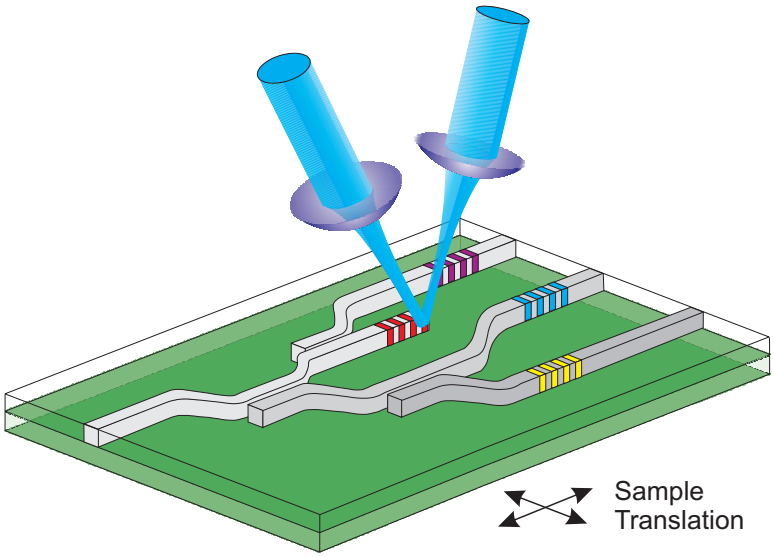

Figure 3.7: Crossed beam writing arrangement for the definition of waveguide and Bragg grating structures.

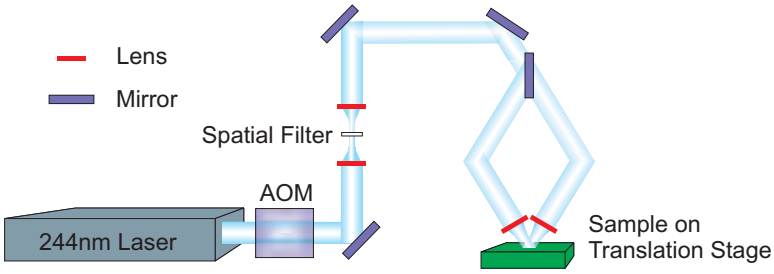

Figure 3.8: Schematic of the cross beam UV writing setup.

use the DGW system may be treated as a standard direct writing system with the UV beam on constantly. In this mode Bragg gratings are not written because the profile resulting from the interference pattern is flattened as the focussed spot translates over the sample resulting in the definition of an unmodulated waveguide. In the same process step, Bragg gratings can be inscribed into the sample through the careful modulation of the UV beam.

The production of gratings can be viewed as the successive definition of multiple, overlapping sub-gratings. When defining a grating the UV beam is modulated using an acousto-optic modulator (AOM) at rate determined by the speed of sample translation and the period of the interference pattern. In the simplest case, the modulation is timed such that each exposure occurs after the sample has been translated by

a distance equal to the period of the interference pattern modulation. The focussed spot diameter of the beam is approximately 4μm with the total angle of intersection between the beams 26° . Thus the intrinsic period of the interference pattern is approximately 542nm resulting in approximately 7 periods being contained within the focussed spot. Therefore each grating plane is the result of 7 exposures.

Translation of the stages is monitored using a Zygo interferometer which provides the input signal to the logic circuits which in turn control the AOM, modulating the beam at the correct points. The translation unit is an Aerotech air bearing stage providing two dimensional movement to a resolution of 500nm. Design and implementation of the UV writing setup was performed by previous members of the author's research group, notably A.Fu, G.Emmerson and C.Gawith.

Where the DGW technique differs from that of the fibre grating is in the fundamental nature of the unwritten samples. Fibres are produced with a refractive index profile such that a waveguide is present before any steps towards defining a grating are taken. In contrast, samples for direct UV writing and DGW do not necessarily have a pre-defined waveguide structure and are effectively 'blank'. The dimensions of a fibre grating waveguide core are predetermined by the fibre core itself whilst in DGW the grating section is automatically of the same dimensions of any accompanying waveguide as both sections are defined by the UV spot.

3.3.5 Wavelength Detuning

In addition to the flexibility allowed by the single stage inscription of waveguides and gratings a further advantage is through the use of the small spot size. Modulation of the laser as described above will result in a grating period equal to that of the UV interference pattern as each intensity peak of the pattern coincides with the position of a grating plane from another exposure. If the translation step between each exposure is made to differ slightly from the period of the interference pattern the result of multiple exposures is a refractive index profile with a period of the translation step size which may be greater or smaller than the period of the interference pattern. As an example, figure 3.9 shows a simple model of the effects of multiple exposures

in a standard and detuned grating using a theoretical spot containing N=4 periods of the interference pattern of period Λ. In the standard case (blue) each translation step is equal to the period of the intensity modulation in the writing spot. The first three (N-1) periods of the refractive index modulation show a smaller amplitude as the first three grating planes are not exposed to each of the peaks of the intensity profile. Such an entrance sequence is always present in DGW gratings. The detuned case (red) is the result of the translation distance being set to δ=0.1 units greater than the intrinsic period of the interference pattern. After the initial N-1 exposures the period of the defined Bragg grating is constant at $\delta + \Lambda$ until the final N-1 grating planes which show a similar exit sequence to the entrance characteristics described above. The detuning process has been further characterised in [11] and is shown to be capa-

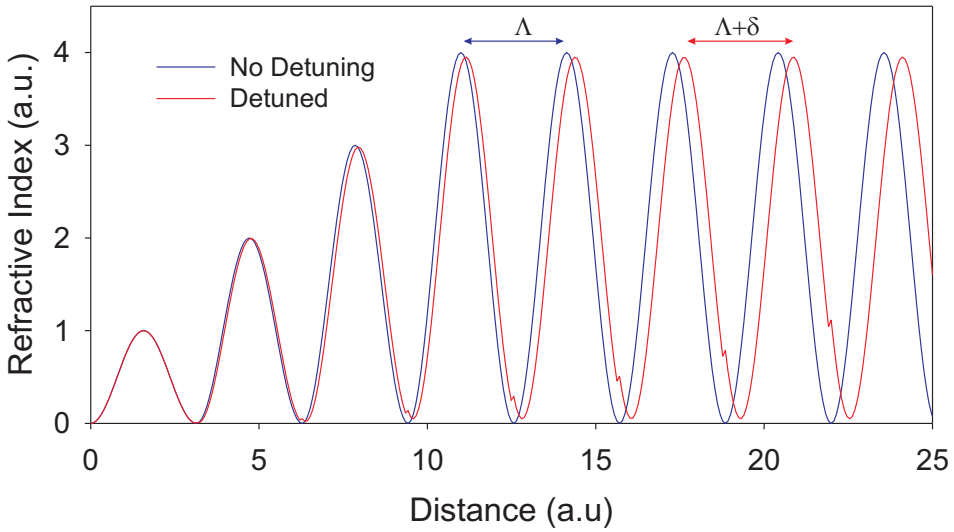

Figure 3.9: Simple mathematical simulation of the effect of detuning on the Bragg grating period. Here the writing spot is treated as containing 4 periods of the interference pattern. After each exposure the writing spot is translated to the right. The difference in resultant period can be clearly seen. Slight discontinuities in the detuned index profile are the result of the relatively low numerical resolution used in this simple model.

ble of a variation of at least 170nm in grating period (480µm variation in Bragg wavelength) purely through control of the translation step size. Consequently, Bragg gratings operating at a wide range of wavelengths can be added, entirely through

software control, to the vast range of structures that may be defined in a single step by direct writing.

3.3.6 Duty Cycle and Fluence Matching

Two terms that are used in later chapters are those of duty cycle and fluence matching. Duty cycle refers to the symmetry of the refractive index profile that is defined to form a Bragg grating. Consider a grating to be made up of alternating high and low index grating planes. The duty cycle is a measure of the width of the high index planes relative to the low. For a uniform grating the frequency of the UV modulation is constant but the proportion of time that the laser is on during each modulation may be varied. The duty cycle is the fraction of each modulation period that the laser is on. Therefore, a 100% duty cycle is equivalent to the laser always on and 0% results in the laser remaining off. All values between these extremes produce a modulation of refractive index. Prior work [11] has shown that the grating index perturbation, and therefore bandwidth, can be controlled through the variation of duty cycle. For a given UV exposure level, higher percentage duty cycles provide reduced bandwidth whilst lower values result in a greater index perturbation.

It is easy to see that variation of duty cycle causes a corresponding variation in the overall fluence delivered to the photosensitive sample. Higher duty cycles, where the UV exposure last for a greater period of time, result in higher total fluence. This can be compensated for using the translation speed of the sample. For example, an unmodulated waveguide may be defined at a fluence of 20kJcm^{-2} , translating at 10mm/min. A concatenated grating section using a 50% duty cycle will therefore receive a total fluence of 10kJcm^{-2} if the translation speed is not changed. Dropping the translation rate to 5mm/min for the duration of the grating exposure results in both the waveguide and Bragg grating being defined with the same fluence. This is a particularly useful feature and offers, for example, the possibility of pure apodisation of grating profiles where no change in average effective index occurs between the input and output waveguides and over the whole length of the grating. In contrast, the refractive index perturbation of fibre Bragg gratings is superimposed onto

a predefined waveguide core. Thus the grating causes a change in the average effective index of fibre over the length of the grating.

Fluence matching is also used in subsequent chapters to infer the effective index of an unmodulated waveguide, demonstrating its use as a design and analysis technique. This relationship can be made due to the matched nature of gratings and waveguides. When matched, the two waveguiding structures are defined under the same UV exposure regimes and can thus be expected to display the same characteristics over time, temperature and other environmental conditions. The same cannot be said for UV defined gratings produced through other techniques such as phase masks. These other methods require that the grating is defined in a pre-existing waveguide and as such the refractive index changes induced must be additive. This means that the effective indices of the waveguide and grating differ, and the waveguide modal index cannot be inferred from the Bragg wavelength. This effect can be alleviated by defining only a weak grating into the pre-defined waveguide to minimise the change to the average effective index but this has the disadvantage that the waveguide, necessarily defined using a much higher fluence regime, is likely to display different stability characteristics to the low fluence grating planes. Thus, additive gratings are less valuable as a diagnostic and analysis technique than their DGW equivalents.

3.4 Summary

After introducing the most common planar waveguide definition technique of photolithography and etching the direct UV writing technique has been discussed and some of the key features of the two techniques compared. The direct writing method is then expanded to detail the direct grating writing (DGW) technique that forms the basis of much of the work in this thesis. To place DGW in context a summary of the key methods of fibre Bragg grating production has been provided.

It is clear that each planar waveguide technique offers particular advantages and it is unlikely that UV writing will replace etched waveguides as the technique of choice

for the mass production of silica waveguides. However, for low production numbers or specialist devices the direct writing and DGW techniques offer some significant advantages in terms of cost and flexibility.

3.5 References

[1] M.Gnan, H.M.H.Chong, and R.M.De La Rue. "Photonic Wire Bragg-Grating Stop-Band Filters in Silicon-on-Insulator". *Proceedings of 12th European Conference on Integrated Optics, Grenoble*, (FrA1-5):310–313, 2005.

[2] E.A.Chandross, C.A.Pryde, W.J.Tomlinson, and H.P.Weber. "Photolocking - A new technique for fabricating optical waveguide circuits". *Appl. Phys. Lett.*, 24(2):72–74, 1974.

[3] M. Svalgaard. "Ultraviolet light induced refractive index structures in germanosilica". *PhD Thesis*, 1997. Technical University of Denmark.

[4] M. Svalgaard and K.Faerch. "High Index Contrast UV-Written Waveguides". *Proceedings of 12th European Conference of Integrated Optics, Grenoble*, pages 522–525, 2005.

[5] K.O.Hill, Y.Fujii, D.C.Johnson, and B.S.Kawasaki. "Photosensitivity in optical fiber waveguides: Application to reflection filter fabrication". *Appl. Phys. Lett.*, 32(10):647–649, 1978.

[6] A.Othonos and K.Kalli. *Fiber Bragg Gratings. Fundamentals and Applications in Telecommunications and Sensing*. Artech House, 1999.

[7] R.Kashyap. *Fiber Bragg Gratings*. Academic Press, 1999.

[8] G.Meltz, W.W.Morey, and W.H.Glenn. "Formation of Bragg gratings in optical fibers by a transvere holographic method". *Optics Letters*, 14:823–825, 1989.

[9] A.Asseh, H.Storøy, B.E.Sahlgren, S.Sandgren, and R.A.H.Stubbe. "A Writing Technique for Long Fiber Bragg Gratings with Complex Reflectivity Profiles". *IEEE Journal of Lightwave Technology*, 15(8):1419–1423, 1997.

[10] W.H.Loh, M.J.Cole, M.N.Zervas, S.Barcelos, and R.I.Laming. "Complex grating structures with uniform phase masks based on the moving fiber-scanning beam technique". *Optics Letters*, 20(20):2051–2053, 1995.

[11] G.D. Emmerson. "Novel Direct UV Written Devices". *PhD Thesis*, 2003. University of Southampton.

Chapter 4

Planar Silica Deposition

4.1 Introduction

This chapter provides an introduction to the methods that can be used to fabricate planar layers suitable for the production of waveguiding structures in silica. A brief discussion of the requirements of the layers is provided along with a description of commonly used dopants and their effects on layer properties. Particular attention is given to the techniques of plasma enhanced chemical vapour deposition and flame hydrolysis deposition as they are the two techniques used to fabricate the planar substrates used in this thesis.

Many routes towards the creation of an optical waveguide exist, perhaps the simplest demonstrated in 1841 by Daniel Colladon. Although more commonly attributed to John Tyndall, Colladon's experiment demonstrated total internal reflection in a jet of water pouring from a tank. Since then, advances in technology have allowed a multitude of materials and techniques to be developed for the purposes of optical waveguiding. Polymers, glasses, crystals and micro- or nano-structured materials have all been researched for a variety of applications. As the focus of the work presented in this thesis is silica waveguides this chapter primarily describes the methods of silica deposition used for waveguide applications.

Silica has been the material of choice for improving optical transmission since the

1960s and vast distances of silica optical fibre are installed across the world in telecommunications systems. Such fibres offer low optical loss in the 1550nm window that is commonly used for such communications. It is of little surprise then that integrated optical components designed to manipulate signals at telecommunications wavelengths are commonly also fabricated using silica. This allows the refractive index of the component waveguides to match that of the silica based optical fibre with which it is coupled, resulting in a low coupling loss.

4.2 Requirements for planar waveguide layers

On the simplest level, the requirements for planar waveguides are that a channel with a given refractive index exists within a medium of somewhat lower refractive index (typically of the order of 1% lower) such that light can propagate with low transmission loss. Practically however, there are various parameters which must be controlled in order to produce high performance waveguides.

4.2.1 Optical Loss

In order that a waveguide lives up to its name and is capable of guiding light for useful distances there must be low levels of optical absorption or scattering. Absorption can be the result of impurities in the silica or a fundamental property of the silica itself. The 1550nm window that is widely used for telecommunications provides a wavelength window allowing low loss optical transmission. Silica exhibits an absorption in the infrared which becomes significant (causes losses of 1dBkm^{-1}) above wavelengths of about 1600nm [1]. Another cause of absorption loss is impurities within the silica, these can be a result of doping the silica to modify its properties or the result of contamination during fabrication. Further discussion of absorption losses is given in section 4.4. The OH^- ion brings about significant absorption peaks at 1240nm and 1380nm which are sufficiently broad to cause additional loss in the 1300nm and 1500nm telecommunications windows. Figure 4.1 shows an experimentally determined attenuation spectrum for an optical fibre with the contributions

from different effects shown for comparison. Thus much effort goes into excluding the OH^- ion and other unwanted impurities from the fabrication process.

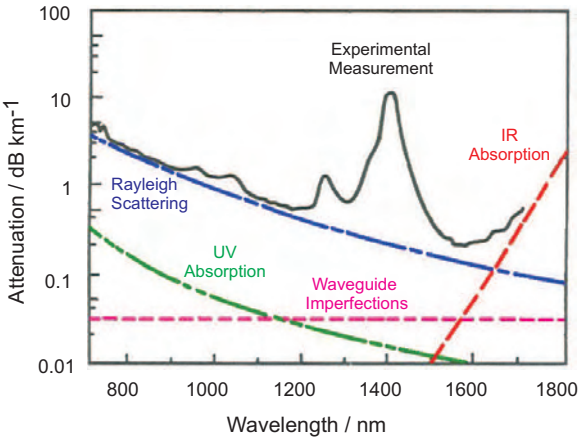

Figure 4.1: Attenuation of an optical fibre. The large peak in the vicinity of 1400nm is due to the presence of OH in the silica. (After [1] and [2])

Scattering of the guided light out of the waveguide core also introduces optical loss. The predominant effect, Rayleigh scattering, is caused by inhomogeneities in the silica that are smaller than the wavelength of light. The loss due to Rayleigh scattering decreases as the fourth power of the wavelength and so drops very quickly with increasing wavelength. Introduction of dopants into the silica can increase the scattering losses so careful process control is critical in order to manage the effects of such dopants.

4.2.2 Thermal Expansion

The requirement for different refractive indices for the cladding and core regions of a waveguide necessarily means that there is some difference in the material structure of the two different regions. As described in chapter 3 for standard etched waveguides as well as UV defined waveguides there are usually at least two materials which are deposited onto the same substrate, usually silicon, in order to fabricate a waveguide. High levels of stress in the deposited layers is generally undesirable as it can result in unwanted waveguide birefringence. It is however advantageous for the layers to be under some compressive stress which prevents the formation and

propagation of cracks throughout the layers. Many deposition techniques are performed significantly above room temperature and so, as the deposited layers cool, the differential thermal expansion of the substrate and layers results in layer stress. Silicon has a somewhat larger coefficient of thermal expansion (about 5 times larger) than the doped silica layers. Thus, as the layers and substrate cool, the silica layers are placed under compressive stress. It is however found desirable to use a buffer layer of silica to act as a stress matching layer in order to avoid abrupt changes in expansion coefficient. Thermal oxidation, described in the next section, is commonly used for this purpose. Although such thermal oxide layers will typically be significantly thinner than the silicon wafer upon which they are grown it is possible that it is the absence of an abrupt step change from silica to silicon that eases the effects of the thermal expansion mismatch.

4.2.3 Uniformity

The importance of the refractive index difference between core and cladding has already been discussed in the context of creating single mode waveguides. Uniformity of refractive index and of the thickness of deposited layers can be critical in the development of high quality devices. Constant effective index of a waveguide, governed by core refractive index, cladding refractive index and waveguide dimensions is vital to the performance of integrated optical components such as arrayed waveguide gratings and Bragg gratings. Should the refractive index or layer thickness vary along the waveguide, the optical path lengths upon which these devices depend will be disrupted and the device performance degraded. Non-uniformity at the core-cladding interface and fluctuations in dimensions can also cause scattering which, as already discussed introduces optical loss.

4.3 Review of Planar Silica Deposition Methods

Many techniques exist for the fabrication of silica or silicon based compounds for the purposes of optical manipulation. A source, which can be either liquid, solid or

gas, is required from which the end product is created. Deposition techniques can be broadly categorised into two groups, namely physical vapour deposition (PVD) and chemical vapour deposition (CVD) [3]. PVD uses an energy source to vaporise a solid material which is then transported in to the deposition substrate. Energy can be provided to the solid thermally or using electron beams, accelerated ions (sputtering) or laser ablation. Such deposition techniques do not play a role in the work presented in this thesis and so are not discussed further. CVD techniques use evaporating liquids or gases as the material precursors and an energy source to initiate molecular decomposition and the subsequent reactions cause deposition on the chosen substrate.

The work presented in this thesis relies on devices fabricated using two forms of chemical vapour deposition, flame hydrolysis deposition and plasma enhanced chemical vapour deposition and both are described below. For completeness a brief review of some other deposition techniques suitable for the fabrication of optical waveguides is also provided. With all fabrication techniques various precautions must be taken to reduce optical absorption, control the layer stress, control thickness uniformity and ensure that the final layers adhere to each other and the substrate reliably.

4.3.1 Thermal Oxidation

One of the most common routes to producing high quality silica on silicon is that of thermal oxidation. The production of the so-called *thermal oxide* is achieved by simply placing silicon wafers into a high temperature and high pressure oxygen or water vapour environment (typically around 1000℃ up to several atmospheres) [4]. The silicon surface in contact with the steam in the atmosphere oxidises to form silica. The interface between the silicon and the newly formed silica moves further into the bulk of the silicon as the reaction proceeds. Silica layers a few microns in thickness can be produced in this way in several hours.

Whilst this method is not a deposition technique, as the native silicon is consumed by the oxidation process, it is worth mentioning in this brief review of silica deposition techniques. Thermal oxidation is commonly used in the formation of buffer layers

or underclad layers for waveguiding structures. However the addition of dopants to control refractive index is not straightforward and so core or overclad layers produced by thermal oxidation are uncommon.

4.3.2 Sol-gel

A particularly flexible route towards the production of silica based planar waveguides is that of sol-gel deposition. A sol consists of colloidal particles suspended in a liquid. Subsequent gelation of the sol and gradual removal of the liquid results in a silica matrix which can be densified by thermal annealing [5]. The gelation of the sol into a gel is the result of the colloidal particles clustering to form a continuous matrix throughout the liquid in which it is contained. Many sol particles still remain within the solution that remains entrapped within the formed matrix. With a carefully controlled ageing process chemical bonds form between the clustered particles to form a more robust, more dense network. As the aged network dries the remaining liquid solution is first forced from the voids within the shrinking network, then evaporates to leave a dry porous silica layer. Annealing at temperatures around 800℃ results in a continuous silica layer.

Care must be taken when fabricating films for waveguiding applications using this method in order to avoid stress cracking as the gel drys to form the silica layer. The volume of the gel can reduce by 20-60% upon drying and in a thin layer this shrinkage occurs in just one dimension meaning that special precautions must be taken to ensure a high quality finished layer.

The flexibility of sol-gel deposition arises from the low temperature at which all stages of the process, excluding final densification, take place. Liquid precursors can be used and owing to their miscibility with a variety of organometallic precursors a wide range of dopants, including rare earth metals, can be easily included [6].

Further advantages of the formation of sol-gel are afforded by exploiting the intermediate stages of the deposition process. Waveguide gratings have been demonstrated by simply imprinting a relief structure into the gel before drying [7]. Also UV expo-

sure, prior to final densification, has been used to alter the reaction chemistry and create waveguiding structures [8]. The latter makes for an interesting comparison with the UV techniques presented in this thesis as no special layer doping or treatments are required to allow the UV induced waveguides to be created.

4.3.3 Flame Hydrolysis Deposition

The process of Flame Hydrolysis Deposition (FHD) is a development of techniques used for fabricating the glass preforms that form the first stage in the production of silica optical fibre. Several techniques exist for the fabrication of preforms by chemical deposition, all rely on the activation (usually thermal) of the hydrolysis or oxidation of vapour phase halide precursors. The precursors react to form fine silica soot which is deposited onto a tube or mandrel. Two significant techniques, vapour-phase axial deposition (VAD) [9, 10] and Outside Vapour Deposition [11] use a two step process to form doped silica glass. Firstly the silica soot is deposited by hydrolysis of the halides before the second stage of consolidation uses high temperatures to convert the low density soot into a fully dense glass layer [12]. A third, slightly different technique, Modified Chemical Vapour Deposition (MCVD) uses oxidation and soot deposition in a first stage followed by a second higher temperature consolidation step.

As VAD and OVD are closely related to FHD they will be discussed in a little more detail to act as an introduction. The silicon tetrachloride can be oxidised or hydrolysed to produce silica with the following overall reactions [13, 14]. Direct oxidation occurs in flames above 1200℃ whilst below this hydrolysis is dominant.

$$SiCl_4 + O_2 \rightarrow SiO_2 + 2Cl_2 \tag{4.1}$$

$$SiCl_4 + 2H_2O \rightarrow SiO_2 + 4HCl \tag{4.2}$$

Silicon tetrachloride, delivered as a vapour in a carrier gas that has been bubbled through the liquid form of the precursor is reacted with hydrogen and oxygen. The subsequent reaction results in solid silica particles and hydrochloric acid. The sil-

ica is deposited onto a supporting structure and the gaseous hydrogen chloride is extracted away.

A wide range of dopants can be used to tailor the composition of the soot and therefore the final glassy layer. Typically phosphorous, boron and germanium can be added using halide compounds ($POCl_3$, BCl_3, $GeCl_4$).

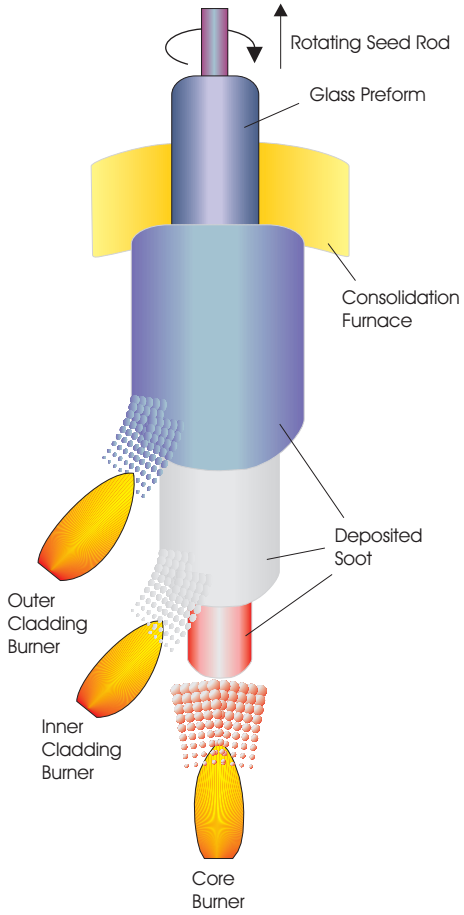

Figure 4.2: Schematic representation of VAD deposition process.

Similar hydrolysis reactions occur with these reactants and the resultant doped silica composition varies with the relative concentrations of precursors used. As already mentioned in reference to optical loss, careful process control is required when doping the silica in order to prevent excessive degradation of the resultant amorphous silica. For example, crystalline forms of the dopants may occur within the silica which can act as scattering centres and increase optical loss.

In VAD the gas phase precursors react in a hydrogen and oxygen flame which provides the necessary energy for dissociation and reaction. The flame impinges on a rotating glass seed-rod so that soot is deposited all around the rod. By translating the seed rod along its axis, whilst it rotates, uniform deposition of soot occurs all around and along the rod. With the use of additional heaters and careful translation it is possible to consolidate the soot at one end of the preform whilst still depositing soot at the other end.

OVD is similar to VAD in that a hydrogen oxygen flame is used to initiate the hy-

drolysis reaction. In contrast, a ceramic mandrel is used as a deposition substrate. As the mandrel is rotated the flame is translated along its length. After deposition the mandrel is removed and the hollow soot preform is transferred to a consolidation furnace to create a solid glass rod.

Within the volume of gas that forms the reaction region a variety of intermediate species of dissociated and ionised molecules will exist and the relative stabilities and concentrations will determine many of the resultant layer properties. It is therefore important to have a controlled flame which does not vary with time and is isolated from potential outside influences such as air flow or pressure fluctuations.

As already mentioned, FHD is essentially a planar version of the techniques used to create cylindrically symmetrical fibre preforms. Instead of axial deposition, a flame essentially identical to those in OVD and VAD, is translated over a planar substrate. Typically the substrate is a silicon wafer. After soot deposition the wafer is transferred to a consolidation furnace at approximately 1300 ℃ to create the dense glass layer.

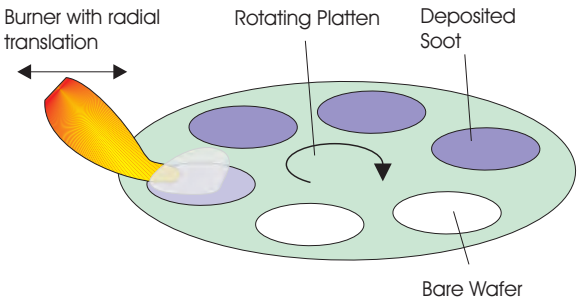

Figure 4.3: Flame Hydrolysis Deposition.

Consolidation temperature, refractive index and inclusion of other dopants can be altered by changing the absolute, as well as relative, proportions of the dopants in the flame. Adding a single dopant to the silica glass allows a relatively straightforward change to the properties, for example, germanium reduces the melting point of the glass and increases both the refractive index and the thermal expansion coefficient. The more of a given dopant that is incorporated into a glass, the stronger its effects will be. The interrelationships between all process parameters are complex and require careful optimisation. As an example, boron doping alone tends to decrease

the refractive index of the glass whilst phosphorous tends to increase the refractive index. However, boron also decreases the required consolidation temperature for an optical quality film. Whilst the effects of boron as a single dopant can be well characterised experimentally, less predictable behaviour can be observed when other co-dopants are used. Phosphorous is known to be a particularly volatile dopant and its incorporation into the finished silica layer depends strongly upon consolidation temperatures and ramp rates [14]. If a slow ramp rate is used to heat the deposited soot up to the required consolidation temperature it is found that dopant volatisation can significantly alter the final layer composition. More aggressive heating rates can be used to produce a 'sealed' structure from the soot and reduce the loss of dopants. Thus whilst adding boron as a co-dopant may be the initial choice to reduce the refractive index of a phosphorus doped layer, the opposite effect may occur. Reduction of the consolidation temperature by the boron will cause a corresponding increase in the phosphorus incorporation due to reduced volatisaion. The resultant layer may therefore have a higher refractive index than the equivalent boron free layer.

4.3.4 Plasma Enhanced Chemical Vapour Deposition

Plasma enhanced chemical vapour deposition (PECVD) is a method of deposition where the energy to dissociate the reactants is provided by RF, microwave or photon excitation [15]. Initially developed for the development of microelectronic components PECVD has an advantage over other forms of CVD in that depositions can be carried out at lower temperatures due to the additional source of energy input. This provides benefits for some production techniques where temperatures above a few hundred degrees cannot be tolerated.

The possibility of using a plasma to assist chemical vapour deposition has been known for many years. Thin films of silica deposited using silane and nitrous oxide (the precursors that form the basis of the work of chapter 6) were deposited with plasma assistance in the mid-1960s [16, 17] onto silicon substrates. These early results used a silica tube to act as a deposition chamber coupled inductively to an RF source by a coil around the chamber. The subsequent development of capacitatively

coupled sources [18] led to much improved layer uniformity and soon after the first commercial deliveries of production systems [19].

In general terms gas phase precursors are delivered into a deposition chamber where free electrons are accelerated by the applied electric field. Collisions of the excited electrons with the precursor molecules results in the production of free radicals (an atom or molecule with an unpaired electron), ions (a charged atom or molecule) and more excited electrons thus creating a plasma. The excited atoms or molecules may then move or be accelerated out of the plasma region towards the chamber walls or deposition substrate where their energy is dissipated and adsorption may occur [3, 20]. The reactive radicals adsorbed to the substrate surface are in fact mobile and can migrate along the surface, helping to ensure a conformal coating. Despite reaching the substrate surface, the radical is not yet bonded permanently to the wafer. Desorption may occur due to continuous ion and electron bombardment, resulting in the radical re-entering the plasma. However, the desired stable film is produced as a result of reactions with other adsorbed species on the surface forming chemical bonds [20].

A cross section of a typical parallel plate PECVD deposition chamber is shown in fig. 4.4. There are a selection of variants on the design in figure 4.4 with different electrode/wafer arrangements and correspondingly different deposition properties. All however rely on the same basic principles which are discussed here.

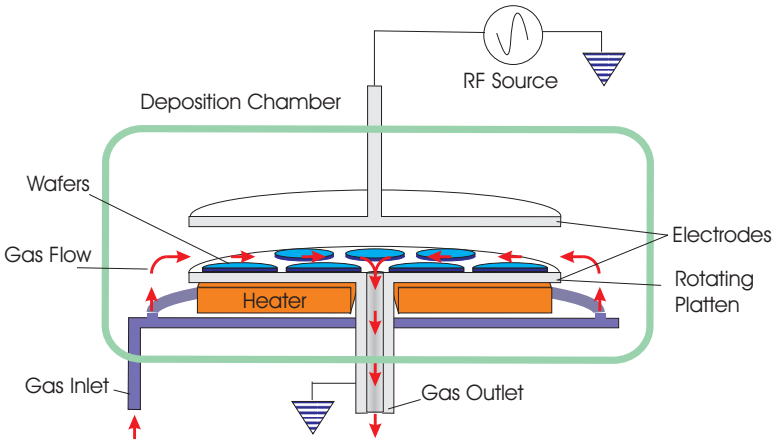

Figure 4.4: Cross section of a typical parallel plate PECVD deposition chamber [19, 20].

For the deposition of silica using silane as the precursor, the overall chemical reaction that takes place in PECVD is

$$SiH_4 + O_2 \rightarrow SiO_2 + 2H_2 \tag{4.3}$$

when oxygen is used and

$$SiH_4 + 2N_2O \rightarrow SiO_2 + 2H_2 + 2N_2 \tag{4.4}$$

or

$$SiH_4 + 4N_2O \rightarrow SiO_2 + 4N_2 + 2H_2O \tag{4.5}$$

when nitrous oxide is used as the oxygen source.

As with FHD there are also a large number of intermediate reaction products which exist in the plasma and with the addition of other dopant precursors to the plasma the variety of species and the complexity of the possible reaction mechanisms becomes great.

The nature of the deposition that occurs in a PECVD system is governed by two main steps; firstly, the plasma initiated chemical reactions that create reactive radicals and ions and secondly, the energy with which these reactive species reach the deposition substrate. The properties of the plasma will have a significant impact on both of these steps and therefore so do the process parameters that are used in the creation of the plasma. Variables that must be considered in PECVD include the plasma uniformity, pressure, RF power/frequency, temperature and the relative proportions of input precursors. Each of these affects the reactions that occur in the plasma and the interactions that occur at the substrate surface.

4.4 PECVD for waveguiding applications

The use of PECVD to create low loss waveguiding devices was demonstrated in 1990 [21] with reproducible losses of 0.1dB/cm using silica on silicon technology. Many microelectronics applications have moved towards the use of the liquid phase silicon precursor TEOS (tetraethylorthosilicate) in PECVD due to its superior performance

in depositions over substrates with deep surface profiles. Waveguiding applications, in particular UV writing applications, can use the gas phase precursor silane as little or no surface structure is present. This can be more easily included in the deposition equipment as delivery of gas to the deposition chamber is less complex than liquid delivery.

Deposition of silica using a flame hydrolysis based technique allows the experimenter to draw upon the well established production methods that have been developed over many years. It is relatively easy to introduce a wide range of dopants into the layers either by adding them to the flame in the gas phase or prior to consolidation by solution doping. PECVD also allows a large range of dopants to be incorporated in the deposited layer and the well established performance in the field of microelectronics also provides a wealth of background literature.

Typically PECVD deposited silica layers for optical applications require a post deposition anneal step to reduce optical losses to below several decibels per centimetre [21, 22]. The deposition of PECVD silica results in the inclusion of free or bonded hydrogen and nitrogen in the amorphous doped silica. Diffusion, oxidation and structural changes can occur with the correct annealing conditions and result in a reduced level of hydrogen and nitrogen impurities [23]. Previous PECVD fabricated waveguides have shown high absorption peaks at wavelengths of 1.4 microns and 1.51 microns [21, 22]. The former is attributed to the well known loss due to O-H bonds, the latter to Si-H and N-H bonds. Annealing processes of several hours at around 1100℃ have been shown to reduce the strength of both absorption peaks allowing for low loss transmission through planar silica waveguides. This does, to some degree, negate the benefits of the low temperature deposition that is allowed by PECVD. To overcome this, careful process control and exclusion of nitrogen from the deposition has allowed waveguide losses of less than 0.2 $dBcm^{-1}$ to be reported without the need for high temperature annealing [24].

The first demonstration of UV writing of waveguides into planar silica layers utilised PECVD deposited silica on silicon layers [25] and so it is well known that PECVD samples are suited to the application. Using germanium doping and hydrogen loading, techniques discussed further in chapter 5, the photosensitivity of the silica al-

lows UV induced index changes of the order of 10^{-2} to be obtained.

Investigations into the photosensitive response of PECVD deposited layers have shown that the deposition parameters can be used to tailor both the magnitude and direction of UV induced refractive index changes through stress control and appropriate doping of the silica [26]. In particular nitrogen doping, resulting in the formation of silicon oxynitride, has been reported to allow negative index changes of the order of 10^{-3} [27]. Thus PECVD provides an attractive route towards the production of low loss waveguides and through variation of deposition parameters allows a large amount of flexibility in refractive index and photosensitive response.

4.5 Comparison of PECVD and FHD

The fabrication of PECVD layers and their subsequent characterisation forms a large part of this thesis. However, FHD fabricated samples are also studied. For this reason some of the salient features of the two deposition methods are compared and summarised in table 4.1.

4.6 Summary

The preceding sections have outlined the requirements for optical planar waveguides and common techniques have been described. Particular attention has been paid to the techniques of FHD and PECVD as they form the basis of all results that are presented later in this thesis. With reference to the underlying processes the complexity and resultant flexibility of plasma based deposition techniques has been introduced.

	PECVD	**FHD**
Deposition Temperature	250℃	500℃
Anneal/Consolidation Temperature	1100℃	1300℃
Deposition Duration	Independent of wafer quantity or size	Increases linearly with increasing wafer numbers/size
Multiple Wafer Depositions	Limited by chamber size (*i.e.* uniformity requirements)	Limited by translation range of burner
As-deposited layer	Dense glass	Low density soot
Maximum single step deposition thickness (post anneal)	$\sim$6μm	Tens of microns, limited by soot layer stability
Energy source	RF	Flame
Precursor source	Gaseous. Typically silane or Tetraethylorthosilicate (TEOS) for Si precursor	Gaseous from evaporated liquid. Typically $SiCl_4$ for Si precursor
Additional Doping Techniques	Addition of liquid vapour to gas supply	Solution doping of soot, Addition of nebulised liquid into flame.
Suitable for Waveguiding applications	Yes	Yes
Clean room compatiblity	Good. Pump systems must be external to clean environment	Poor. Production of soot not compatible with strict clean room requirements.

Table 4.1: Comparison of typical features of PECVD and FHD systems used for silica deposition.

4.7 References

[1] A.Ghatak and K.Thyagarajan. *Introduction to Fiber Optics*. Cambridge University Press, 1998.

[2] T.Miya, Y.Terunuma, T.Hosaka, and T.Miyashita. "Ultimate Low-Loss Single-Mode Fibre at 1.55μm ". *Electronics Letters*, 15(4):106–108, 1979.

[3] Donald L. Smith. *Thin-Film Deposition Principles and Practice*. McGraw Hill, 1994.

[4] S.M.Sze. *VLSI Technology*. McGraw Hill, 1983.

[5] J.D.Wright and N.A.J.M.Sommerdijk. *Sol-Gel Materials, Chemistry and Applications*. Taylor and Francis, 2001.

[6] W.Huang, R.R.A.Syms, E.M.Yeatman, M.M.Ahmad, T.V.Clapp, and S.M.Ojha. "Fiber-Device-Fiber Gain From a Sol-Gel Erbium-Doped Waveguide Amplifier.". *IEEE Photonics Technology Letters*, 14(7):959–961, 2002.

[7] W.Lukosz and K.Tiefenthaler. "Embossing technique for fabricating integrated optical components in hard inorganic waveguiding materials.". *Opt. Lett.*, 8(10):537–539, 1983.

[8] P.Coudray, J.Chisham, A.Malek-Tabrizi, C.-Y.Li, M.P.Andrews, N.Peyghambarian, and S.I.Najafi. "Ultraviolet light imprinted on sol-gel silica glass waveguide devices on silicon.". *Opt. Comm.*, 128:19–22, 1996.

[9] T.Izawa. "Early Days of VAD Process". *IEEE Journal on Selected Topics in Quantum Electronics*, 6(6):1220–1227, 2000.

[10] S. Sudo, M. Kawachi, T. Edahiro, and T. Izawa. "Low-OH-Content Optical Fibre Fabricated By Vapour Phase Axial Deposition Method". *Electron.Lett*, 14(17):534–535, 1978.

[11] M.Blankenship and C.Deneka. "The outside vapor deposition method of fabricating optical waveguide fibers". *IEEE Journal of Quantum Electronics*, 18(10):1418–1423, 1982.

[12] S. Sakaguchi. "Consolidation of silica glass soot body prepared by flame hydrolysis reaction". *Journal of non-crystalline solids*, 171:249–258, 1994.

[13] R.F. Cuevas, E. Gusken, D.Y. Ogata E.H. Sekiya, D. Torikai, and C.K. Suzuki. "Effect of H_2/O_2 Ratio on the GeO_2 Concentration Profile in SiO_2:GeO_2 Glass Preforms". *Journal of non-crystalline solids*, 273:252–255, 2000.

[14] S.P. Watts. "Flame Hydrolysis Deposition of Photosensitive Silicate Layers Suitable for the Definition of Waveguiding Structures through Direct Ultraviolet Writing". *PhD Thesis*, 2002. University of Southampton.

[15] R.F.Bunshah. "Critical Issues in Plasma-Assisted Vapor Deposition Processes". *IEEE Trans. Plasma Sci.*, 18(6):846–854, 1990.

[16] H.F.Sterling and R.C.G.Swann. "Chemical Vapour Deposition Promoted by R.F. Discharge". *Solid-State Electronics*, 8:653–654, 1965.

[17] R.J.Joyce, H.F.Sterling, and J.H.Alexander. "Silicon Oxide and Nitride Films Deposited by an R.F. Glow-Discharge". *Thin Solid Films*, 1:481–494, 1967/68.

[18] A.R.Reinberg. *U.S. Patent No. 3 757 733*, Sept. 11 1973.

[19] R.S.Rosler, W.C.Benzing, and J.Baldo. "A Production Reactor for Low Temperature Plasma-Enhanced Silicon Nitride Deposition". *Solid State Technology*, 19(6):45–50, 1976.

[20] C.Y.Chang and S.M.Sze. *ULSI Technology*. McGraw Hill, 1996.

[21] G.Grand, J.P.Jadot, H.Denis, S.Valette, A.Fournier, and A.M.Grouillet. "Low-Loss PECVD Silica Channel Waveguides for Optical Communications". *Elec. Lett.*, 26(25):2135–2137, 1990.

[22] C.H.Henry, R.F.Kazarinov, H.J.Lee, K.J.Orlowsky, and L.E.Katz. "Low loss Si_3N_4-SiO_2 optical waveguides on Si.". *Applied Optics*, 26(13):2621–2624, 1987.

[23] A.Borghesi, A.Sassella, B.Pivac, and L.Zanotti. "Si-H Bonding Configuration in SiO_x:N,H Films Deposited by Chemical Vapour Deposition". *Solid State Communications*, 100(9):657–661, 1996.

[24] M.V.Bazylenko, M.Gross, P.M.Allen, and P.L.Chu. "Fabrication of Low-Temperature PECVD Channel Waveguides with Significantly Improved Loss in the 1.50-1.55-μm Wavelength Range.". *IEEE Phot. Tech. Lett.*, 7(7):774–776, 1995.

[25] M. Svalgaard. "Ultraviolet light induced refractive index structures in germanosilica". *PhD Thesis*, 1997. Technical University of Denmark.

[26] H.N.J.Fernando, J.Canning, L.Wosinski, and B.Jaskorzynska. "Engineering UV-photosensitivity in planar lightwave circuits by plasma enhanced chemical vapour deposition". *J.Phys.D: Appl. Phys*, 37:2804–2809, 2004.

[27] D.Wiesmann, J.Hübner, R.Germann, I.Massarek, H.W.M.Salemink, G.L.Bona, M.Kristensen, and H.Jäckel. "Large UV-induced negative index changes in germanium-free nitrogen-doped planar SiO_2 waveguides". *Elec. Lett.*, 34(4):364–366, 1998.

Chapter 5

Photosensitivity

5.1 Introduction

Whilst photosensitivity has been recognised and exploited for over a century in the field of photography it was not until 1978 when Hill and coworkers [1] observed changes in germanium doped silica that such effects could be utilised in fibre optics. This discovery initially spawned an area of research which allowed, and grew into, the extensive field of Bragg gratings in fibre and integrated optics that exists today.

The term 'photosensitivity' generally refers to a sensitivity to electromagnetic radiation, particularly light. The particular effect that is considered in this work is a change in refractive index induced by exposure to light and throughout this thesis reference to photosensitive media will refer to materials that display a change in refractive index in response to an applied optical signal. In order to control and make effective use of optically induced behaviour of this nature, some understanding and appreciation of the underlying effects is required.

The phenomenon of photosensitivity in silica is key to the work presented in this thesis. Here, with references to the thorough reviews in [2] and [3], a summary of the discovery, theoretical mechanisms and observed effects is provided to act as a background to the complex study of photosensitivity. With reference to the effects of hydrogen loading techniques the effects of thermal treatment pre- and post-UV-

exposure are introduced.

5.2 Photosensitivity

The initial discovery of photosensitivity in silica by Hill et. al. [1,4] occurred during investigations into non-linear effects in germanium doped silica fibre. Such work necessitated coupling high optical powers into the fibre, in this case using an argon ion laser at 488 and 514.5nm. It was observed that over time, the transmitted power decreased, almost to zero, due to the formation of a periodic modulation of refractive index. Light reflected from the cleaved end of the fibre had interfered with the forward propagating light and set up and standing wave along the fibre length. At the high intensity peaks along the standing wave, changes in the local refractive index occurred. This structured change of refractive index acted as an improved reflector of the incoming radiation and thus increased the standing wave amplitude and further increased the periodic refractive index modulation until saturation occurred.

The resulting structure was found to act as a very narrowband (<200MHz) filter operating at the original laser wavelength. Such devices, known as self-induced, or Hill gratings are of limited practical use as they are limited to operation at the writing wavelength.

It was some years later, following the observation that the optically induced refractive index change depended on the square of the writing power at 488nm [5], that it was discovered that strong changes in refractive index could be induced using wavelengths in the region 240-250nm [6]. These wavelengths correspond to photon energies that match an absorption peak associated with material defects due to germanium doping in the silica matrix [7]. This discovery allowed greater flexibility in making refractive index gratings in fibre. An interference pattern using two coherent beams at 244nm was used to illuminate a silica fibre from one side and created periodic index modulation [6]. The significance of this step is that the periodicity, and therefore the wavelength of reflection, is controlled by the angle at which the two coherent beams interfere. This step opened the door for the production of refractive

index gratings that reflect at any chosen wavelength using a method restricted to just one writing wavelength. In the subsequent years the study of photosensitivity and of Bragg gratings has continued and has proven to be of commercial and academic importance.

5.2.1 Classification

The development of fibre Bragg gratings and improvements in understanding of the photosensitive response of doped silica are inextricably linked. A wide range of published results using various materials, fibre types and light sources exist and even a brief review highlights the complexity of the subject of photosensitivity. It is apparent that the response of doped silica to irradiation depends on many parameters and although superficial similarities may exist between two silica samples fabricated by different methods, their photosensitive response and the underlying mechanisms can be markedly different. However, despite this, the observed changes in refractive index can be grouped into three broad categories that are used to classify the phenomenon [8].

Type I: The characteristic behaviour displayed in type I photosensitive materials is a monotonic increase of refractive index with time whilst the material is exposed to UV. This class of photosensitivity is commonly used to create fibre Bragg gratings.

Type IIA: Following a 'type I' positive index change, extended exposure of some materials can lead to an erasure of the induced refractive index increase and a subsequent further time varying negative index change.

Type II: The third group of photosensitivity is the result of exposing the material in question to high intensity light. With sufficiently high exposure physical damage results which has an associated index change. Such changes of refractive index can be of the order of 1×10^{-2} and are stable up to high temperatures because of the nature of their formation.

Although these general groups are often used in descriptions of photosensitivity, care must be taken with their use as alternative titles are sometimes used and various

research groups have defined other more specific sub-categories.

5.2.2 Photosensitivity through Defects

As already mentioned above, the photosensitive behaviour of doped amorphous silica varies with composition and fabrication methods. These factors directly impact the molecular structure of the silica matrix and it is this that ultimately defines the material behaviour. Although the three broad types of photosensitivity outlined above serve well as a general means of classification, it is widely accepted in the published literature that there are multiple mechanisms that give rise to a single type of photoinduced refractive index change.

Whilst defects in the structure of silica used for optical transmission are usually kept to a minimum to reduce the losses caused by the associated absorption bands, they are also found to play a significant role in photosensitivity. These point defects, also known as colour centres, can arise from intrinsic material defects or be induced by processing methods such as the drawing of fibre. The variation of defects with processing goes some way to explain the variety and complexity of photosensitivity data published. Results in bulk glass can reasonably be expected to differ in some way from those in drawn optical fibre which, in turn, can differ from deposited planar substrates. Even within the relatively specific class of planar silica layers there will be variation due to the different process temperatures used and resultant layer densities and stresses in various deposition or growth techniques.

Pure amorphous silica follows a tetrahedral structure where each silicon atom bonds to four oxygen atoms in a quasi-periodic structure. Within this regular structure defects, or deviations from the regular tetrahedral lattice, occur. Examples of these are silicon-silicon bonds, or non-bonding electrons on a silicon atom or on an oxygen atom. The various defects have particular absorption bands and can often be associated with physical effects such as radiation damage. When the silica is fabricated under oxygen deficient conditions, the number of defects is found to increase and they are therefore refered to as oxygen deficient centres [2].

It is however, the defects associated with incorporation of germanium into the silica matrix that have significant effects on photosensitivity and it is these defects that play the predominant role in the work of this thesis. Like silicon, germanium has a valency of four so can act as a direct replacement in the silica matrix. Doping the silica with germanium provides an additional set of possible defects in the material and several of these defects are widely considered to be responsible for the photosensitivity observed in germanosilicates. These germanium related defects are found to absorb in the range 180 to 350nm and of particular interest here are the absorptions clustered around 240nm. It is found that some of these absorption peaks are bleached by UV irradiation [9] and therefore, through the Kramers-Kronig relation (5.1), a corresponding change in refractive index occurs.

$$\triangle\, n(\lambda) = \frac{1}{2\pi^2}\int_0^\infty \frac{\triangle\, \alpha(\lambda')d\lambda'}{1-(\lambda'/\lambda)^2} \tag{5.1}$$

Here, $\Delta n(\lambda)$ denotes the change in refractive index n at wavelength λ due to a change in absorption α at wavelength λ'.

A variety of mechanisms have been proposed to explain the observed index changes and the accompanying experimental results do not always provide results that are in agreement. This indicates the underlying complexity and dependence of phenomena on the fabrication method and processing history of the silica being studied. It is however generally accepted in the literature that the formation of particular point defects associated with germanium play a significant role in the photosensitive response. Like pure silica, germanosilicates form defects, particularly when fabricated with an oxygen deficiency. Increasing the germanium content is known to increase the concentration of the related germanium oxygen deficiency centres (GODCs). Two such defects which appear to play significant roles are the Ge^{2+} defect with an absorption at 241nm and the neutral oxygen vacancy with an absorption at 245nm (figure 5.1). The latter, also referred to as NOV, is a Ge-Ge bond or an Si-Ge bond (or in the case of pure silica, an Si-Si bond) rather than the usual Si-O-Ge bond (or Si-O-Si).

It is the absorption related to the GODCs that is bleached by UV exposure, indicating

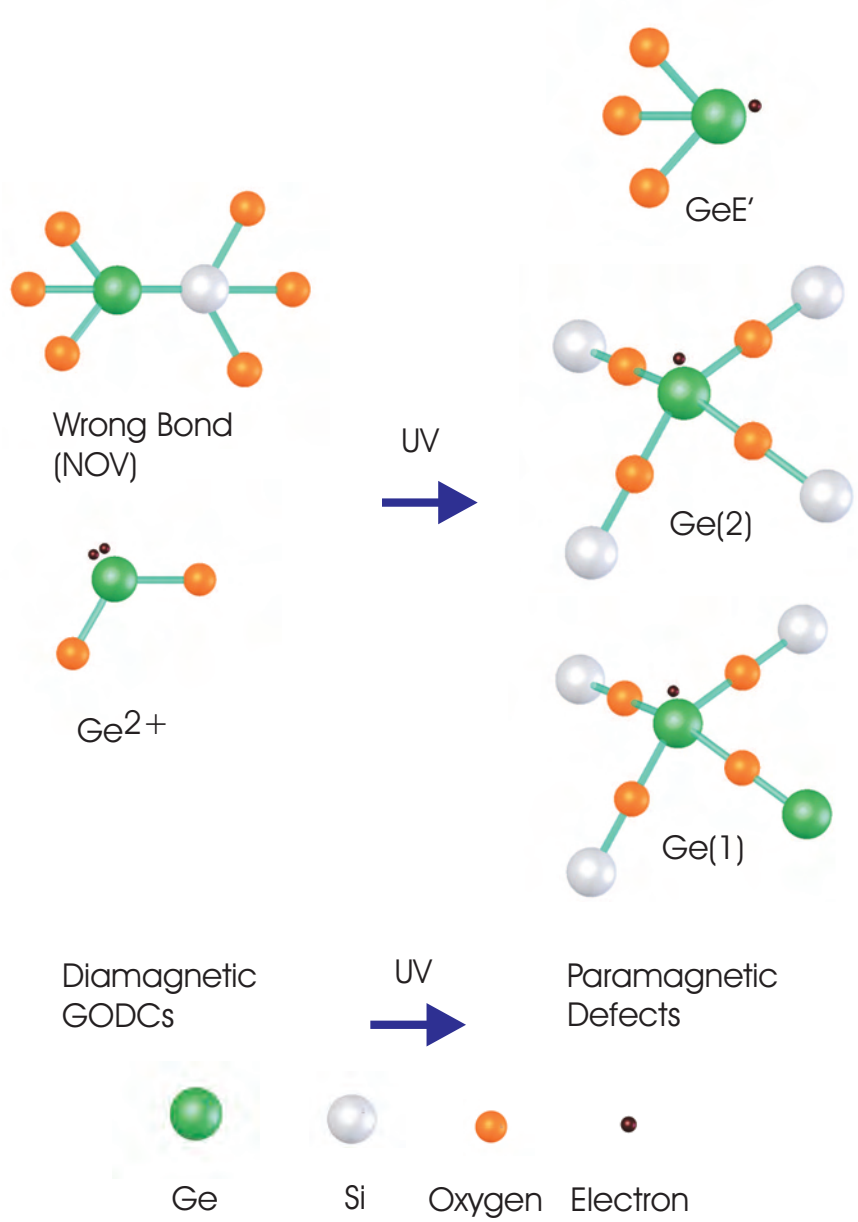

Figure 5.1: Common point defects of germanosilica thought to be responsible for photosensitivity. GODCs (*Left*) which are believed to absorb around 244nm and produce the GeE′ defect and liberate electrons which are captured to form Ge(1) and Ge(2) sites (*Right*)

that the defects are modified upon exposure to the UV resulting in the formation of new defects with new absorption bands. The creation of the GeE′ shown in figure 5.1 liberates an electron which it is thought becomes trapped elsewhere in the matrix forming an additional defect such as the Ge(1) [10].

The change from the diamagnetic (where all electrons spins are paired) GODC defects to paramagnetic defects (where unpaired electrons exist) is widely thought to be responsible for the observed photoinduced change in refractive index. However, conversion of GODCs to the paramagnetic defects is predicted, using the Kramers-Kronig relation to be responsible for refractive index changes around an order of magnitude less than is observed in experimentally achieved results. It is therefore apparent that additional mechanisms occur, possibly based around thermal effects, stress modification or compaction of the silica resulting in additional levels of index modification. Indeed densification is known to occur in UV exposed germanosilicates with resultant variations of stress and refractive index [8]. When no additional photosensitivity enhancements are used densification is predicted to account for 40% of photosensitivity in germanosilicate plates.

5.3 Photosensitivity Enhancement

Germanium is not the only dopant that can be added to the silica matrix to provide useful levels of photosensitivity. For example, type I and IIA effects have been observed in germanium free, nitrogen doped silica [11]. It is however, frequently convenient to use germanium as a dopant as it allows the refractive index of silica to be increased, providing greater design and fabrication flexibility. Raising germanium dopant levels (typically a few mol%), increasing the number of defects present, results in higher photosensitivity. However, if dopant levels are too high, the refractive index can become higher than desired and, more significantly the optical loss can be increased and mechanical strength decreased.

To avoid the undesirable effects of excessive geranium doping levels, additional co-dopants can be used. For example, the addition of boron into the silica lowers the refractive index, thus compensating for some of the refractive index increase due to germanium inclusion, and is also found to enhance photosensitivity [12]. Many other dopants have been used to control refractive index and demonstrate photosensitivity including tin, nitrogen, europium and cerium [2] although as single dopants none enhance the response to the same level as germanium.

5.3.1 Hydrogen Loading

As an alternative to increasing dopant levels in germanosilicate glasses, techniques have been developed to improve photosensitivity without dramatically altering the physical properties of the glass. A commonly used method is that of hydrogen loading. First reported by Lemaire in 1993 [13], high pressures are used to diffuse hydrogen into the silicate matrix. Exposure of the loaded glass to UV allows permanent index changes as high as 2×10^{-2} to be induced in planar waveguides [14]. Such loading procedures have been shown to be effective at enhancing photosensitivity in both germanium doped and germanium free fibres, and have the advantage that the hydrogen in the unexposed glass will diffuse out, leaving the glass as it was prior to loading.

It is well known that OH groups in silica have a characteristic absorption at 1.4μm which extends into the 1550nm telecommunications wavelength band. Hydrogen loading and UV irradiation are known to form such OH groups within the silica matrix and therefore the technique can increase transmission loss in the resultant structures. To avoid this deuterium can be used instead of hydrogen. Whilst the chemical properties of deuterium are almost identical to hydrogen, the higher atomic mass shifts the OD bond resonance to much higher wavelengths than that associated with the OH group (close to 1.9μm), thereby preventing the tail of the absorption band reaching into the 1550 wavelength band.

As with the defect centre theory outlined earlier, the mechanisms behind the photosensitivity improvement due to hydrogen loading are complex. It is thought however, that upon UV exposure the hydrogen molecules form Si-OH and Ge-OH groups and also react at germanium sites to produce GODCs with absorption resonances at around 240nm thereby producing defects sensitive to irradiation in the UV [2]. Such a theory is consistent with results showing that hydrogen loading does not result in any additional densification upon UV exposure [8], showing that the hydrogen loading process is most likely to provide enhancements due to interactions with defect centres.

For practical purposes, all experimental work carried out in the formation of this

thesis used hydrogen loading rather than deuterium loading. Primarily, hydrogen was used due to its availability at higher pressures than deuterium therefore allowing more rapid diffusion into the silica matrix. The resultant additional loss of the fabricated devices was not ideal, but tolerable for two reasons. Firstly, the optical path length of the devices fabricated was, at most, a few tens of millimetres and thus the extra OH loss will be minimal. Secondly, the main goal of the work presented here is to provide insight into material effects and to demonstrate prototype devices. As such, an incremental loss is not detrimental to the goals of this thesis. Further development of the work presented would inevitably involve loss reduction schemes which would include the use of deuterium loading, but with the associated higher cost.

5.3.2 Hydrogen Diffusion

The diffusion coefficient, or diffusivity, of hydrogen in silica is measured in units of cm^2s^{-1} and given by [15,16]

$$D = D_0 e^{\left(-\frac{E}{RT}\right)} \tag{5.2}$$

where D_0 is a constant independent of temperature and ambient pressure, E is the diffusion activation energy, R is the gas constant $8.3JK^{-1}mol^{-1}$ and T is the absolute temperature. The values of D_0 and E are found experimentally to be 5.65×10^{-4} cm^2s^{-1} and $43.55kJmol^{-1}$ respectively and are almost identical for both pure and doped silica. Thus diffusion occurs more quickly at higher temperatures but since gas solubility is higher at low temperatures heating is not desirable when maximum hydrogen concentrations are required. The diffusivity of hydrogen in silica therefore has a value of $4.3\mu m^{\,2}$ per hour.

For planar samples, the time for the indiffused hydrogen concentration at a depth d to reach 95% of the equilibrium value can be estimated by [17,18]

$$\tau_{0.95} \approx \frac{0.8d^2}{D} \tag{5.3}$$

Therefore, the $18\mu m$ thick silica layers developed in this thesis will reach 95% of the equilibrium value in approximately 2.5 days. It is noted that this time is not

dependent on the hydrogen pressure but that the indiffused hydrogen concentration is pressure dependent. Whilst no hydrogen dissociation occurs the solubility and therefore the equilibrium concentration in the silica varies linearly with pressure [19]. Therefore minimum temperature, maximum indiffusion time and maximum pressures are desirable to gain the highest possible hydrogen concentration in the silica. The apparatus used in this work allowed silica samples to be stored in a hydrogen atmosphere at approximately 150 bar at room temperature. Samples were always left for at least three days to ensure hydrogen concentrations were close to the equilibrium value.

Should hydrogen be replaced with deuterium the process remains the same. Slight differences in the diffusivity exist but are small enough that very little effect is made on the required indiffusion times.

5.3.3 Non Volatile Enhancement

A disadvantage of hydrogen loading is that out-diffusion of the hydrogen begins as soon as the sample is removed from a high pressure atmosphere. The geometry, core and cladding thickness of the sample will determine the rate at which the hydrogen concentration decreases in the waveguide or fibre core where it is of use for photosensitivity enhancement. It has been shown that even outdiffusion times of just a few minutes are enough to significantly alter the photosensitivity of a sample [20, 21]. The technique of *thermal locking* or *OH flooding* has been developed as a means of overcoming this.

Following observations that thermal treatment can induce refractive index shifts of photosensitive silica [13], Fokine [22] demonstrated that rapid heating of hydrogen loaded fibre to 1000°C created OH groups which gave rise to an increase in photosensitivity. Similar results were later demonstrated in planar samples deposited by flame hydrolysis deposition [23]. Perhaps more significant for the work described here, the effects of thermal locking are not volatile and out-diffusion of the OH groups does not occur. Consequently the UV writing times, which can run into tens of minutes for large samples being exposed at high fluences, have no impact on the

finished waveguiding device.

5.4 Summary

More than a quarter of a century has passed since the initial discovery of photosensitivity in silica but the field remains one of active research. The above discussion has outlined some of the basic principles and introduced the role of defects in the effects of UV exposure. The enhancement of the photosensitive response using hydrogen loading has been introduced along with the process of thermal locking to provide a non-volatile sensitivity increase.

5.5 References

[1] K.O.Hill, Y.Fujii, D.C.Johnson, and B.S.Kawasaki. "Photosensitivity in optical fiber waveguides: Application to reflection filter fabrication". *Appl. Phys. Lett.*, 32(10):647–649, 1978.

[2] A.Othonos and K.Kalli. *Fiber Bragg Gratings. Fundamentals and Applications in Telecommunications and Sensing*. Artech House, 1999.

[3] R.Kashyap. *Fiber Bragg Gratings*. Academic Press, 1999.

[4] K.O.Hill. "Photosensitivity in Optical Fiber Waveguides: From Discovery to Commercialization". *IEEE Journal on selected topics in quantum electronics*, 6(6):1186–1189, 2000.

[5] D.K.W.Lam and B.K.Garside. "Characterization of single-mode optical fiber filters". *Applied Optics*, 20(3):440–445, 1981.

[6] G.Meltz, W.W.Morey, and W.H.Glenn. "Formation of Bragg gratings in optical fibers by a transvere holographic method". *Optics Letters*, 14:823–825, 1989.

[7] R.M.Atkins, V.Mizrahi, and T.Erdogan. "248nm Induced Vacuum UV Spectral Changes in Optical Fibre Preform Cores: Support for a Colour Centre Model of Photosensitivity". *Electronics Letters*, 29(4):385–387, 1993.

[8] M. Douay, W.X. Xie, T. Taunay, P. Bernage, P. Niay, P. Cordier, B. Poumellec, L. Dong, J.F. Bayon, H. Poignant, and E. Delevaque. "Densification Involved in the UV-Based Photosensitivity of Silica Glasses and Optical Fibers". *IEEE Journal of Lightwave Technology*, 15(8):1329–1342, 1997.

[9] R.M.Atkins and V.Mizrahi. "Observations of changes in UV absorption bands of singlemode germanosilicate core optical fibres on writing anf thermally erasing refractive index gratings". *Electronics Letters*, 28(18):1743–1744, 1992.

[10] D.P.Hand and P.St.J.Russell. "Photoinduced refractive-index changes in germanosilicate fibers". *Optics Letters*, 15(2):102–104, 1990.

[11] E.M.Dianov, K.M.Golant, R.R.Khrapko, A.S.Kurkov, B.Leconte, M.Douay, P.Bernage, and P.Niay. "Grating formation in a germanium free silicon oxynitride fibre". *Electronics Letters*, 33(3):236–238, 1997.

[12] D.L.Williams, B.J.Ainslie, J.R.Armitage, R.Kashyap, and R.Campbell. "Enhanced UV Photosensitivity in Boron Codoped Germanosilicate Fibres". *Electronics Letters*, 29(1):45–47, 1993.

[13] P.J. Lemaire, R.M. Atkins, V. Mizrahi, and W.A. Reed. "High Pressure H2 Loading as a technique for achieving ultrahigh sensitivity and thermal sensitivity in GeO2 doped optical fibres". *Electronics Letters*, 29(13):1191–1193, 1993.

[14] M. Svalgaard and K.Faerch. "High Index Contrast UV-Written Waveguides". *Proceedings of 12th European Conference of Integrated Optics, Grenoble*, pages 522–525, 2005.

[15] R.W.Lee, R.C.Frank, and D.E.Swets. "Diffusion of Hydrogen and Deuterium in Fused Quartz". *The Journal of Chemical Physics*, 36(4):1062–1071, 1961.

[16] J. Stone. "Interactions of Hydrogen and Deuterium with Silica Optical Fibres: A Review". *IEEE Journal of Lightwave Technology*, LT-5(5):712–733, 1987.

[17] P.J. Lemaire. "Reliability if optical fibres exposed to hydrogen: prediction of long term loss". *Optical Engineering*, 30(6):780–788, 1991.

[18] M. Svalgaard. "Ultraviolet light induced refractive index structures in germanosilica". *PhD Thesis*, 1997. Technical University of Denmark.

[19] J.F.Shackelford, P.L.Studt, and R.M.Fulrath. "Solubility of Gases in Glass. II. He, Ne and H_2 in Fused Silica". *J.Appl.Phys*, 43(4):1619–1626, 1972.

[20] K. Faerch and M. Svalgaard. "Symmetrical Waveguide Devices Fabricated by Direct UV Writing". *IEEE Photonics Technol. Lett.*, 14(2):173–175, 2002.

[21] M. Svalgaard. "Effect of D2 outdiffusion on direct UV writing of optical waveguides". *Elect. Lett.*, 35(21):1840–1842, 1999.

[22] M. Fokine and W. Margulis. "Large increase in photosensitivity through massive hydroxyl formation". *Opt. Lett.*, 25(5):302–304, 2000.

[23] C. Riziotis, A. Fu, S. Watts, R. B. Williams, and P. G. R. Smith. "Rapid heat treatment for photosensitivity locking in deuterium-loaded planar optical waveguides". *BGPP, Stresa, Italy*, BThC31, 2001.

Chapter 6

Development of Silica Samples for UV Writing

6.1 Introduction

Following the previous introduction of silica deposition techniques and UV writing for the definition of planar waveguides, this chapter describes the first steps in the development of photosensitive, three layer, refractive index matched silica samples fabricated by plasma enhanced chemical vapour deposition. The successful creation of these structures was achieved by controlling deposition and annealing parameters to tailor individual layer refractive indices and thicknesses.

To describe the process route taken some general details on the equipment and processes are provided before specific details on deposition and annealing parameters are provided. An important finding was that core and cladding layers must be deposited separately with individual anneal steps between each deposition.

6.2 PECVD Layers for UV writing applications

The goal of research presented in this section was to develop processes based on PECVD for the production of index matched three layer samples with photosensitive cores for UV writing, as described in chapter 3. It is known from [1] that such a process is possible and offers low loss, single mode waveguides. Ideally a basic production route would be developed and then subsequently modified to allow a systematic study and optimisation of the properties of the resultant structures. Further development then provides the opportunity to explore a vast array of integrated optical structures. Unfortunately, owing to time constraints imposed by a variety of practical difficulties with equipment and facilities the development of such structures was more limited than originally intended. Appendix A outlines some of the issues that hindered development work along with a brief description of the solutions and additional relevant comments. Nonetheless, the following sections describe the successful development of three layer photosensitive structures with controlled layer thicknesses which proved to be suitable for the definition of waveguides and Bragg gratings using direct UV writing.

6.3 Deposition Equipment

The equipment used for all of the layers described below was an STS Mesc Multiplex Chemical Vapour Deposition V1 Tool (Figure 6.1). All chemical sources used were gas phase, namely silane (SiH_4), diborane (B_2H_6), germane (GeH_4), phosphine (PH_3) and nitrous oxide (N_2O) for the purposes of doped silica deposition along with tetrafluoromethane (CF_4) as an etchant for chamber cleaning and ammonia (NH_3) as a source of nitrogen for the deposition of silicon nitride and silicon oxynitride. In subsequent descriptions of process recipes, gas flow rates are quoted as the total gas flow of each supply into the chamber. It should be noted that the actual phosphine and diborane supply rates were in fact 10% of this value as they were supplied diluted with nitrogen and hydrogen respectively. Similarly, values quoted for the germanium supply are as entered into the equipment operating software. The

germanium supply made use of a smaller mass flow controller and so these quoted values are 100 times greater than the actual supply rates in use. This flow rate convention is used throughout this chapter and is chosen in preference to quotation of the actual volume of each gas delivered. As this is the standard format that was used to enter each flow rate into the tool each recipe quoted may be entered, in the form presented, directly into the deposition equipment recipe editor to duplicate that particular process step.

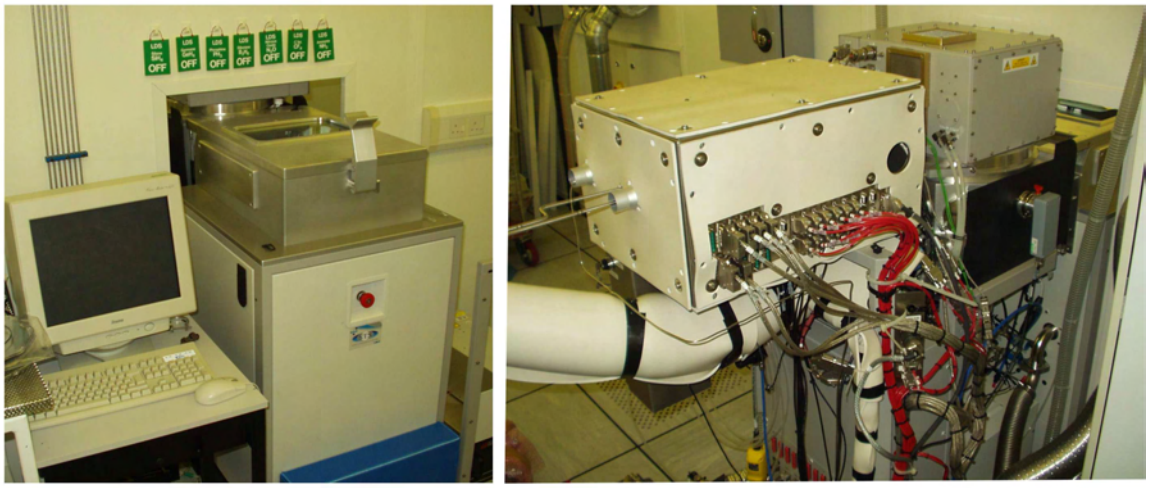

Figure 6.1: The PECVD deposition equipment. *Left:* The control PC and wafer load-lock. *Right:* External view of deposition chamber.

Through the use of a liquid delivery system (LDS) it is possible to pump liquids towards the deposition chamber and vaporise them before combining them with the standard gaseous inputs. The addition of the LDS provides the potential for a wider range of dopants to be incorporated into the deposited layers, notably rare earth dopants. However, owing to technical difficulties with the equipment and limited time available no liquid delivery has been investigated to date.

The gas phase reagents are injected into the deposition chamber where they are distributed evenly across the deposition area by an aluminium 'showerhead', a spreader plate with multiple evenly spaced holes through which the gases pass (fig. 6.2). The substrate for deposition lies directly below the shower head such that the plasma formed by the ionisation of the gases is directly above. The deposition substrate is mounted upon a platen, also aluminium, a few centimetres below the showerhead.

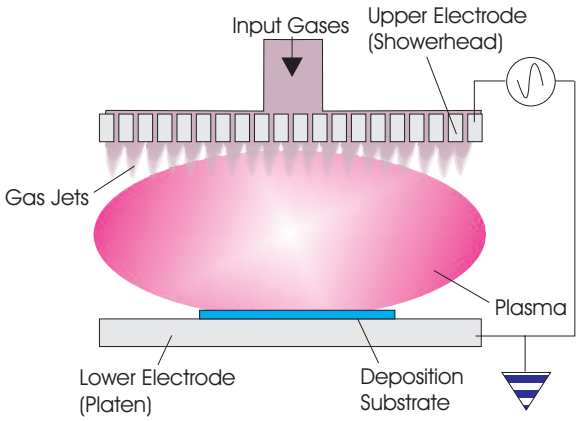

Figure 6.2: Cross section of PECVD deposition chamber.

Precursor gases enter the chamber travelling vertically downwards and centred over the deposition region. Waste gas is extracted such that the gas flow has radial symmetry as in the case of the PECVD equipment described in chapter 4. Evidence of this is seen in figure 6.3 where a thin test deposition shows defects with radial symmetry associated with gas flow. The cause of this particular pattern will be discussed in further detail in section 6.4.4.

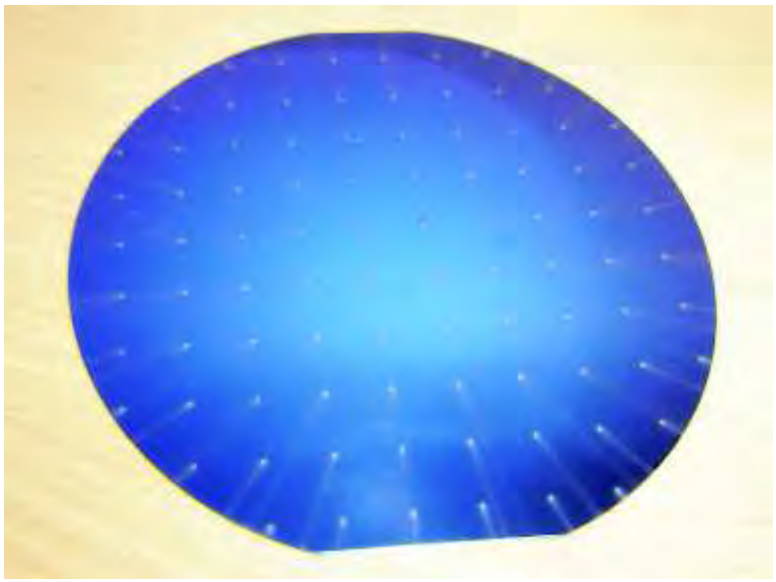

Figure 6.3: Radially symmetric defects on test deposition....

Two RF sources are available to provide the energy to create the plasma used for depositions. For the purposes of silica deposition, 13.56MHz and 380kHz are used.

The choice of frequency is for the deposition of silicon nitride when it can be advantageous to alternate between the high and low frequency sources to reduce layer stress.

To tailor the deposited layer to specific requirements the following parameters may be controlled; Showerhead and platen temperature, plasma pressure, RF power, RF frequency, absolute and relative gas flow rates and total deposition time. For all depositions described here the platen was maintained at 300 ℃ and the showerhead at 250 ℃ , values that have been determined by the manufacturers as suitable for providing stable performance. The RF source used was always the low frequency option of 380KHz. Deposition parameters are also determined by the material from which the electrodes are formed, the chamber geometry and the pump by which by-products are exhausted from the system. None of these factors are available for modification and are determined by the equipment design.

6.4 Development of PECVD Deposition Process

As already discussed in chapter 3 the process of UV writing requires a three layer, index matched, photosensitive sample. This section describes the development of index matched layers and the subsequent creation of multilayer samples of controlled thickness.

6.4.1 Characterisation Trials

In order to establish the performance of the deposition equipment a series of test depositions were performed in conjunction with STS plc. The recipes used for these layer depositions were then used as a starting point from which to develop specially tailored compositions.

Four silica compositions were deposited, undoped silica, germanium doped silica, phosphorous doped silica and boron/phosphorous doped silica. The thickness and refractive index measurements were performed by STS plc.

Dopant	N_2O sccm	SiH_4 sccm	B_2H_6 sccm	PH_3 sccm	GeH_4 sccm	Uniformity n	Uniformity %
Undoped	2000	17	0	0	0	1.4583	6.1
Ge	2000	17	0	0	175	1.4603	5.5
P	2000	17	0	12	0	1.4605	4.9
P, B	2000	17	30	12	0	1.4552	5.7

Table 6.1: Gas flows for doped and undoped silica test depositions. Resultant refractive indices (n measured at 633nm) and thickness uniformities are mean values from three depositions

Additionally run-to-run uniformity measurements were made, also performed by STS plc. Based on three silica depositions of approximately 6.5µm in thickness the variation in measured thickness (as measured by STS) was found to be 0.36% and $\pm 5.3 \times 10^{-5}$ in refractive index. Of these three depositions, the maximum variation of refractive index across a wafer was measured to be 2.4×10^{-4} . Thus depositions of this thickness could be performed without raising concerns over wafer uniformity or run-to-run performance variations.

Clearly, from table 6.1 the germanium and phosphorous doped layers form an excellent starting point from which to base a deposition process for three layer, index matched samples. These recipes therefore provide the foundations of the development of index matched three layer structures.

6.4.2 General Deposition Details

All depositions that are discussed subsequently used 1mm thick silicon wafers as the substrate. Each wafer was processed to provide a 2 micron thick thermal oxide layer to act as a buffer layer between the silicon and the deposited silica. For reasons of consistent performance, it is recommended by the manufacturer that the thickest deposition that may be performed in a single step is 6 microns. As the waveguide core layer is known to require approximately this thickness, efforts were concentrated on the development of correct refractive index layers of 6 microns or less in

thickness. Commercial planar waveguides deposited using FHD or PECVD would typically utilise cladding layers of 20 microns or thicker for such structures. The creation of thick, single composition layers has not been attempted to date as this was not required for the goal of the research.

Annealing of the deposited silica layers is mentioned frequently in the following sections. For the purposes of this discussion an annealing stage consists of the removal of the substrate from the PECVD equipment after deposition and heating in a furnace at the temperature and for the duration specified. Aside from temperature control, no special precautions were taken to control the atmosphere of the furnace.

Measurement of refractive index and layer thickness was determined on all samples with the use of a Metricon 2010 prism coupler. Use of this equipment requires layers with thicknesses of several microns and so the maximum single step thickness of 6 microns was used for process development unless otherwise stated. Measurements using this method were taken using critical angle measurements for refractive index as this was found to be reliable and repeatable. When measuring layer thickness the full modal structure of the prism coupler output was used. It must be noted that although the intended application of the layers is at 1550nm, prism coupling measurements were only available at 633nm. Therefore the actual refractive indices at 1550nm will not be fully characterised by these measurements. Additionally, awareness is required that layers that are index matched at 633nm may not be so at 1550nm due to differences in material dispersion. At this early stage of development it was considered acceptable to use 633nm measurements as a basis for developing layer compositions.

6.4.3 Single Layer Depositions

As discussed above, the equipment characterisation trials provided two layers with similar refractive indices which act as an excellent starting point for further development. As a first step, deposition rates and refractive index measurements were determined for each layer composition. Depositing a layer several microns thick allows thickness and index values to be measured by prism coupling. It was found

that deposition rates for all layers of interest were approximately 0.2 microns per minute and so typically a half hour deposition would be used to provide a layer thick enough for prism coupling and leaving the chamber ready for an etchback prior to the next deposition.

As a general rule, providing appropriate precautions are taken in performing the deposition, very few problems were encountered when depositing a single silica layer onto the thermal oxide coated silicon wafers. With the usual cleanliness considerations when handling wafers for deposition, contaminant free layers were achieved. Once removed from the heated, evacuated deposition chamber all layers were annealed within three hours. During characterisation trials doped silica layers were observed to become cloudy due to micro-cracking over the surface if not annealed within this time. It should be noted that the characterisation depositions were performed directly onto silicon rather than the thermal oxide used as standard procedure in the bulk of this work. Thus, this example is an extreme case and the problem will be mitigated for the production of normal samples. It was however considered good practice to adhere to this simple rule.

Annealing was performed over a range of temperatures and durations but always under atmospheric conditions. It may have been advantageous to use a dry nitrogen or oxygen atmosphere to assist in minimising the hydrogen content of the finished layers. Unfortunately such facilities were not readily available so no such precautions could be taken.

The silicon carbide lining of the furnace used had a tendency to shed particulates and contaminate layers. In contrast to FHD this is not a serious issue as the deposited silica is already in a solid layer upon being placed into the furnace and the majority of furnace particulates can be cleaned off after anneal. Where particulate contamination had occurred prior to annealing, it was removed before the sample was placed into the furnace as the particles had a tendency to bond to the surface during the anneal and could not be removed without damaging the layer. It was found that compressed air was the most suitable route to removing particulates prior to anneal (or, if necessary prior to deposition) as physical contact with the wafer resulted in visible contamination or defects in the finished layer.

6.4.4 Multi-layer Depositions

Whilst single layer depositions were found to be relatively straightforward with smooth, uniform contaminant free layers of up to six microns thick produced in a single stage, multiple layers proved to be more complex.

PECVD tools utilising the showerhead electrode/gas distribution system as used here are known to have the potential to cause 'defects' in the planar surface due to the nature of the gas flow. Each gas outlet hole has an associated flow of gas where the precursors enter the plasma. With incorrect deposition parameters it is possible for these localised high gas flow regions to cause defects in the deposited surface. This is due to the variation and non uniformity of the gas flow in the vicinity of the showerhead holes. The effect of such defects can be seen in minor cases as mild bubbling or micro-cracking of the deposited layer (as presented earlier in figure 6.3) and in serious cases as large scale (several millimetre diameter) bubbles or delaminated layers. Such defects are clearly shown in figure 6.4. This particular case was the

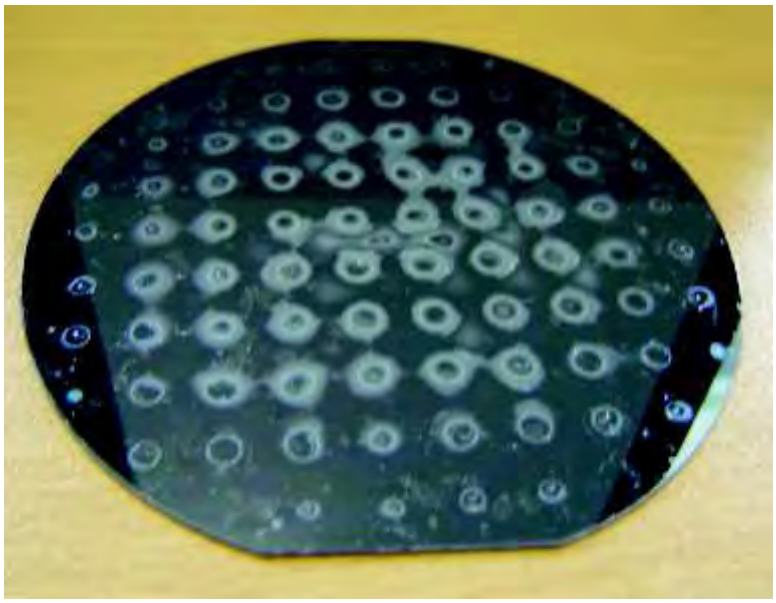

Figure 6.4: Large scale bubbling and delamination of deposited layers

result of depositing three successive 6 micron thick layers in an attempt to create a 3-layer sample suitable for UV writing. After each 6 micron deposition step the wafer was transported into the machine loadlock and stored under vacuum whilst the de-

position chamber was etched back using CF_4. Following the etch back the wafer was returned to the chamber for the next deposition. After all three depositions the wafer was annealed at 1100 ℃ for 1 hour. It was clear that this process route required significant alteration to produce high quality layers.

In addition to the gross level of layer disruption observed in figure 6.4 much smaller bubbling and delamination can occur. These are observed to be uniformly distributed over entire wafers or around the edges and not centred about the regular grid pattern associated with showerhead effects. Examples of this are shown in figures 6.5 to 6.7. These figures are of a two layer sample with a 6 micron thick germanium doped layer deposited on top of a 6 micron thick boron and phosphorous doped underclad an intermediate anneal at 1100℃ was performed between each deposition. Such results are typical of this combination of layers if no special precautions are taken.

Figure 6.5: Wafer showing delamination and bubbling after annealing

Thus there are two issues to be overcome in developing a multi-layer deposition process. Firstly process parameters must be controlled such that gas flow and plasma density (controlled through the chamber pressure during depositions) prevent localised defects. Secondly the layer recipes, deposition and anneal steps must be tailored such that the layers adhere without bubbling to the substrate and other de-

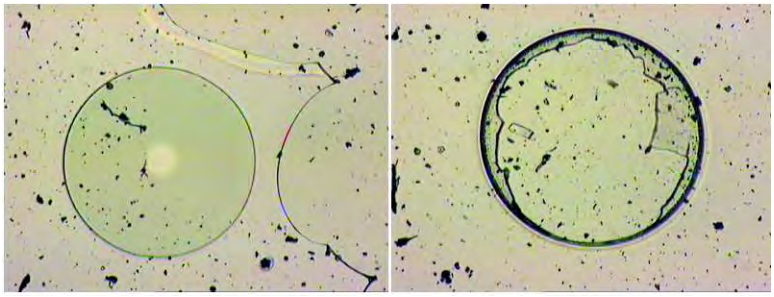

Figure 6.6: Surface bubbles after annealing. *Left:* Bubble still intact. *Right:* A burst bubble. Both bubbles have a diameter of approximately 1mm.

posited layers.

To overcome showerhead defect formation and delamination, the chamber pressure during deposition can be controlled. By increasing the chamber pressure the effective density of the plasma can be increased. This has the effect of 'dispersing' the individual gas jets more efficiently such that gas flow and plasma uniformity at the substrate surface is improved. Care must be taken after changing chamber pressures that deposition rate and refractive index are adjusted to compensate for the slight changes that will occur as a result of the change in deposition conditions.

An alternative method to avoid showerhead patterns in deposited layers is to rotate the wafer slightly from its usual position prior to processing. Ordinarily wafers are aligned to always have the same orientation when entering the deposition chamber. Thus, each showerhead outlet is always directly above the same point on the wafer. It was found that this procedure reduced showerhead defects but the delamination still occurred. It should be noted however, that this procedure should be avoided when many wafers are to be processed. As wafers are not completely circular, rotating them results in areas of the platten building up different thickness of deposited silica. Even though the chamber is frequently etched back, this may ultimately result in a build up of deposited material causing the wafers not to sit flat. This will vary both the height and thermal contact of the wafer with the platten resulting in non uniform depositions. Therefore, showerhead effects were minimised through the control of deposition chamber pressure.

Overcoming the second type of layer delamination issue was found to be less straight-

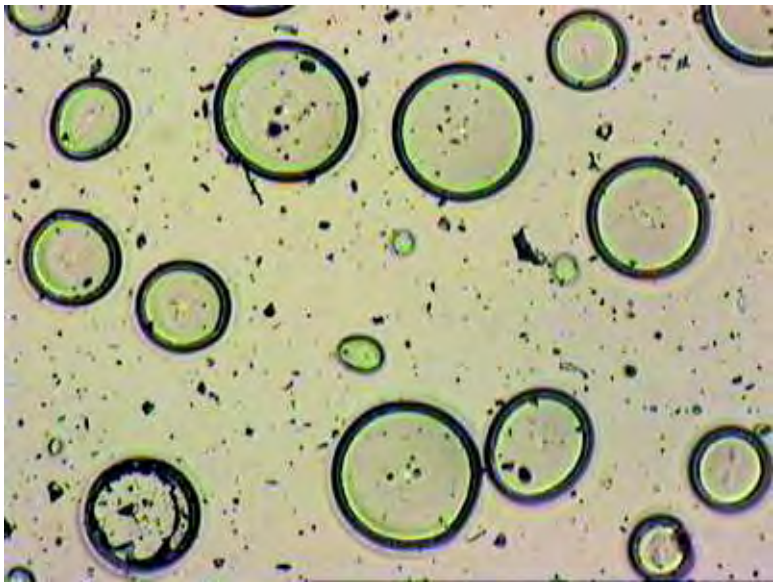

Figure 6.7: Multiple closely spaced bubbles. These are typically less than 1mm in diameter. The apparent dirt on the sample is flakes of silica from delamination across the wafer.

forward and a combination of deposition parameters and annealing regimes was used to develop a suitable process. The development of these two aspects of the processing were largely concurrent but for clarity they will be separated somewhat into distinct sections.

6.4.5 Effects of Annealing

Whilst freshly deposited layers can be removed from the deposition equipment apparently in pristine condition it is readily apparent from the photographs in the previous section that after annealing the layer can be dramatically degraded. In addition to the temperature and duration of anneal it is also possible to control the rate at which the substrate is taken up to, and down from, the anneal temperature. The atmosphere in which the anneal takes place can also be varied. Although there may be considerable benefits obtained by such atmospheric control during annealing, all work presented here was carried out with an air atmosphere controlled only to the extent required by the class 10,000 clean room in which the furnace was housed.

Two general process routes were investigated as a means of developing three layer structures. The initial route of investigation centred around successive layer depositions (e.g. clad, core, clad with the wafer being transferred between deposition chamber and loadlock and not removed from the equipment) followed by a single anneal step. This would be a particularly desirable route towards the fabrication of samples for UV writing as it would allow generic photosensitive wafers to be produced in very short time scales with the substrate remaining in a very clean environment (i.e. within the deposition equipment) right up to the anneal stage. The second route was that of a pairing of each deposition step with an anneal step such that there would be at least as many anneal stages as there were depositions per wafer.

6.4.5.1 Multiple Deposition - Single Anneal

As shown earlier in figure 6.4 the three-step deposition followed by a single anneal can fail drastically. Success of this technique will amongst other things rely on very carefully matched layer expansion coefficients. Nonetheless the attractiveness of this process route made some investigation of the effect of annealing worthwhile.

Two six micron thick layers of doped silica were deposited onto a wafer with no intermediate anneal. The first layer was predominantly phosphorous doped and the second layer, predominantly germanium doped was deposited on top using the following total gas flows

Layer	N_2O sccm	SiH_4 sccm	B_2H_6 sccm	PH_3 sccm	GeH_4 sccm
Upper (Ge Doped)	2000	17	1	1	500
Lower (P Doped)	2000	15	1	24	5

The wafer was then cleaved into four before annealing. Each quarter was placed into the furnace at a different temperature and annealed for 45 minutes before removal. No ramping of temperature was used. The four temperatures used were 800℃ , 900℃ , 1000℃ and 1100℃ . The subsequent state of each sample is shown in figure 6.8.

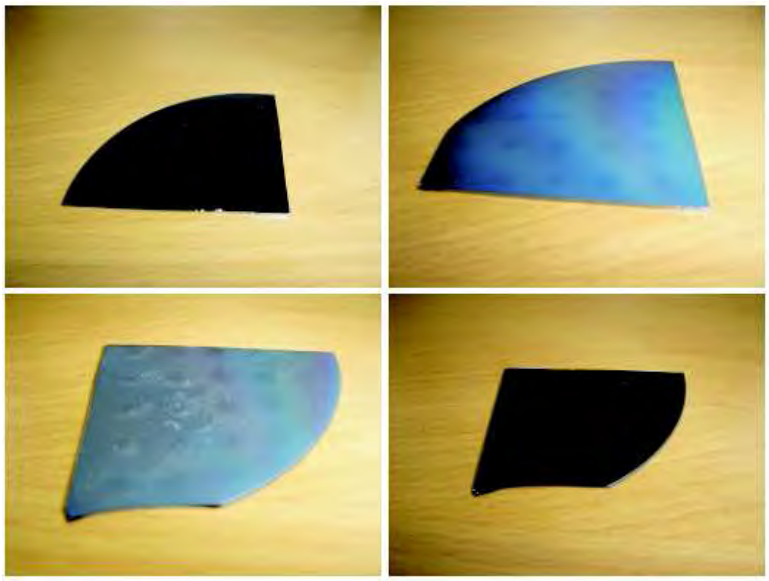

Figure 6.8: Effects of annealing at different temperatures. *Top Left:* 800°C , *Top Right:* 900°C , *Bottom Left:* 1000°C and *Bottom Right:* 1100°C

The 800°C anneal had no visible effect on the layer which remained smooth and bubble free. In contrast the 900°C and 1000°C samples showed marked changes. The 900°C anneal caused the layer to become cloudy indicating the presence of microcracking and there was also clear evidence of showerhead induced features. The surface however remained smooth. After 1000°C the visible cloudiness became more apparent as did the showerhead patterning. More significant is that one or both of the layers began to delaminate and flake from the wafer. Perhaps the most interesting outcome of these trials is the effect of the 1100°C anneal. The expected result was a layer even more disrupted than those obtained at lower temperatures. Instead the annealed sample showed no cloudiness and no obvious pattern due to the showerhead. This sample did however show small bubbles across the surface similar to those shown in figure 6.7 and also delamination of both layers occurred from one edge. It should be noted however that this latter feature could be a consequence of the cleaving process rather than of the anneal.

These results would at first sight indicate that an anneal process at 800°C should be investigated further. However, in the next section it is shown that annealing at this temperature is unsuitable. Clearly annealing in this way at 900°C and 1000°C is un-

suitable and reproduced to some extent the large scale damage demonstrated earlier in figure 6.4. A definitive explanation of the relatively high quality layer achieved using the 1100℃ is not possible without further analysis of the relative thermal behaviour of the component layers.

It is most likely that the disruptive effects seen on the layers as a result of thermal annealing are due to relative differences in thermal expansion. Thus it would be expected that an increase in temperature from 1000℃ to 1100℃ would cause a similar increase in damage as that from 900℃ to 1000℃ . As this is not the case, the two most likely reasons are that the layers are close to, or at their melting point at 1100℃ causing a reduction in viscosity and avoidance of the micro-cracking observed in other samples. It is also possible that at the higher temperatures the layer stress that causes delamination is released by a process other than cracking or bubbling at showerhead points. This would explain the appearance of bubbles in the annealed sample with no apparent showerhead pattern present. Such a possibility is discussed in [2] where microscopic blistering of PECVD layers is attributed to stress relief from the outgassing of dissolved hydrogen from compressive layers. It is known that both hydrogen and nitrogen are released from PECVD layers [3, 4] upon annealing. Indeed with all dopant precursor gases being compounds of hydrogen and with large volumes of N_2O flowing through the deposition chamber it is indeed probable that large amounts of hydrogen and nitrogen will be present in the as-deposited layers and that such outgassing will occur.

Regardless of the cause it is apparent that such blistering of the layers prevents them from being suitable for waveguiding applications. Whilst the bubbling of the layer annealed above at 1100℃ is relatively mild, other similar examples demonstrate much more serious blistering as shown in figure 6.9.

Although the work described above is by no means a comprehensive study on annealing multiple layers it does indicate the difficulty of the process particularly as just two layers were used here in contrast to the three layers required for UV writing. Whilst it may be possible to develop a fabrication route using just a single anneal it is likely to require very careful balancing of each deposition and of the anneal process used. As such, the main focus of the development work presented is based around

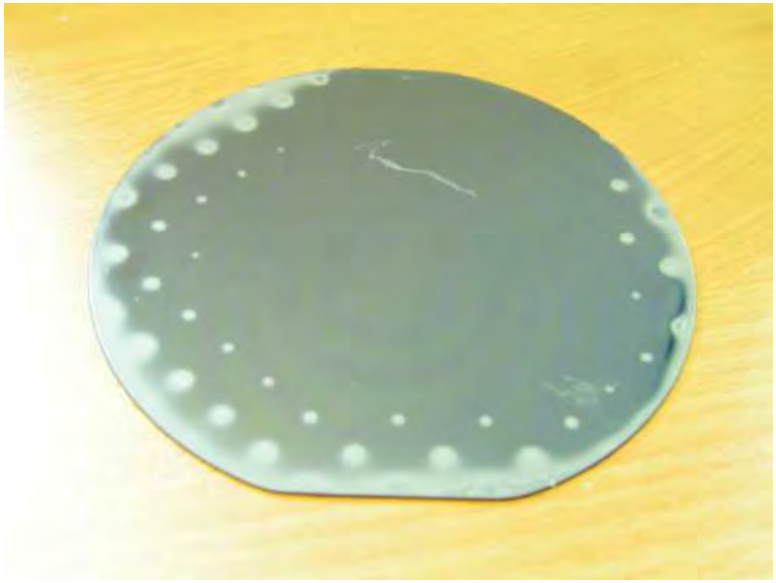

Figure 6.9: Two layer sample fully covered by blisters after anneal. Individual bubbles cannot be resolved in the image but unlike as-deposited layers the wafer is no longer smooth and reflective. This example also demonstrates showerhead patterning around the wafer edge.

each deposited layer having its own anneal stage.

6.4.5.2 Single Deposition - Single Anneal

Analysis of the multi-deposition, single-anneal process in the previous section was limited to visual comparisons. Whilst in principle, prism coupling is capable of characterising two layers it was found with the equipment available that this was not practically possible, primarily due to damage to the prism surface after extensive use. In contrast, it is relatively straightforward to measure the thickness and refractive index of a single layer deposition. Therefore two single layer samples were used to investigate the effect of annealing on refractive index and layer thickness. The two layer recipes used for this were identical to those used for the multi-layer work of the previous description. Thus one germanium doped and one phosphorous doped layer was studied.

Two sets of measurements were performed on each layer which was again cleaved

into four. An 800℃ anneal was first performed for different lengths of time (1 hour, 2 hours and approximately 17 hours). Subsequent to this, the sample annealed for 17 hours (i.e. overnight) was then annealed for two hour periods at successively higher temperatures. The results of these procedures are presented in figures 6.10, 6.11, 6.16 and 6.17.

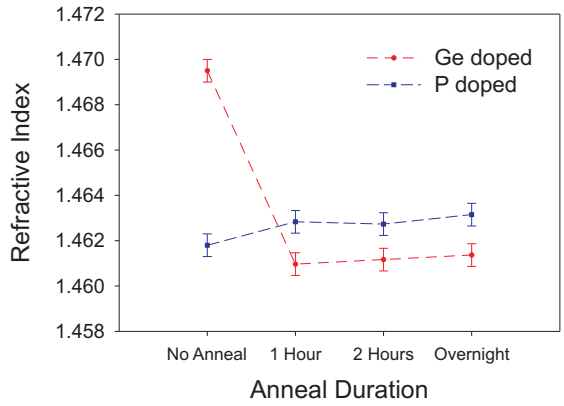

Figure 6.10: Variation of layer refractive index at 633nm with anneal time at 800℃

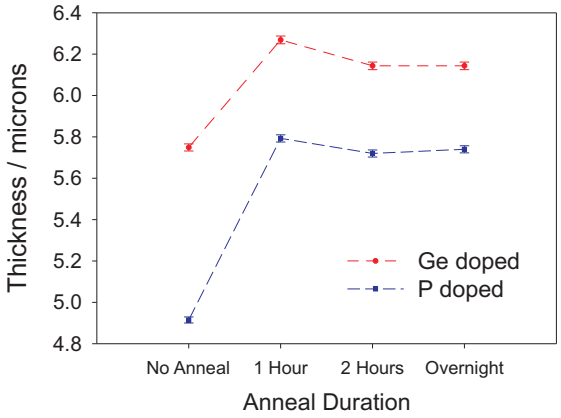

Figure 6.11: Variation of layer thickness with anneal time at 800℃

The most obvious features of all four figures is the significant changes from the pre-anneal state to the post-anneal state. It appears that both the germanium and phosphorous doped layers increase in thickness after a one hour anneal at 800℃ . Although anneal induced volume increases have been reported in the literature [4] the effect is observed only up to anneal temperatures of 500℃ before layer shrinkage occurs at higher temperatures. The thickness changes shown in 6.11 represent

increases in excess of 10%. Considering figure 6.10 we see that the data for the germanium layer shows a large (approximately 1×10^{-2}) decrease in refractive index. Such a decrease in index could be linked to a change in layer density. However, the data for the phosphorous layer shows no such change. Instead there is a small increase in refractive index despite the thickness change of approximately 1 micron shown in 6.11.

It was expected from the literature that the annealing of the silica layers would result in a slight decrease in thickness due to a combination of outgassing of nitrogen and hydrogen and to the effects of increased cross linking within the silica matrix [4].

Thus the initial, pre-anneal data points of all four figures are to be treated with caution as they appear to be inconsistent. With the use of a scanning electron microscope (SEM) the pre- and post-annealed layers were imaged to obtain additional measurements of layer thickness. The images of the two layers are shown in figures 6.12,6.13 (Germanium doped) and 6.14,6.15 (Phosphorous doped).

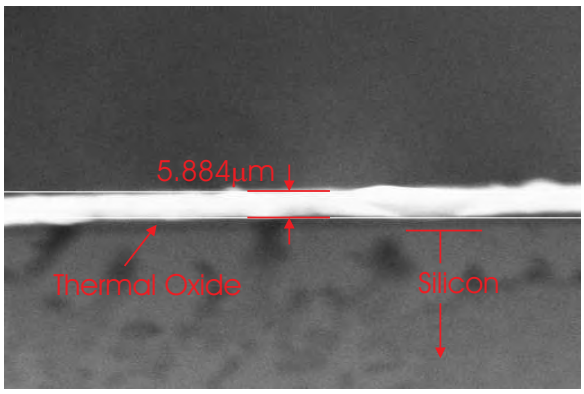

Figure 6.12: SEM image of germanium doped layer as deposited

Owing to the poor image quality of the figures determining the layer thickness using the measurement function of the SEM is a slightly subjective affair. Nonetheless it is possible to make out both the deposited silica and the thermal oxide layers. Both layers show a decrease in thickness; approximately 0.06 microns for the germanium doped layer and 1.2 microns for the phosphorous doped layer. Whilst the absolute thickness values of the two methods differs somewhat, the decrease in thickness observed using the SEM is the expected trend.

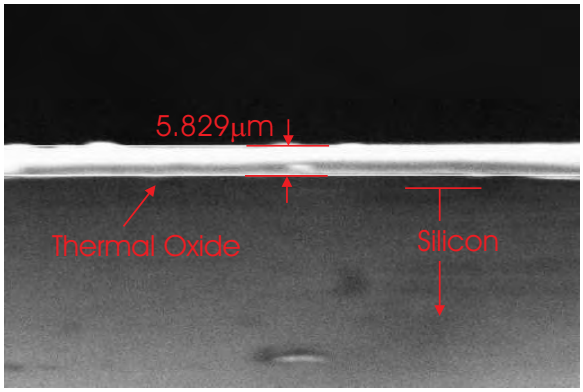

Figure 6.13: SEM image of germanium doped layer after a 1 hour anneal at 800°C

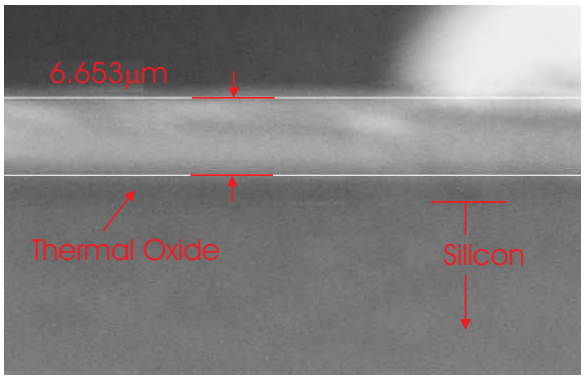

Figure 6.14: SEM image of phosphorous doped layer as deposited

The inconsistencies associated with the pre-anneal prism coupled data point may be linked to the pressures used to hold the prism against the deposited layer. After measurements on non-annealed layers it was possible to see where the prism was in contact with the layer. Should the layer, which is not fully dense before anneal, be deformed by the pressure applied it is possible that the results could become unreliable. Unfortunately, owing to equipment and time limitations it was not possible to investigate this further.

In the light of these comments, the initial pre-anneal data points of the prism coupling data will be disregarded and discussion limited to the more reliable post-anneal measurements.

Aside from the discounted results from the start of the annealing process the behaviour of the two layers is similar.

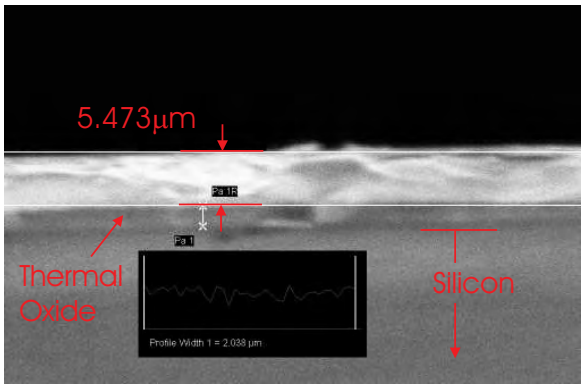

Figure 6.15: SEM image of phosphorous doped layer after a 1 hour anneal at 800℃

The slight decrease in thickness and corresponding increase in refractive index observed with the extended 800℃ anneal is similar to behaviour seen in other reports [4]. Annealing of PECVD silicon oxynitride above 600℃ causes densification that is attributed to the formation of Si-O and Si-N bonds within the glass matrix. This in turn causes an increase in density and increase in refractive index. Whilst there will be considerably lower concentrations of nitrogen present in the samples studied here it is very likely that cross linking of the matrix increases the number of Si-O bonds present. Outgassing of both nitrogen and hydrogen from the glass matrix is also expected to be occurring during the anneal process.

Figures 6.16 and 6.17 show refractive index measurements and thickness measurements after successive anneals each performed at a temperature higher than the preceding one. It should be noted that the initial pre-anneal points are again shown for reference but treated as anomalous. Also shown are data points measured on a non-annealed sample but recorded at the end of the experiment (i.e. after all other samples had been annealed) in order to provide control data. It can be seen that despite the extended dwell at 800℃ (approximately 17 hours) further anneals at higher temperatures cause further changes. The key features of figure 6.16 are that the germanium layer only appears to stabilise with a 1000℃ anneal and also that it is not until the same temperature that the two layers become index matched as they are intended to be. Temperatures above 1300℃ were not used as these would be approaching the melting point of the silicon substrate (1414℃).

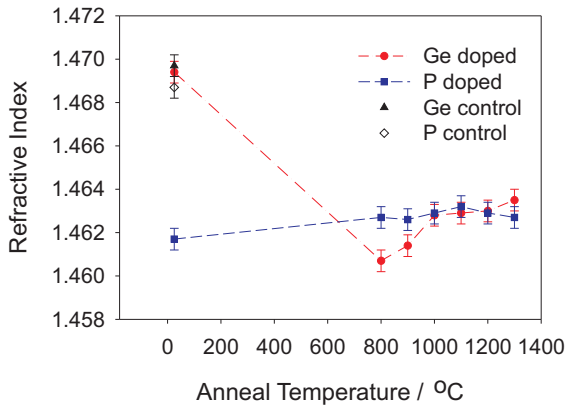

Figure 6.16: Variation of layer refractive index at 633nm with successive anneal steps of increasing temperature

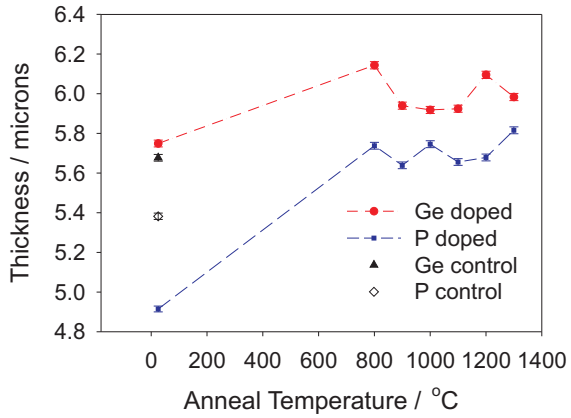

Figure 6.17: Variation of layer thickness with successive anneal steps of increasing temperature

Although this does not represent a comprehensive study of annealing effects the outcomes are nonetheless useful in defining a suitable process for the deposition of three layer structures. Whilst the mechanisms taking place during anneal steps are not fully characterised at this stage, it is the final annealed layers that are of interest in this work. The conclusions from these annealing tests are as follows:

• Based on the 800℃ anneal, a one hour dwell at the anneal temperature is sufficient to stabilise refractive index. A slightly longer anneal may be required to stabilise thickness.

• Anneal temperatures between 1000℃ and 1100℃ are optimal to stabilise refractive

index of both the germanium and phosphorous compositions used. Thickness of the germanium doped layer is stable over these temperatures. The phosphorous based composition appears to be less stable but as this layer will be used as a cladding, not as a waveguide core, the absolute thickness is less critical.

An additional point of note is that in annealing phosphorous doped layers of different but similar compositions to those above, using a slow ramping and a near instantaneous ramping of temperature, produced the same outcome. In one case the sample was placed into a furnace at 1100℃ for one hour and then removed. In the second case the sample was placed into a furnace at 500℃ , ramped up to 1100℃ at a rate of 20°/minute, held at 1100℃ for 4 hours before the furnace was allowed to cool radiatively overnight to ambient temperature. Despite the difference in anneal, the final refractive indices were found to be within 3×10^{-5} of each other, well below the resolution limit of the prism coupler (5×10^{-4}). This, combined with the conclusions above indicates that a 1 hour anneal, with no ramping of temperatures produces the same outcome in terms of refractive index as more controlled, gentle annealing regimes.

It is clear that further study of the annealing process is required to gain a complete understanding of the deposited layers and their behaviour. Unfortunately this was not possible due to time constraints imposed by some of the difficulties outlined in appendix A.

6.4.6 Deposition Parameters

Using the germanium and phosphorous doped characterisation trials as a starting point multiple layer depositions were made. The recipes and process parameters used evolved based on the outcome of the previous deposition. As the core and cladding layers are required to be index matched the development of one layer is dependent upon the other. The most significant single layer depositions that were performed are listed in table 6.2.

The evolution of the deposition parameters was based primarily on the requirement

	Germanium Doped layers for Waveguide Core							
	SiH_4	GeH_4	PH_3	B_2H_6	N_2O	Pressure	Power	Refractive
	sccm	sccm	sccm	sccm	sccm	mTorr	W	Index
1	17	175	0	0	2000	300	700	1.4605
6	17	175	1	1	2000	500	700	*
7	17	300	1	1	2000	400	700	1.4612
9	17	500	1	1	2000	400	700	1.4633
10	17	400	1	1	2000	400	700	1.4622
11	17	430	1	1	2000	400	700	1.4627
12	17	500	1	1	2000	500	700	1.4634
	* *Deposited onto pre-existing cladding layer with improved bubbling characteristics but layer too thin for prism coupling*							
	Phosphorous Doped layers for Waveguide Cladding							
	SiH_4	GeH_4	PH_3	B_2H_6	N_2O	Pressure	Power	Refractive
	sccm	sccm	sccm	sccm	sccm	mTorr	W	index
2	17	0	12	5	2000	300	900	1.4602
3	17	0	12	1	2000	300	900	1.4610
4	17	0	24	5	2000	300	900	1.4628
5	17	0	12	5	2000	500	900	1.4590
8	17	5	24	1	2000	400	900	1.4623
13	15	5	24	1	2000	400	900	1.4634

Table 6.2: List of key single layer depositions in the development of three layer structures. The leftmost column contains the order of progress to indicate the development route.

that the core and cladding layers must remain approximately index matched. The secondary criteria used was to reduce or eliminate the effects of showerhead induced patterning. It can be seen that the layer refractive indices are somewhat lower than that of standard single mode fibre (approx. 1.47 at 1550nm). Whilst this is not necessarily desirable, given that all devices fabricated were intended to be fibre coupled, this did provide the freedom to dope the layers with larger amounts of germanium or phosphorous if the development so required.

The evolution of deposition parameters can be summarised in general terms as follows:

• Following initial germanium and phosphorous doped layer deposition the dopant levels of the cladding were increased. This had the twin benefit of raising the refractive index closer to that of fibre and also allowed more germanium to be incorporated into a index matched core layer. Increasing the dopant levels required an increase in deposition chamber pressure to overcome the effects of showerhead patterning. Increasing the pressure was observed to decrease both refractive index and deposition rate. Consequently the minimum acceptable chamber pressure is desired for a given deposition recipe.

• The germanium content of the core layer was increased to help maximise potential photosensitivity and also to remain closely index matched to the cladding layers. Chamber pressure was modified to avoid showerhead patterning.

• Both layer dopant levels were modified further to re-index match the layers. Following difficulties in flowing high levels of PH_3 during depositions (see appendix A) the silane flow was reduced in order to provide a higher effective dopant level in the finished cladding layer.

Concurrent to this layer evolution, a variety of attempts were made to deposit multiple layers. Primarily this was based around the necessary step of depositing a germanium doped core layer onto a phosphorous doped under cladding layer. Initial indications were that multiple layers were not possible due to the showerhead related defects. Thus fresh attempts to deposit multiple layers were made as showerhead defects were reduced in an attempt to determine appropriate deposition pa-

rameters. To eliminate the possibility that surface contamination occurred during the inter-deposition anneal step an additional step was added to all layer deposition processes. Before deposition of any layer each substrate was subjected to a nitrogen plasma treatment. Nitrogen flow of 2000sccm was used with an RF power of 900 Watts. This is unlikely to cause significant alteration to the substrate and would assist in removal of any organic contamination on the surface and prevent delamination.

Despite these precautions, no successful results were obtained in trying to deposit a full thickness core layer onto a cladding layer. In addition to the bubbling and delamination already discussed, pullback of the layers from the edge of the wafer was also observed (figure 6.18). The reason for this observation remains unclear but the phenomenon was observed only occasionally so is likely to be related to contamination of a wafer that was not sufficiently cleaned by the pre-deposition plasma cleaning process.

Figure 6.18: A sample demonstrating layer pullback from the wafer edge. In this case layer 11 (see table 6.2) was deposited on layer 8. Slight bubbling was also present over the whole wafer.

6.4.6.1 Reduction of Layer Bubbling

Whilst deposition of germanium doped core layers onto phosphorous doped cladding proved to be less than straightforward, deposition of a phosphorous doped layer onto an identical phosphorous layer with an intermediate anneal was success-

ful. No bubbles or delamination occurred giving an indication that showerhead defects alone were not responsible for the difficulties in producing multi-layer samples.

Another observation was related to the deposition listed as number 6 in table 6.2. The purpose of this process was to investigate whether inclusion of small amounts of both phosphorous and boron into the germanium layer would help in the successful production of two layer depositions. In previous work by members of the group, notably that by Sam Watts [5], the introduction of a new dopant was observed to sometimes abruptly change the layer properties of FHD layers. However, increasing the concentration from a very low concentration to a more significant level resulted in a somewhat more predictable change. Although the conditions and techniques differ considerably between FHD and PECVD the effects of dopants are similar. Therefore it may have been beneficial to maintain a small quantity of each dopant in each layer to assist in matching properties such as thermal expansion and melting points. Owing to a shortage of N_2O the deposition of this multi-dopant silica was cut short and did not run to completion leaving a much thinner layer than originally intended, estimated at less than 4 microns thick. However, upon annealing the sample, although the usual small bubbles occurred over the surface there were noticeably less over the wafer than in previous attempts. As this was the goal of the experiment the improvement was attributed to the inclusion of phosphorous and boron in the germanium layer.

Subsequently however, in producing further variations of two layer samples it was observed that the successful deposition of two layer structures could be achieved but success was related more to the thickness of the germanium layer than to the composition of the layer. With this observation, using recipes 12 and 13 of table 6.2 multi-step depositions were performed. Firstly, a six micron layer of underclad was deposited and annealed. Then a three micron layer of core-silica was deposited and annealed. This was repeated to build up a six micron core layer.

After the first three micron germanium core layer had been annealed only slight signs of bubbling were apparent, barely visible to the naked eye. After the second germanium layer just a few very small ($\ll$1mm diameter) bubbles could be seen over the surface. Expanding on this success, the process was repeated but using three 2

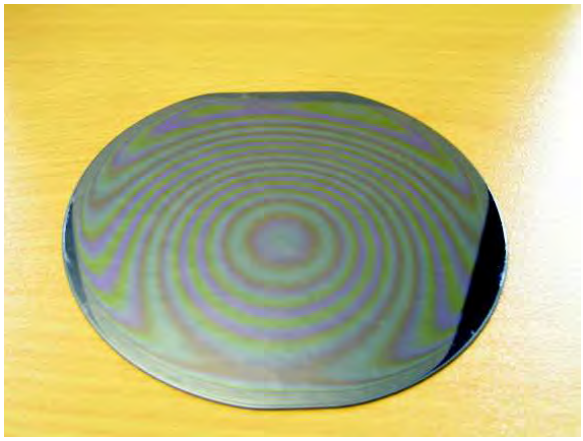

Figure 6.19: The first successfully deposited three layer sample using a 6 micron core layer deposited in three 2 micron thick steps.

micron deposition-anneal stages to produce the six micron core layer. The first two micron layer showed no visible bubbling after annealing and although the second and third layers resulted in very slight blistering there were clearly defect-free areas of the sample large enough to define UV written structures in. The final step of the process was to deposit an overcladding. This was achieved in a single process step, depositing 6 microns of the phosphorous doped layer and annealing it with no degradation of the final surface finish. This first index matched, three layer structure with photosensitive core is shown in figure 6.19.

For comparison, figure 6.20 shows the result of depositing just an underclad and core layer, using exactly the same process parameters but using a single deposition-anneal step for the germanium doped layer. The difference is striking and it is clear that the thickness increment used to build up the germanium layer plays a highly significant role.

Again, for the purposes of comparison, figure 6.21 shows a layer of the geranium doped silica approximately 6 microns thick, deposited using identical parameters. Clearly, it is possible to deposit this layer and anneal it without any layer defects being introduced. Thus it is a combination of the underclad properties and the layer thickness that determine the success with which a germanium doped silica layer can be deposited onto a phosphorous doped layer.

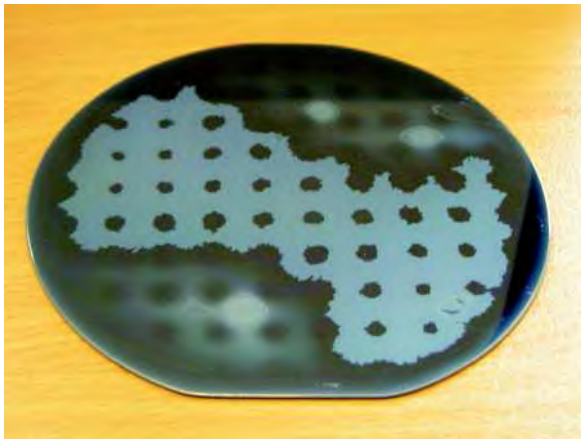

Figure 6.20: In contrast with fig.6.19 when the same core layer recipe is deposited as single 6 micron layer onto the same cladding, delamination and bubbling are clearly observed.

Figure 6.21: A 6 micron layer of the final recipe, germanium doped core layer.

As discussed in section 6.4.5.1 the outgassing of hydrogen and nitrogen during annealing may be responsible for the bubbling that is observed across germanium doped layers deposited over phosphorus doped underclad. Thin layers may allow gaseous hydrogen or nitrogen to escape more easily resulting in a reduction of bubbling due to trapped gas. Additionally, any rearrangement of the silica structure that may occur due to outgassing or to the formation of new chemical bonds will not be constricted by such a large volume of material in the surrounding area. Thus localised stress in the layer may be reduced as a result of the lower layer thickness leaving a lower likelihood of surface disruption or delamination from the underlying substrate.

6.5 Final 3-layer Process

Based upon the results described above it became apparent that in order to achieve a high quality (i.e. smooth and bubble free) germanium doped layer on top of the boron and phosphorous doped undercladding it was necessary to perform the deposition in several steps. The final process developed for depositing three layer structures was as follows

Layer	**Preparation**	**Deposition**	**Anneal**
Underclad	N_2 Plasma Clean	30 Minute Underclad Deposition	1 Hour 1100℃
Core (Process repeated 5 times)	N_2 Plasma Clean	Timed deposition for one fifth of total layer thickness	30 Minute 1050℃
Overclad	N_2 Plasma Clean	30 Minute Overclad Deposition	1 Hour 1025℃

The process recipes for the index matched layers is provided below. Underclad and overclad were deposited using the same parameters.

	N_2O sccm	**SiH_4** sccm	**B_2H_6** sccm	**PH_3** sccm	**GeH_4** sccm	**Pressure** mTorr	**Power** W
Cladding	2000	15	1	24	5	400	900
Core	2000	17	1	1	500	500	700

	Refractive Index at 633nm	**Deposition Rate** microns / minute
Cladding	1.4630	0.257
Core	1.4631	0.257

Here we again note that the germane flow rates are multiplied by a factor of 100 and that the phosphine and diborane flows are diluted such that the actual supply of each gas is 10% of the total quoted flow.

It may be noted that anneal temperatures were decreased for each successive deposition stage *i.e.* underclad layers were annealed at 1100℃ , core layers at 1050℃

and overclad layers at 1025℃ . This regime was chosen when depositing the initial successful three layer structure to reduce the possibility of bubbling effects being caused by heating previously deposited layers back to their original anneal temperature. The temperatures used all fall within the region over which refractive index and thickness are stable (figures 6.16, 6.17) so the resultant layer properties remain known. Owing to time constraints and concerns over equipment reliability, the process was subsequently duplicated exactly to ensure production of successful samples. However, it is considered unlikely that performing all anneals at 1100℃ would make a significant change to the outcome of the three layer deposition process.

The resultant layers produced using this process were found repeatedly to be suitable for UV writing. A very low level of showerhead defects can just be observed by eye. Time and equipment constraints prevented further enhancement of the process to eliminate this. However, these slight defects were not considered problematic owing to their magnitude and regular spacing. When dicing wafers into smaller samples for UV writing the saw cut was aligned to the grid defined by the showerhead pattern. In this way the areas used for UV writing were always between and well away from the affected areas. No additional limitations were therefore imposed on the dimensions of any UV written structures that were required for the work presented in subsequent sections.

A potential flaw in the design of the three layer structures described here is that the overclad is identical to the underclad. Although not fully confirmed it is highly likely that blistering observed in the germanium doped silica is due to high levels of compression in the layers when deposited on phosphorous doped silica. It is therefore possible that the overclad, deposited over the germanium doped core layer, is under tensile stress. This has the potential the cause the layer to degrade over time. However, 18 months after deposition, three layer structures processed according to the method above remain identical in appearance with no apparent clouding or cracking of the layer. Whilst this is not a confirmation that no degradation has occurred it is a very good indication that devices using such layers will be stable in the short to medium term and possibly longer.

Another related issue is that of the layer refractive index when combined in a mul-

tiple layer structure. All quoted refractive index values are measured with the layer deposited as a single layer onto the silicon wafer with thermal oxide. As it is believed that the layers are under some level compressive or tensile stress it is reasonable to assume that there will also be a stress induced variation of refractive index. No attempt has been made to quantify this to date but given some of the complexities in determining exact values of UV induced refractive index change this does not greatly hinder development of UV induced structures.

6.6 Layer Composition

A fully developed deposition process should include determination of the composition of the various layers that can be produced. One method of finding the composition is through secondary ion mass spectroscopy (SIMS). This would be the most appropriate method for accurate analysis of the layers developed here, however for several samples the technique becomes expensive and relies on external institutions with the correct equipment. Energy dispersive x-ray analysis (EDX) may also be used but is a less accurate technique and without an appropriate known standard glass composition can provide results with high uncertainty levels. Thus, to date the composition of the layers described in this chapter remains to a large extent unknown.

However, based upon similar boron, phosphorous and germanium doped silica produced and characterised by another group using a PECVD system, some initial estimations have been made [6]. Comparison of the refractive index changes caused by addition of the dopants indicates that the core layer was approximately 10mol% GeO_2 and the cladding approximately 5mol% P_2O_5. It must be stressed that this is only an estimate as the processes and resultant layers used in [6] are likely to differ substantially from those developed here. Thus, accurate determination of layer composition remains an area for future study.

6.7 Process Refinements

Although the development process described here ultimately produced successful three layer structures there are a number of tools that would assist in the further development and in the understanding of the process. Perhaps the most enlightening of these would be stress and thermal expansion measurements of the deposited layers. This would help confirm whether difficulties in the deposition of germanium doped layers onto phosphorous was due to excessive compression of the germanium layer as suggested in previous sections. Such measurements would also allow deposition parameters, particularly the RF power, to be tailored to assist in stress control.

In order to fully characterise the layers it is also necessary to determine the dopant concentrations in the final layers as discussed in the previous section. This would primarily be of interest for understanding optimum deposition parameters but also could be compared to the results of UV writing experiments to find the most suitable layer composition for waveguide definition.

Similarly, other procedures that would be beneficial when carried out in conjunction with UV writing would be the effects of a controlled atmosphere during the anneal stage on improving photosensitivity or optical loss.

6.8 Summary

The successful deposition of three layer structures for UV writing has been described. Core and cladding layers matched in terms of refractive index to 1×10^{-4} are deposited using carefully controlled deposition parameters and annealing regimes. It is found that in order to prevent blistering of the germanium doped core when deposited onto the predominantly phosphorous doped undercladding, it must be processed in several steps with intermediate anneals.

6.9 References

[1] M. Svalgaard. "Ultraviolet light induced refractive index structures in germanosilica". *PhD Thesis*, 1997. Technical University of Denmark.

[2] W.Kern and R.S.Rosler. "Advances in deposition processes for passivation films". *J. Vac. Sci. Technol.*, 14(5):1082–1099, 1977.

[3] A.Borghesi, A.Sassella, B.Pivac, and L.Zanotti. "Si-H Bonding Configuration in SiO_x:N,H Films Deposited by Chemical Vapour Deposition". *Solid State Communications*, 100(9):657–661, 1996.

[4] K.E.Mattsson. "Plasma-enhanced growth, composition, and refractive index of silicon oxy-nitride filmes". *J. Appl. Phys.*, 77(12):6616–6623, 1995.

[5] S.P. Watts. "Flame Hydrolysis Deposition of Photosensitive Silicate Layers Suitable for the Definition of Waveguiding Structures through Direct Ultraviolet Writing". *PhD Thesis*, 2002. University of Southampton.

[6] T. Bricheno formerly of Pi Photonics Ltd. *Personal Communication*.

Chapter 7

Definition and Characterisation of UV Written Structures

7.1 Introduction

In the following sections the layers produced using the processes described in the previous chapter are exposed to UV light and the resultant waveguides characterised. The direct grating writing (DGW) system was used to define both waveguides and Bragg gratings. With the use of various process parameters and characterisation techniques the photosensitive properties and optical performance of the samples were measured. The response to UV fluence, waveguide numerical aperture, birefringence, optical loss, mode profiles and the effects of hydrogen outdiffusion are all discussed to provide a thorough overview of the waveguiding structures that have been produced.

The Bragg gratings defined in the samples represent the first use of the DGW technique in PECVD layers. The levels of UV exposure required for a given refractive index increase were found to be somewhat higher than in previous UV writing work into layers fabricated by FHD, highlighting that sample performance is highly dependent upon processing history. Despite the use of exposures over 120kJcm^{-2} no damage to the silica layers was observed.

The propagation loss of the waveguides was found not to be as low as other examples of UV written waveguides in silica. The reasons for this are most likely to be a combination of non-optimised deposition processes and the effects of hydrogen loading to enhance photosensitivity.

7.2 Characterisation Techniques

Once the required silica layers have been deposited there are a variety of techniques that can be used to characterise the structures and subsequent UV defined devices. For clarity the methods used are described together below. All samples were polished on both end facets to allow butt coupling of fibres to the waveguides.

7.2.1 Grating Spectra

Perhaps the most important analysis technique of this section is that of determining the Bragg wavelength of gratings from reflection or transmission spectra. This was achieved using the experimental arrangements shown in figure 7.1. Using the fixed

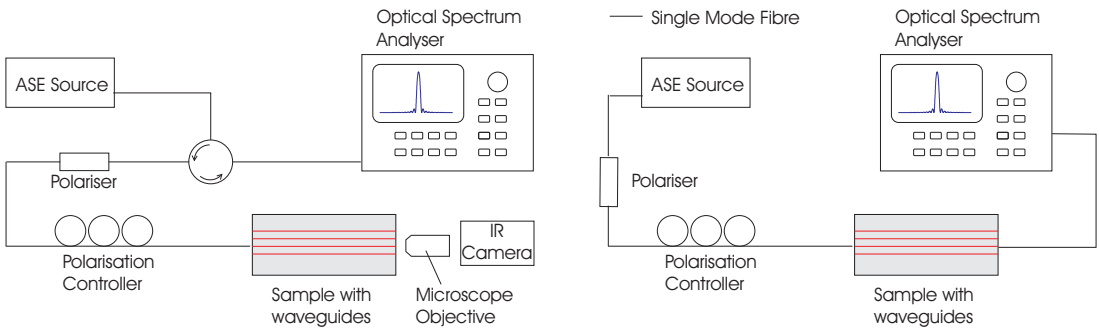

Figure 7.1: Experimental arrangement used to record Bragg *Left:* reflection and *Right:* transmission spectra.

polariser, polarisation controller and a polarising beam splitter TE or TM polarisation can be selected from the ordinarily unpolarised output of the ASE source. The light is then coupled into the sample from single mode fibre by butt-coupling with the use

of index matching oil to reduce reflections at the interfaces. Unless otherwise stated, all characterisation used TM polarisation.

7.2.2 Numerical Aperture

Determination of the UV induced refractive index change is not as straightforward as it might seem at first consideration. Unlike conventional etched waveguides where the core and cladding refractive indices can be measured separately as complete layers, it is only the pre-exposed core layer that can be measured in the UV writing case. Chapter 8 demonstrates how the technique of Direct Grating Writing goes some way to solving this issue. Whilst the determination of clad and core index for optical fibres can be measured at the preform stage when the dimensions of the structure are still large, this is not the case with planar structures. One method to determine the index contrast of a waveguide is to measure the *numerical aperture* (NA), given by equation 7.1

$$NA = \sqrt{n_{core}^2 - n_{clad}^2} \tag{7.1}$$

The NA, approximated by the sine of the half angle of the divergence of the light output of a waveguide, is a measure of the Δn of the waveguide core/cladding. Collection of mode profiles and subsequent calculation of NA was performed using a semi-automated system designed and implemented by G.D.Emmerson (fig.7.2). The method images and records the waveguide output using a calibrated CCD camera. Taking such intensity profiles at several distances from the waveguide facet allows the mode size and therefore the half angle and NA to be determined. NA measurements were taken in the vertical and horizontal directions and therefore correspond to the upperclad / core layer / overclad refractive index structure and the core layer / UV waveguide / core layer structure respectively.

The wavelength used for NA measurements was 633nm, a wavelength at which the waveguides, intended to be single mode at 1550nm, will support several modes. It should be noted that this may introduce a source of error into the determination of

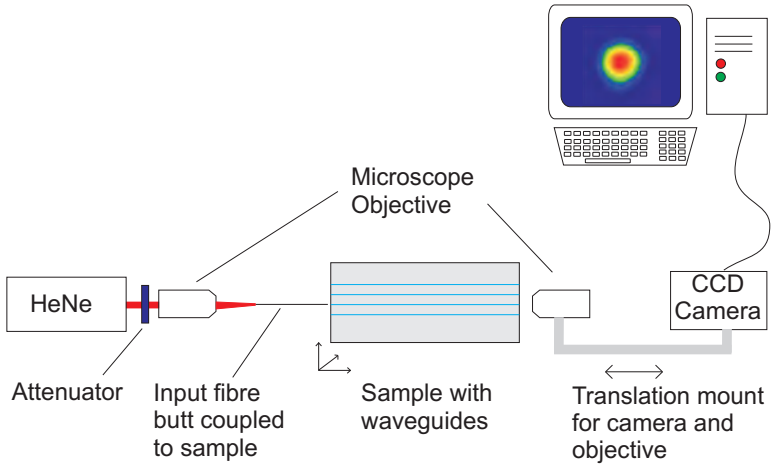

Figure 7.2: Experimental setup used to make estimates of numerical aperture

NA as the output mode may have a level of structure due to the various supported modes.

7.2.3 Transmitted Power

For the purposes of measuring propagation loss and absorption spectra absolute transmitted power measurements were recorded as shown in figure 7.3.

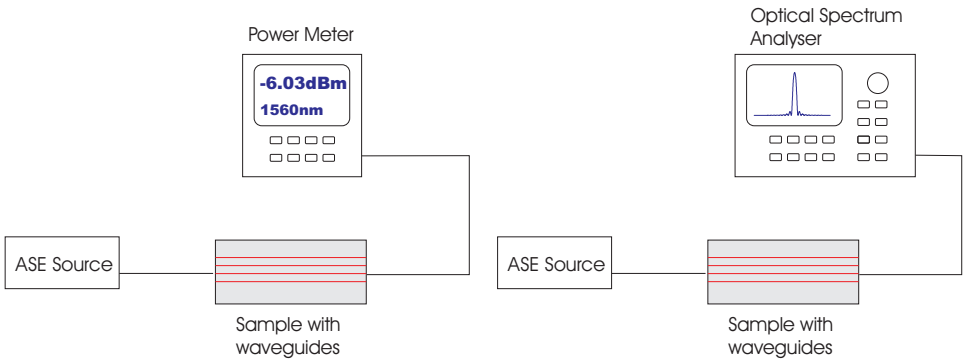

Figure 7.3: Experimental arrangement used to record *Left:* transmitted power readings and *Right:* absorption spectra.

7.2.4 Mode Profiles

Although mode profiles are recorded as part of the NA measurement process described above, all results from this process are at a wavelength of 633nm. To record profiles at 1550nm the grating spectra setup for reflection measurements was used. The waveguide output was imaged onto the IR camera with a $\times 40$ microscope objective. The camera output was then recorded with video capture software on a PC. To calculate dimensions of the measured profiles a pinhole of known dimensions was first imaged and recorded to provide a calibration reference. A simple Matlab program was written to convert the recorded images into a dimensioned intensity map suitable for plotting in standard graphing software.

7.3 UV Writing into PECVD Layers

In order to characterise the first three layer index matched wafer that had been processed it was first hydrogen loaded to enhance the available photosensitivity. As with all samples discussed in this and other chapters, unless otherwise stated the samples were placed into a $\geq$120bar hydrogen atmosphere at room temperature for at least three days. Upon removal from the hydrogen cell samples were stored in liquid nitrogen to prevent outdiffusion until the UV writing process began. The UV power applied to all samples was determined by the maximum stable laser power output that could be achieved. The required fluence was then controlled using the sample translation speed.

The first successfully deposited sample, consisting of 6 micron thick underclad, core and overclad was UV exposed to check that a waveguide and Bragg grating could be defined using this method. In common with all other samples used the layers were all deposited onto a 2 micron thick thermal oxide buffer layer on a 1mm thick silicon wafer.

The structure was written into the first PECVD sample with the parameters given in table 7.1. Explanations of these values are provided in chapter 3. Gratings were

written over the full 26mm length of the sample. Figure 7.4 shows the transmission and reflection spectra of the first Bragg structures written into PECVD silica by direct grating writing.

Duty Cycle	35%
Period	530nm
UV power	80mW
Translation speed	5mm min^{-1}
Average fluence	10.7 kJ cm^{-1}

Table 7.1: UV writing parameters for first DGW PECVD sample.

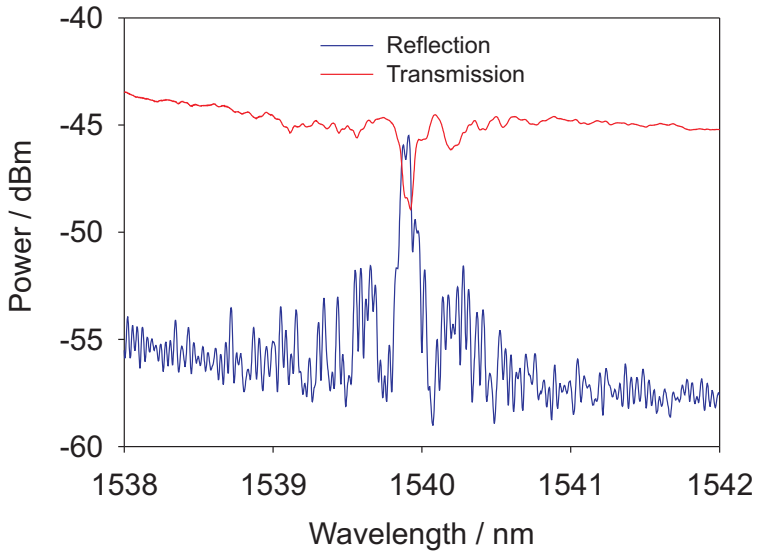

Figure 7.4: Reflection and transmission spectra of first results of direct grating writing into PECVD silica.

It can be clearly seen that a Bragg grating is successfully defined into the three layer structure with the peak reflectivity some 10dB above the background noise level. The waveguide could be easily located by using the IR camera to view the waveguide output facet. Two key features can be observed from fig. 7.4. Firstly, the centre wavelength of the response is around 1539nm, some distance from the target Bragg wavelength of 1550nm. This can be easily remedied by correct detuning of the grating period. Secondly, and more significantly, the response of the grating is not the clean, single peak spectrum that would be expected from an idealised Bragg grating.

The multiple-peak and somewhat noisy spectrum of the grating response can be explained by the waveguide dimensions. A multimode waveguiding structure will display more than one reflection peak as each mode propagates with a different effective index and thus has a different Bragg wavelength according to

$$\lambda_b = 2\Lambda n_{eff} \tag{7.2}$$

as already defined in chapter 2. To overcome this problem and obtain the expected Bragg spectrum a thinner core layer is required. To reliably calculate the required core thickness would prove very difficult as the UV induced index change as well as the size and profile of the resultant waveguide are unknown. Instead, the more practical route of fabricating a number of samples each with different thickness core layers was chosen.

It is also apparent from the characterisation of this sample that although the core and cladding refractive indices are very closely matched ($< 1 \times 10^{-4}$) at 633nm, this is not the case at wavelengths around 1550nm. When aligning the input fibre to the UV written waveguides a 'planar stripe' is easily seen using the IR camera. This is the result of the photosensitive core being somewhat higher in index than the cladding at 1550nm, causing a planar guiding layer that is seen as a horizontal bright stripe at the output facet. Although such an index contrast between the layers is not desirable when developing symmetrical, circular mode waveguides it is does in fact greatly ease the process of fibre coupling to the waveguides. For this reason it was decided not to attempt to obtain perfect index matching of the layers at 1550nm at this early stage of development.

7.3.1 Variations of Core Thickness

To investigate the maximum core thickness that will allow single mode behaviour at 1550nm four new three layer structures were deposited. Underclad and overclad layers were identical and were the same 6 micron thick depositions for all samples. The germanium doped core layer was deposited according to the same recipe as the waveguide presented in the previous section but the thickness was controlled

using the deposition time. With the assumption that deposition rate is constant up to the equipment manufacturer's recommended maximum single-deposition thickness (6 microns), it is simple to control the layer thickness. The deposition rate of 0.26 microns per minute makes it very easy to control layer thicknesses to fractions of a micron. In this way the new samples were prepared to have core thicknesses of 5.5, 5.0, 4.5 and 3.6 micron core thicknesses. It must be mentioned that the 3.6 micron core layer was a thinner core layer than originally intended, but owing to hardware failure during the deposition it was necessary to cut short the process time. In the interests of maintaining a constant deposition procedure, the resultant thinner core layer was kept rather than attempting to proceed to the desired thickness once the equipment was back in use. Aside from thickness control, all aspects of the three layer deposition process were as described in the previous chapter.

Comparison of the behaviour of the different thickness cores was achieved by writing identical sets of gratings into each and recording the reflection spectra. This procedure was carried out at four average fluences and at two duty cycles. Therefore, in total eight waveguides were written into each 11mm long sample.

The two most obvious properties of the gratings, those of centre wavelength and multi mode behaviour, were immediately seen to be improved on all samples. Figure 7.5 shows a significantly reduced bandwidth response. Defining the bandwidth as the wavelength difference between the first minima either side of the grating peak [1] gives a bandwidth 0.13nm and 3dB down from the peak reflectivity a bandwidth of 7.0×10^{-2} nm.

The effect of core thickness on Bragg response is shown in figure 7.6 for samples with core layers of 5.5, 5.0 and 4.5μm thick. The response of the 3.5μm core layer was found to be almost indistinguishable from the background level of reflected light and is not included in the figure. No further trials were performed with the 3.6μm sample. The responses shown in figure 7.6 are presented on the same scale axes to allow direct comparison. It must however be noted that variations in polish quality and fibre-waveguide coupling mean that direct comparisons of absolute values from the graphs are limited.

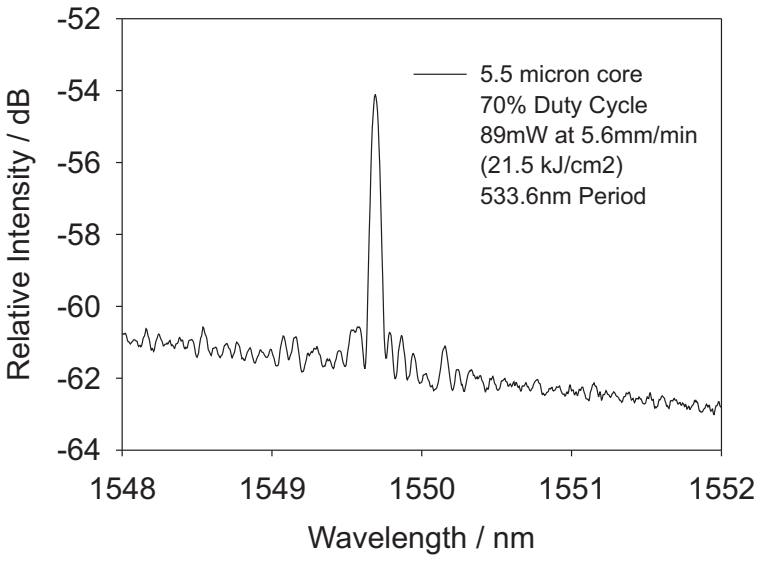

Figure 7.5: Narrowband Bragg reflection spectrum.

Although the response of the 5.5μm core sample shows the largest peak there is clearly a high level of structure to the response. This indicates that the waveguide is still supporting more than the fundamental mode. It has been observed that the quality of response from the 5.5μm sample varies somewhat when waveguides are written under nominally identical conditions. This implies that the dimensions of the core and the index change induced result in a waveguide that is on the threshold of single mode behaviour. Slight variations in the alignment of the two UV beams and in the beam quality itself are probably responsible for determining whether the resultant guide supports one or more modes.

The response of the 4.5μm sample, even when allowing for variations in coupling efficiency and polish quality is significantly weaker than the other responses shown in the figure. Thus the 5.0μm thick core sample provides the most suitable and repeatable response of the three for single mode waveguide devices. Some structure can still be seen in the reflection peak but it is considerably less than that of the 5.5μm sample.

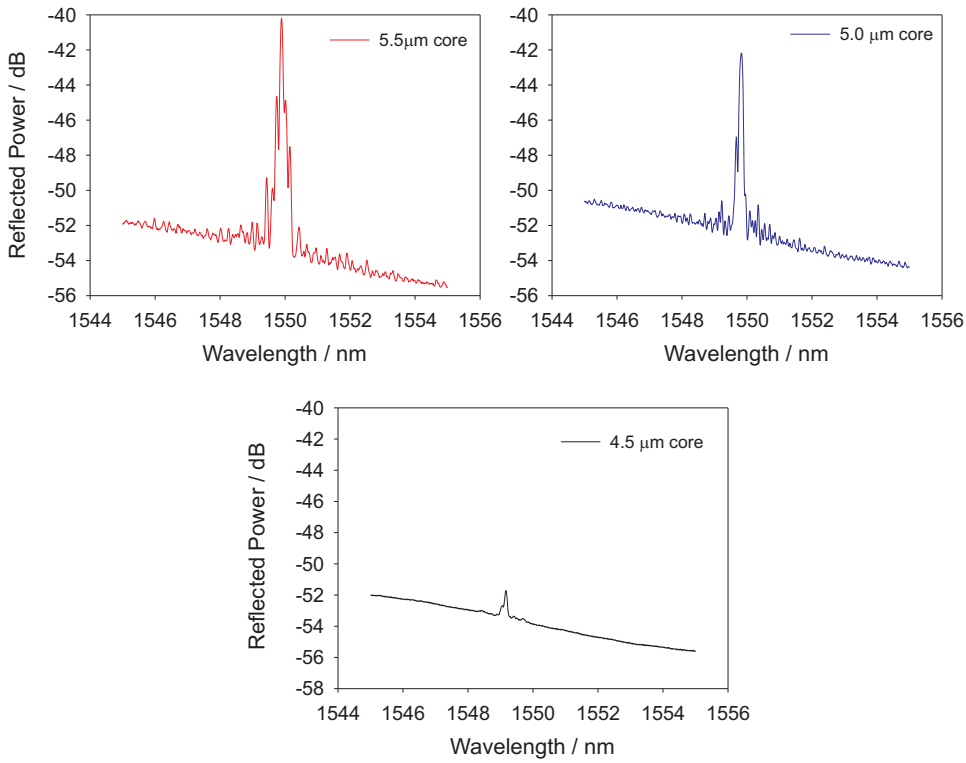

Figure 7.6: The effects of core thickness on Bragg response. All samples written at 21kJcm^{-2} and 50% duty cycle.

7.3.2 Effect of Duty Cycle

As discussed in chapter 3, control of the duty cycle can be used to control grating refractive index modulation whilst keeping a constant fluence and therefore a constant waveguide effective index. A higher percentage duty cycle results in a smaller bandwidth and a correspondingly reduced grating contrast [2]. Figure 7.7 shows qualitatively that the experimental data meets this expectation as the grating written with 70% duty cycle provides a smaller but narrower peak than that written at 50% duty cycle but at the same fluence. An exhaustive characterisation of the effect of duty cycle has not been performed here as the variation of grating response has already been demonstrated [2]. Again, it should be noted that the effects of hydrogen outdiffusion have been neglected in this comparison. This is believed to be a valid comparison due to the relatively small impact after the initial few minutes of outdiffusion time (section 7.3.7).

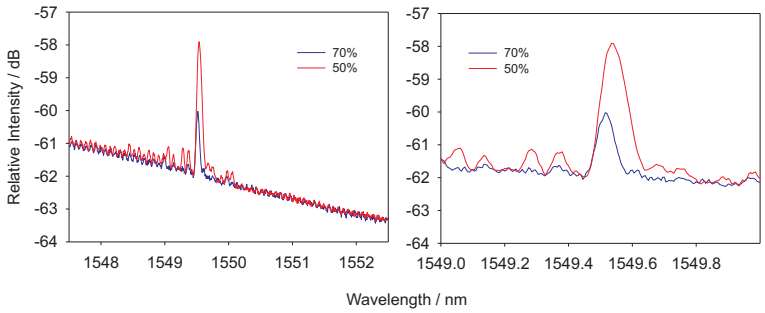

Figure 7.7: Comparison of two identical gratings written with 50% and 70% Duty cycle. Left: Wide wavelength range data. Right: The same data over a smaller wavelength span.

7.3.3 Fluence

In the fabrication of the waveguides produced in this work the UV exposure used to induce refractive index change is perhaps as critical to the final result as the deposition of the layers themselves. Determination of optimal exposures is critical to many of the characteristic parameters of the finished devices. The number of propagating modes that are supported, the birefringence, the maximum Bragg grating strength and even propagation loss can be determined by the UV exposure.

Initial investigations centred on the development of a *fluence curve*, a variation of waveguide effective index with UV writing fluence. In general terms an increase in the UV fluence can be expected to result in a higher refractive index change as the increased exposure 'activates' more defect centres. Clearly there will be a maximum index change that can be induced (without introducing severe structural damage) as all germanium and hydrogen related sites within the silica will be activated and a further increase in fluence cannot cause any additional change in refractive index.

The technique of direct grating writing is a particularly convenient method of determining a fluence curve. With the assumption that waveguides and Bragg gratings are perfectly fluence matched as described in chapter 3, the effective index as measured from the Bragg wavelength also provides the waveguide effective refractive index. Figure 7.8 shows the variation of waveguide effective index with fluence.

The most obvious features of the fluence curve are that as expected, the effective

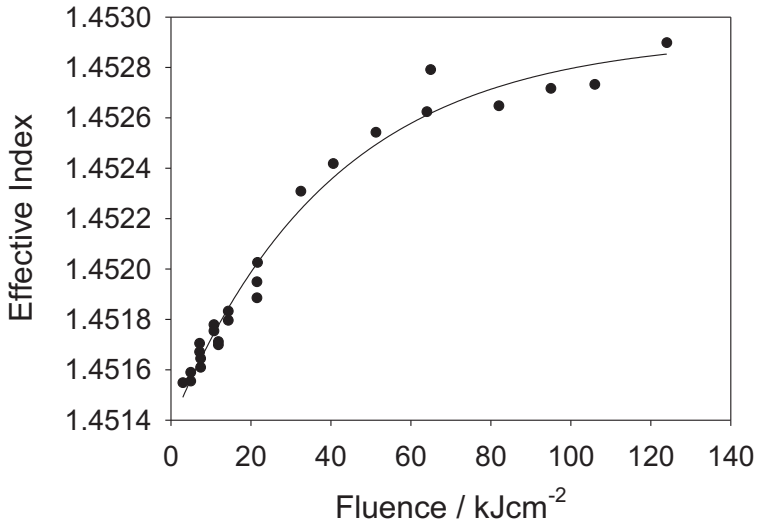

Figure 7.8: Fluence curve for samples with a 5.0μm thick core layer.

index increases linearly at low fluences (<30kJcm^{-2}) and tends towards a very low rate of increase at high fluences. Such a curve shape is expected as the UV induced index change will begin to saturate at higher fluence levels.

It can be expected that the waveguide effective index will vary with UV exposure as will the grating strength. Generally speaking, a higher intensity exposure will result in each grating plane have a higher refractive index relative to the background level of the unexposed core layer. Both of these effects can be seen in fig 7.9. The figure shows four reflection spectra written into the same sample, at the same period and the same duty cycle (50%). The speed of translation is the only parameter that was varied when writing these waveguides. The spectra are shown plotted on the same scale axes for comparison. It is reasonable to compare the spectra in this way as the coupling efficiency between the input fibre and waveguide will be near identical. Had the waveguides been written into different samples that were not processed at the same time in the same way such a comparison may not be valid. It must be remembered however that owing to hydrogen outdiffusion over the course of the UV writing process, the writing conditions do differ slightly from waveguide to waveguide. The effects of outdiffusion are discussed in section 7.3.7.

It can be clearly seen from fig 7.9 that the higher fluence exposures show a significantly stronger reflection peak as expected. The Bragg wavelength also decreases

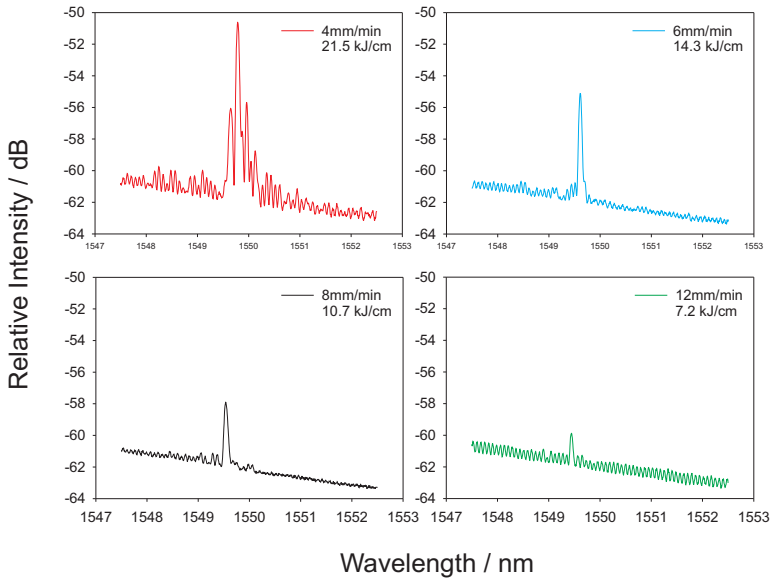

Figure 7.9: Variation of Bragg reflection spectrum with writing fluence. Top left: 21.5 kJcm^{-2}. Top right: 14.3 kJcm^{-2}. Bottom left: 7.7 kJcm^{-2}. Bottom right: 5.1 kJcm^{-2}.

with decreasing fluence indicating that the waveguide effective index is also reducing. This variation of effective refractive index with fluence will be discussed further in the subsequent sections.

Although in general terms, an increase in UV fluence provides an increase in refractive index change the maximum available fluence may not be the optimal condition to use. Observations by other UV writing groups have highlighted the possibility of significant degradation of PECVD doped layers [3]. Clearly visible damage was observed with fluences of comparable magnitude to the maximum values of figure 7.8. However, no such damage has been observed in the layers discussed here and surface profile measurements showed no change in surface structure as a result of UV exposure at fluences up to 124kJcm^{-2} . This suggests that for pure waveguiding structures fluences of around 100kJcm^{-2} may be optimal to ensure good mode confinement and allow smaller bend radii in curved guides. This of course is subject to waveguides remaining single mode given the associated dimensions and refractive index changes.

A second reason why the highest fluence may not be the best is particularly important for much of the work presented in this thesis. When defining Bragg gratings

into the UV written waveguides it is generally desirable for the index modulation between grating planes to be as high as possible to allow a strong Bragg response. High fluence levels can however produce the opposite effect.

Absorption of the UV light in the silica will inevitably result in thermal effects occurring in the layers. It is known from thermal locking work (chapter 8) that heat treatment of hydrogen loaded silica can cause a change in refractive index. Thus there will always be some level of refractive index change due to thermal effects even if the predominant increase is non-thermal. In this way there will be a thermal 'background' refractive index which occurs alongside the pure UV induced index change. A high level of thermal effects may in an extreme case saturate the available index change. As this point is approached, the purely optical refractive index change becomes swamped and grating contrast is reduced as shown in figure 7.10. Grating strength is discussed further in section 7.3.6.

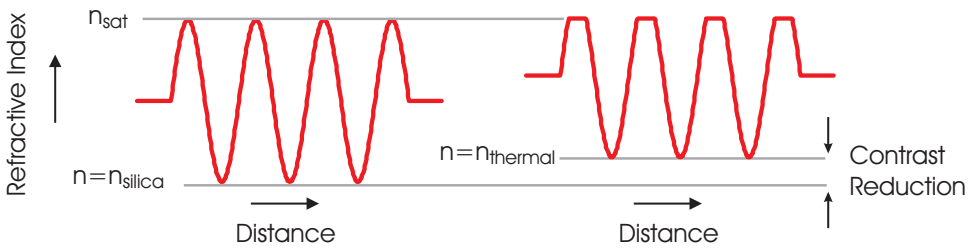

Figure 7.10: Left: - An idealised refractive index variation in a Bragg grating with no thermally induced backgroud. *Right:* The decrease in grating contrast due to thermally induced refractive index background. $n_{thermal}$ represents the thermally induced refractive index change, n_{silica} the unexposed silica refractive index and n_{sat} the saturated maximum refractive index available.

One of the most interesting features of the data plotted in figure 7.8 is only seen when making a comparison with data previously obtained in [2] where a similar experiment was performed to determine the fluence curve for FHD deposited samples (figure 7.11). The FHD samples used in that study were developed commercially but not specifically for the purposes of UV writing. The shape of the fluence curves for PECVD and FHD are similar but the magnitudes of the fluences used are remarkably different. The curve shown in figure 7.8 displays an index change of approximately 1.4×10^{-3} over a 120kJcm^{-2} fluence range. In contrast, the FHD fluence curve of

figure 7.11 recorded in [2] using similar levels of hydrogen loading shows a larger index change of 3×10^{-3} over a fluence range of just 22kJcm^{-2} .

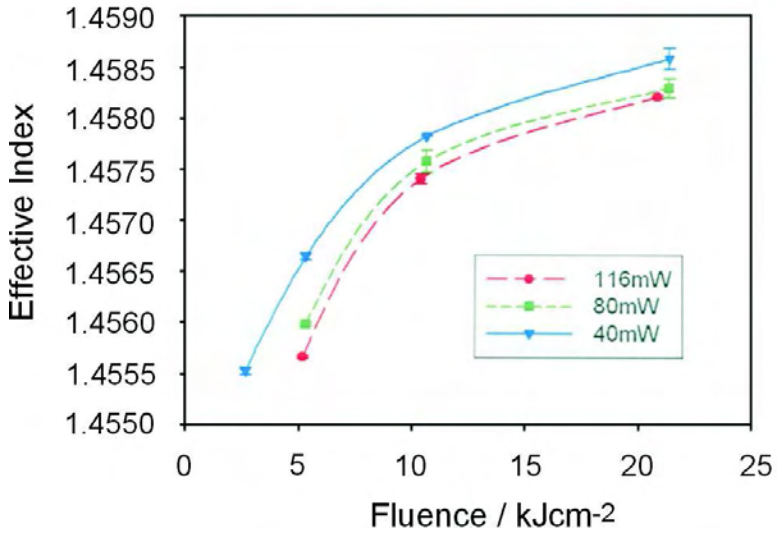

Figure 7.11: Fluence curve obtained by DGW in FHD samples (*after* [2])

It is possible that there is a higher level of germanium doping in the FHD sample although this has not been determined for both sample types. More likely is that there is a considerable difference in the properties of the two silica layers used. Further work is required to study this.

Additional differences between the PECVD and commercial FHD layers is seen qualitatively when performing the UV writing procedure. Upon exposing the FHD layers to the UV laser, the associated fluorescence of the sample is observed to build up to a maximum brightness over time. In contrast, the PECVD layers show a significantly more rapid, almost instantaneous fluorescence. The explanation for this is at present unknown. It is interesting to note that the FHD samples, when thermally treated to 'lock' in the hydrogen (chapters 3 and 8), show no such fluorescence build up and behave in a similar manner to the PECVD layers studied here.

7.3.4 Numerical Aperture

Numerical aperture measurements were taken, as described in section 7.2.2 for waveguides defined using a wide range of fluences. The results of these measurements are displayed in figure 7.12.

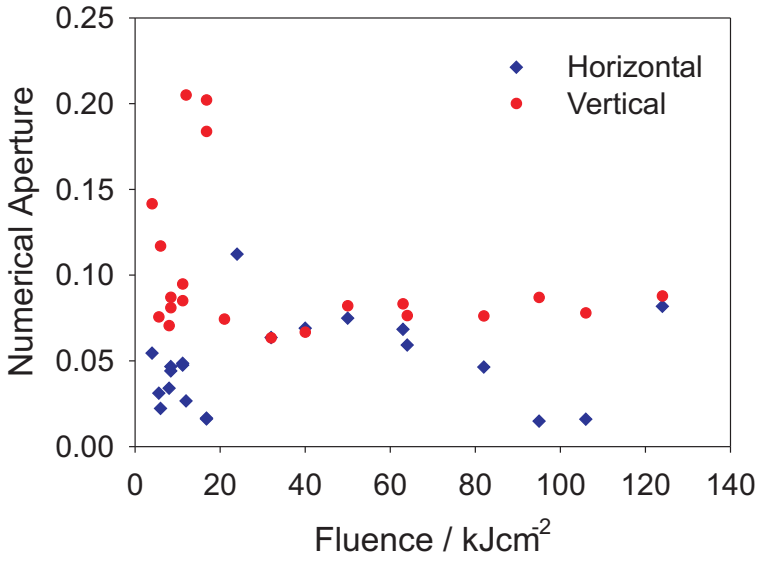

Figure 7.12: Variation of measured numerical aperture with fluence for 5.0 micron thick core waveguides

It is very clear from figure 7.12 that the data displays a high level of scatter, particularly for waveguides defined with fluences less than 20 kJcm^{-2}. There is also a significant difference to be seen between the data taken in the vertical direction and that in the horizontal.

Significant levels of scatter are to be expected from this style of NA measurement. Firstly, the shape of the recorded mode profile will be affected by the cleanliness and polish quality of the output facet. Secondly, the UV writing conditions will also have some effect on the shape of the mode which in turn will affect the calculated NA. The noise associated with this data set serves to highlight one of the advantages of the direct grating writing technique. Although the response of the Bragg gratings does not provide insight into the refractive index profile along different directions, it does provide very accurate measurements of the actual waveguide effective re-

fractive index. Additionally, the waveguides will be multimode at the measurement wavelength of 633nm. To obtain a reliable NA measurement it is desirable to have a smooth intensity profile from which to make measurements. At 633nm there may not be sufficient propagating modes to provide the required smooth profile thus further error may be introduced into the determination of NA.

It is also not surprising that NA differs when measured in the vertical or horizontal direction. It is readily observed when viewing the waveguide output with an IR camera that the three layer structure is not perfectly index matched as a 'planar stripe' can be seen where light is guided within the core layer as it has a higher index than the over/under cladding. This effect is also seen to a lesser extent at visible wavelengths and indicates that before UV writing there is a refractive index contrast resulting in a planar slab guide. Clearly, although the core and cladding layers are close to being truly index matched at 633nm, as shown by prism coupling, this is not the case at 1550nm.

7.3.5 Birefringence

Birefringence in waveguiding applications, particularly those that use filters such as Bragg gratings, is generally undesirable. As in conventional etched waveguides, birefringence in UV written guides depends largely on the symmetry of the waveguide and the stress within the layers. A uniform, circular waveguide core surrounded by uniform refractive index on all sides will have zero birefringence. In the case of UV writing, this symmetry can be broken due to a number of reasons. Firstly, if the three layer structure is not perfectly index matched, the waveguide cladding refractive index will not be uniform in all directions for the finished waveguide. Secondly, the geometry of the waveguide cross section depends on the writing beam. A non symmetric beam profile, incorrectly focussed crossed beams or a beam with too high/low fluence can all result in a refractive index increase that varies either in the vertical direction, the horizontal direction or both.

Both UV-defined and etched waveguides have been demonstrated with very low birefringence by control of layer stress and mode symmetry [4,5,6].

Incorporating a Bragg grating into a waveguide by direct grating writing allows a very simple means of measuring birefringence. If effective refractive index varies for different polarisations then so will the corresponding Bragg wavelength. Launching unpolarised light or light with controlled polarisations allows the difference in Bragg wavelength to be measured and birefringence calculated.

Using a polarising beam splitter TE and TM polarisations were launched into a UV written waveguide with grating. A third measurement was recorded with no polarisation imposed on the output of the ASE source. The core layer thickness was 5.5 microns thick and waveguides were defined at 4mm/min, 90mW (21.5kJ cm^{-1}). Figure 7.13 shows the variation of Bragg wavelength for the three launch conditions.

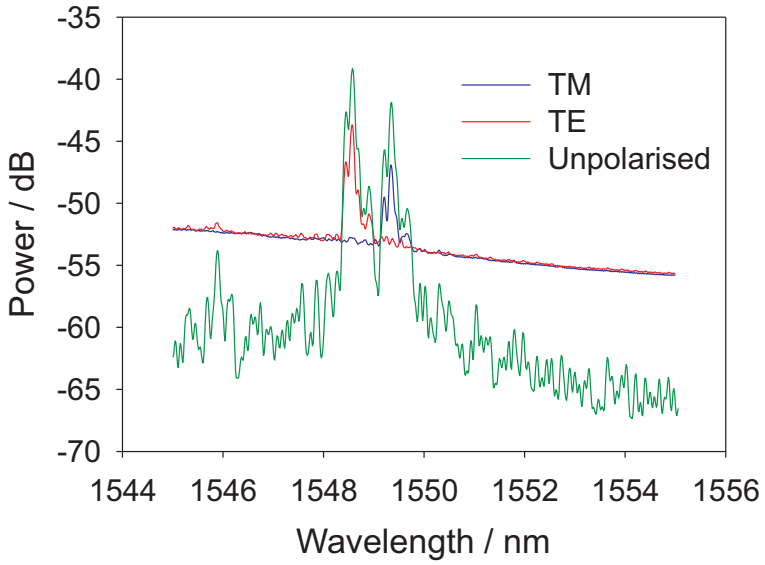

Figure 7.13: Grating spectra showing the different response for TE and TM polarisations.

Conversion of the Bragg wavelengths into the domain of effective index provides a TE effective index of 1.4509 and a TM effective index of 1.4516. Thus a birefringence of 7.3×10^{-4} is measured. The spectrum of unpolarised light in figure 7.13 shows that the Bragg wavelengths of the two polarised measurements are in agreement with that of the unpolarised light.

The same sample, written at half the fluence of that described above (10.7kJcm^{-2}) showed a birefringence of 7.4×10^{-4} indicating that writing power is not critical to

birefringence in this exposure range.

7.3.6 Transmission Response

Although the magnitude and centre of the Bragg reflection peak is perhaps the most straightforward way of assessing the performance of a Bragg grating, further analysis is required to characterise the behaviour more fully. The response measured in transmission is of importance as many potential applications rely on the grating's impact on transmitted light and the transmission response also provides a measure of the grating reflectivity. Additionally, with the experimental arrangement used to measure reflection spectra a wide variation in the magnitude of the measured Bragg reflection was observed due to variable reflections from the variety of connectors in the optical path.

Prior work on direct grating writing has shown that gratings with a transmission dip of 35dB at 1550nm can be written into three layer structures [2]. It was therefore expected that dips in the transmission response of the Bragg gratings defined in the layers developed in the work presented here would provide a comparable response. However, this was found not to be the case and the strongest transmission dips recorded were approximately 4.1dB, representing a reflectivity of 61%. Figure 7.14 shows such a transmission response along with the corresponding reflection spectrum.

Two possible reasons for the relatively weak transmission response are that the waveguides are multimode and that the index perturbation that forms the grating is weak. A low index modulation would be consistent with the low bandwidth grating responses that have been measured (e.g. figure 7.5). To investigate this the bandwidth, as measured from the first minima either side of the Bragg resonance, has been used to calculate the index perturbation [7]. Using a range of waveguides written at different fluences the index perturbation has been plotted in figure 7.15.

It is clear from figure 7.15 that there is little or no variation in the refractive index modulation in gratings written over a wide range of fluences and that the perturba-

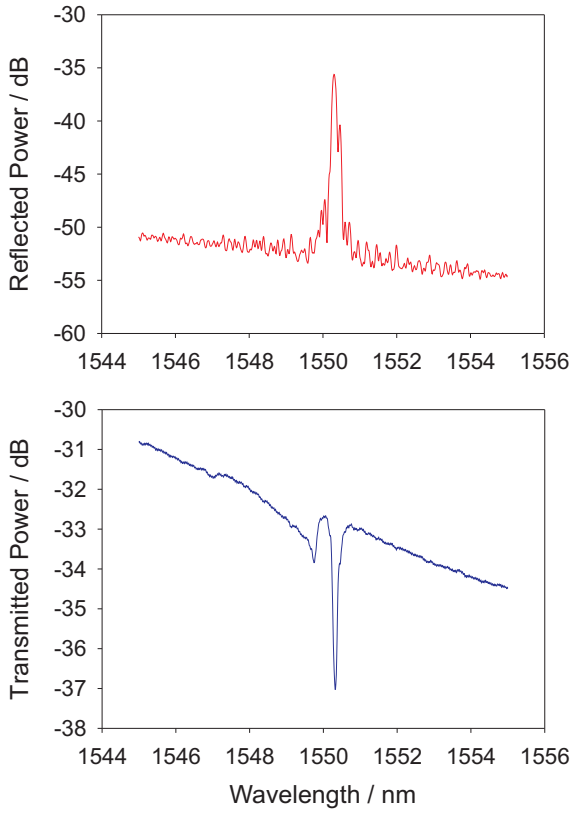

Figure 7.14: Spectra demonstrating strong measured reflection response (*top*) but weak transmission response (*bottom*).

tion is roughly constant at approximately 4×10^{-4}. As it is known that the DGW system is capable of producing perturbations an order of magnitude higher than this [2] it is unlikely that the weak contrast seen here is due to the writing technique. A more likely explanation is that of thermal effects as described in section 7.3.3. It is thought that thermal background raises the sample refractive index, reducing the available index contrast that can be used to create the grating. The lack of variation of index perturbation with fluence suggests that the thermal effects are not dependent on fluence and that the temperatures seen by the silica do not vary significantly over the fluence range used.

Mode profiles, along with the Bragg response of a grating are a means to check that waveguides are propagating only the fundamental mode. Multimode waveguides should show distinctly structured mode profiles unless so many modes are present that the end result appears to be roughly circular.

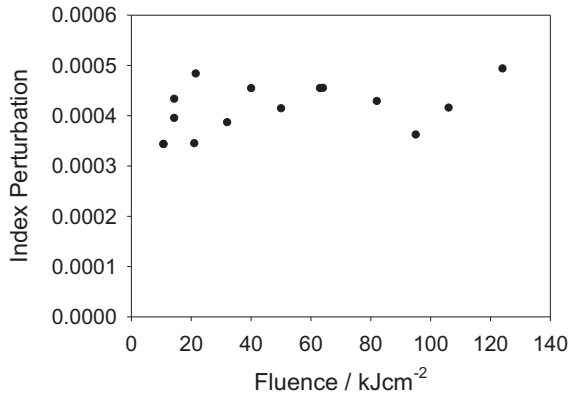

Figure 7.15: Variation of refractive index perturbation with UV writing fluence.

It can be seen in figure 7.16 that as expected, the propagating mode at 1300nm is more tightly confined than at 1560nm. It is also apparent that the writing fluence has little impact on the mode size. The slightly oval shape of the profiles is consistent with the discovery that the core layer has a slightly higher refractive index at 1550nm than the cladding layers. This results in slightly stronger confinement in the vertical direction that in the horizontal and the oval mode profiles that are shown. At 1300nm the mode appears more circular, possibly due to a smaller difference in the refractive index of the layers at this wavelength.

As discussed in earlier sections, the 5.5μm core samples show a structured Bragg reflection spectrum indicative of slight multimode behaviour. At lower wavelengths more modes will be present, this could explain the very smooth, rounded appearance of the 1300nm mode profiles. The 1560nm profiles are not expected to show a significantly multimode structure but do appear slightly distorted from a smooth profile. Poor end face polish could be responsible for this, but if this were the case the distortion would also show up in the 1300nm profile. Thus the images suggest that the waveguides are slightly multimode at 1560nm.

Slightly multimode behaviour of the waveguides coupled with the relatively small refractive index perturbation of the gratings would explain the relatively weak Bragg transmission response. The above results seem to suggest that both of these effects are indeed affecting the overall grating reflectivity.

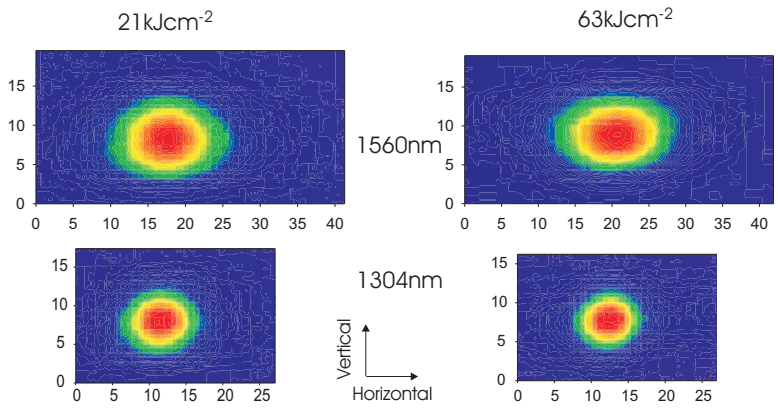

Figure 7.16: Mode profiles of a UV written sample with 5.5μm thick core layer. UV fluences used were 21kJcm^{-2} (*left*) and 63kJcm^{-2} (*right*). The images shown were recorded at 1560nm (*top*) and 1306nm(*bottom*).

7.3.7 Hydrogen Outdiffusion

In section 7.3.3 an application of direct grating writing was discussed to allow the UV induced waveguide effective refractive index to be measured. Other aspects of the UV writing process can be characterised using the same basic principles. Chapter 5 introduced the use of hydrogen loading as a means to enhance photosensitivity and also some of the limitations imposed by the outdiffusion of hydrogen during the writing process. By defining multiple Bragg gratings over a period of time using exactly the same process parameters the effects of outdiffusion on the UV induced effective index can be measured. This is of particular interest here as the silica samples used have an overcladding thickness of 6μm , around 20μm thinner than a typical silica waveguide structure and over 100μm thinner than a typical 1550nm single mode fibre. Such thin overcladding could result in very rapid outdiffusion rates which could limit the potential processing times for such layers.

The results of such a procedure a shown in figure 7.17. The data shows the resultant waveguide effective index plotted against the outdiffusion time measured from the point at which the sample was removed from its liquid nitrogen storage.

As the fitted curve shows, the variation of waveguide effective index approximately fits an exponential curve although arguably a linear fit could also be applied.

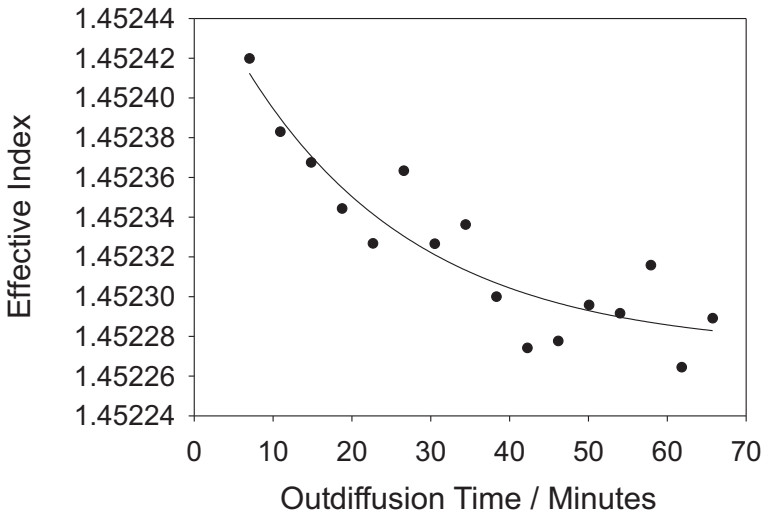

Figure 7.17: Variation of waveguide effective index with hydrogen outdiffusion time. The solid line is an exponential fit to the data points. The sample used had a 5.5μm thick core layer written at a fluence of 21kJcm^{-2}.

Two features of the graph are particularly noticeable. Firstly, there is a relatively small change in effective index with time. Using the fitted curve shown in the figure, the variation of refractive index is approximately 1×10^{-4} over the 57 minute period of UV writing shown, corresponding to 0.15nm. Whilst this is a relatively large shift in terms of modern telecommunications systems (approaching 200GHz) it represents a mean wavelength drift of approximately 3GHz or 2.5pm per minute.

A second feature of the curve in figure 7.17 is the level of noise on the data. This is unexpected and a smooth curve was the predicted outcome. Other authors have reported non-continuous changes in UV induced refractive index changes when varying the hydrogen content of the samples [8] but the mechanisms behind this are not clear. The noise on the data seen here are not considered to be linked to the reports in [8] where thermally accelerated outdiffusion and much higher hydrogen concentrations were used, leaving the possibility that additional factors affect the results. The variations from the smooth curve seen here are most likely due to variations in the shape of grating response due to the multimode response of the 5.5μm thick core layer that was used.

After leaving the sample overnight to allow almost all hydrogen to outdiffuse a fur-

ther Bragg grating was written using identical conditions. Upon examination of the resultant structure, the sample was found to still act as a waveguide but no grating response could be determined with the equipment in use. Thus it is concluded that there is a small level of intrinsic photosensitivity in the PECVD deposited silica possibly due to residual hydrogen content from the deposition process and this is sufficient to yield waveguides but not gratings.

In principle, with the assumption that the waveguide effective index is approximately proportional to the hydrogen concentration at the time of writing, it is possible to determine approximate outdiffusion rates and thus predictions of available UV writing times at different temperatures. Experimental work where the wavelength shift of a single UV defined planar Bragg grating was used to monitor hydrogen outdiffusion has determined that the hydrogen concentration reaches $\frac{1}{e}$ of its initial value after nearly 12 hours in samples somewhat thicker but otherwise comparable to those used here [9].

Such an analysis does not appear to be valid for the samples used here. Using the exponential fit to the data in figure 7.17 indicates that the $\frac{1}{e}$ decay time due to outdiffusion is 22 minutes. Such a low figure for the time constant indicates that the outdiffusion cannot be treated in this way. The value of 22 minutes is not only significantly shorter than the value of 12 hours determined in [9] but is also not consistent with the duration of 2.5 days for the diffusion process to reach 95% of its equilibrium value (discussed in chapter 5). This discrepancy could be due to the scatter on the experimental data or a result of the relatively short timescales over which the the UV writing took place.

Diffusion coefficients have to date not been determined for the PECVD fabricated samples developed in this thesis but the data above does provide a quantitative estimation of the effects of hydrogen outdiffusion over extended writing times. More detailed study could be achieved by defining a Bragg grating by DGW and then reloading the sample with hydrogen. Subsequent monitoring of the Bragg wavelength as outdiffusion occurs could provide further insight.

7.3.8 Propagation Loss

Propagation loss is obviously a key parameter in any optical waveguiding component. In some cases, notably sensing applications, high loss can be tolerated as changes in output are required rather than an absolute output quality. Although UV written waveguides are presented in this thesis in the context of sensor applications (Chapter 9) it is nonetheless important to determine the optical losses of the waveguides produced.

Loss measurement of optical fibres is a simple procedure as lengths of hundreds, or thousands of metres of fibre can be produced in a single process. It is therefore easy to use the method of 'cut-back' to determine the loss per unit length by cleaving the fibre to known lengths and measuring transmitted power. Planar waveguides are somewhat more complicated to measure. Typically, propagation lengths of a few centimetres are used for waveguide devices and the input/output facets require careful polishing to allow efficient coupling of light into and out of the device. The requirements for short path length and high quality polishing mean that cut-back measurements are subject to much higher uncertainties than the corresponding fibre based characterisation. Variation in polish quality and in coupling between input and output fibres along with the considerably shorter lengths involved make accurate, repeatable measurement of waveguide propagation losses difficult. These problems are somewhat negated by the higher, easier to measure, losses of planar devices compared to typical fibre losses. Typically however, completed commercial waveguide components are fibre pigtailed with connectorised fibre. In this way it is possible to measure a total insertion loss rather than a loss per unit length of a device.

Waveguides prepared using direct UV writing have been demonstrated to be low loss ($<$0.2 dBcm^{-1}) [3] and indeed suitable for lasing when doped with rare earth ions [10]. It is however known that PECVD produced layers often require special annealing treatments in order to produce low loss structures.

Initial measurements to determine the propagation loss of UV written PECVD fabricated sample used two samples of different lengths processed at different times with

slightly different exposure fluences. In this way it was hoped to avoid the cut-back approach and achieve a propagation loss measurement by comparison of the two sample lengths. The results however highlight the importance of careful control of such measurements.

An unfortunate consequence of instabilities in the UV laser means that from day to day there is the possibility of the UV spot changing in shape and intensity profile. Therefore it is possible that waveguide mode profiles also vary as a result. This, along with variations in polish quality mean that between two samples there can be a significantly different coupling efficiency, manifested as erroneous propagation loss readings. The results taken using the two samples produced on different dates showed unacceptably high levels of uncertainty (approximately 1.5 ± 2 dBcm^{-1}).

Therefore, to obtain a more reliable estimate of the waveguide losses true cut-back measurements were made. A sample with a 5.0 micron thick core was used. Waveguides (with no gratings) were written into the full length of the sample at 30kJcm^{-2} (70mW at 4.5 mm min^{-1}). Two waveguides were written into the sample. The sample before cut-back was 35.5mm in length. Transmitted power measurements were taken at 1550nm and 1300nm on each waveguide a total of ten times. To reduce uncertainties in fibre to waveguide coupling the angle of launch between input fibre and waveguide was held constant. This was achieved by retaining the input fibre in a fixed position. The sample was mounted onto a translation stage and mechanically positioned using one edge as a reference for angular alignment. In this way sources of uncertainties were limited to the relative positions of the input fibre and waveguide and to the position and angle of the output fibre. After every measurement both the sample and output fibre were removed from the setup before being replaced and realigned. Each measurement was performed by manually controlling the position of the sample and output fibre in order to optimise the transmitted power.

After 10 readings the sample was diced into two and repolished on the two sawn facets resulting in samples 21.0 and 10.5 mm in length. Measurements were taken as described above with the same sample edge used for mechanical registration. Following the final polish stage it was observed that the output facet on one waveguides of the 10.5mm sample caused anomalously low transmitted power readings.

Consequently, complete readings at three lengths were only recorded for a single waveguide.

The results of all ten readings for each waveguide length at 1560nm and 1300nm respectively are shown in figures 7.18 and 7.19. Linear fitting has been achieved using a standard linear regression from a graphing software package.

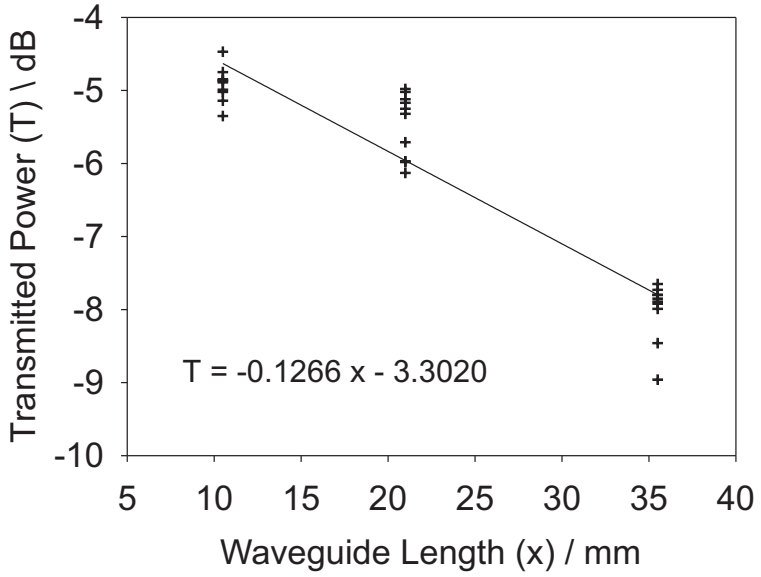

Figure 7.18: Transmitted power against waveguide length at 1560nm

The linear fits to the data points provide estimates of the propagation loss of the two samples as $1.27 \pm 0.09 \text{dBcm}^{-1}$ at 1560nm and at $0.29 \pm 0.10 \text{dBcm}^{-1}$ at 1300nm. These values are somewhat higher than values previously obtained in other PECVD and FHD UV written waveguides of around 0.2dBcm^{-1} [3, 10, 11]. It is perhaps not surprising however that the propagation loss is higher than in these cited examples. As already mentioned, various groups have shown that careful process control and annealing regimes can be used to optimise layer properties and minimise optical losses primarily through OH group reduction. Unfortunately, owing to the limitations imposed by equipment availability it was not possible to cycle through the layer development process to improve upon these losses. Possible causes of the relatively high losses observed here are those of scattering by impurities or crystallisation of dopants in the layer or, more likely due to absorption by OH groups in the silica layers.

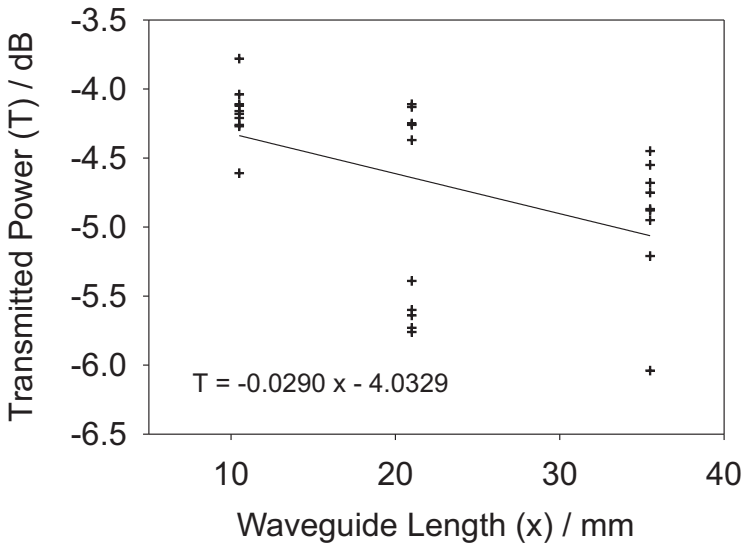

Figure 7.19: Transmitted power against waveguide length at 1300nm

Another consideration is the use of hydrogen loading to enhance the photosensitive response. In [3] it was found that hydrogen loaded PECVD silica samples exhibited absorption peaks at 1.4μm and 1.5μm that were 1dBcm^{-1} stronger than in deuterium loaded or unloaded samples. Therefore additional loss reduction can be expected if the samples used here were loaded using deuterium rather than hydrogen to shift absorption peaks away from the 1.5μm window.

To investigate the possibility of high OH content, broadband spectra of waveguides were recorded. By first recording a spectrum with input fibre coupled directly to output fibre it is possible to obtain a referenced spectrum by subtracting the fibre-fibre spectrum from the fibre-sample-fibre spectrum. This style of measurement provides a relatively simple means of assessing transmission over a wide wavelength range. However, when using an optical spectrum analyser (the technique used here) it is important to realise that the extended measurement time (>15 minutes) required for a scan of this nature imposes limitations on the accuracy of the technique. Even with translation stages stabilised using active feedback loops there will be drift in the relative positions of the input fibre, the sample and the output fibre which will appear as a variation in transmitted power. Such a spectrum is shown in figure 7.20.

The most significant feature of this spectrum is the dip in transmission just below

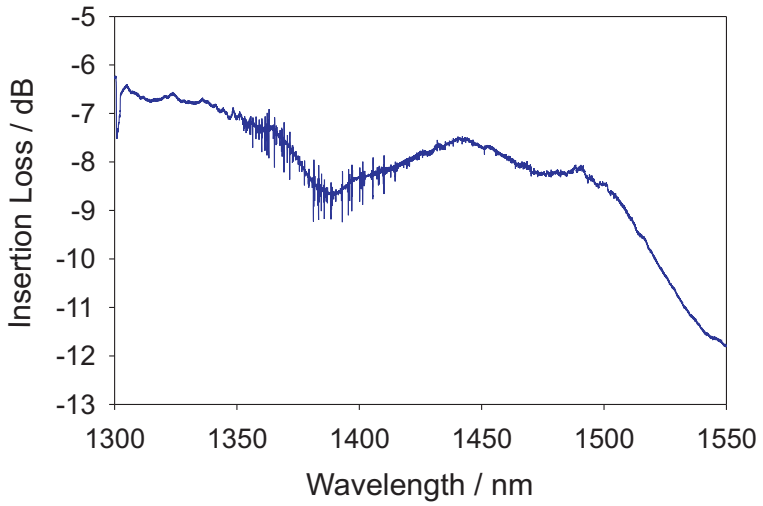

Figure 7.20: Normalised transmission spectrum of 35.5mm long waveguide

1400nm. This peak indicates the presence of OH groups within the silica. At 1390nm the presence of OH^- impurities with a concentration of 1ppm in pure silica causes an absorption of 48 dB km^{-1} [12]. To estimate the concentration of OH^- in the PECVD silica waveguides the depth of the dip at 1380nm of figure 7.20 can be used. This dip is approximately 1.4dB deep when compared to the 'background' level on either side. This equates to an OH^- concentration of 822 ppm or a little below 0.1% which, whilst somewhat high is perhaps unsurprising given the relatively high propagation loss already measured.

A clear and rapid decrease in transmitted power is seen between 1500 and 1550nm. It is most likely that this is due to drift in the relative positions of fibres and the sample rather than due to a real increase in propagation loss at these wavelengths. Lower resolution wavelength scans were recorded using lower resolutions over shorter timescales to attempt to avoid the effects of drift and such a sharp drop in transmitted power was not reproduced in a repeatable manner. Figure 7.21 displays two such spectra measured from two waveguides a 20.5mm long sample where drift is less apparent that in the previous broadband measurement. Again, the broad OH peak is observed at around 1400nm and smaller peaks close to 1500nm also appear to be present. Absorptions close to these wavelengths (1508 and 1520nm) have previously been associated with the presence of Si-H, Ge-H or N-H bonds [3, 13] and

it is indeed likely, given the high levels of hydrogen and nitrogen in the deposition process that these bonds do indeed occur in the deposited silica.

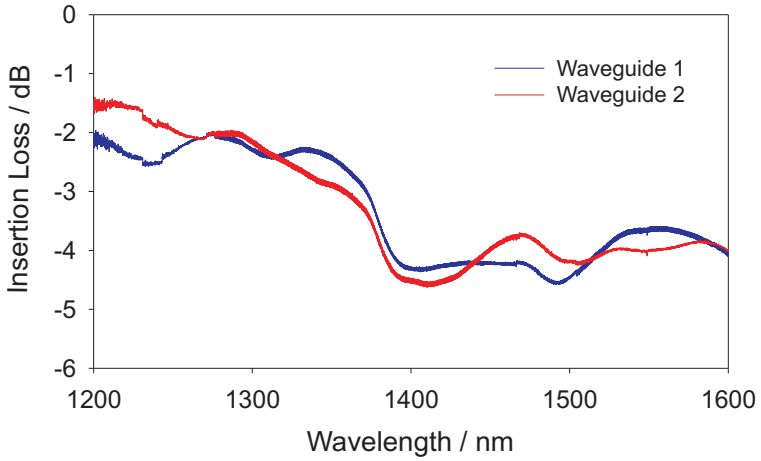

Figure 7.21: Normalised transmission spectra of two 20.5mm long waveguide

One possible source of propagation loss that has not been discussed in this section is the possibility of scattering due to imperfections in the deposited layers. Particulate contamination is not considered significant as all depositions were performed in a clean environment. It is possible that crystallisation of the dopants has occurred in the deposited layers but this has not, to date, been investigated. However, when performing NA measurements using a 633nm source, no scatter from the upper surface of the sample was visible. This provides an initial indication that any scattering occurring in the waveguide is of a low level. Additionally, given the magnitude of the OH peak discussed above, loss due to scattering is likely to be of a considerably lower magnitude and thus of secondary concern.

It is worth noting that although the optical losses of these guides would perhaps be prohibitively high for modern telecommunications applications it would not be a hindrance in sensing applications such as those described in chapter 9. In this case absolute propagation losses become less critical as it is only changes in the waveguiding properties that are of significance in the context of a waveguide sensor.

7.4 Summary

The results presented here show that the PECVD samples fabricated for this work are suited to the production of UV written waveguides. With the levels of germanium used and the hydrogen loading apparatus available it is found that a 5.0μm thick germanium doped core layer provides the most repeatable and single mode results. Unexpectedly weak Bragg transmission responses have been observed and are thought to be a consequence of both low refractive index modulation within the Bragg gratings and very slight multimode behaviour.

With the use of cutback measurements propagation losses of 1.27 ± 0.09dBcm^{-1} at 1560nm and at 0.29 ± 0.10dBcm^{-1} at 1300nm have been measured. Scope for loss reduction exists via the use of deuterium, rather than hydrogen loading and through investigation of optimal annealing regimes.

Birefringence of the samples is measured at 7.3×10^{-4}. Numerical aperture measurements made by imaging the waveguide output facet exhibit a high level of noise and demonstrate the limitations of this technique. However, by generating a fluence curve it has been shown that UV induced changes in refractive index of at least 1.5×10^{-3} are possible with the processes used. The index perturbation in Bragg gratings was weaker than initially expected and using the bandwidth of reflection spectra has been calculated to be approximately 4×10^{-4} over all fluences used. The maximum reflectivity of all gratings written, as determined from grating transmission measurements, was 61%.

Fluences required to saturate the available photosensitivity are found to be in the region of 125kJcm^{-2} or more, approximately 100kJcm^{-2} greater than the value found in prior work on FHD samples.

7.5 References

[1] A.Othonos and K.Kalli. *Fiber Bragg Gratings. Fundamentals and Applications in Telecommunications and Sensing*. Artech House, 1999.

[2] G.D. Emmerson. "Novel Direct UV Written Devices". *PhD Thesis*, 2003. University of Southampton.

[3] M. Svalgaard. "Ultraviolet light induced refractive index structures in germanosilica". *PhD Thesis*, 1997. Technical University of Denmark.

[4] M. Svalgaard. "Direct UV-written integrated optical components". *Optical Fiber Communication Conference*, 2(FK2), 2004.

[5] S.M.Ohja, C.Cureton, T.Bricheno, S.Day, D.Moule, A.J.Bell, and J.Taylor. "Simple method of fabricating polarisation insensitive and very lw crosstalk AWG grating devices". *Electron. Lett.*, 34(1):78–79, 1999.

[6] A.Kilian, J.Kirchhof, B.Kuhlow, G.Przyrembel, and W.Wischmann. "Birefringence Free Planar Optical Waveguide Made by Flame Hydrolysis Deposition (FHD) Through Tailoring of the Overcladding". *IEEE Journal of Lightwave Technology*, 18(2):193–198, 2000.

[7] A.Ghatak and K.Thyagarajan. *Introduction to Fiber Optics*. Cambridge University Press, 1998.

[8] M. Svalgaard and K.Faerch. "High Index Contrast UV-Written Waveguides". *Proceedings of 12th European Conference of Integrated Optics, Grenoble*, pages 522–525, 2005.

[9] M. Svalgaard. "Effect of D_2 outdiffusion on direct UV writing of optical waveguides". *Electron Lett.*, 35(2):1840–1842, 1999.

[10] D.A.Guilhot. "UV-written devices in rare-earth doped silica-on-silicon grown by FHD". *PhD Thesis*, 2004. University of Southampton.

[11] S.P. Watts. "Flame Hydrolysis Deposition of Photosensitive Silicate Layers Suitable for the Definition of Waveguiding Structures through Direct Ultraviolet Writing". *PhD Thesis*, 2002. University of Southampton.

[12] S.R.Nagel, J.B.MacChesney, and K.L.Walker. "An Overview of the Modified Chemical Vapor Deposition (MCVD) Process and Performance". *IEEE Journal of Quantum Electronics*, QE-18(4):459–476, 1982.

[13] G.Grand, J.P.Jadot, H.Denis, S.Valette, A.Fournier, and A.M.Grouillet. "Low-Loss PECVD Silica Channel Waveguides for Optical Communications". *Elec. Lett.*, 26(25):2135–2137, 1990.

Chapter 8

Thermal Behaviour of UV Written Planar Waveguides

8.1 Introduction

Refractive index modulations caused by UV exposure are often described as permanent changes. However, it has been shown that the induced changes vary in a manner that is dependent on both the photosensitivity type and the processing history. The study of the stability of UV induced refractive index change is of interest for several reasons. Firstly, for such devices to be of practical use, data is required on their operating lifetimes and performance over a wide range of conditions. Additionally, monitoring how the performance of UV written devices degrades over time, or with other variables, can provide insight into material characteristics and also into the photosensitivity mechanisms that have taken place in the material. In the following sections data is presented, primarily on the thermal degradation of UV induced refractive index change, with the aim of demonstrating how useful insights can be gained from such work.

Given the photosensitivity dependence on point defects, it is unsurprising that fabrication history affects both the nature of the induced index change as well as the decay characteristics. Comparison of UV written waveguides in layers deposited by

flame hydrolysis deposition with similar layers fabricated using plasma enhanced chemical vapour deposition towards the end of this chapter shows similarities and differences in the way the the waveguides and gratings degrade with thermal treatments.

Rather than being an exhaustive study into the photosensitive and thermal response of the FHD and PECVD fabricated layers, this chapter acts more as an introduction to applications of the DGW technique as a research tool. Nonetheless the outcomes from the two sample types do highlight some of the interesting differences between the two layer types used.

8.2 Bragg Grating Decay

A particularly convenient means of interrogating changes in the refractive index of a channel waveguide is to monitor shifts in the Bragg wavelength, λ_b, given by

$$\lambda_b = 2\Lambda n_{eff} \tag{8.1}$$

where n_{eff} gives the effective refractive index of the waveguide and Λ is the period of the Bragg grating. Therefore, changes to the effective index of the guided mode can be detected by measurement of the Bragg response. In this way, thermally triggered grating decay can be monitored and interpreted as a refractive index shift.

The vast majority of investigations into thermal decay of Bragg gratings has been carried out in silica based fibre [1,2,3] as this is a well established fabrication method readily lending itself towards constant monitoring during thermal treatment. Despite the predominance in fibres, the technique has a very high potential in planar geometries where decay of a grating inscribed in a UV written waveguide provides data on the lifetime of the UV inscribed *waveguide* as well as the thermal behaviour of the grating planes.

Until the development of the direct grating writing (DGW) technique [4] by members of this research group, waveguide stability analysis using grating decay was limited by the additive nature of the gratings. Before DGW, gratings could only be super-

imposed using phase masks onto UV written [5] (or etched [6]) waveguides. This secondary process, by its very nature, altered the waveguide that was to be studied, causing a degree of uncertainty in the results. Low fluences can be used to define a grating with minimum perturbation to the original waveguide but this also suffers from resultant uncertainties. Measurements of grating decay will in this case be providing information on the degradation of the grating planes, written at low fluence, as well as the degradation of the original waveguide, necessarily written at significantly higher fluences. It is possible, and indeed likely, that the difference in writing fluences for the two exposures results in two separate regimes of photosensitivity coming into play.

DGW overcomes the problems of de-convoluting the waveguide and grating decay routes. Fluence matched writing of waveguide and grating (i.e. the same average fluence for both) in a single step allows little or no variation in the mechanisms responsible for index change. Consequently, measured decay of the grating response is directly correlated to decay of the waveguide itself.

Thermal decay studies of fibre Bragg gratings have given rise to two well accepted models which may be used to predict the behaviour of a UV defined Bragg grating over time and temperature [1]. Known as the power law approach and the ageing curve approach, both rely on the same underlying physical principles. UV exposure is assumed to excite electrons in the silica into metastable states. Owing to the amorphous nature of the silica these states exhibit a wide range of activation energies which are required to release the electrons. Thus there is no threshold temperature at which UV induced refractive index changes are erased but a continuous range of temperatures and times over which thermal treatment will affect refractive index changes. The power law model is based on the decay of refractive index being characterised by a function of time raised to the power of a small exponent. The ageing curve approach, found to be somewhat more general than the power law model [2], uses a function of both time and temperature upon which predictions of future stability can be based. Both of these techniques depend upon frequent measurements during the waveguide anneal. Owing to the non-packaged, non-pigtailed nature of the waveguides used in this work such stability predictions have not been made.

However, should a thermally stable fibre coupling and packaging method be developed in the future the work described below could be applied to such stability predictions.

8.3 Thermal Annealing of DGW Samples

Whilst a complete study of the thermal stability of planar UV written waveguides would follow the methods similar to those used in [2], an initial study demonstrating the potential of DGW as a tool is presented here. The work is based on both FHD and PECVD fabricated samples. Those samples fabricated by FHD were UV written after hydrogen loading and after thermal locking treatments. Waveguides produced via these two process routes are annealed and the changes in waveguide effective refractive index monitored using the Bragg resonance. Samples fabricated by PECVD were subject to the same procedure but work to date has been restricted to hydrogen loading. Throughout this chapter the use of the phrase *thermal locking* refers to the process of hydrogen loading for over three days followed by a rapid thermal anneal at temperatures in excess of 1100℃ for over one second.

8.3.1 Optical Characterisation

Bragg grating characteristics were taken by recording the reflection spectrum of each written waveguide. The optical source used was an erbium doped fibre amplifier operating as an ASE source and the detector was an optical spectrum analyser. The equipment used for experimental measurements was identical to that described in the previous chapter (chapter 7). TM polarised light was used for all measurements.

The broadband optical input was coupled into the UV written waveguides by butt-coupling an input fibre with index matching fluid between the fibre and the end facet of the sample. To assist in optimising the fibre launch, the output of the sample was imaged onto an infra-red camera. This arrangement also allows mode profiles to be recorded if desired. Alternatively the camera can be replaced with a fibre coupled

to the waveguide output facet to allow recording of grating transmission measurements.

8.4 FHD Samples

The flame hydrolysis deposition (FHD) samples used here were fabricated commercially by a company known, at the time of production, as Kymata. Each sample is taken from a three layer silica-on-silicon wafer with a 5.5μ thick germanium doped core. Owing to the commercial sensitivity of the wafers provided by Kymata, the refractive index of the three layers was not disclosed. This places a restriction on the conclusions that can be drawn from thermal annealing studies as absolute UV induced index change cannot be known.

Prior to UV exposure, all samples were hydrogen loaded at 150 bar for over a week to allow hydrogen to diffuse into the core layer. To provide variation in the processing history seen by each sample, a range of thermal locking treatments were applied upon removal from the high pressure hydrogen. Thermal locking was carried out at a furnace temperature of 1100℃ , 1300℃ and 1400℃ for periods of 1, 3 and 5 seconds. The samples were placed on a preheated silica plate and pushed into the furnace for the specified time. The actual temperature that the samples reached was not determined and can be expected to be somewhat lower than the preset furnace temperatures. Thus a total of nine samples were thermally locked prior to UV writing. A tenth sample was not thermally treated before exposure but was stored in liquid nitrogen to prevent out-diffusion until UV exposure occurred. To perform the thermal locking process the samples were removed from their liquid nitrogen storage and placed on a silicon wafer. The wafer and sample was then transferred directly into a furnace held at the appropriate temperature for the required duration.

Each sample received the same UV exposure consisting of waveguides/gratings written at three fluences (2.6, 5.2 and 10.3kJcm^{-2} at 30% duty cycle). Bragg gratings were written over the entire length of the samples. The UV writing procedure for these samples was performed with the assistance of Corin Gawith and Greg Em-

merson.

8.4.1 Optical Response

Of the 10 samples exposed to UV, Bragg grating reflection spectra could only be measured in 5. Those samples thermally locked at 1100℃ or for 1 second displayed no Bragg response in reflection when measured using the OSA and of these samples, only one, processed for 5 seconds at 1100℃ , contained detectable waveguides. The likely reason for this is a combination of thermally accelerated out-diffusion of hydrogen combined with the small but finite delay before the sample reaches the locking temperature after entering the furnace. It is also possible that the thermal locking process is not fully complete after one second. The remaining five samples all displayed Bragg reflection peaks in reflection; a typical spectrum is shown in figure 8.1. It can be noted that whilst the reflection peak can be clearly distinguished from the background the level of noise is significant.

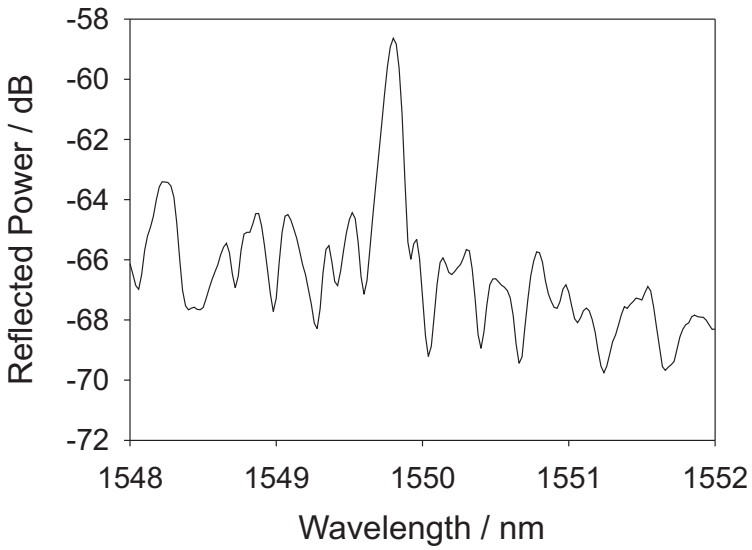

Figure 8.1: Reflection spectrum of a sample thermally locked for 5 seconds at 1400℃ . This data was taken after the 200℃ anneal step.

Transmission measurements were not recorded as owing to the relatively low magnitude of the Bragg response good quality transmission peaks could not be detected from the noise. This imposes the restriction that the grating strength cannot be de-

termined from measurements and, owing to variability in the optical input path and of fibre-waveguide coupling, relative reflection strengths are not an accurate means of determining relative changes in the grating strength before and after annealing. Similarly, the relatively small reflection peaks and high noise levels mean that bandwidth measurements, and thus index modulation calculations, are not possible.

The as-written, pre-anneal effective indices are shown in figure 8.2. The sample that was not thermally treated shows the predictable response of an increase in effective index with increasing fluence. As a group, the thermally locked samples appear to show less predictable behaviour. The reasons behind this are not fully understood although uncertainties due to the relatively poor quality of the grating response will play some role in this. The two samples processed at 1400℃ show very similar behaviour in that they display almost the same waveguide effective index which varies very little over the three fluences used.

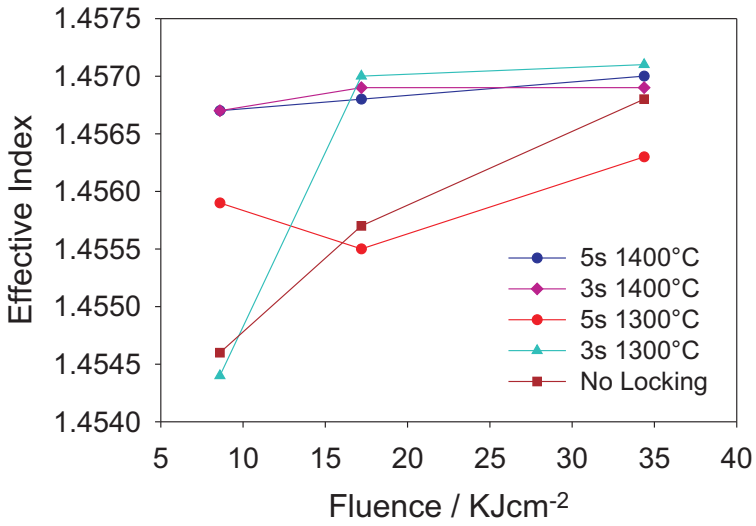

Figure 8.2: The effective index of waveguides written into hydrogen loaded and thermally locked samples before annealing.

8.4.2 Annealing of Hydrogen Loaded Samples

Thermal annealing steps of 30 minute duration were used sequentially to measure the degradation of the grating response. After each anneal, reflection spectra were

recorded at room temperature. The resultant waveguide effective index after annealing of the hydrogen loaded (not thermally locked) sample is shown in figure 8.3. It is known that thermal relaxation of UV induced refractive index changes occurs rapidly during the first few minutes of treatment before proceeding at a much lower rate [1]. It is also shown in [1] that the effect of a 150 minute long anneal at 550℃ produces very similar results to a 75 minute anneal at 350℃ followed by a 75 minute anneal at 550℃ . Thus 30 minute anneal steps will provide data which to a good approximation represents the effect of each temperature on the planar waveguides and gratings.

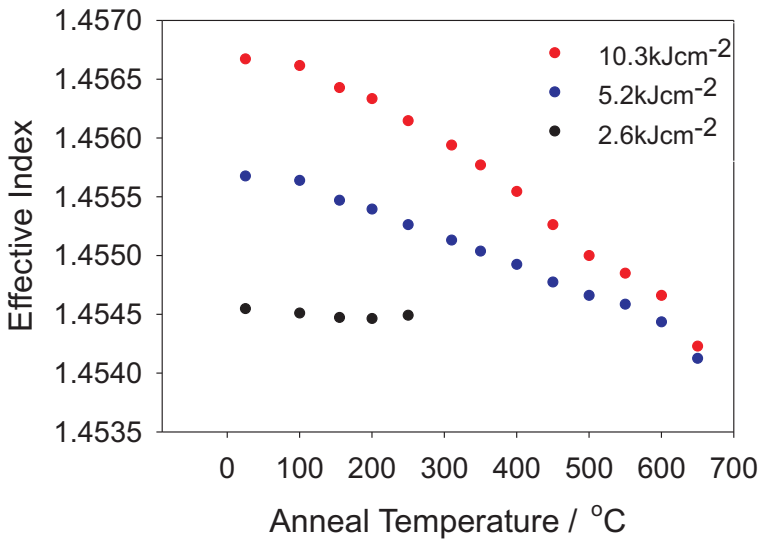

Figure 8.3: Variation of hydrogen loaded waveguide effective index with successive anneal steps. Annealing of waveguides written with three UV fluences are shown.

As expected, higher effective indices are created by higher fluences when the gratings are first written. The reduction of effective index with annealing temperature shows that the waveguide refractive index is decreasing, also as expected. In addition to the Bragg wavelength shift with temperature, a decrease in grating strength is observed in all samples by a reduction in the size of peaks in the reflection spectra. As already mentioned the magnitude of reflection peaks is not an accurate means of assessment and firm conclusions cannot be drawn from such data. The anneal temperature was increased and measurements repeated until the grating response could no longer be measured due to the grating reflection strength being too weak.

Thus each sample saw all temperatures successively with a period of analysis at room temperature between each increase in temperature. Above 650℃ no grating contrast could be resolved with the equipment in use on any waveguides however waveguide outputs were still visibly present on the IR camera.

It is interesting to note that despite the initial strong dependence of effective index on writing fluence, as the gratings decay with temperature the waveguides tend towards approximately the same effective index state in the region of 1.4540 to 1.4545. The variation for all waveguides is approximately linear.

8.4.3 Annealing of Thermally Locked Samples

Each of the thermally locked samples that showed grating responses was subjected to the same sequence of annealing as the hydrogen loaded waveguides. The behaviour of the sample processed for 5 seconds at 1400℃ is shown in figure 8.4. For comparison the responses of the waveguides written at 10.3kJcm^{-2} in all of the thermally locked samples are shown in figure 8.5.

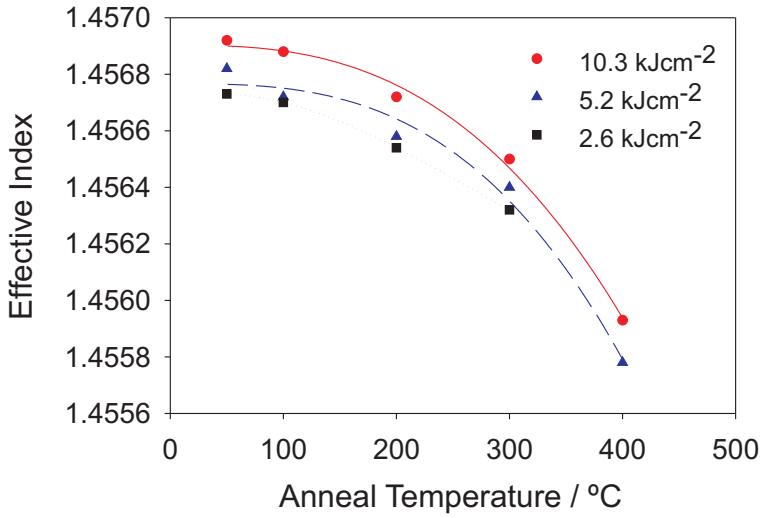

Figure 8.4: Effective index variation with successive 30 minute anneal steps on thermally locked samples. All samples processed for 5 seconds at 1400℃ . Note that lines are shown only to highlight data trends

It must be noted that the lines shown with the data points in figures 8.4 and 8.5

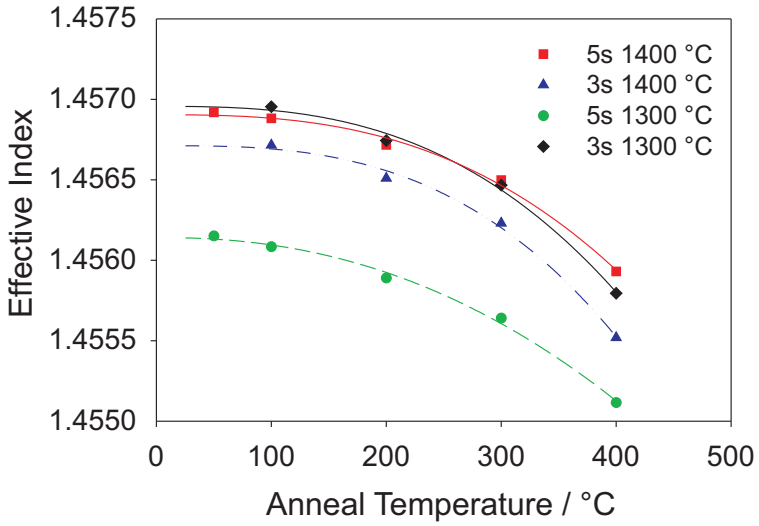

Figure 8.5: The effect of annealing on effective index for thermally locked samples. Note that lines are shown only to highlight data trends

are provided to help highlight the trends and distinguish the data points from one another. Whilst these lines may not provide an accurate representation of the actual trends of the data they do help to highlight the fact that the trends for all fluences, in all samples follow very similar shapes.

Perhaps the most interesting feature of figure 8.4 is the variation of effective index when contrasted with that shown for the hydrogen loaded sample in figure 8.3. Whereas the hydrogen loaded waveguides show an initial variation of effective index of over 2×10^{-3} but appear to decay towards the same value, the thermally locked behaviour is very different. The initial variation of effective index over fluence is an order of magnitude smaller and remains constant over the annealing steps. The range of effective index that the thermally locked samples are measured over is only half that of the hydrogen loaded samples but it must be noted that the temperature ranges over which measurements could be made is different for the two samples.

8.4.4 Numerical Aperture

To contrast with the results of the DGW based trials described above, the more 'conventional' technique of measuring numerical aperture (NA) was also utilised.

Figure 8.6 shows the measured NA for all samples showing a measurable grating response. There is a clear split between measurements taken in the vertical and horizontal directions. The vertical NA has a much higher value due to the refractive index contrast between the core and cladding layers. The lower horizontal NA is due only to the UV induced refractive index change. The data shows that the horizontal NA increases slightly with increasing fluence as expected. Changes to the vertical NA are not seen against the higher intrinsic background level.

Data for the hydrogen loaded sample shows a slightly higher value for NA, particularly in the horizontal direction. This indicates a slightly higher index contrast between the waveguide core and cladding than in the locked samples and is consistent with observations made in [7].

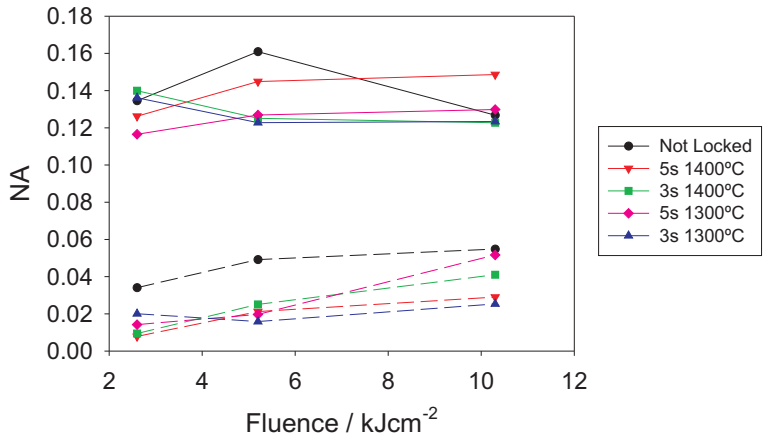

Figure 8.6: NA measurements for thermally locked and hydrogen loaded samples. Solid lines (*top*) represent measurements in the vertical direction, dotted lines (*bottom*) represent horizontal measurements.

Figure 8.7 shows the effects of annealing on NA measurement for the sample thermally locked at 1400°C for 5 seconds. No clear trends can be discerned in the NA data after the 300°C anneal even though the effective index data of figure 8.4 shows

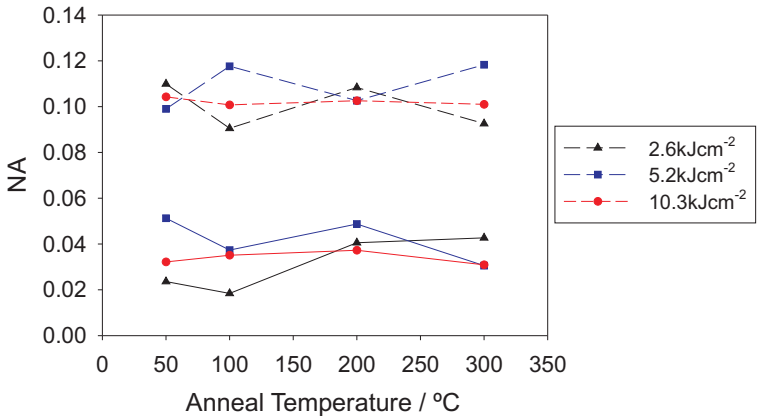

Figure 8.7: Variation of measured NA with successive anneal steps. Dotted lines (*top*) represent measurements in the vertical direction, solid lines (*bottom*) represent horizontal measurements. This sample was thermally locked for 5 seconds at 1400°C
.

a significant drop.

Although some comparisons can be made between the samples measured, the data presented using numerical aperture serve to highlight the strengths of the DGW technique in allowing very small changes in effective refractive index to be easily detected. The technique of using mode profiles to determine numerical aperture and then imply refractive index profiles is inherently much less sensitive and prone to error than that using Bragg gratings.

8.5 Discussion of FHD Annealing

Whilst monitoring small shifts in Bragg resonances provides a very sensitive way to assess the behaviour of UV written waveguides, it is important to note the limitations of DGW as an analysis technique. Monitoring the Bragg wavelength alone does not provide information on the waveguide core or cladding refractive index or the relationship between the two. Also, owing to the nature of the recorded spectra, reflectivity and grating index modulation cannot be determined from the data presented here.

Another important consideration is of the relative behaviour of samples processed in different ways. It can be seen that the thermally locked samples and the hydrogen loaded layers exposed to the highest fluence all exhibit an effective refractive index of approximately 1.4568. Whilst this information can be used in the design of components using such waveguides it does not imply that the actual structure of the guides is similar. For example, it is known (figure 8.8) that the 3-layer FHD samples show a change in refractive index as a result of the thermal locking process. The figure shows the effect of the locking process on the refractive index of the overcladding layer, measured by prism coupling. It is clear that the refractive index drops by around 4×10^{-3} as a result of the treatment (5 seconds at 1400℃) and that the waveguide effective index is therefore not solely due to the UV induced changes.

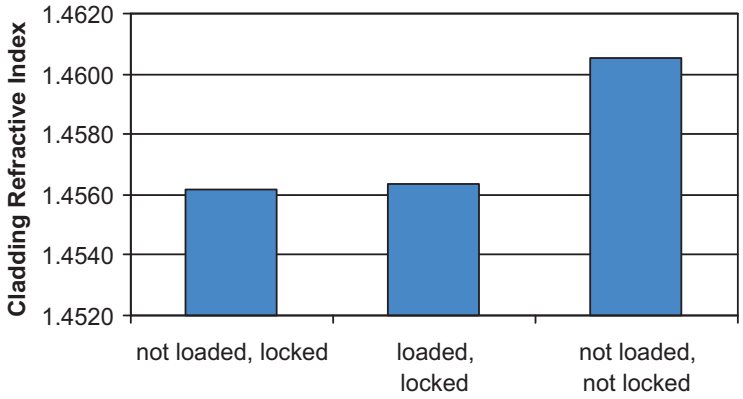

Figure 8.8: Effect of thermal and hydrogen processing on overclad refractive index of FHD samples. Measurements performed by prism coupling on a full three layer sample.

The results of the preceding sections indicate that the thermal locking and UV exposure steps may be two stages of the same process in the FHD samples. The low fluence dependence in the thermally locked samples suggests that the rapid heat treatment is initiating a nonvolatile change in the material that is required before a further UV index change can be induced. When thermal locking is not carried out, a fraction of the applied UV power may cause a similar change before the remaining power is used to induce the expected refractive index changes that are observed. This effect could explain the fluence dependency seen in hydrogen loaded samples

that have not been thermally locked. The results complement qualitative observations that in hydrogen loaded silica UV induced fluorescence increases in strength during the first moments of exposure before decreasing again with time whereas in thermally locked samples the fluorescence is instantaneous and for low exposures is constant over time. This effect could indicate that hydrogen loaded silica undergoes an initial 'burn-in' period causing hydroxyl formation [8] followed by an additional index increase due to absorption in the vicinity of 244nm. These observations correlate with the two step photosensitisation scheme proposed in [3] and the permanent UV induced sensitisation seen in fibre in [9]. The thermal locking work carried out in [8], showing that UV irradiation and thermal treatment cause similar trends in refractive index change also suggests a link between the two processing steps. These observations suggest that the thermal locking treatment provides the initial 'burn-in' period creating hydroxyl groups which then play an onward role in the localised refractive index changes.

Looking at the shapes of the curves showing the variation of effective index with anneal provides useful information on the behaviour of the samples. It is apparent that annealing the hydrogen loaded waveguides at 100℃ or over results in a measurable reduction in the effective index. Reduction of the waveguide core refractive index is assumed to be responsible for this effect as the anneal temperature is significantly lower than the silica fabrication temperatures and is not expected to cause any change in anything other than the UV exposed areas. The results here are limited to the effects of a thirty minute anneal but it is generally observed in accelerated ageing studies (summarised, for example in [10]) that degradation of UV defined Bragg gratings is most rapid during the first few minutes of a thermal anneal. Thus with the assumption that the effect of successive anneals will approximate the effect of longer timescales at a constant temperature [1], figure 8.3 can be used to estimate the effects of temperatures up to a few hundred degrees for up to a few hours. For example, the waveguide written at a fluence of 10.3kJcm^{-2} may be expected to reduce in effective index by approximately 8×10^{-4} if it was annealed at 300℃ for timescales of two or three hours.

The thermally locked data may appear to show a slower decrease in effective index

with temperature than the hydrogen loaded samples but such a conclusion is hard to validate. As the magnitude of the induced index change is not known in the two samples a direct comparison cannot be made between the two process routes especially as it is seen from the hydrogen loaded sample that the stronger waveguides degrade more rapidly. Bearing these considerations in mind it is worth noting that prior work summarised in [11] shows that photosensitisation treatments such as hydrogen loading or the addition of co-dopants does indeed alter the temperature at which grating index perturbations start to be erased.

Whereas the thermally locked samples appear to follow approximately the same rate of decay for all fluences the hydrogen loaded samples appear to decay towards the same effective index value. Why this occurs is not clear as it might be expected that the three fluence lines would run approximately parallel to each other until the point at which no further grating response can be detected. The results may indicate that there are two photosensitivity mechanisms coming into play with one degrading at temperatures from 100℃ and being responsible for the gradients of the three curves shown in figure 8.3. The second mechanism may be more stable and be responsible for the remaining effective index value at the point where the curves appear to coincide.

It is known (Chapter 5) that refractive index changes in germanosilicates can be due to both defect centre related mechanisms as well as compaction effects. Another feature observed when writing Bragg gratings into fibres is that the refractive index modulation behaves differently to the change in mean core refractive index. One may postulate that here there is a difference in the stability of the defect centre related refractive index change and the changes due to possible thermal effects or compaction associated with the focussed UV beams. This would suggest that the grating modulation is due primarily to defect related effects, the magnitude of which increases with increasing fluence. This is consistent with observations that defect related UV induced index changes have been found to be thermally reversible [11,12]. A background level of photoinduced refractive index remains after a measurable grating response has disappeared and this is likely to be due to compaction or stress effects. It would seem unlikely, given the fluences used, that type II photosensitivity

(physical damage) is occurring in the layers and being the second photosensitivity mechanism.

Unfortunately as no further grating responses could be measured in these samples above 650℃ data is unavailable at higher temperatures. To study this further, stronger grating responses are required to investigate the possibility of obtaining data up to higher temperatures and also to allow index perturbation and grating reflectivity measurements to be made.

8.6 PECVD Samples

Investigations on thermal annealing of PECVD fabricated waveguides used the same methods as those for FHD samples. Waveguides written at a variety of fluences were annealed for 30 minutes at successively higher temperatures. The samples used here have been hydrogen loaded. Work on thermally locked PECVD samples has been limited and remains an area for further study. The fluences used for PECVD samples were necessarily higher than those for FHD. As discussed in the previous chapter much higher fluences are required in the PECVD layers to achieve a similar effective index change. All Bragg gratings written into these samples utilised a duty cycle of 50%. The same limitations apply to the PECVD effective index measurements as to the FHD layers described earlier. In this case, more detailed information is known about the refractive index of the unexposed three layer sample but exact refractive indices of the structures remain unknown at 1550nm and the waveguide index profile is also unknown. Following the inconclusive results of NA measurements on FHD layers and on PECVD layers in the previous chapters, further measurements were not made to investigate the effects of annealing.

The results of annealing the waveguides are shown in figure 8.9. It is interesting to note that, given the wide range of fluences used, that the variation of effective index with UV exposure is at most 3×10^{-4} . Although direct comparisons with the FHD samples are limited due to the difference in writing fluences and unexposed index structure, it is perhaps nonetheless significant that this variation in index is

remarkably close to the variation shown in figure 8.4 for the thermally locked sample and correspondingly different to the variation shown in the FHD hydrogen loaded waveguides.

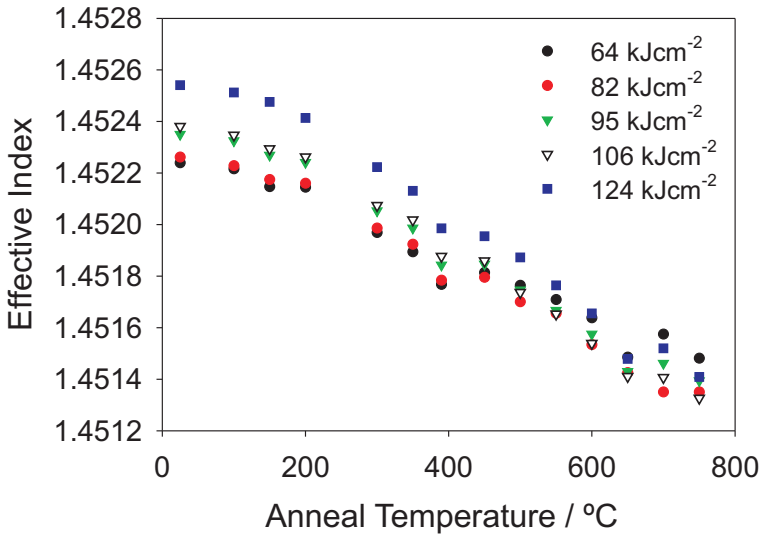

Figure 8.9: Variation of waveguide effective index of PECVD hydrogen loaded samples with thermal annealing.

Higher anneal temperatures were possible when studying the PECVD layers. Again, this cannot be used to infer relative stability as it is found that measurements of the Bragg grating provided higher quality spectra (*i.e.* resonances more clear against background noise) in the PECVD samples as shown in figure 8.10. The reason for this is unclear but as it is known that high quality gratings may be written into the FHD layers it is likely that the difference is due to laser stability at the time of UV writing. The higher quality of the PECVD gratings used for this work allowed transmission measurements to be made and thus the reflectivity and refractive index perturbation of the gratings to be determined. These are plotted against the anneal temperatures in 8.11 and 8.12 respectively.

Figure 8.12 shows an approximately linear decrease in the reflectivity of the gratings as the anneal temperature is increases. Like the FHD hydrogen loaded samples, the effective index appears to converge towards a common value. It can be seen in figure 8.11 that the index perturbation over the same anneal processes appears to remain constant or perhaps even show a slight enhancement before dropping sharply

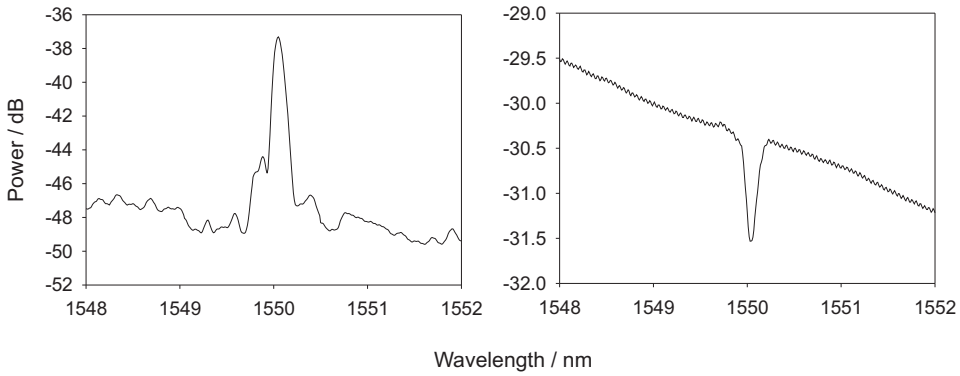

Figure 8.10: Example of reflection and transmission spectra from a PECVD samples used in annealing work. This grating was written at 95kJcm^{-2} and the measurements were taken after a 200℃ anneal.

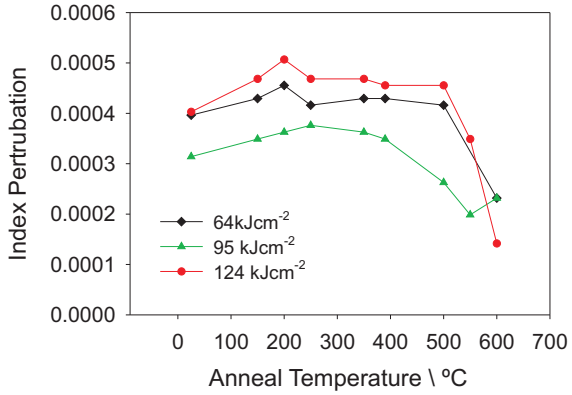

Figure 8.11: Variation of Bragg refractive index perturbation with successive 30 minute anneal steps.

after annealing temperatures of around 400 or 500℃ . The reduction in effective index with annealing will result in weaker mode confinement and the reflectivity will indeed drop as more of the optical signal propagates through the unmodulated cladding. It is interesting however, that the refractive index modulation does not degrade in the same manner and does not fall below its initial value until after the 500℃ anneal. It may be speculated that, in contrast to the FHD layers, the compaction or stress related background refractive index is relaxing at lower temperatures than the defect centre related variation, causing a decrease in overall effective index but not in the modulation of refractive index that forms the grating. This however would seem to be contradicted by the apparent convergence of the different fluences in fig-

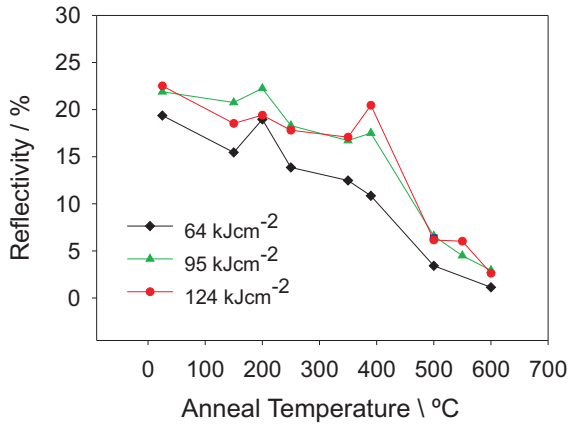

Figure 8.12: Variation of Bragg grating reflectivity with successive 30 minute anneal steps.

ure 8.9 towards a common value previously suggested to be due to a more stable compaction related mechanism.

To confirm this a repeat study is required to produce higher reflectivity gratings and reduce the noise on the data. Like the FHD layers, the PECVD samples show a degradation of effective index after annealing at 50℃ or above, but the sharp fall of index perturbation at temperatures over 400℃ does provide an approximate upper limit to which the UV waveguides should be exposed without entering a regime of more rapid degradation.

8.7 Comparison of FHD, Thermally Locked and PECVD Samples

In the introduction to this chapter it was mentioned that the DGW technique allows insights to be gained on the behaviour of UV written structures over time and temperature. Limitations of the technique are apparent when for example, comparing thermally locked samples with freshly hydrogen loaded samples or when contrasting FHD samples with PECVD samples with a different intrinsic refractive index structure. Despite this, the data presented in the preceding sections and the previous chapter may provide relevant detail on the PECVD samples developed as part

of this work.

Comparison of the thermally locked and freshly loaded samples from the two fabrication routes indicate the possibility that the hydrogen loaded PECVD samples are in fact behaving as though they are both thermally locked and hydrogen loaded. Factors which point towards this conclusion are;

• The near instant fluorescence on exposure to UV light is shared by both the thermally locked FHD samples and the hydrogen loaded PECVD layers.

• The relatively low dependence of effective index on fluence is shared by thermally locked FHD and the PECVD samples.

• The PECVD demonstrates slight photosensitivity without hydrogen loading although Bragg responses cannot be detected with the equipment in use.

• Hydrogen loading enhances the photosensitive response of the PECVD samples.

• Observations on thick germanium doped PECVD layers and measurements of propagation loss indicate high levels of hydrogen and/or OH groups in the PECVD silica.

It is proposed therefore, that the thermal annealing stages of the PECVD deposition process are acting in a similar manner to the thermal locking procedure. It is possible that the hydrogen contained in the as-deposited PECVD layers undergoes the same reaction as the indiffused hydrogen present from the hydrogen loading process.

Confirmation or contradiction of this assertion will require further study with more investigation into the effects of germanium concentration, hydrogen concentration and annealing regimes in particular.

8.8 Summary

Freshly hydrogen loaded FHD and PECVD samples along with thermally locked FHD samples have been studied using the DGW technique and thermal annealing studies.

In the FHD samples it is found that the effective index of waveguides in the hydrogen loaded substrates is significantly more fluence dependent on UV fluence than in the thermally locked samples. This, coupled with observations of the UV induced fluorescence in the samples indicates that thermal locking may be a process comparable to that which occurs in the first moments of UV writing into freshly loaded samples.

Despite the wide variation of effective index with fluence displayed by the hydrogen loaded FHD samples, thermal anneal causes the effective indices to converge towards a common value. It has been suggested that this is due to thermally reversible, defect related mechanisms being predominantly responsible for the grating modulation and a more stable compaction or stress related mechanism being largely responsible for a more stable background refractive index level.

The effective index of PECVD samples reduces in an approximately linear fashion with increasing anneal but the Bragg grating refractive index modulation appears to show a sharp drop after annealing above 400℃. As with the FHD samples this appears to be due to more than one mechanism being responsible for the refractive index change, specifically that the compaction or stress related background refractive index may degrade at a different rate to point defect related changes.

Observations also suggest that the PECVD samples may be partially thermally locked as a result of high levels of hydrogen in the structure and the thermal annealing process used in their production.

It is clear that there is considerable scope for further work into the complex field of photosensitivity in these layers. Nonetheless, the presented result clearly demonstrate the power of the DGW technique as an analysis tool for UV induced refractive index changes.

8.9 References

[1] T. Erdogan, V Mizrahi, P.J. Lemaire, and D. Monroe. "Decay of ultravioletinduced fiber Bragg gratings". *J. Appl. Phys.*, 76(1):73–80, 1994.

[2] S.Kannan, J.Z.Y.Guo, and P.J.Lemaire. "Thermal Stability Analysis of UV-Induced Fiber Bragg Gratings". *IEEE Journal of Lightwave Technology*, 15(8):1478–1483, 1997.

[3] J. Canning. "Photosensitization and Photostabilization of Laser-Induced Index Changes in Optical Fibres". *Opt. Fib. Tech.*, 6:275–289, 2000.

[4] G.D. Emmerson, S.P. Watts, C.B.E. Gawith, V. Albanis, M. Ibsen, R.B.Williams, and P.G.R. Smith. "Fabrication of directly UV written channel waveguides with simultaneously defined integral gratings". *Electron. Lett.*, 38(24):1531–1532, 2002.

[5] L. Leick, A. Harpøth, and M. Svalgaard. "Empirical model for the waveguiding properties of directly UV-written waveguides". *App. Opt.*, 41(21):4325–4330, 2002.

[6] C.V. Poulsen, J. Hübner, T. Rasmussen, L.U.A. Andersen, and M. Kristensen. "Characterisation of dispersion properties in planar waveguides using UV induced Bragg gratings". *Elec. Lett*, 31(17):1437–1438, 1995.

[7] G.D. Emmerson. "Novel Direct UV Written Devices". *PhD Thesis*, 2003. University of Southampton.

[8] M. Fokine and W. Margulis. "Large increase in photosensitivity through massive hydroxyl formation". *Opt. Lett.*, 25(5):302–304, 2000.

[9] G.E.Kohnke, D.W.Nightingale, P.G.Wigley, and C.R.Pollock. "Photosensitization of optical fiber by UV exposure of hydrogen loaded fiber". *OFC., San Diego, USA*, page PD20/1PS20/3, 1999.

[10] A.Othonos and K.Kalli. *Fiber Bragg Gratings. Fundamentals and Applications in Telecommunications and Sensing*. Artech House, 1999.

[11] M. Douay, W.X. Xie, T. Taunay, P. Bernage, P. Niay, P. Cordier, B. Poumellec, L. Dong, J.F. Bayon, H. Poignant, and E. Delevaque. "Densification Involved in the UV-Based Photosensitivity of Silica Glasses and Optical Fibers". *IEEE Journal of Lightwave Technology*, 15(8):1329–1342, 1997.

[12] R.M.Atkins, V.Mizrahi, and T.Erdogan. "248nm Induced Vacuum UV Spectral Changes in Optical Fibre Preform Cores: Support for a Colour Centre Model of Photosensitivity". *Electronics Letters*, 29(4):385–387, 1993.

Chapter 9

Detection of Phase Transitions

9.1 Introduction

Sensing devices permeate all aspects of modern day society. Ranging from industrial to domestic applications, air travel to space travel, the role of sensors is fundamental to the smooth and safe running of a vast range of technologies. Unsurprisingly, such a technical challenge has triggered considerable academic and commercial interest.

Optical techniques for sensing cover a broad range of techniques and applications [1, 2]. They can be both clean and compact, operate remotely and non-invasively, and provide a high level of sensitivity with low power consumption. The technologies used for optical detection include particle scatter detection [3], surface plasmon resonance [4], Mach-Zehnder interferometers [5], grating couplers [1, 6], relief gratings [7], long period gratings [8] and fibre Bragg grating sensors [9].

The use of Bragg gratings as sensor elements is not new and fibre based gratings offer many advantages. Design and production of the Bragg sensing structure in planar waveguiding devices is a less well established procedure than the equivalent fibre process but the resultant sensing device offers a number of additional advantages. Whereas optical fibre without ruggedised cladding is a flexible but fragile material, planar silica on silicon structures are intrinsically more robust although somewhat larger in size. The principal strength of planar optical sensors lies in the scope for

integration of multiple functions, sensing or otherwise, onto a single detector-chip. This provides a route to low cost, flexible and compact devices that would be considerably more complex if realised in fibre technology.

The majority of fibre grating sensor designs are based around the shift in Bragg wavelength due to strain or temperature. Strain on a grating alters the period due to the changes in the physical size and also due to stress effects on the refractive index whereas temperature changes are detected due to thermal expansion and the temperature dependence of refractive index . However, it is also possible, by exposure of the waveguiding core layer, for a Bragg grating to act as an evanescent field sensor [10]. External changes in refractive index alter the effective index seen by propagating modes due to the interaction of the evanescent field. This technique has been demonstrated in UV written planar waveguides by removal of the upper cladding layer to expose the waveguide core [11, 12].

As discussed in chapter 2 the effective index, and therefore Bragg wavelength, of a waveguide or fibre Bragg grating is determined by the refractive index of both the core and the cladding. Thus a change in the cladding refractive index of a waveguide will result in a shift in the Bragg wavelength. This is the approach used here in the demonstration of planar Bragg sensors.

This chapter demonstrates the use of planar Bragg gratings as sensing components, specifically as refractometers used in the detection of phase transitions from one physical state to another. Initially focussing on the change of a liquid crystal from an ordered to isotropic state, the chapter then moves on to show how the technology is able to detect changes in, and identify the physical state of water.

A feature of this work is the use of wavelengths close to 1550nm. Although these wavelengths are common for telecommunications applications, refractive index measurements for substances such as liquid crystals and refractive index standards are generally quoted at visible wavelengths such as 589nm or 633nm (the sodium D-line and He-Ne lasers respectively) due to readily available, well characterised light sources. In itself this may prove to be a useful application as it allows substances that may be of use in the optical path of telecommunications components to be char-

acterised.

9.2 Phase Transitions

Phase changes can be grouped into first order or second order transitions and are characterised by changes of thermodynamic properties around that transition, such as order, enthalpy and heat capacity. First order transitions are characterised by a discrete change in order and have an associated latent heat, whereas second order transitions display continuous changes. The melting and evaporation of water and the transition between isotropic and nematic liquid crystal states [13] are first order transitions. The change in order of the substances can be expected to have an associated change of refractive index, the property that is measured here.

9.3 Design Considerations

The basic design and fabrication method of the planar sensors is shown in figure 9.1. A UV written waveguide with integrated Bragg grating is written into the sample as described in chapter 3. The overclad directly above the Bragg grating section is removed using an etch process. In this way the waveguide remains in its as-written state whilst the Bragg grating is exposed to atmosphere. The hole in the overcladding is then simply filled using the analyte to be studied. Changes in the analyte refractive index can then easily be monitored by interrogation of the Bragg response.

Whilst the cylindrical symmetry of optical fibre lends itself readily towards modification of the cladding index all around the core, planar geometries are more restricted as shown in figure 9.2. Consequently planar sensors of the type presented in this chapter can be expected to have a somewhat lower sensitivity to refractive index changes than their equivalent fibre based designs. For practical reasons the work described here is restricted to modifying the cladding refractive index above the waveguide core whilst leaving the cladding either side and below the core unchanged.

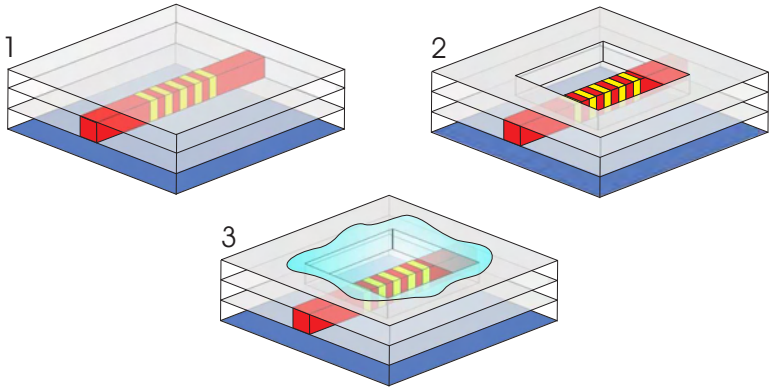

Figure 9.1: From planar waveguide to planar sensor. 1) The waveguide and Bragg grating are defined in the core layer, 2) The overclad above the grating is etched away and 3) replaced by the analyte.

The principles used here to allow a Bragg grating to act as a sensing element apply equally well to Bragg devices produced by any method. For some applications however, there are advantages to using a UV writing approach. A planar waveguide fabricated using standard etch process will not have a truly planar surface. Even when planarisation steps are taken it is very difficult to avoid surface relief above the waveguide core. In UV writing all depositions are performed prior to the waveguide definition and so no surface relief is introduced to the layers. Thus when the upper layer is etched away to uncover the grating, it is a smooth, flat surface that is being etched, allowing the resultant etched surface to also be smooth and flat. This chapter centres on the use of liquid crystal and water overlayers on the exposed grating. It is important, due to reasons discussed in section 9.6, that the surface structure is as homogeneous, clean and smooth as possible to allow the liquid crystal - silica surface interface to act in a controlled predictable way. Any surface structure, such as that over an etched waveguide, will degrade performance. When monitoring the phase changes of water, consideration must be given to the expansion and contraction that is known to occur as water thaws and freezes. A relief grating which by definition has a structured surface, is susceptible to 'weathering' by water. Again, the smooth, flat surface allowed by UV writing is an advantage in this case.

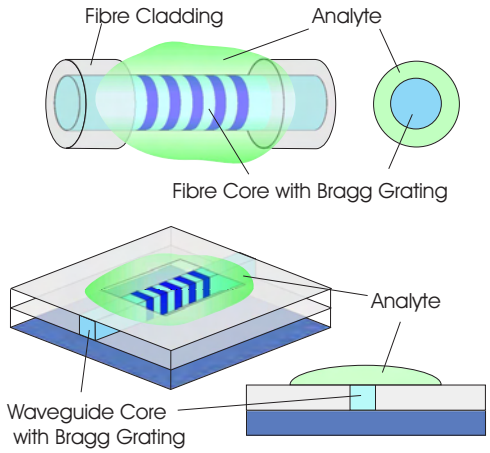

Figure 9.2: Schematic showing restricted contact of Bragg grating core with analyte in planar relative to fibre geometries

9.4 Device Modelling

To asses the expected sensitivity of Bragg wavelength to variations in overclad refractive index the structure shown in figure 9.3 has been modelled according to the method proposed by Marcatili [14]. This technique is used to estimate the effective index of a waveguide with a range of overclad refractive indices, the results of which are shown in the graph of figure 9.3.

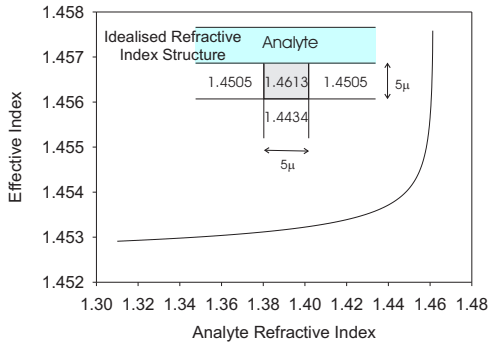

Figure 9.3: Sensitivity curve for a planar sensor with a refractive index structure as shown.

As previously mentioned in chapter 7, the exact refractive index structure of the UV written waveguides presented here is not known. However, approximate values of the refractive index of the layers can be estimated based on prism coupling and data

from fluence curves. Using experimentally obtained effective index measurements presented later in this chapter, the parameters used in the Marcatili model have been refined such that the modelled results match the experimental data. This was done using the known refractive index of air (n=1.0) and of water (n≈1.31) [15, 16] at 1550nm. The refractive index profile of the modelled waveguide shown in figure 9.3 is such that the model predicts the correct effective index (the values of which are presented later in this chapter) with overclad refractive indices of 1.0 and 1.31. A superior index structure could be generated using more calibration points closer to the refractive index of the doped silica where the gradient of the sensitivity curve is higher. There are however several assumptions that must be made in order to use this model and as such the use of improved calibration points would be of limited value. In addition to the simplifications inherent to the Marcatili method, the waveguide core has been treated as a symmetrical step index structure with a perfectly etched overclad.

Recalling that the Bragg wavelength varies linearly with effective index it can be seen that the sensitivity of the sensor to refractive index variation is given by the gradient of the graph, $\frac{\delta n_{eff}}{\delta n_{clad}}$. For an overcladding very close to the waveguide core in terms of refractive index the gradient of the sensitivity curve is high showing that there is a large variation of Bragg wavelength with overclad index. With cladding index above that of the core the structure ceases to act as a waveguide and the sensor no longer functions. As the overclad index drops, the dependence of effective index becomes weaker and thus the sensor is less sensitive.

A modelled sensitivity of unity is achieved with an analyte refractive index of 1.4606 i.e. a change in overclad index causes a change of equal magnitude in the effective index. As figure 9.3 shows this drops rapidly with decreasing analyte index. At the refractive index of water the modelled sensitivity is reduced by a factor of approximately 500. Even with this reduced sensitivity, the model predicts that the typical wavelength resolution of a standard optical spectrum analyser (10pm) allows the detection of refractive index changes in water of 5×10^{-3} or lower despite its relatively low refractive index. Specialist grating interrogation equipment with resolutions an order of magnitude higher allow detection of index changes a corresponding order

of magnitude smaller.

The reduced sensitivity at high analyte refractive index values is due to variation of the penetration of the mode into the analyte. This is shown graphically in figure 9.4 which has been generated using the Marcatili model discussed earlier. The graph shows the variation of the depth to which the electric field penetrates before decaying by 1/e.

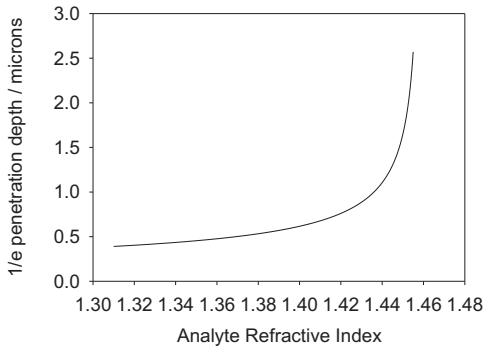

Figure 9.4: Variation of electric field penetration with analyte refractive index.

It can be seen that with water as an overlayer (n≈1.31) the penetration depth is a few hundred nanometres but increases rapidly with analyte index, explaining the similarly rapid increase in sensitivity.

Figure 9.5 is shown to compare the sensitivity of the planar device presented here with the possible response of a similar fibre based device. The same modelling method described above was used but for the case of the fibre sensor the entire cladding surrounding the core was used to vary the effective index. It can be seen that the fibre based design with analyte entirely surrounding the core shows a higher sensitivity as expected, with a wider range of effective indices for the given range of cladding indices.

The relative sensitivities of practical sensor devices will depend significantly on the thickness of cladding layers between the analyte and the waveguide core as well as on the proportion of the core circumference that is exposed to analyte instead of overcladding. As such, the modelling presented here does not provide an exact determination of the sensitivity of the devices described. Rather, it demonstrates how the sensitivity varies with the penetration of the mode into the analyte.

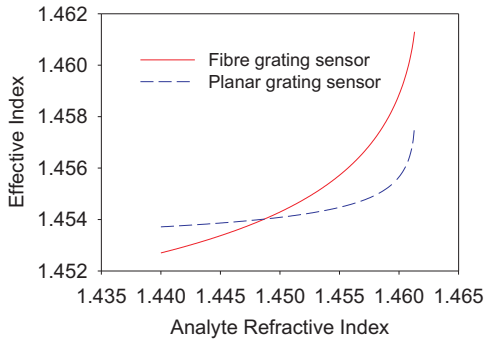

Figure 9.5: Comparison of sensitivity curves for fibre Bragg grating and planar Bragg grating sensor designs.

For practical reasons, a fibre grating sensor of this nature is likely to be encapsulated in some way to enhance the physical strength. Such pseudo-planarisation will inevitably reduce the sensitivity towards that of the planar device modelled above.

It is of course possible, with additional engineering to develop a planar sensor structure with three sides of the waveguide core (making the assumption of a rectangular cross-section guide) in contact with the analyte as shown in figure 9.6. In this case the sensitivity improves towards that of the fully surrounded version possible with fibre based designs. To date this has not been studied experimentally so further discussion is restricted to the case where only variations in overclad refractive index are detected.

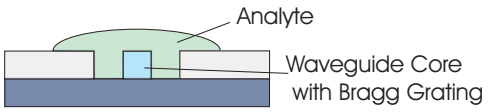

Figure 9.6: Schematic of route towards enhanced sensitivity planar sensor.

It is worth commenting that the asymmetry of the waveguiding structure used in these devices causes a high level of birefringence. Whilst such a property would be of concern in, for example, high bit rate telecommunications systems where polarisation insensitivity is desirable, it is not of significant concern in a sensing device.

9.5 Device Fabrication

Two devices were used for the experiments described in this chapter. Both were fabricated from FHD deposited samples and were UV written, etched and fibre coupled by G.D. Emmerson [11]. A schematic representation of the device design is given in figure 9.7.

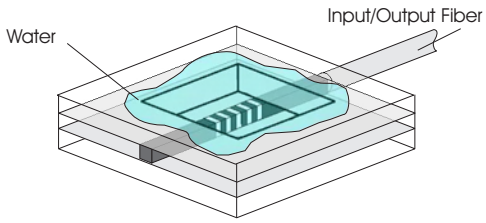

Figure 9.7: Schematic representation of fibre coupled three layer sample with liquid crystal (or water) over Bragg grating.

The uppercladding directly above the Bragg grating of period 537nm was removed by a hydrofluoric acid etch step. To obtain the correct etch depth, previously determined etch rates (measured using surface profile measurements and SEM imaging) were used to calculate etch times required to remove the overcladding, known to be approximately 20μm in thickness. The exposed section was then covered with the analytes to be studied, specifically Merck 18523 (a nematic liquid crystal) and water. The grating itself was 2mm in length with the etched window slightly longer than this to allow for small errors in the positioning of the etch window.

9.6 Nematic Liquid Crystal

Chapter 10 provides a more detailed description of the properties of liquid crystals but for completeness a brief description of the behaviour of nematic liquid crystals is given here.

In contrast to liquids, which are isotropic and have no order amongst the constituent molecules, liquid crystals display a level of order and therefore anisotropy. There are several classes of liquid crystals each of which posses a range of characteristics

making them suitable for various applications. In a nematic liquid crystal, the least ordered class of liquid crystals, there is no positional order amongst the molecules but there is a degree of orientational order. As the name suggests, liquid crystals are generally able to flow and their molecules are free to diffuse as they would in a liquid. Over time the molecules' individual positions and orientations will evolve. It is found however, that under constant conditions, the average molecular orientation in a nematic liquid crystal will remain constant. This average orientation is known as the director as shown in figure 9.8.

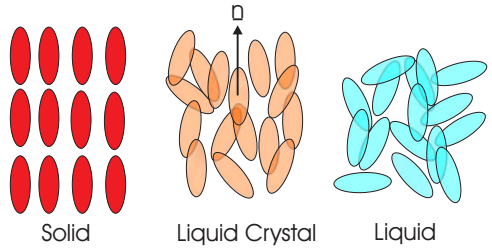

Figure 9.8: Schematic representation of molecular order and orientation of crystals, liquid crystals and liquids. The director, n, of the liquid crystal is shown by the black arrow.

As the temperature is increased the thermal energy of the liquid crystal molecules increases and the associated level of order is reduced. At a temperature known as the clearing point all order is lost and the nematic liquid crystal makes a transition from the anisotropic state to an isotropic liquid. The clearing point is so-called as below this temperature the liquid crystal appears cloudy, above the transition the liquid is clear. The reason for cloudiness below the clearing point is that point defects and disclinations (defects along a line) exist throughout the liquid crystal causing localised variations in the director to scatter light.

The phase transition from nematic liquid crystal to isotropic liquid is known to be a first order transition [13] and as such a discontinuity in behaviour can be expected at the clearing point.

Measurement of the clearing point can be made simply by heating the liquid crystal and visually observing the temperature at which the cloudiness associated with the liquid crystal state disappears. For Merck 18523, the liquid crystal used here, the

clearing point has been experimentally determined by A. Dyadyusha to be approximately 60℃ .

The surface properties at the interface between a liquid crystal and its container are critical to its behaviour as the director orientation can be strongly influenced. Similarly, control of the naturally occurring defects and disclinations discussed above are also of importance to the performance of a liquid crystal device. Microscopic structure or dirt on the surface that confines the liquid crystal will affect or control the orientation of the director in the vicinity. A free surface, i.e. when exposed to air, is also known to exhibit complex alignment orientations [17]. It is common therefore for devices such as liquid crystal displays to use only thin layers (∼10μm) of liquid crystal constrained on either side by a specially treated surface. In this way, director alignment, disclinations and defects are controlled between the surfaces due to the influence of the surface alignment.

For the work described here the silica grating surface was not treated in any way other than a pre-application clean with acetone. The liquid crystal was applied as a drop and allowed to freely expand over the surface. No additional layers were used to constrain the liquid crystal and the upper surface was exposed to air. The liquid crystal used here was chosen for its refractive index compatibility with the silica used to fabricate the sensor. At 589nm the liquid crystal extraordinary and ordinary refractive indices are 1.5089 and 1.4599 respectively, and have been estimated [18] at 1.489 and 1.444 at 1550nm.

9.6.1 Thermal Behaviour of Liquid Crystal

In order to measure thermal effects on the liquid crystal covered waveguide it was mounted onto a brass plate, within which a thermocouple was positioned. The brass mount was in turn clamped onto a resistive heater allowing the temperature to be raised from room temperature to 100℃ whilst measurements were recorded (Figure 9.9). The whole arrangement was allowed to cool radiatively back to room temperature whilst recording additional data to check for hysteresis. All data was taken in the form of reflection spectra recorded by an optical spectrum analyser with the

sample temperature recorded as each spectrum was taken.

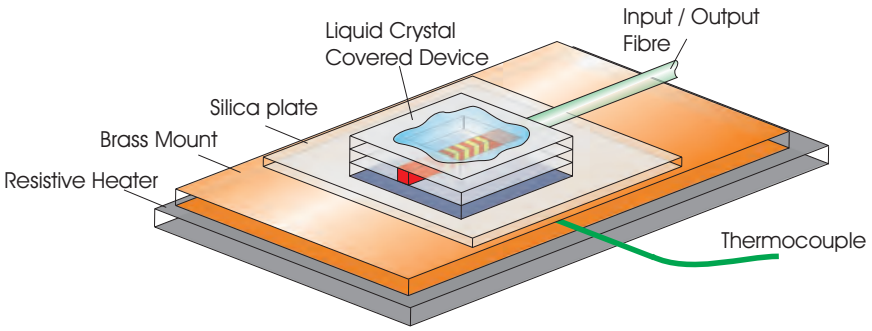

Figure 9.9: picture of LC on heater with thermocouple

All reflection spectra were observed to display a large amount of structure superimposed on the expected Bragg response. This is thought to be the result of interference from reflections from the edges of the etched window which were perpendicular to the waveguide. When using the Bragg spectra to determine the waveguide effective index it was found that the additional structure made determination of the Bragg wavelength inaccurate. Therefore a moving average technique was employed to smooth the data. Examples of the structured and subsequently smoothed data are shown in figure 9.10. The chosen method performed a moving average over 23 data points (equivalent to a wavelength span of 41pm). This procedure was performed twice, resulting in the smoothed data shown in figure 9.10 which allowed centre wavelengths to be determined using the mean wavelength values either side of the Bragg peak. The smoothed data can be seen to provide a good fit to the unmodified spectra even when the levels of additional structure are significant compared with the magnitude of the Bragg response.

The alternative to this averaging approach would be to use a curve fitting routine to provide an estimate of centre wavelength. However, the simplicity of the moving average technique allowed easy application whilst retaining the ability to detect small changes in the Bragg wavelength.

As figure 9.10 shows, the grating response for the liquid crystal covered grating is centred around 1561nm. The variation of the effective index with temperature of the liquid crystal covered planar waveguide is shown in figure 9.11 a). The liquid

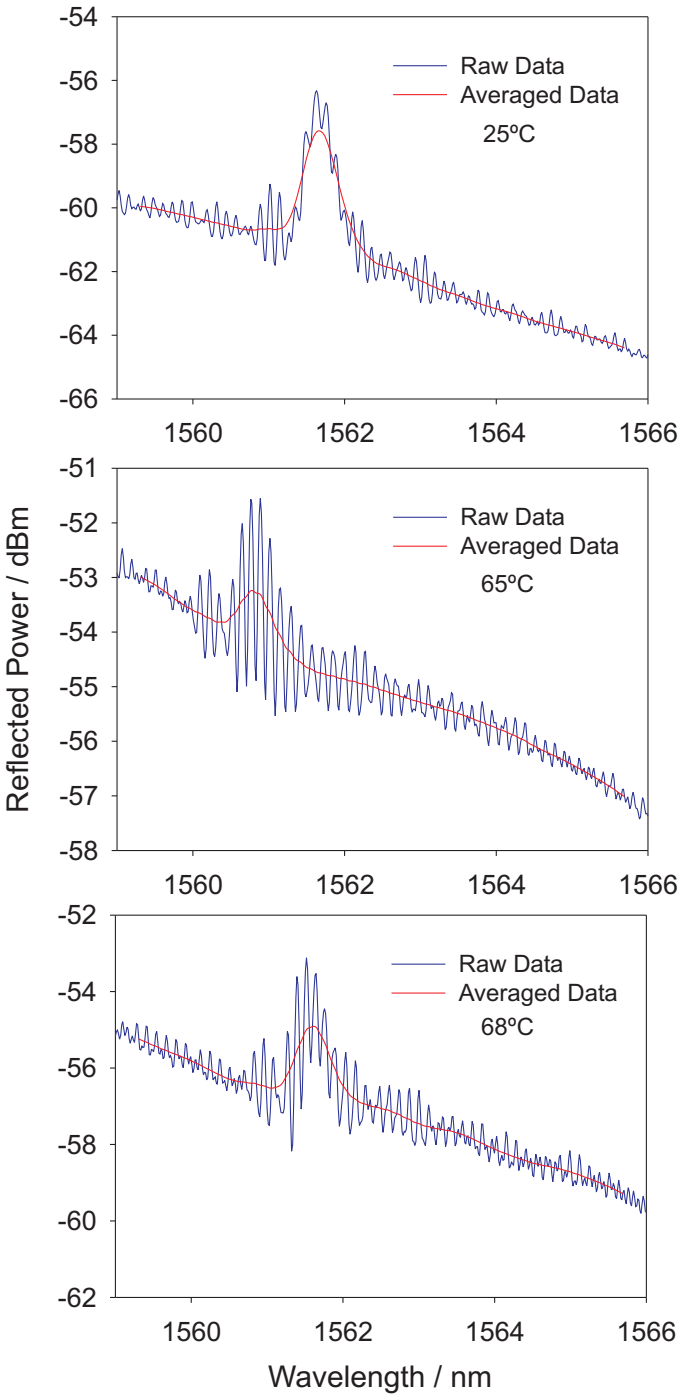

Figure 9.10: Reflection spectra as recorded and after smoothing with a moving average. Spectra were recorded at the measured temperatures shown, the data at 65°C and 68°C represent measurements below and above the clearing point respectively.

crystal was applied as previously described. No hysteresis was observed in the heating/cooling cycle. Error bars have been added to the figure based on estimated uncertainties for both the temperature measurements and wavelength determination used in the calculation of effective index. The temperature control used in this work used a simple feedback loop to control the heater but this was found to be inadequate to control and stabilise the temperature. The temperature was therefore increased by manually incrementing the set point by a few degrees and recording reflection spectra as the temperature increased. The estimation of the associated uncertainty is thus $\pm 0.5℃$. Uncertainty in the effective index measurement is estimated at a maximum of $\pm 2 \times 10^{-5}$ based on a typical OSA resolution of 10pm and a similar wavelength uncertainty from the determination of centre Bragg wavelength after data averaging.

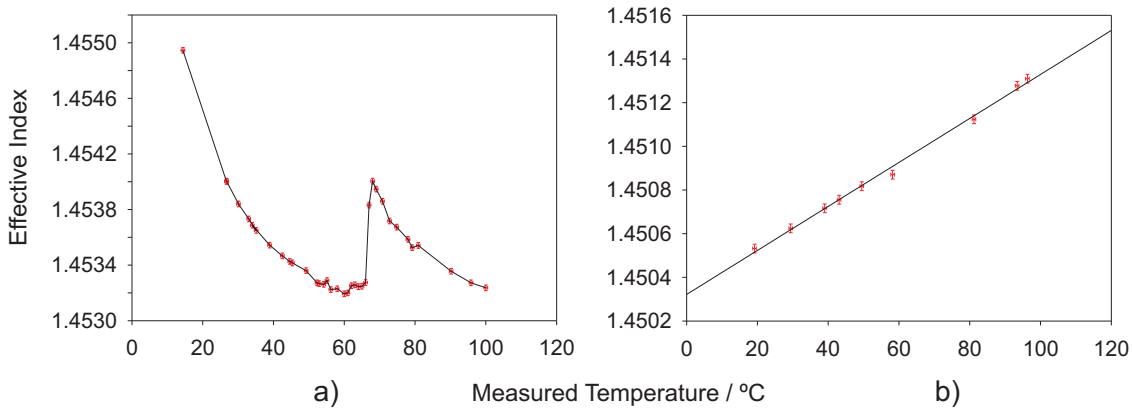

Figure 9.11: a)Variation of centre wavelength with temperature for liquid crystal covered planar Bragg grating. b)Linear thermal response of sensor in air.

The most obvious feature of the data shown in figure 9.11 a) is the sharp discontinuity at $66℃$. This is the clearing point of the liquid crystal . The difference between this value and the previously quoted value of $60℃$ is due to the relative positioning of the thermocouple and sample on the heater. The first order phase transition between ordered liquid crystal and isotropic liquid is shown clearly as a discreet jump in refractive index, a characteristic feature of this class of phase transitions. Below the clearing point increasing temperature reduces the order of the liquid crystal and the refractive index drops. The range of effective index with temperature seen here

(approximately 2×10^{-3}) corresponds to a variation in Bragg wavelength of 1.88nm.

Looking at figures 9.10 and 9.11 a) together allows the variation in the magnitude of the Bragg reflection peak to be seen in the context of the state of the liquid crystal. Here, we can assume that the coupling between waveguide and input/output fibre was approximately constant and independent of temperature as the device was pigtailed and less susceptible to variation than if alignment had been held using translation stages. As the liquid crystal refractive index drops, the overall level of reflected light increases due to the change in effective index over the whole exposed section of waveguide/grating.

Figure 9.11 b) shows the temperature response over the same range of the device in air with no liquid crystal covering. As expected the thermal behaviour is linear [19] and shows a variation of effective index with temperature of 1.03×10^{-5} C^{-1} equivalent to a wavelength dependence of 10.8 pmC^{-1} . This variation of effective index with temperature compares well with measured variations of the refractive index of silica with temperature. Fused silica has been measured to display a variation of refractive index of 1.1×10^{-5} C^{-1} at 1550nm [20]. Also for comparison, a germanium doped silica optical fibre [19] displays a change in refractive index over temperature of 12.8pmC^{-1} indicating a similar thermo-optic coefficient.

With a range of refractive index standards it would be possible to determine the effective index of the grating with a range of overlayer refractive indices and produce a curve similar to that modelled in figure 9.3. Knowledge of the linear temperature coefficient of figure 9.11 b) allows the thermal response of the grating to be compensated for and thus the actual refractive index of the liquid crystal overlayer could be determined at each temperature.

The conclusions that can be drawn about the liquid crystal behaviour over the temperature range used here are limited by the unknown surface alignment of the liquid crystal. With no surface preparation it is likely that there is a wide variation in director orientation across the exposed grating and thus the behaviour shown in figure 9.11 a) can be due to reorientation in multiple directions. Nonetheless, despite the restrictions imposed by lack of knowledge of the liquid crystal alignment, the re-

sults show that the planar sensor discussed here allows easy detection of a relatively subtle change from a low level of order to a disordered state.

9.7 Phase Changes of Water

In contrast to the preceding section where the refractive index of the liquid crystal is close to that of the waveguide core, this section presents the use of water, a much lower refractive index overlayer, on the sensor. The refractive index of water at 1550nm is approximately 1.31 [15,16] and thus a much lower sensitivity to changes in refractive index can be expected from the sensor than with the liquid crystal case previously described.

From everyday experience we know that the solid form of water is less dense than the liquid form as ice floats in water. The refractive index of ice can therefore be expected to be somewhat lower than that of water and the point at which the phase transition from solid to liquid (and vice versa) will be detected as a shift in the Bragg wavelength of the sensor.

A similar experimental procedure was used here to that described above for the liquid crystal experiments. In this case however, the device was mounted onto a thermoelectric cooler (TEC) to allow both heating and cooling of the sensor without the need for repositioning of the device. Thermally conductive paste was used hold the TEC in position on an optical bench which acted as a heatsink. The edges of the TEC were masked with plastic tape to prevent water condensing on the chilled upper surface from dripping onto the electrical connections. It was again found, when using a 10kΩ thermistor as the temperature sensor, that the PID temperature control did not provide adequate thermal stability when recording reflection spectra. To overcome this the TEC controller was set to a current limited mode to allow manual control over the current supplied to the TEC. The target temperature of the TEC controller was set several degrees beyond the desired device temperature. The current limit was then manually selected in order to prevent the TEC reaching the temperature set-point. This resulted in the TEC output remaining constant at the preset current

limit. In this way the output of the controller, and therefore the device temperature, was always determined by the manually chosen current limit. Temperature control through variation of the current limit was found to provide a more stable device temperature than through the use of the integrated PID function of the TEC controller.

Initially the thermistor was positioned adjacent to the sample and glued to its silica mount (position 1, figure 9.12). It was subsequently found (discussed further during the analysis of figure 9.13) that measuring the temperature at this point resulted in a thermal offset between the thermistor and the Bragg grating surface. The thermistor was therefore replaced with a thermocouple in direct contact with the exposed silica surface (position 2, figure 9.12). Careful bending of the thermocouple wires was found to provide a spring-like arrangement that held the thermocouple in direct, constant contact with the exposed silica surface of the device. The thermocouple output was monitored by a dedicated thermocouple temperature meter. To ensure that the presence of water did not short circuit the thermocouple electrical connections it was coated in photoresist to provide a thin insulating layer. This new arrangement was found to almost entirely eliminate the thermal offset observed with the thermistor. For this particular application, the thermocouple was advantageous as it was less bulky than the thermistor which, owing to the design of its electrical insulation and wiring required glue to bond it securely to the silica. Use of glue on the etched region of the device was avoided to prevent contamination of the surface.

No additional averaging of the data was required to obtain reliable values of Bragg wavelength from the reflection spectra.

Figure 9.13 shows the results of cooling the sample in air to allow water to condense and then freeze on the sensor. This figure clearly shows the detection of phase transitions from vapour to liquid and from liquid to solid. The right hand of the figure, above 14 ℃ , shows the expected linear thermal variation of effective index. As the temperature drops below 14℃ there is a sharp increase in the measured effective index. This is due to formation of condensation on the silica surface. The temperature at which condensation just starts to form is known as the dew point and is a valuable parameter to know. Dew point hygrometers are designed and marketed specifically to determine the dew point as it allows the relative humidity of the air to be found.

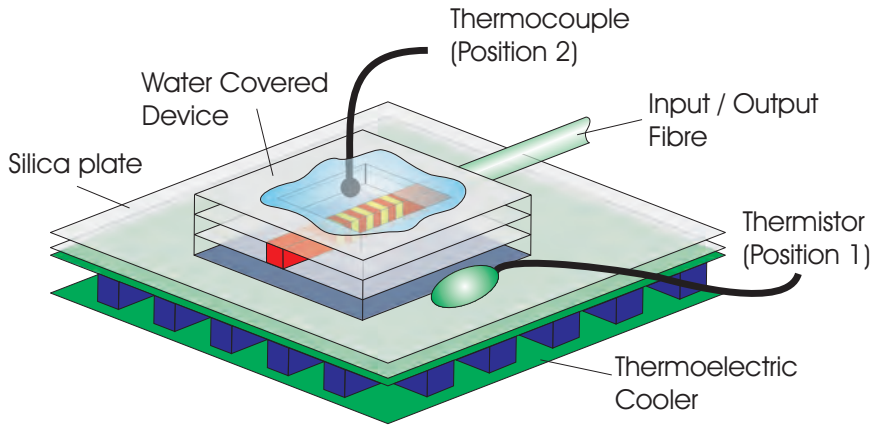

Figure 9.12: Experimental arrangement used for measurements with water as the Bragg grating overlayer. Positions used for the thermistor and thermocouple are shown.

As the sensor is cooled below the dew point condensation will form continuously under constant ambient conditions. To allow for this, successive measurements were taken at intervals of approximately ninety seconds with a corresponding temperature change of approximately $0.3℃$. As more water forms above the exposed grating the effective index continues to increase until, at approximately $8℃$ the surface is fully covered with a continuous layer of water. Further cooling of the sensor produces a linear variation of effective index with temperature until the sensor is cooled to $0℃$.

Although water is known to be most dense at $4℃$ [21] it is not feasible to expect data recorded in this way to show any features at this temperature. This is due to the relatively low sensitivity of the sensor to small modulations of refractive index well below the refractive index of the waveguide core.

At $0℃$ the condensed water freezes causing a sharp discontinuity in the data. As expected, the effective index drops due to the lower density state of ice. With further cooling, another linear thermal response is observed.

The horizontal axis of figure 9.13 has been corrected to account for the thermal offset between the surface of the grating and the thermistor. This offset, as mentioned earlier, was due to the positioning of the thermistor. The offset is such that the ther-

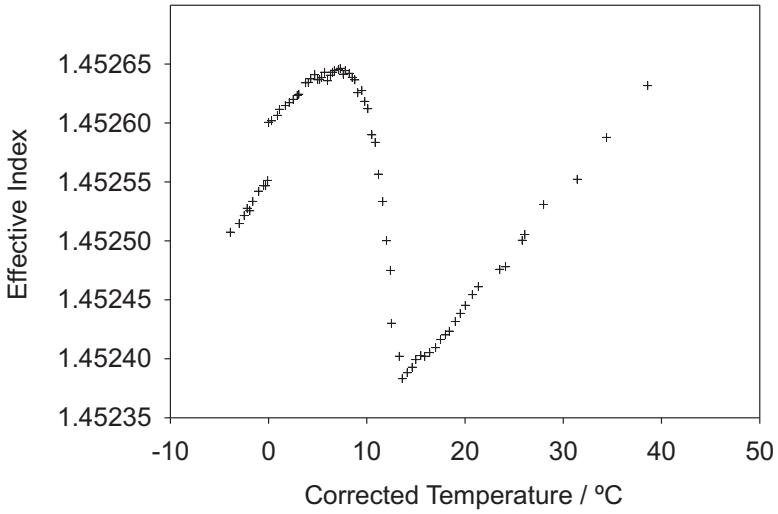

Figure 9.13: Variation of sensor effective index as water condenses on the silica surface. The temperature scale has been corrected by +4.0℃ to correct for the thermal offset between the grating and thermistor used for temperature measurements.

mistor is several degrees cooler than the grating surface. An offset of 4.0℃ has been used for this to allow the freezing transition to occur at 0℃ . All subsequent results in this chapter used the repositioned thermocouple to eliminate this offset.

Knowledge of the dew point, obtained from figure 9.13, allows calculation of the relative humidity of the laboratory at the time of the experiment. The relative humidity (*RH*)is given by the ratio of the water vapour pressure to the saturated vapour pressure which can be reduced to the following expression

$$RH = e^{\frac{5423}{T} - \frac{5423}{T_d}} \tag{9.1}$$

where T is the air temperature in Kelvin and T_d is the dew point in Kelvin. Thus with a laboratory air temperature of 22℃ the relative humidity was approximately 60%.

When increasing the temperature from below 0℃ to allow frozen water to melt the data shown in figure 9.14 is obtained. The graph is made up of two linear sections - one is the response of the grating with ice overcladding, the other the response of the grating with a liquid overlayer. Again a discreet transition is seen at 0℃ where the phase transition occurs.

The variation of the refractive index of water with temperature at 1550nm has been

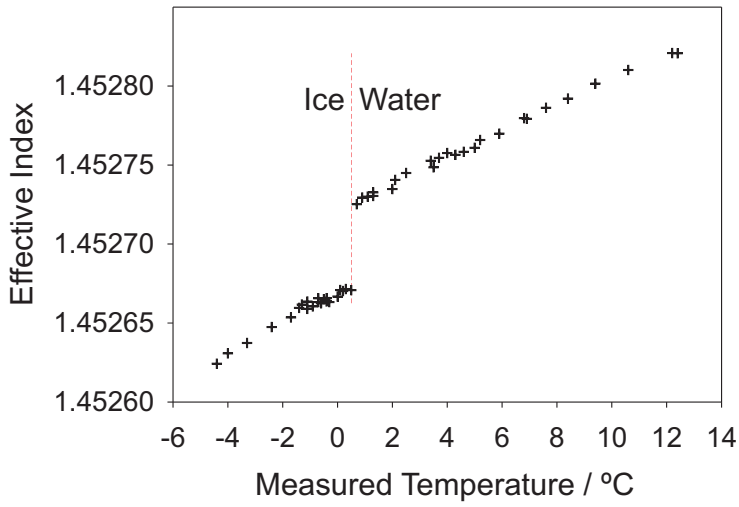

Figure 9.14: Variation of sensor effective index as ice warms and melts.

measured [16] to be approximately -1$\times$ 10^{-4} C^{-1}. Clearly the water covered sensor does not display a negative variation of effective index with temperature. This is because the thermo-optic behaviour of the silica dominates as the waveguide core most of the cladding is silica and only the overcladding is water.

Grating spectra corresponding to the three states of water (gaseous, liquid, solid) are given in figure 9.15. The variation of Bragg wavelength can be clearly seen between the three spectra. It is worth noting the slightly larger bandwidth of the trace corresponding to liquid water at approximately 0℃ . The reason for the broader reflection response is attributed to the possibility of localised temperature variation as the water approaches the phase transition. The resultant non-uniformity across the grating could explain the difference in bandwidth. The narrow bandwidth ($<$0.25nm) of the reflection peaks assists in the detection of small variations in the Bragg wavelength.

An additional, initially unexpected feature of using the planar Bragg grating as a sensor device is the detection of supercooling. It is widely known that a mixture of liquid and solid water will remain at 0℃ as long as both phases are present. This is an equilibrium temperature at which both states co-exist in stable forms. However, at atmospheric pressure, water can in fact remain a liquid at temperatures as low as approximately -42℃ [22]. This sub-zero liquid state, referred to as supercooled, is a metastable state of water that is easy to create experimentally. Although extensive

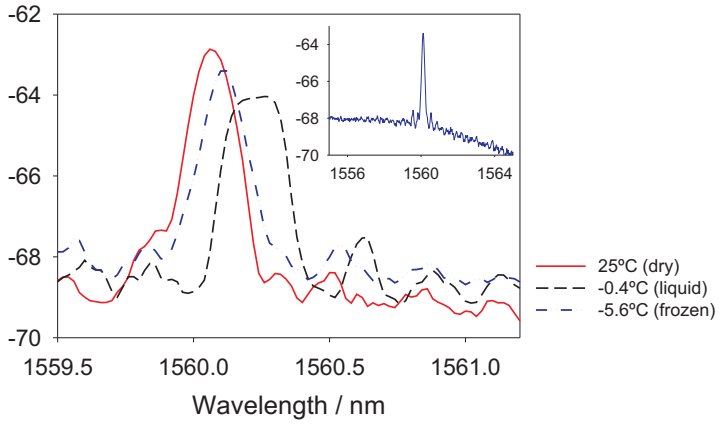

Figure 9.15: Comparison of reflection spectra with gas, liquid and solid water overlayers. Inset: Spectrum taken with ice covering shown with wider wavelength scale.

research continues into the properties of the supercooled and solid states of water [21, 23] the phenomenon of supercooling has been known for around 200 years. A thorough description of the physical reasons for supercooling and the properties of the state is far outside the scope of this thesis. It is sufficient to say that a nucleation point is required to initiate the freezing of a liquid to a solid and that the volume of water and the environment it is in determine the degree of supercooling that can be obtained. Generally speaking, the less impurities there are in a sample of water, the greater the level of supercooling that can be achieved. As the water samples used here were condensed from the atmosphere the only contamination is from the surface of the device which, with repeated cleansing between tests is likely to have become increasingly clean with time. This could be one explanation why the initial set of data recorded (figure 9.13) does not show evidence of supercooling that is seen in data recorded subsequently and given below.

The data presented in figure 9.16 shows how the supercool state of water can be distinguished from the solid. The same method used to obtain figure 9.13 was applied however a slower cooling rate was used to allow the formation of supercooled water to be easily observed. An annotated schematic of the data is shown next to the graph to clarify the significance of the various stages of the experiment. The results indicate that the level of ambient humidity whilst the data was recorded was somewhat

higher than when recording the data shown in figure 9.13. This is shown by the dew point occurring at a temperature a few degrees higher than in figure 9.13. Despite

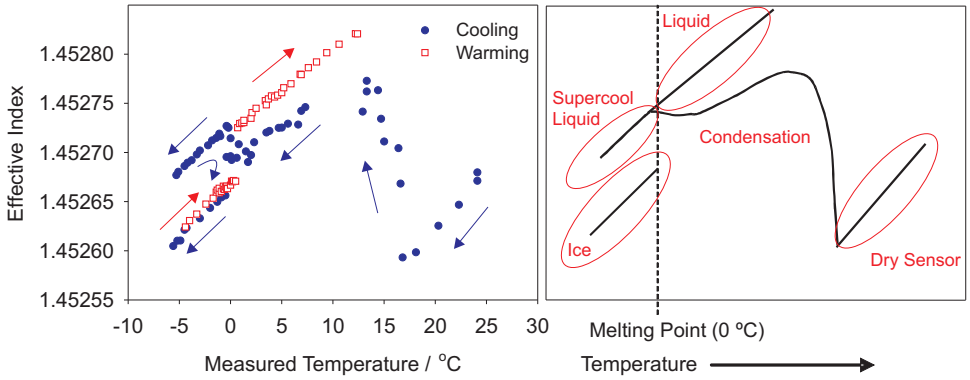

Figure 9.16: Demonstration of supercooling. Left: Experimental data showing double-valued behaviour below zero degrees due to solid and supercooled water. Right: Schematic representation of data to highlight specific regions of data.

the higher humidity, it can be observed that the data from the condensation phase of the graph shows a higher level of noise than figure 9.13. This is believed to be due to the way that water droplets formed upon the silica surface. Owing to surface effects, relatively large beads of water can form upon the device surface without coalescing together to form a continuous layer. In contrast to figure 9.13 where the individual water drops coalesced readily to form a continuous layer, the process was slower when recording figure 9.16. It is likely that this is due to the effects of surface contamination resulting in a surface with slightly hydrophobic or hydrophilic characteristics.

It is however easy to see the contrast in refractive index between solid and liquid water below 0℃ . As the temperature falls below zero, the data follows a linear trend that is continuous with that of liquid water above zero (shown in red for comparison). At approximately -5℃ all of the water over the sample froze sharply and the temperature of the system was raised back to 0℃ due to the latent heat of the phase transition. As the water cools again the expected linear variation is observed, as also seen in figure 9.13.

Although the phenomenon of supercooling was not an expected result, it is easy to see why the observed trend occurs. The supercool state has the same disordered

structure as normal liquid water and so it can be expected that the variation of refractive index with temperature will continue the trend seen above 0℃ . To demonstrate the continuous linear variation of effective index for liquid water above and below 0℃ figure 9.17 shows the results of cooling a complete water overlayer to below freezing. Supercooling is again observed before sudden freezing and further cooling.

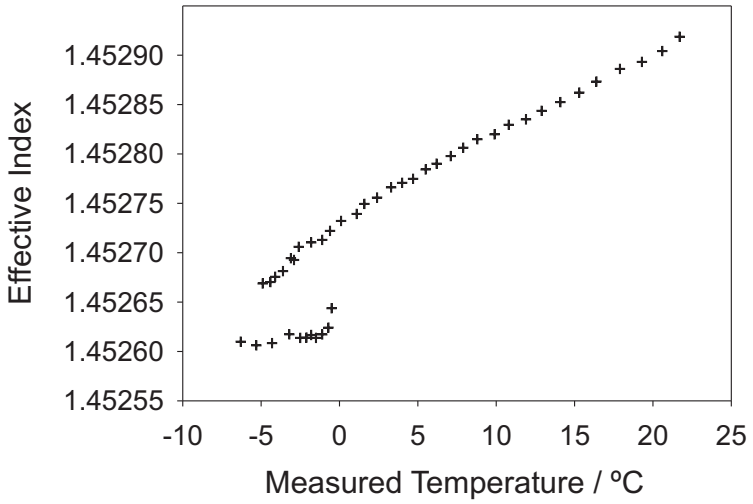

Figure 9.17: Demonstration of supercooling of liquid overlayer.

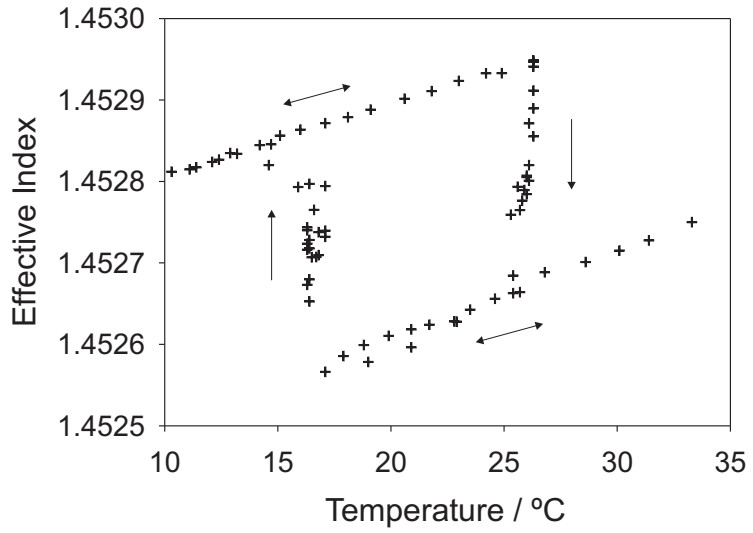

Figure 9.18: Cycling of sensor between wet and dry states.

Figures 9.13 and 9.17 show that the effective index does not jump sharply when con-

densation occurs and the sensor moves from 'dry' to 'wet' states. Therefore, with appropriate calibration of the variation of effective index with condensation it should be possible to use such a planar sensing device to monitor the mass of condensed water on the substrate. The same is also true of evaporation from a wet sensor towards a dry surface. This is shown in figure 9.18 where the grating was held at temperature to allow evaporation to take the device from completely dry to saturated or condensation allowed to cause the opposite. Over timescales of several hours the variation in the volume of water over the sensor device can be tracked as the water slowly evaporates or condenses. At the lower right and upper left corners of the hysteresis curve shown in figure 9.18 the linear variation of effective index with temperature can be seen for the dry and wet sensor respectively.

The above results demonstrate how the simple fabrication methods used to define a Bragg grating and etch a window can result in a sensitive means of identifying and detecting transitions in the physical state of water. Whilst this appears, at first sight to be a trivial task it has proven to be a less than straightforward task to achieve in the past. Previously, to detect supercooling of water significantly more complex methods of sensing have been required [24, 25]. These include the deposition of fine period interdigitated electrodes to allow capacitance measurements and the use of complex image processing to asses the state of the water.

In addition to the relative simplicity of Bragg wavelength measurements, the planar sensors described here can have a temperature reference grating easily included. By a simple modification of the code used in the UV writing system an additional Bragg grating, operating at a different wavelength, can be added to the device. If the overcladding above this second grating is left intact the linear variation of Bragg wavelength with temperature can be used to provide an inbuilt thermometer for the sensor. Knowledge of the temperature and the waveguide effective index allows the physical state of the water to be determined from, for example, a look up table of the effective index versus state generated from data such as that presented in figure 9.13.

9.8 Summary

The results of this section demonstrate how a relatively simple planar grating device allows the detection of phase transitions in chemicals. The relative sensitivity of stripped-fibre Bragg sensors and planar sensors has been modelled. Despite the lower relative sensitivity of the planar devices presented here they have been demonstrated to provide a level of sensitivity that allows them to be applied in widely differing situations. Although water has a relatively low refractive index the very obvious change in density between liquid, solid and gas states mean that the phase transitions can be easily detected. In contrast, the far more subtle change from slightly ordered liquid crystal to isotropic liquid can be observed due to the refractive index being much closer to that of the waveguide core.

The two chemicals used here are of course only an example of the possible applications that the etched sensor could be used for. As already discussed, the devices presented offer potential for use as a dew point hygrometer as well as a means for monitoring all manner of chemical processes.

Planar Bragg devices of this nature offer a combination of the performance of a fibre Bragg grating sensor coupled with the robust nature of a planar device. In particular, the direct grating writing approach allows standard deposition techniques to be combined with the flexibility and simplicity of the software controlled UV writing process. Not only can refractometers operating at 1550nm be created, as demonstrated here, but using the DGW technique to define gratings with different periods means that other wavelengths can be exploited and devices tailored to specific applications.

9.9 References

[1] W. Lukosz. “Integrated optical chemical and direct biochemical sensors”. *Sensors Actuators B*, 29:37–50, 1995.

[2] R.A. Yotter, L.A. Lee, and D.M. Wilson. “Sensor Technologies for Monitoring

Metabolic Activity in Single Cells - Part 1: Optical Methods". *IEEE Sensors Journal*, 4(4):395–411, 2004.

[3] S.G.Demos and R.R.Alfano. "Ice detection on metal surfaces using the degree of polarisation of diffusely reflected light". *Elec. Lett.*, 32(24):2254–2255, 1996.

[4] J. Homola, S.S. Yee, and G. Gauglitz. "Surface plasmon resonance sensors: review". *Sens. Actuators B*, 54:3–15, 1999.

[5] B.J. Luff, J.S. Wilkinson, J. Piehler, U. Hollenbach, and J. Ingenhoff N. Fabricius. "Integrated Optical MachZehnder Biosensor". *J. Lightwave Technol.*, 16(4):583–592, 1998.

[6] K. Tiefenthaler and W. Lukosz. "Sensitivity of grating couplers as integrated-optical chemical sensors". *J. Opt. Soc. Am. B*, 6(2):209–220, 1989.

[7] G.J. Veldhuist, J.H. Berends, R.G. Heideman, and P.V. Lambeck. "An integrated optical Bragg-reflector used as a chemo-optical sensor". *Pure App Opt*, 7:L23–L26, 1998.

[8] V.Bhatia and A.M.Vengsarkar. "Optical fiber long-period grating sensors". *Opt. Lett.*, 21:692–694, 1996.

[9] A.D. Kersey, M.A. Davis, H.J. Patrick, M. LeBlanc, K.P. Poo, C.G. Askins, M.A. Putnam, and E.J. Friebele. "Fiber Grating Sensors". *IEEE Journal of Lightwave Technology*, 15(8):1442–1463, August 1997.

[10] A. Asseh, S. Sandgren, H. Åhlfeldt, B. Sahlgren, R. Stubbe, and G. Edwall. "Fibre Optical Bragg Grating Refractomer". *Fiber and Integrated Optics*, 17:51–62, 1998.

[11] G.D. Emmerson. "Novel Direct UV Written Devices". *PhD Thesis*, 2003. University of Southampton.

[12] G.D.Emmerson, C.B.E.Gawith, I.J.G.Sparrow, R.B.Williams, and P.G.R.Smith. "Physical observation of single step UV-written integrated planar Bragg structures and their application as refractive-index sensors". *Applied Optics*, 44(24):5042–5045, 2005.

[13] D.Demus, J.Goodby, G.W.Gray, H.-W.Spiess, and V.Vill. *Handbook of Liquid Crystals. Vol.1: Fundamentals*. Wiley-VCH, 1998.

[14] E.A.J.Marcatili. "Dielectric Rectangular Waveguide and Directional Coupler for Integrated Optics". *The Bell System Technical Journal*, 48(7):2071–2012, 1969.

[15] G.M. Hale and M.R. Querry. "Optical Constants of Water in the 200-nm to 200-μm Wavelength Region". *Applied Optics*, 12:555–563, 1973.

[16] C.-B. Kim and C.B. Su. "Measurement of the refractive index of liquids at 1.3 an 1.5 micron using a fibre optic Fresnel ratio meter". *Meas. Sci. Technol.*, 15:1683–1686, 2004.

[17] S.Chandrasekhar. *Liquid Crystals. Second Edition*. Cambridge University Press, 1992.

[18] R.-P.Pan, S.-R.Liou, and C.-K.Lin. "Voltage-Controlled Optical Fiber Coupler Using a Layer of Low-Refractive-Index Liquid Crystal with Positive Dielectric Anisotropy". *Jpn. J. Appl. Phys.*, 34:6410–6415, 1995.

[19] A.Othonos and K.Kalli. *Fiber Bragg Gratings. Fundamentals and Applications in Telecommunications and Sensing*. Artech House, 1999.

[20] L.H.Malitson. "Interspecimen Comparison of the Refractive Index of Fused Silica". *Journal of the Optical Society of America*, 55(10), 1965.

[21] P.G.Debenedetti. "Supercooled and glassy water". *J. Phys.:Condensed Matter*, 15:R1669–R1726, 2003.

[22] B.J. Mason. "The Supercooling and Nucleation of Water". *Advances in Physics*, 7:221–234, 1958.

[23] C.A.Angell (Editor C.Franks). *Water - a Comprehensive Treatise*, volume 7 Water and Aqueous Solutions at Subzero Temperatures. Plenum Press, 1982.

[24] R.Jachowicz and J.Weremczuk. "Sub-cooled water detection in silicon dew point hygrometer". *Sensors and Actuators*, 85:75–83, 2000.

[25] J.Weremczuk, Z.Wawrzyniak, and R.S.Jachowicz. "A new method of super-cooled water recognition in dew point hygrometer by morphology-based image processing". *Sensors and Actuators A*, 111:240–244, 2004.

Chapter 10

Tunable Planar Gratings

10.1 Introduction

The work of this chapter is in many ways a logical extension of the previous chapter. Whereas the refractometer devices presented previously use Bragg gratings to monitor the behaviour of analytes on their surface the situation is reversed here. Instead, the properties of an overlayer placed on the device are controlled with the specific intent of changing the Bragg response. Using this principle tunable filters have been fabricated which are controlled through an applied electric field.

Development of tunable filters is desirable for a variety of reasons. The ability to dynamically alter the centre wavelength of a filter response allows the effects of external influences such as temperature fluctuation to be compensated for. With sufficiently large tunability 'colourless' components may be designed. Such devices can be designed to a very general specification but then tuned for optimal performance at an application specific wavelength. Such devices are attractive in telecommunications wavelength division multiplexing systems as it reduces the component count of the total system. It also provides the opportunity to dynamically reconfigure a particular optical path to operate at a new wavelength.

The tunable filters designed and fabricated in this chapter used a liquid crystal overlayer. The particular liquid crystal (LC) used, Merck 18523, was the same as that

described in the previous chapter when monitoring the phase transition. This LC was chosen due its refractive index compatibility with silica. It is the electrically controlled birefringence of the LC that is exploited here for the purposes of filter tunability.

To introduce the device principles some elementary background to the field of liquid crystals is provided, with particular attention being paid to the class of nematic liquid crystals. Specific device design details are then discussed along with prior work of a related nature. The work presented in this chapter represents the first realisation of an electrically tuned planar Bragg grating using liquid crystals and so discussion of the results of previous related components highlights some of the difficulties associated with the realisation of such a device.

The initial results that are presented show that a Bragg grating operating at 1560nm with an electrically tunable range of 35GHz has been fabricated. This early result demonstrates the potential of the technique and developments to improve the tunable response are discussed along with some possible extensions of this approach.

Planar silica Bragg gratings using liquid crystals to tune their response have never before been demonstrated experimentally and so the results of this chapter represent the first realisation of a device of this kind. It is the author's belief that this claim also applies to the field of fibre Bragg gratings. Indeed, published work on such devices is restricted to modelling or to developments where the Bragg grating is defined within the liquid crystal itself, not in a fibre or waveguide core (e.g. [1]). A brief description of related prior work is given in order to provide an overview of some of the applications made available through the use of liquid crystals in integrated optics.

10.2 Introduction to Liquid Crystals

As the name suggests, liquid crystals share some characteristics with both liquids and crystals. Like liquids they are fluid but unlike liquids they display a level of order somewhat reminiscent of crystal structure. This description is perhaps a little

oversimplistic but provides a general introduction to liquid crystal properties. Liquid crystal molecules are not bound into a lattice as in a typical crystal but may move and reorient relative to other molecules. It is found however that different levels of order are displayed which may be used as means of categorising different groups of liquid crystals. Here, it is only the class of nematic liquid crystals that will be discussed as that is the group to which the liquid crystal of interest belongs. A thorough examination of their properties is not appropriate given the main subject of this thesis and so a very general overview and presentation of key results is provided.

Nematic liquid crystals, introduced in chapter 9, display orientational order in their molecules but no positional order. On average the molecules, typically long chains up to a few nanometres in length, will orient in a preferred direction referred to as the director. In contrast, an isotropic liquid will have randomly oriented molecules and on average no preferred direction. The molecules in a nematic liquid crystal will however be positioned randomly. Other classes of liquid crystal exist where, for example, positional order is displayed and the molecules have a tendency to be positioned in layers.

10.2.1 Director Alignment

For the purposes of this discussion, liquid crystal molecules will be viewed and displayed as rod-like structures. Typically liquid crystals display a level of anisotropy, notably in their dielectric constant and refractive index. For the case of a positive dielectric anisotropy an applied field polarises the molecules along their long axis and consequently the molecules tend to reorient so that their long axis is parallel to the electric field (figure 10.1).

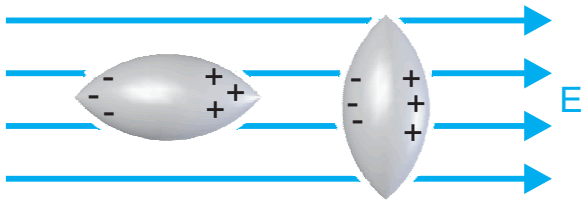

Figure 10.1: Positive (*left*) and negative (*right*) dielectric anisotropy.

The opposite is true of molecules with a negative dielectric anisotropy and they will tend to align with their long axis perpendicular to the electric field.

Similarly, the birefringence of a liquid crystal may be controlled with an applied electric field. Due to the anisotropy of the molecules and the level of orientational order the refractive index has a directional dependence. As the molecules, and therefore the director, reorient due to an applied field the refractive index viewed from a fixed direction will change. It is found that the torque on a molecule depends on the square of the electric field and consequently the reorientation remains the same if the electric field direction is reversed. This fact is fundamental to the operation of many liquid crystal devices. Constant ('dc') fields can cause charge movement in the liquid crystal and degrade the response to electric field. Thus many common liquid crystal devices, including those presented in this chapter, use alternating electric fields. Typical values for Δn, the difference between the ordinary and extraordinary refractive indices, are in the range 0.05 to 0.25 for a nematic liquid crystal.

Director alignment is also affected by the surfaces that it is in contact with. The interface between the liquid crystal and its container can have a very strong influence on the director orientation at the surface and also in the bulk of the fluid. This is often exploited by treating the surface to encourage preferential alignment in a chosen direction. Mechanical rubbing, chemical treatment and UV exposure are all known to assist in providing a preferred direction at the surface. The two extreme cases of alignment are shown in figure 10.2 where the long chain molecules are shown to lie in the plane of the surface (homogeneous) or perpendicular to the surface (homeotropic).

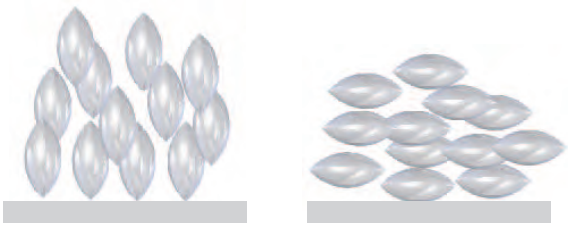

Figure 10.2: Homeotropic (*left*) and homogeneous (*left*) director alignment.

Associated with this surface orientation is an anchoring force which must be over-

come in order to change the director at the surface. Molecules oriented by the surface will cause preferential alignment of the molecules above them and they in turn will affect the molecules above them. However, the further a molecule is from the surface the weaker the orientational effect will be. Consider a cell made up of a nematic liquid crystal sandwiched between two surfaces with identical surface alignment treatments. A thick liquid crystal cell may require only a weak electric field to reorient the director in the centre of the cell where the surface influence is low. A thinner cell may exhibit higher director uniformity, as the central molecules are more strongly influenced by surface effects and so higher applied fields may be required to cause significant reorientation.

10.2.2 Deformations

The deformations of a liquid crystal due to an applied field and commonly referred to as splay, twist and bend each of which is shown schematically in figure 10.3.

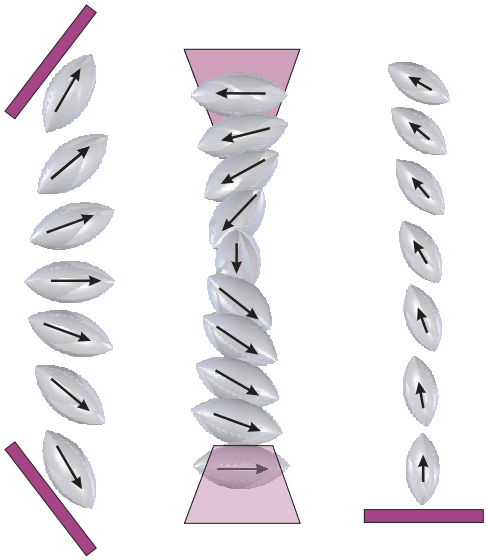

Figure 10.3: Representation of the splay, twist and bend deformations (*left to right respectively*). Each 'bead' represents the director orientation.

Each of these deformations may be assigned an elastic constant which is a measure of resistance to that particular deformation. It is informative to provide more detail on a liquid crystal cell like that described earlier. The nematic liquid crystal is sandwiched

between two electrodes so that a voltage may be applied as shown in figure 10.4.

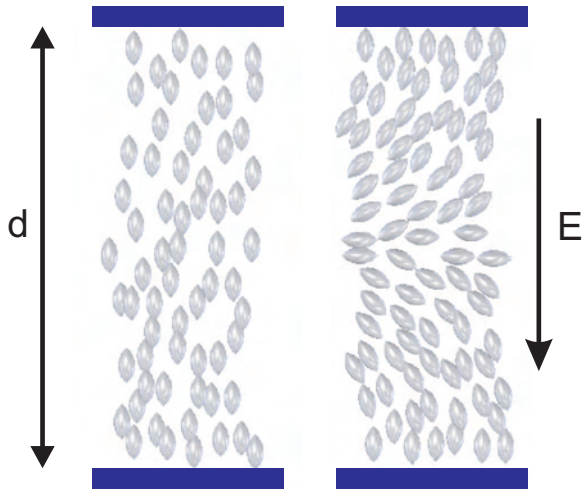

Figure 10.4: Liquid crystal cell with deformation of director due to applied field. Surface effect limit the director realignment at the electrodes.

In this case the surface induced alignment is shown to be homeotropic and the liquid crystal has a negative dielectric anisotropy such that it rotates towards the plane of the electrodes when electric field is applied. It may be shown both experimentally and theoretically [2] that there is a threshold voltage that must be applied before any deformation takes place. This is true for each of the splay, twist and bend geometries. The threshold field is given by

$$E_{threshold} = \frac{\pi}{d}\sqrt{\frac{K}{\epsilon_0 \Delta\chi_e}} \tag{10.1}$$

where K is the elastic constant for the particular deformation in question, d is the thickness of the cell, $\Delta\chi_e$ is the anisotropy of the electric susceptibility and ϵ_0 is the permittivity of free space. Further analysis shows that the variation in angle of the director, θ, half way between the two electrodes varies as shown in figure 10.5 [2]. The threshold is clearly seen and it is unsurprising that with increasing voltage the director rotates towards the maximum rotation of 90° . The transition between the undistorted and distorted director states is known as the Fréedericksz transition. It is this rotation of the director angle that is of interest in this chapter.

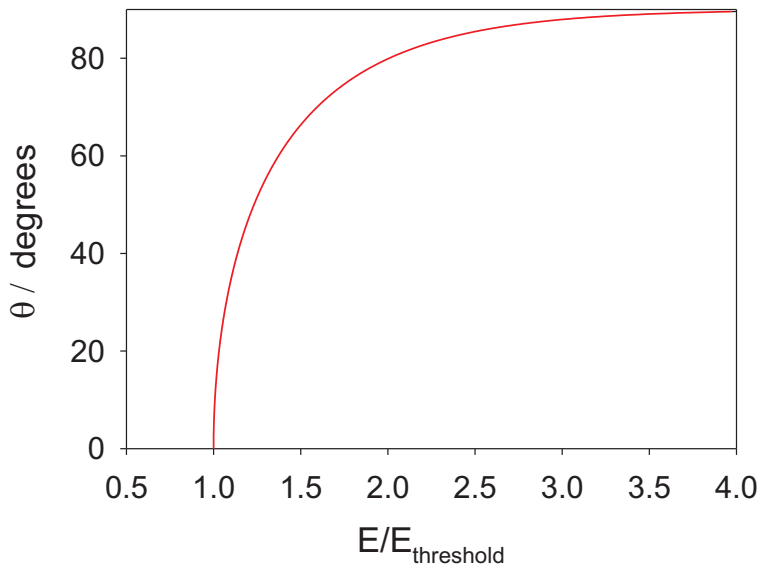

Figure 10.5: Variation of mid-point angle with applied electric field

10.3 Liquid Crystal Based Devices

Liquid crystals are often attractive to device designers as the ability to control their properties allows a variety of functions to be realised. Variable couplers [3], optical switches [4] and tunable long period fibre gratings [5] have all been demonstrated by combining liquid crystals with waveguiding structures. It is interesting and perhaps surprising to note that published work on combinations of fibre or waveguide Bragg gratings with liquid crystals is very limited. In the introduction to this chapter it was mentioned that the results of presented here provide the first experimental realisation of a tunable planar Bragg grating using liquid crystal.

10.3.1 Device Principles and Prior Work

Chapter 9 demonstrated the use of overlayers replacing waveguide overcladding to modify the modal effective index. The same basic design principles are used here but with the addition of electrodes to the device.

Liquid crystal overlayers on planar waveguide gratings have previously been suggested by Sirleto et.al. [6] where a surface relief grating capped with a smectic liquid

crystal sandwiched between electrodes was proposed and modelled (figure 10.6). These proposals have not however been demonstrated practically.

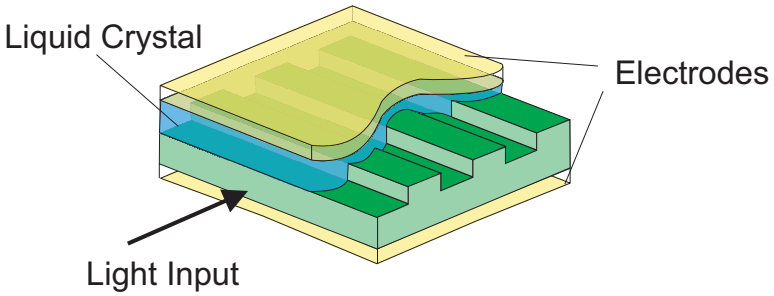

Figure 10.6: Schematic of the tunable filter design proposed by Sirleto et. al. Upper electrode and liquid crystal is shown cut away to reveal the relief grating.

Two key features of the design are worth noting. Firstly, as the liquid crystal penetrates the relief structure it is essentially forming grating planes. Thus the index perturbation, and therefore bandwidth, may be controlled by the liquid crystal refractive index. Secondly, the liquid crystal is in contact with planes in two directions as well as the sharp edges at which the planes coincide. This may ultimately restrict the dimensions, and therefore operating wavelengths of the devices due to surface/edge alignment and anchoring effects which limit director reorientation by an applied field.

The device design that was proposed for this work is shown in figure 10.7. Directly above the Bragg grating the overclad layer is removed and replaced with liquid crystal. The similarities with the devices of the previous chapter are clear but the addition of electrodes allow an electric field to be applied.

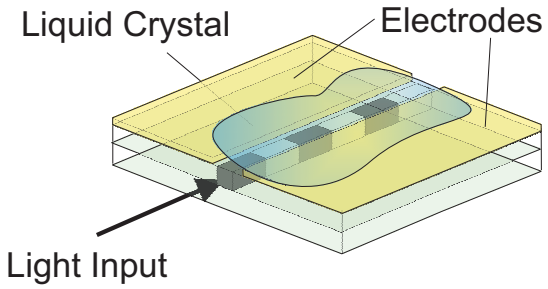

Figure 10.7: The tunable filter design developed for and presented in this chapter.

The features of the design are that the Bragg grating is entirely contained within the

waveguide core and the liquid crystal acts only as the waveguide cladding. Consequently the liquid crystal is in contact with just one surface which is flat, smooth and uniform. This reduces the limitations that may be imposed by relief structures. In contrast to the design of figure 10.6, the electrodes are in the plane of the substrate. The reason for selection of this configuration of electrodes was primarily based on the simplicity and robustness of construction.

Using a nematic liquid crystal two configurations of the device are possible. These are shown schematically in figure 10.8 and will be subsequently referred to as the homeotropic and homogeneous designs, as labelled in the diagrams. For both configurations a simplifying assumption is made that the electric field is uniform between the two electrodes as if they were parallel plates. The homeotropic configu-

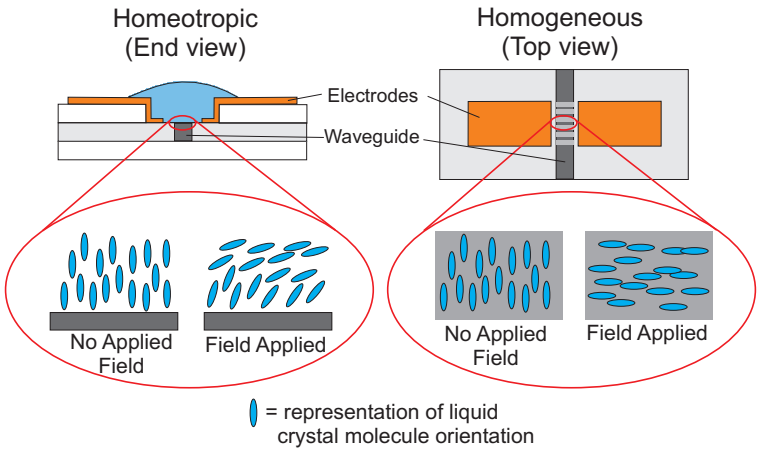

Figure 10.8: Two possible configurations of the planar tunable filter. The difference is in the director alignment with no applied electric field.

ration is designed so that in the absence of an applied electric field the director is perpendicular to the plane of the substrate. Application of the electric field tends to reorient the director towards the substrate plane. In the homogeneous configuration the director always lies flat to the substrate surface but is made to rotate by 90° upon application of the electric field.

Operation of both designs is critically dependent on uniformity of the director orientation across the Bragg grating. For maximum tunability, the director reorientation should be as close to 90° as possible over the full grating length. This requires both a

uniform surface profile and a uniform electric field. Localised structure or contamination of the silica surface will result in unpredictable director orientation, increased Bragg bandwidth and reduced tuning range.

10.3.2 Expected Performance

In section 10.2 the fundamental deformations of liquid crystals in cells were introduced. The cell configuration used in these examples had the liquid crystal sandwiched between electrodes above and below it. The designs of the tunable grating described above have both electrodes in the same plane which is the plane of the silica substrate. The same principles of deformation and a threshold field still apply to this configuration. As an aside, both of these electrode structures are used in liquid display applications with the common electrode plane arrangement used here referred to as the in-plane switching (IPS) design [7,8].

In the case of the homeotropic configuration described above the director will be subject to the bend deformation and in the homogeneous configuration, the twist deformation.

From the previous chapter it is known that thermal tuning of a device such as that described here will provide at least 1.8nm of tunability. This represents the overclad refractive index change when the liquid crystal changes from an unknown level of order and director orientation to the disordered isotropic liquid. It is reasonable to assume that a tunability of a similar order is available electrically where, in the ideal case, the director will reorient by 90° , providing the maximum possible refractive index change. However, inserting the liquid crystal's estimated extraordinary and ordinary refractive indices at 1550nm (1.489 and 1.444, [9]) into the waveguide model (chapter 9) based on the Marcatili method presents a problem. The extraordinary refractive index is greater than the waveguide core refractive index. Thus if complete director orientation is achieved mode confinement may be lost and the device will no longer function as intended. In the ideal case, this problem may be avoided by carefully choosing the control voltage to ensure that the guidance condition is not lost and that the effective overclad refractive index is always lower than the waveg-

uide core. Practically, the extremes of the refractive index range may not be reached due to surface anchoring effects and director non-uniformities so the problem will be alleviated.

Using the assumption that the range of effective overclad indices possible range from 1.444 (n_o) up to the waveguide core index (1.4613) the maximum possible tunability will be approximately 4.4nm.

It can be expected therefore that the response of the device to electric field will demonstrate a threshold effect and a change in centre wavelength that increases in magnitude as the applied voltage gets larger up until a point at which maximum director reorientation is achieved. The threshold is unlikely to be a sharp transition as suggested by figure 10.5 as it is not just the director in the centre of the liquid crystal layer that are of interest. In fact, the response will be dominated by the molecules closest to the waveguide surface. Thus the threshold can be expected to be somewhat more rounded and the overall wavelength-voltage curve will be a characteristic 'S' shape or its mirror image.

A more quantitative description of expected behaviour is not feasible at present. This would require modelling of the director orientation over a range of distances away from the silica surface and the corresponding impact on waveguide effective index. Such study falls beyond the scope of the present work and remains an opportunity for further work.

10.4 Fabrication

Two devices were investigated during the development of the tunable filter. The first was produced from a commercial three layer wafer fabricated by FHD. The UV writing and overclad etch was performed by Greg Emmerson. The second was fabricated using the PECVD process detailed in chapter 6. The majority of results were obtained from the FHD sample and so subsequent discussion is based around this sample. Section 10.5.4 specifically details work relating to the PECVD device development.

The sample used for the FHD device had a Bragg grating length of 2mm and was the same device that was used for the liquid crystal work of chapter 9. The overclad, approximately 20μm in thickness, was removed above the Bragg grating using a hydrofluoric acid etch in several steps to obtain the correct etch depth. It is considered likely, but not confirmed experimentally, that a slight level of over-etch occurred resulting in the possibility that the waveguide had microscopic relief structure due to the grating planes as shown in [10]. Surface structure of this nature may cause the liquid crystal to have preferential alignment parallel to these grating planes causing an increase in the anchoring and a reduction in tuning range. For this reason, the homeotropic configuration was chosen as it was hoped that this zero-field arrangement would be less susceptible to the possible effects of grating plane corrugation.

10.4.1 Electrode Design

Initially, electrode definition was attempted using conductive paint or conductive adhesive tape. Both methods were rejected, the former as it was found to contaminate the liquid crystal with conductive particles, the latter as reliable positioning and adhesion was not possible. It was therefore decided that deposition of metallic electrodes via evaporation would provide a far more accurate and reliable means of electrical contact. At this early stage it was decided not to use photolithography to produce a mask for electrode definition. A more crude but cheaper and quicker method was chosen instead. Using an optical microscope, adhesive tape was carefully placed either side of the waveguide by hand. The thin (tenths of a mm) exposed strip above the waveguide was then covered using photoresist. Removal of the adhesive tape therefore left the majority of the substrate exposed with the exception of the area directly above the waveguide. A metallic layer could then be evaporated onto the surface and the photoresist cleaned away to leave two electrodes that were electrically isolated.

Gold was the first choice for electrode material and was deposited onto a chromium underlayer to provide improved adhesion to the silica. Gold was selected to provide the opportunity to make electrical connections using wires soldered directly to the

sample. Practically this selection proved to be unsuitable, the coating was found to be too easily damaged for the reliable connection of solder joints, possibly due to residue from the adhesive tape used in the masking process. More significantly it was found that over time and with the necessary surface cleaning steps, small gold particles detached from the electrodes and became suspended in the liquid crystal. Consequently the liquid crystal became slightly conductive and on applying an electric field was found to increase in temperature causing erratic results. Therefore the chromium/gold electrodes were replaced with aluminium, deposited by the same method. The deposited layers were estimated to be approximately 100nm in thickness.

Electrical connection to the electrodes was found to be most reliably achieved using probes in physical contact with the deposited electrodes. The probes, mounted in a specially designed clamp, each contained a spring to push the tip firmly onto the sample as shown in figure 10.9. Wires could be soldered to the probes to provide a robust electrical contact. The arrangement allowed the probe mount to be firmly clamped to the sample mount whilst allowing the sample and input fibre to be observed from above.

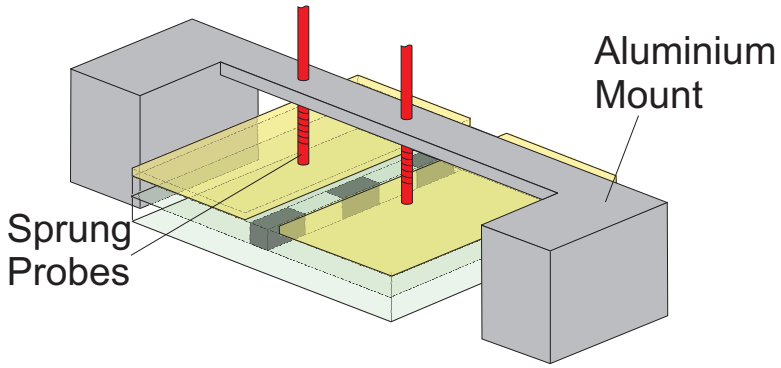

Figure 10.9: Spring loaded probes for electrical contact with device electrodes.

10.4.2 Liquid Crystal Alignment

The two design configurations, homeotropic and homogeneous, described earlier were approached in different ways. Homogeneous alignment can be assisted using

a rubbed polyimide layer which encourages the director to align parallel to the rubbing direction. However, these layers are relatively thick (∼100nm) and if placed on the etched silica surface could cause a reduction in the device sensitivity to refractive index changes. Consequently polyimide layers must be applied to separate layers (*e.g.* glass slides) and positioned on the device from above. The use of coated cover layers such as this have the advantage that they help isolate the liquid crystal from external influences such as contamination or air currents. Performance of the whole device will however be affected by the thickness of the liquid crystal. As the liquid crystal becomes thicker, the effect of any alignment due to the polyimide at the upper surface becomes less at the silica surface. Additionally, as the silica itself remains untreated it is likely that the critical director orientation close to the silica will be dominated by unknown and unpredictable surface effects. This method of liquid crystal alignment was therefore rejected at an early stage

Homeotropic alignment of the liquid crystal in the absence of electric field may be achieved in a slightly different manner. Again surface treatment is required to induce the desired alignment but in this case the surfactant used forms a layer of a few nanometres or less so may be applied directly to the etched silica with minimal degradation of sensitivity to refractive index changes. The surfactant used was a 0.2% solution of Merck Liquicoat PA ZLI-3334 in ethanol, provided by A.Dyadyusha. A droplet of surfactant was applied and allowed to freely run over the surface and air dry at room temperature for 2 hours. The sample was then baked for half an hour at 180℃ . At the time it was not possible to establish the success of this surface treatment but more recent studies by A.Dyadyusha have confirmed and begun to investigate the effects, this is briefly mentioned in chapter 11. There are two advantages to the homoetropic configuration. Firstly, the surfactant is applied at the silica surface and therefore helps to provide good uniformity over the surface where director alignment is most critical. Secondly, the anchoring of the homeotropic alignment is generally weaker than that of the homogenous alignment. This may allow lower threshold and operating voltages for the finished device.

The homeotropic configuration is likely to benefit from the addition of a surfactant treated cover layer. This has the advantages described earlier of helping to isolate the

liquid crystal layer from external influences but more significantly provides alignment at the top of the liquid crystal layer. Thus director uniformity will be improved throughout the volume of the liquid crystal.

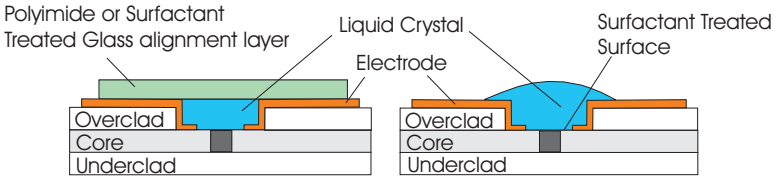

Figure 10.10: Schematic diagrams of tunable device with and without surface treated cover layers for enhanced director alignment.

10.4.3 Electrical Control

To apply a potential across the electrodes a signal generator was used. The output of the generator was limited to 10 volts so a high voltage amplifier was used to provide higher electric fields. Using an oscilloscope the symmetry of the alternating signal was monitored and the RMS voltage was measured using a digital voltmeter. All of the results presented here were obtained with the signal generator producing a symmetrical square wave at 250Hz. This has not been determined as the optimal frequency but qualitative observations of the performance indicated it to be suitable. Given the sensitivity of this prototype device to other factors, in particular liquid crystal alignment, the frequency was kept constant for the majority of experimental work to avoid the addition of other another variable affecting performance.

All optical measurements were taken using an optical spectrum analyser to record reflection spectra as described in chapter 7.

10.5 Obtaining a Tunable Response

To achieve tunable operation great care was needed in constructing and using the experimental setup. The sensitivity of the liquid crystal to its surroundings also re-

quired that precautions be taken in its application and in the preparation of the device surface. Physical contact with the silica surface was avoided where possible to avoid the possibility of reducing the effects of the surfactant treatment. It was however found that in laboratory conditions contamination and degradation occurred, in particular due to mixing of the liquid crystal with refractive index matching oil from the input fibre. Thus regular cleaning and re-application of the liquid crystal was required. Gentle cleaning was performed using cotton buds and isopropanol. To retain some process consistency cotton buds were always moved parallel to the waveguide direction. Application of the liquid crystal was achieved using the tip of a clean optical fibre to apply small drops to the surface. The minimum volume of liquid crystal required to cover the Bragg grating was used to reduce problems associated with it moving over the substrate and potentially coming into contact with refractive index matching fluid. Qualitative observations showed that during the first few hours after application any results obtained were erratic and not repeatable. This is likely to be due to the liquid crystal "settling" and disclinations or defects due to the application process relaxing to a more uniform layer.

Two simple tests were possible to check for basic device performance. When illuminating the sample from above with polarised white light and viewing it (also from above) through a polariser, reflections from the metallic electrodes on the sample were observed to vary as the applied electric field was changed. This did not indicate that the device would act as a tunable filter but was a useful indication that the electric field was present and also highlighted if any large areas were not affected by the field. A second check was performed once the device was fibre coupled. To align the fibre to the waveguide/grating the transmitted output of the waveguide was observed using an infra red camera. Once aligned, the image on the screen remained constant with the waveguide output standing out from the associated 'planar stripe'. On applying the electric field a rippling or shimmering effect was observed in the IR camera image. Overall the waveguide output remained stationary but the brightness and size varied over time and space. This was a very easy test that the liquid crystal director was rotating but provided no information on uniformity or on the magnitude or reorientation. Typically the shimmering effect could be observed for

a duration of a few tenths of a second up to one second indicating that expected response times for the tunable device will be of the same order.

Devices of this type will be inherently birefringent due to the asymmetry resulting from the etched overcladding. The effects of polarisation on performance have, to date, not been extensively characterised. Initial studies indicated that the waveguide output polarisation was not rotated relative to the input polarisation. It was however observed that optimal Bragg response (*i.e.* the largest magnitude reflection peak) occurred at different polarisations for different applied voltages. It is therefore thought that the waveguide loss varies with the liquid crystal alignment, possibly indicating that the waveguide core refractive index is very close to that of the extraordinary index of the liquid crystal and that the guidance condition is lost for some alignment states.

Optimal configuration of polarisation was found to vary somewhat with each iteration of the test cycle. In the absence of a truly repeatable device construction process, polarisation was optimised to provide a reflection peak that was approximately constant over the range of voltages to be used. This method was far from ideal and would be unsatisfactory for full device development. It did however provide a means of testing samples that were particularly sensitive to a wide range of factors and allowed a reflection peak that varied little in shape over applied voltage, a necessary characteristic for a device of this type.

10.5.1 Design Iterations

As already stated, early tests exhibited heating effects due to contamination of the liquid crystal causing electrical current to flow. Both positive and negative wavelength changes were displayed by the device in this state and the sign of the change is believed to be dependent on the initial liquid crystal director distribution across the grating. Upon discovery of the heating effect these results were disregarded as they were neither repeatable or representative of the device performance under electric field. All subsequent tests used a thermocouple mounted in contact with the device to ensure that no heating occurred.

A range of trials were carried out using surfactant treated cover layers (figure 10.10) to constrain the liquid crystal's upper surface and attempt to gain more uniform director alignment. It was found particularly challenging to position the overlayer in a stable position such that there were no voids in the liquid crystal below. A large part of this problem was due to the device dimensions (10×13mm) and resultant difficulty in handling the small pieces of silica used as overlayers. With the inter-probe distance being just a few millimetres the small silica overlayers had a tendency to slide over the device surface, lubricated by the liquid crystal. Whilst this route is expected to ultimately provide the most reliable, repeatable and tuneable filter, no success was achieved using overlayers in this study. Subsequent design iterations (section 10.5.4) have been fabricated with larger dimensions to overcome the issues of overlayer positioning. Figure 10.11 shows the device configuration used with dimensions for the inter-electrode distance and approximate liquid crystal depth shown. All results using the FHD fabricated sample therefore used no upper layer

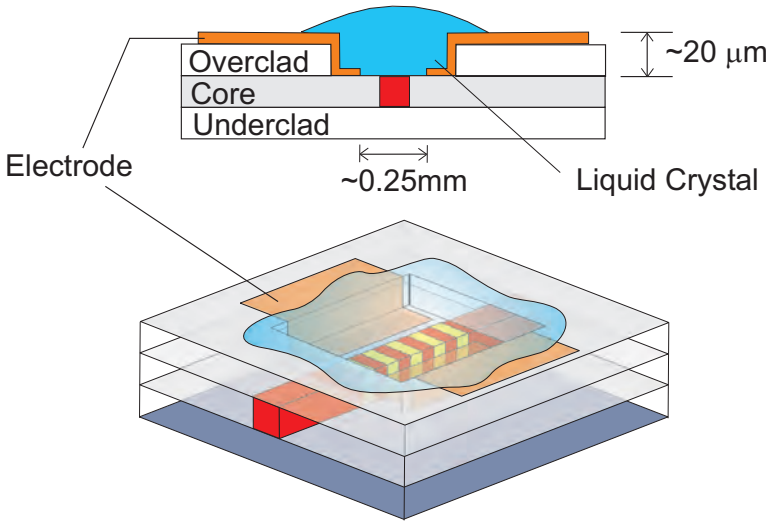

Figure 10.11: Schematic diagram of the tunable planar grating.

to constrain the liquid crystal. The resultant effects on the upper surface of the liquid crystal pool are unknown but at this early stage are neglected. It was assumed that the liquid crystal layer was sufficiently thick in this arrangement that alignment in the close vicinity to the silica surface was well isolated from effects at the upper surface of the liquid crystal.

10.5.2 Results

Once electrode design had been engineered to provide reliable performance without liquid crystal contamination, repeatable trends in behaviour could be observed.

As with the liquid crystal work of the previous chapter it was found that a certain amount of additional structure, attributed to the effects of the etched window, was superimposed onto the expected grating response. An identical moving-average approach was used to smooth the data for determination of centre wavelengths. A comparison of the device refection spectrum with and without liquid crystal on the etched window is shown in figure 10.12.

It is interesting to note that there is not a significant change in bandwidth when the liquid crystal is added to the device. This suggests that either the liquid crystal alignment has a relatively high level of uniformity on the silica surface or that the effects of surface structure due to the etch process are dominant over variations in waveguide effective index due to director non-uniformity.

A second feature to be noted from figure 10.12 is the relative sizes of the two peaks obtained when the liquid crystal was applied to the device. It was mentioned earlier that qualitative observations indicated a "settling" time which was required before predictable and repeatable results could be obtained. The reduction of peak size after several hours is believed to be related to this stabilisation period. The actual processes that occur are not well characterised but it is likely that the effects are due to variation in alignment both at the Bragg grating surface and throughout the whole liquid crystal layer.

After the initial settling time, characteristic behaviour could be observed. Figure 10.13 shows one such behaviour. The graph shows the effect on centre wavelength of cycling the applied voltage. At approximately 15V a decrease in centre wavelength is observed with increasing voltage. However, in the region of 30-40V the direction of this trend reverses. After reaching the maximum applied voltage and lowering it back towards zero the total tuning range can be seen to be reduced. Another cycle of the voltage causes another reduction in total tuning range. At low voltages however,

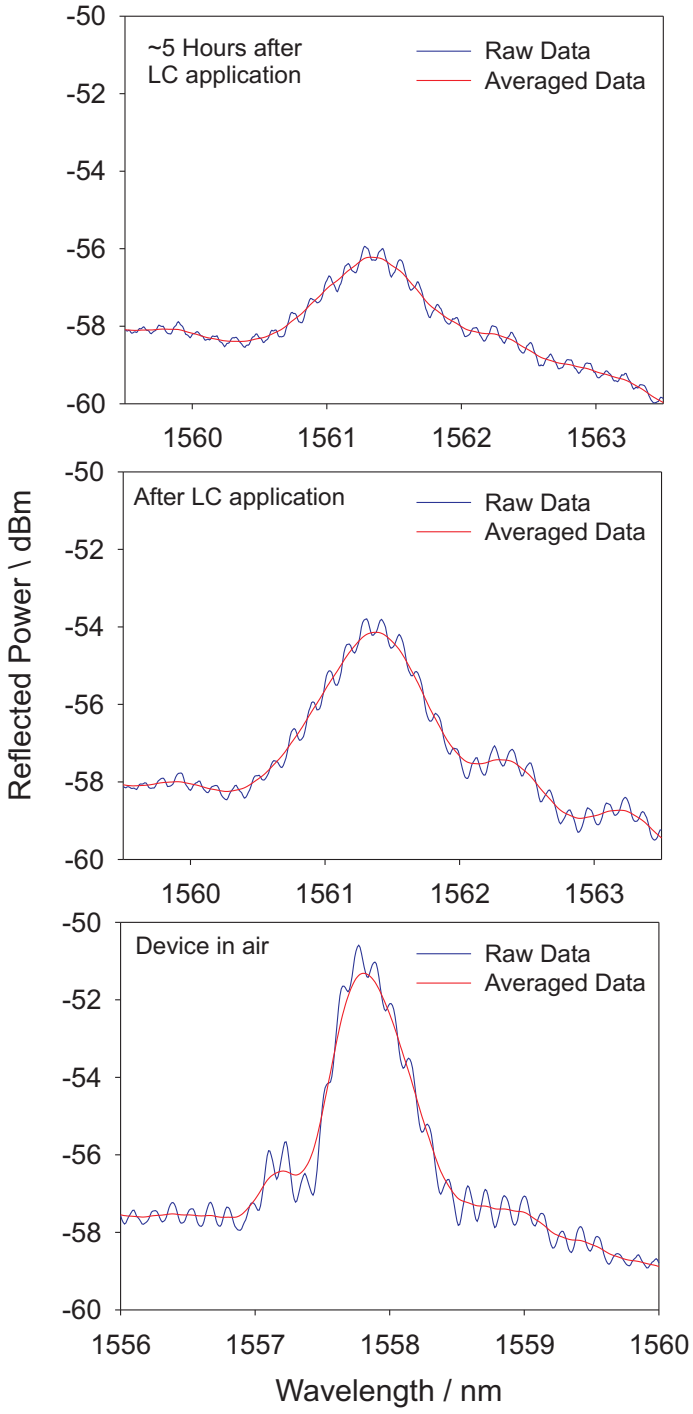

Figure 10.12: Bragg reflection spectra for device in air without liquid crystal (*bottom*) and with liquid crystal (*Middle: Shortly after LC application. Top: Approximately 5 hours after application.*)

the wavelength-voltage (λ-V) characteristic remains repeatable It is postulated that

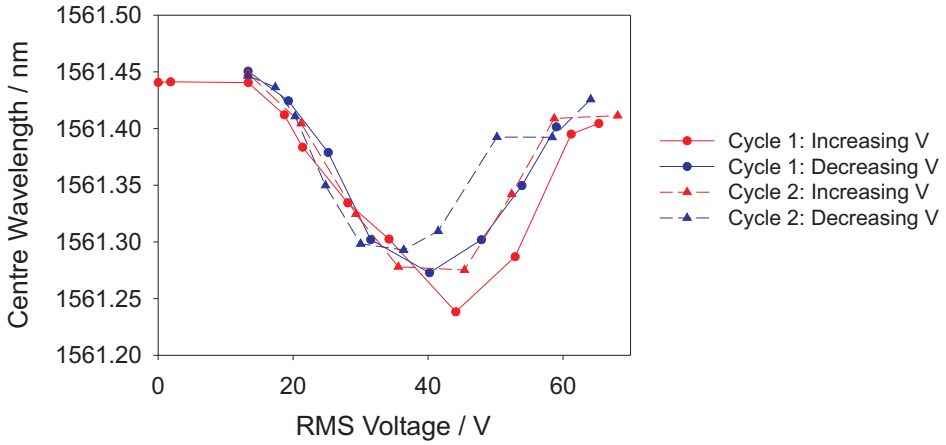

Figure 10.13: Variation in tuning range after with cycling voltage.

at approximately 40 volts currents (fluid, not electrical) are induced in the liquid crystal causing disruption to the director alignment and reducing the tuning range. This would explain why, upon increasing the applied voltage the λ-V curve retraces its steps from the previous reduction in voltage. After exceeding the 40V threshold further disruption is caused and the tuning range drops accordingly.

At the current stage of development this explanation is somewhat speculative but the existence of a threshold at approximately 40V is not in doubt and was repeatedly observed. Electrohydrodynamic convection effects are known to occur in liquid crystal cells [2] but without further study this cannot be confirmed as the effect occurring here.

It was when attempting to avoid this threshold effect that the widest tuning range achieved to date was recorded. Selecting a maximum applied voltage of 40V was intended to prevent the possible convection regime from being reached. The results are plotted in figure 10.14 The graph shows a characteristic S-shaped curve demonstrating the threshold of director reorientation (at approximately 15 volts) and a maximum average reorientation at a little over 30V. The data suggests that in fact a maximum applied voltage of 35V should have been used here as the gradient of the λ-V curve changes direction at this point despite the still increasing voltage.

Figure 10.15 shows reflection spectra from the device at different applied voltages.

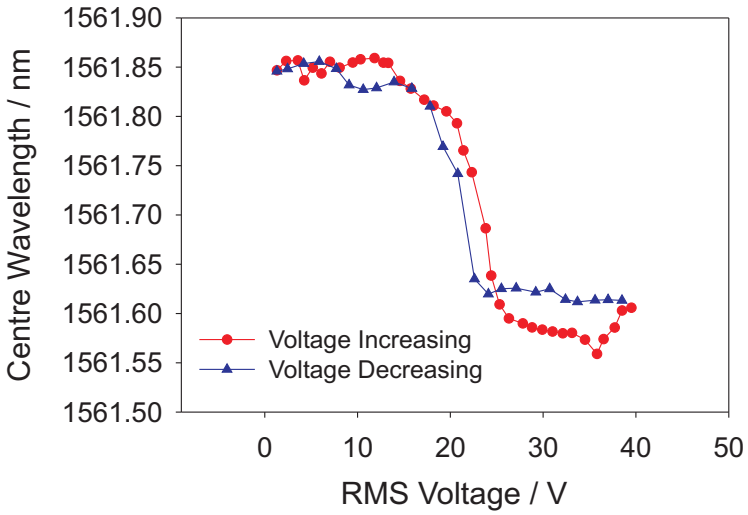

Figure 10.14: Device tuning curve demonstrating approximately 0.29nm range (∼35GHz).

The data is plotted after application of the smoothing moving average process. The shape of the reflection spectra is approximately constant over the three voltages shown but all peaks are only approximately 1dB in magnitude. It may be noted that the moving average has not in this case entirely removed the additional structure believed to result from reflections at the interfaces of the etched window. Additional averaging was not applied as the spectra is constant in shape and the repeatable nature of the data in figure 10.14 indicates a reliable determination of centre wavelength.

10.5.3 Discussion of Results

10.5.3.1 Electric Field

Typical electric field strengths used for nematic liquid liquid crystal displays are of the order of 1×10^6 Vm^{-1}. Assuming that the electrodes here are acting as parallel plates in the region of most interest, the field here is approximately 1.6×10^5 . Thus the fields used here are perhaps a little lower than may be expected. It is possible that this is due to the lack of additional covering layer on the upper surface of the

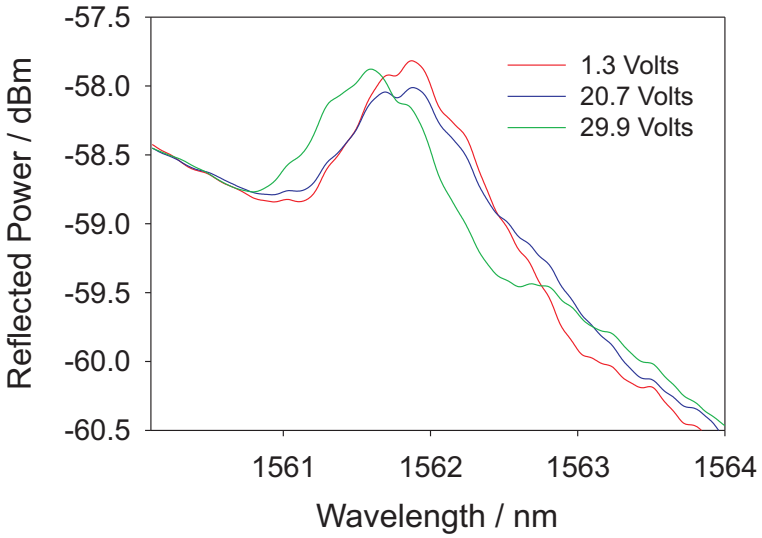

Figure 10.15: Averaged reflection spectra recorded at three applied voltages.

liquid crystal. This will mean that surface alignment effects at the air-liquid crystal boundary are weak and have little influence over the response to applied voltage in the rest of the liquid crystal volume.

10.5.3.2 Repeatability

Although the lack of cover layer may be responsible for a low 'saturation' voltage it is thought that run to run repeatability would be significantly enhanced by the addition of such a cover. Comparison of figures 10.13 and 10.14 reveals that the zero-field centre wavelengths are different by 0.4nm. This variation is larger than the tuning range achieved and is therefore unacceptable for the majority of applications of a device of this type. The source of the difference is believed to be variation of the surface alignment as a result of day to day effects such as repeated cleaning or variations in ambient temperature or humidity.

Future design iterations will require not just an overlayer to provide protection and enhanced alignment uniformity but also a well characterised silica surface preparation process to avoid these variations.

10.5.3.3 Limitations

When comparing the electrically induced tuning range of 0.29nm with the thermal equivalent of the previous chapter (1.9nm) it is obvious that the full potential of the electrical device is not being realised. The following factors are considered to be responsible for the relatively low tuning range observed here.

- Profile of the silica surface
- Possible over-etch of the overcladding
- Thickness of the liquid crystal layer
- Uniformity of director alignment

Ultimately these all determine the liquid crystal anchoring and the director uniformity. Visually, the etched surface of the device is not shiny, indicating surface roughness. Similarly, the possibility of over-etch could mean that surface relief due to preferential etching of the grating planes has occurred. Both will tend to influence the zero-field orientation and the direction of reorientation when a field is applied. Initial work to improve these characteristics is presented in the next section.

All of the results presented above correspond to a liquid crystal layer at least as thick as the standard overclad of the FHD sample ($\sim$20μm). Reduction of the liquid crystal layer thickness and addition of a surfactant treated cover slip will provide increased director uniformity. When a field is applied the director will reorient but maintain uniformity across the grating. Thus counteracting effects from different regions of the liquid crystal can be avoided and tunability maximised.

10.5.4 PECVD Device

Having identified means to improve the tunable response of the liquid crystal covered grating a new device was fabricated. Three layer structures fabricated using the PECVD process developed in chapter 6 were chosen primarily because of their relatively thin upper cladding layer ($\sim$6μm). This has two key benefits. Firstly the more controlled process of reactive ion etching (RIE) can be used for overclad removal without requiring excessively long process times. Secondly, the non-etched over-

clad provides a conveniently dimensioned spacer upon which a surfactant treated overlayer could be positioned and held.

The sample used for the PECVD based work had a total length of 18mm and the UV defined grating was 5mm in length and written at a fluence of 25kJcm^{-2} . A core layer of 5.5μm in thickness was used.

Reactive ion etching of the PECVD samples used here was performed by D.Sager. Etch rates were determined by measuring surface profiles after a timed etch and found to be approximately 0.6μm per 30 minutes etch of the overcladding layer (using 100W and CF_4 gas). To avoid accidental over-etch, an initial etch time of 5 hours was used to attempt to remove 6μm of cladding layer, believed, after careful examination of overcladding deposition parameters, to have a total thickness of between 6.5μm and 7.0μm .

The improvement to the surface profile when using RIE instead of hydrofluoric acid is shown in figures 10.16 and 10.17 which show 2 dimensional surface scans and overhead photographs respectively. The PECVD surface shows approximately 150nm of variation in height after etching compared to a value, limited by measurement noise, of 80nm beforehand. The wet etched FHD surface shows variation approaching 800nm, at least an order of magnitude worse than the as-deposited PECVD. Thus it is expected that the improved surface profile will have less influence and allow more control over director orientation at the surface. It should be remembered that the lower etch depth of the PECVD sample (∼6μm compared to ∼20μm for the FHD layers) may help with the improved surface uniformity. Over the course of a deep etch, particularly one carried out in several steps, it is possible for surface structure to be exaggerated and produce lower quality results.

After etching, aluminium electrodes were evaporated onto the surface using the same masking technique described earlier for the FHD device.

To test the refractive sensing capability of the etched PECVD sample the Bragg wavelength with the device in air was compared with the wavelength when the device was covered by refractive index matching oil (1.450 at 589nm). Addition of the index match caused a measured shift in Bragg wavelength of 0.42nm, somewhat less

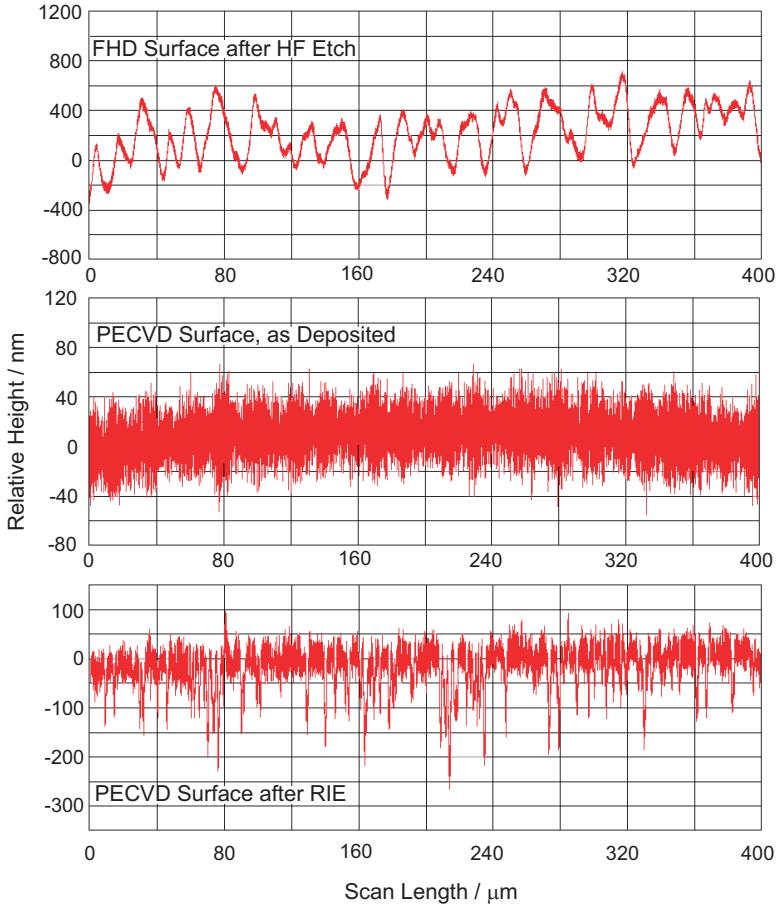

Figure 10.16: Comparison of surface profiles for wet etched FHD surface (*top*), as-deposited PECVD silica (*middle*) and reactive ion etched PECVD silica (*bottom*.

than the 1.20nm recorded for the same measurement on the FHD sample previously fabricated. On taking surface profile measurements it was revealed that the etched window was in fact approximately 5μm deep rather than the intended 6μm , explaining the lower sensitivity to index change at the etched surface.

Despite the reduced sensitivity, liquid crystal was placed into the etched window and electric field applied but no correlation between electric field and centre wavelength was found. The variations in centre wavelength measured were governed by temperature oscillations resulting from the cycling of the laboratory air conditioning.

To improve the tuning range of the device, a further etch process was used to reduce the cladding thickness by a further 1.5μm . Given the existing 5μm etch, should any over-etch occur it would be of a low magnitude and unlikely to damage the guidance

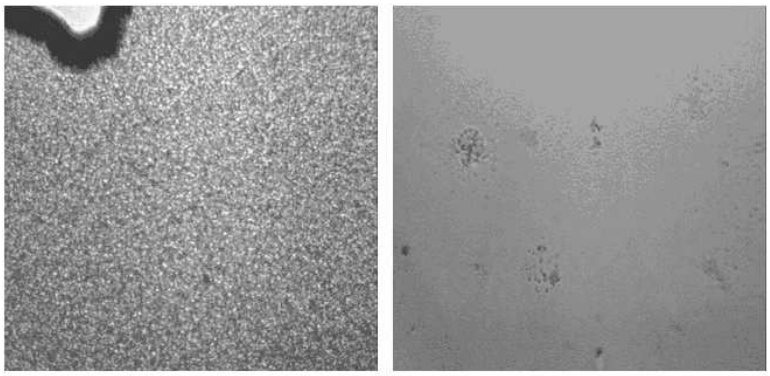

Figure 10.17: Visual comparison of surface profile of wet etched FHD (*left*) and reactive ion etched PECVD (*right*) silica.

properties of the waveguide enough to prevent device operation.

However, after etching and reapplying the liquid crystal it was found that the transmitted power, as viewed using an infra red camera, was very poor and only just sufficient to allow the waveguide to be distinguished from the "planar stripe" of the sample. No grating response could be resolved in the reflection spectra. The reason for the loss of waveguiding and Bragg response is most likely to be due to the relative refractive index of the waveguide core and the liquid crystal. The effective index of the waveguides written into the PECVD samples are known (chapter 7) to be around 5×10^{-3} lower than those in the FHD samples. It is therefore likely that the liquid crystal refractive index is higher than that of the PECVD waveguide core and that the guidance condition is lost. The test for guidance was performed with and without surfactant treatment of the layer to investigate whether guidance could be regained through different director orientations but no improvement was observed.

10.6 Summary

The development of an electrically tunable planar Bragg grating using a liquid crystal overlayer has been described. This is the first practical realisation of a device of this type. The waveguide effective index and therefore the Bragg wavelength is controlled by reorienting the director of the nematic liquid crystal with an applied

electric field. A tunability of 0.29nm at 1560nm (35GHz) has been obtained. Several design improvements have been identified to enhance the tuning range and initial work to realise these changes has been presented.

A second generation device, fabricated by PECVD, has been constructed but the waveguide core refractive index is found to be too low to maintain optical guidance with the liquid crystal as the overcladding. An alternative liquid crystal or a specifically tailored three-layer refractive index structure is required to exploit the benefits potentially provided by such PECVD samples.

Work is continuing on the development of liquid crystal tuned UV written devices and this will be briefly mentioned in chapter 11.

10.7 References

[1] S.Yeralan, J.Gunther, D.Ritums, R.Cid, and M.Popovish. "Switchable Bragg grating devices for telecommunications applications". *Opt.Eng.*, 41(8):1774–1779, 2002.

[2] P.J.Collings and M.Hird. *Introduction to Liquid Crystals Chemistry and Physics*. Taylor and Francis, 1997.

[3] E.S. Goldburt and P.St.J. Russel. "Nonlinear single-mode fiber coupler using liquid-crystals". *Appl. Phys. Lett.*, 46(4):338–340, February 1985.

[4] L. Sirleto, D.S. Hermann, G. Scalia, and L. Komitov. "Integrated Electro-Optics Switches Based on Ferroelectric Liquid Crystal Waveguides". *Fiber and Integrated Optics*, 21:277–293, 2002.

[5] X. Zhu S. Yin, K-W. Chung. "A highly sensitive long period grating based tunable filter using a unique double-cladding layer structure". *Optics Communications*, 188:301–305, February 2001.

[6] L. Sirleto, G. Coppola, G. Breglio, G. Abbate, G.C. Righini, and J.M. Otón. "Electro-optical switch and continuously tunable filter based on a Bragg grating

in a planar waveguide with a liquid crystal overlayer". *Opt. Eng*, 41(11):2890–2898, November 2002.

[7] R.A.Soref. "Field effects in nematic liquid crystal obtained wit interdigital electrodes". *Journal of Applied Physics*, 45(12):5466–5468, 1974.

[8] M.Oh-e and K.Kondo. "Electro-optical characteristics and switching behavior of the in-plane switching mode". *Appl. Phys. Lett.*, 67(26):3895–3897, 1995.

[9] R.-P.Pan, S.-R.Liou, and C.-K.Lin. "Voltage-Controlled Optical Fiber Coupler Using a Layer of Low-Refractive-Index Liquid Crystal with Positive Dielectric Anisotropy". *Jpn. J. Appl. Phys.*, 34:6410–6415, 1995.

[10] G.D.Emmerson, C.B.E.Gawith, I.J.G.Sparrow, R.B.Williams, and P.G.R.Smith. "Physical observation of single step UV-written integrated planar Bragg structures and their application as refractive-index sensors". *Applied Optics*, 44(24):5042–5045, 2005.

Chapter 11

Future Work

11.1 Introduction

There is of course a vast range of additional work that can be performed to extend the work of this thesis. The work presented in the preceding chapters was in some cases limited by the availability of the appropriate equipment and in other cases simply due to the development time available. Here, on a chapter by chapter basis some of the potential key developments that could be made to extend this work are discussed. In some cases the work goes hand in hand with the developments from other sections and where possible duplication is avoided whilst maintaining a coherent explanation of the possible future advances.

In a few cases early progress has been made into the extension of the work and where relevant this is commented upon.

11.2 Deposition Development

Ultimately all of the development work of techniques and applications uses the deposition process as a foundation. Having developed a basic process for the fabrication of three layer structures index matched at 633nm there are several design itera-

tions that would prove valuable. These include

- Index matching at 1550nm
- Accurate determination of silica composition
- Variation of germanium levels to control photosensitivity
- Incorporation of additional dopants
- Reduction of hydrogen and nitrogen incorporation

The outcomes of these work packages are not expected to provide any unexpected or fundamental developments but would allow improved performance of devices developed on the resulting substrates.

11.3 UV Written Structures

The scope for the development of UV written devices is vast but many of the potential applications can be realised equally well, or better, by etched waveguide structures. With the emphasis on development and further characterisation of the UV writing process the following future studies are proposed.

In conjunction with the previously mentioned deposition developments a more thorough investigation on the effects of fluence on UV induced refractive index would prove valuable. This would allow further insight into the mechanisms of photosensitivity in the PECVD silica as well as potentially providing greater refractive index changes. In particular, a route towards lower fluence requirements may assist in providing greater index perturbations in Bragg gratings defined by DGW.

Given the relatively high propagation loss of the waveguides measured in chapter 7 several steps may be taken. The exclusion of hydrogen and nitrogen from the deposited layers has already been mentioned. It would also be beneficial to use deuterium instead of hydrogen to enhance the photosensitive response. Annealing the samples in an oxygen atmosphere prior to hydrogen (or deuterium) loading may also assist in reducing hydrogen and nitrogen present in the silica after deposition.

11.4 Thermal Treatments

The thermal locking process offers non-volatile photosensitivity enhancement. However, this was not exploited in PECVD fabricated samples. Generation of a fluence curve on thermally locked samples was attempted in order to compare with standard hydrogen loaded substrates. It was however found that the resultant devices had unexpected properties. When polishing it was found that the end facets were very prone to chipping making a suitably high quality optical coupling problematic. The results of the fluence variation were therefore inconclusive. Development of a thermal locking process to provide the permanent photosensitivity enhancement without the side effects of brittle layers would allow further characterisation to be performed.

The effects of thermal locking on propagation loss must also be taken into account in such process development. Initial work to compare waveguides in thermally locked and hydrogen loaded samples indicates that the loss penalty could be severe. Figure 11.1 compares transmitted power measurement over a broad wavelength range for two such samples. The magnitude of the loss peak associated with OH groups is approximately the same but the thermally locked sample is half the length of the hydrogen loaded waveguide. This indicates that the thermal treatment could seriously limit the performance of waveguides so produced due to the higher hydrogen content of the thermally treated layers. The use of deuterium over hydrogen may negate this issue and this variation would also require characterisation.

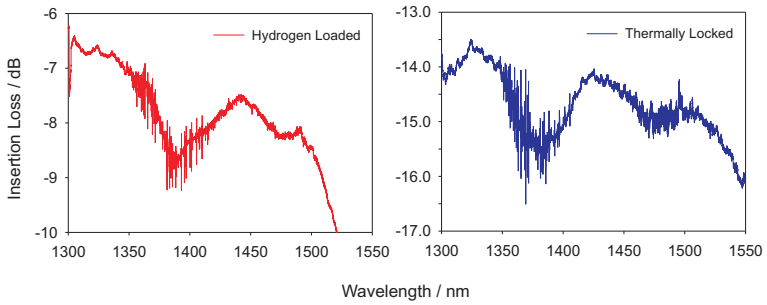

Figure 11.1: Comparison of broadband spectra of 35.5mm long hydrogen loaded waveguide (*Left*) and 18.0mm long thermally locked waveguide (*Left*)

11.5 UV Written Devices as Sensors

Demonstration of the UV written devices as sensors to detect phase changes provides only an example of their use. Further developments could include the use of substrates with refractive indices tailored to provide optimal sensitivity in specified analyte refractive index changes.

The use of the ability to use direct grating writing to produce Bragg gratings operating at a range of wavelengths could also be used to create a "chemical fingerprinting" device. A set of gratings, each operating at distinct wavelengths could be integrated onto a single device to act as refractometers and measure analyte optical properties over a wide wavelength range. This could allow identification of liquid contaminants or determine the specific composition of mixtures of substances.

11.6 Development of Liquid Crystal Devices

Some of the key improvements necessary for the further development of the tunable Bragg grating of chapter 10 were described in that chapter. Work is continuing on the development of these devices with the aim of developing pre-fabricated electrode layers that may be positioned onto the waveguiding substrate. This allows both electrical control and a surfactant treated cover layer to be provided simultaneously. Part of this development by the author's colleagues will investigate the liquid crystal alignment behaviour to allow full characterisation of the device performance. Early work by A.Dyadyusha, using indium tin oxide (ITO) electrodes spaced approximately 200μm apart on a glass substrate, shows that a 13V applied field provides nearly complete director reorientation. Images recorded through crossed polarisers at different applied fields are shown in figure 11.2. It is hoped that ITO electrodes deposited onto a glass cover layer will allow both small electrode spacing and accurate positioning relative to the waveguide.

An initial step in the production of further devices would be based on the deposition of slightly higher refractive index three layers samples than those fabricated by

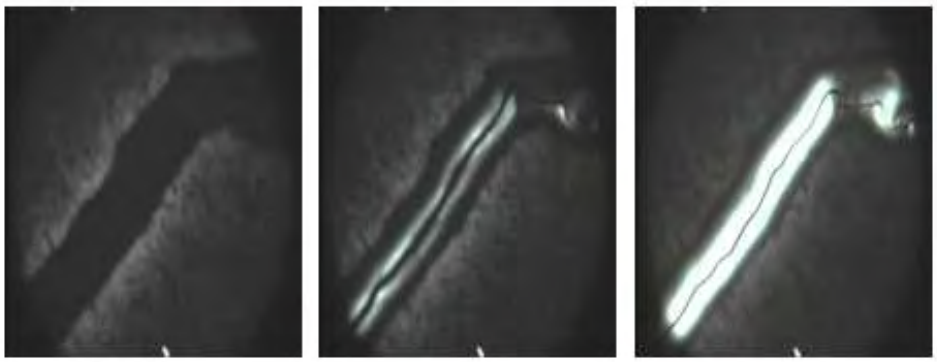

Figure 11.2: Work by A.Dyadyusha showing homeotropic alignment switching to in-plane alignment in a 12μm thick liquid crystal cell for different applied voltages: 0V(*left*), 5V(*middle*) and 10V(*right*). Bright areas indicate polarisation rotation by the reoriented liquid crystal.

PECVD (Chapter 6). This would allow the benefits of a thin (∼6μm) overcladding to be exploited without the loss of guidance that was observed due to the low core index compared to the liquid crystal used. Alternatively a lower refractive index liquid crystal could be sourced but as commercially available liquid crystals in the correct refractive index range are uncommon this would be an unlikely route to success.

Another possible route to tunable structures would be to perform UV writing on a substrate that did not have an overcladding layer. This would avoid the need for etching a window above the Bragg grating and allow the smoothest possible surface for the liquid crystal to be in contact with. Isolation of the input and output waveguides of the rest of the device could be achieved using a polymer layer produced by spin coating or possibly through a low temperature silica deposition technique that would not degrade the UV induced structure.

The same liquid crystal techniques could be applied to Mach-Zehnder based modulators, variable couplers or any device where dynamic changes to refractive index may be used to trim or tune performance.

11.7 Integrated Devices

All of the above suggestions are targeted at expanding the range of applications and techniques available from UV writing systems. In turn this will open new avenues for integration of optical functionalities either by combining UV writing with other technologies or by improving the performance of purely UV written devices.

Chapter 12

Conclusion

When introducing this thesis the reasons for extending the production methods and applications of integrated optics were briefly discussed. Within this context the development of direct-UV written waveguides and some potential applications have been presented. In the extensive framework of integrated optics these developments play just a small role in the ever evolving set of techniques and functions. Nonetheless the developments that have been presented can be used as the foundations of more extensive characterisation techniques and in particular in the evolution of new optical devices based on the combination of liquid crystals and waveguides.

A three layer PECVD deposition process for the production of three layer samples has been developed. The wafers produced with this technique have been demonstrated to be suitable for their intended purpose of providing the generic substrate required for the UV writing of waveguides.

The characteristics of the deposited silica and the UV written waveguides were shown to be somewhat different to those produced previously by FHD. A wider range of fluences were required for the PECVD samples in order to define an equivalent range of waveguide effective indices. It has been proposed, by comparison with the effects of thermal locking treatment, that the presence of hydrogen in the PECVD silica contributes to the difference in the photosensitive response of the two types of sample. Other observations of the effects of UV writing and thermal annealing encourage

comparisons of the initial stages of the exposure step and the effects of thermal locking, suggesting that the same underlying mechanisms occur in both processes.

The use of UV written devices as refractive index sensors has been shown in the context of detection and identification of physical transitions of state. As examples a liquid crystal with refractive index close to that of the waveguide core and water (with a significantly lower refractive index) were used. The first order phase transitions between liquid crystal and liquid, gas and liquid, liquid and solid and the equivalent reverse transitions were observed via changes in refractive index. Additionally the planar sensors allowed detection of the supercool state of water where the physical state remains liquid below the melting point.

Finally the development of an electrically tunable Bragg grating has been described. This represents the first practical realisation of such a device and its fabrication is made possible by the unique properties of UV written devices. The 35GHz tuning range achieved to date is not believed to be the maximum possible and initial studies to increase the range have been presented.

Some of the development work described in the thesis does not represent new or novel work but was nonetheless necessary in order to proceed with the further developments that extend this work into new directions. For clarity, the specific advances and novel steps that have been achieved in the work of this thesis are;

• The definition of Bragg gratings by Direct Grating Writing into PECVD layers.

• Demonstration of the use of the Direct Grating Writing technique to monitor waveguide stability and to compare devices fabricated by PECVD and FHD.

• The simple detection of phase changes and supercooling of water using an integrated optical sensor.

• Demonstration of a first of its kind integrated tunable filter.

Several areas for future development of this work have been proposed with the aim of improving the deposition process for the production of UV written devices and also to extend understanding of the UV exposure process and to allow is application to new and enhanced devices.

Appendix A

PECVD Operation Notes

Throughout the course of the work presented in this thesis a variety of difficulties presented themselves when operating the PECVD equipment. As a guide to some of the repairs or alterations that have been made, the key events are listed here with the corresponding solutions and points of interest to future users.

Issue	**Solution**	**Notes**
LDS Hard Drive Failure	Disk drive replaced with pre-loaded software	CD with image of all software required is stored inside the PC housing. Temporary earthing problem when PC correctly mounted in rack, pressure of being held into rack appeared to disrupt wiring and cause breakers to trip.
Main Control PC Hard Drive Failure	Disk drive replaced with pre-loaded software	CD with image of all software required is stored inside the PC housing
Showerhead not heated	Heater replaced	

Table A.1: (continued)

Issue	Solution	Notes
LDS Rack will not power up	Safety power relay replaced	
Intermittent Coolant Errors	Remove housing from electrical connector on chiller	Connector was rewired but this made no improvement
Loss of RF Power at start of deposition	Power off RF supply and reboot	Intermittent problem. To date, cause remains undetermined
Error: Brake Signal Absent	Ambient temperature too high, wait until clean room is cooler or improve air flow around equipment	
Repeated Error: Compressed Air Fault	Nitrogen supply to loadlock valve disconnected and replaced with compressed air. A temporary solution was to perform depositions around lunch time when compressed air/nitrogen demand is low.	Ultimate cause is due to insufficient supply of nitrogen. If either nitrogen or air supply is low an interlock is tripped. Both gas inputs are now connected to a common compressed air line. This is an acceptable solution. Problems will only occur if the compressed air fails just as a wafer is loaded or unloaded from the chamber.
Wafer carrier remains in chamber when attempting to remove a newly deposited wafer	Open loadlock valve by manually depressing the 'Gate' and 'Gate Interlock' pneumatic relays.	Cause unknown

Table A.1: (continued)

Issue	Solution	Notes
Chiller Failure	Motor replaced in chiller	
CF_4 gas leak	Regulator replaced	

The above maintenance was performed by combinations of STS service engineers, staff from the Southampton University Microelectronics Centre staff and by the author.

Additional points of use to the operator are given below.

Issue	Solution	Notes
Error on startup: Waiting for handler	Reboot the Loadlock PC	
No power to LDS unit when starting up equipment	Check breakers at rear of LDS rack	
Chamber not pumping down to pressure after period of non-use	Set platten and showerhead temperatures to usual values	May be a symptom of more serious problem
Unable to shutdown LDS software	Ensure dump ampoule is installed and then change software to have higher level user priveleges	If software is not exited correctly all settings will be lost.
The phosphine MFC has been observed to oscillate widely (>10sccm) when near the upper limit of flow rate (30sccm).	Maximum of 24 sccm flow used for all depositions	Cause unknown and recurrence of the oscillation not investigated.

Appendix B

Publications

B.1 Journal Articles

Assessment of waveguide thermal response by interrogation of UV written planar gratings.
I.J.G.Sparrow, G.D.Emmerson, C.B.E.Gawith, S.P.Watts, R.B.Williams, P.G.R.Smith.
IEEE Photonics Technology Letters, Vol.17(2) pp.438-440, 2005

Planar waveguide hygrometer and state sensor demonstrating supercooled water recognition.
I.J.G.Sparrow, G.D.Emmerson, C.B.E.Gawith, P.G.R.Smith.
Sensors and Actuators B: Chemical, Vol.107, pp.856-860, 2005

First order phase change detection using planar waveguide Bragg grating refractometer.
I.J.G.Sparrow, G.D.Emmerson, C.B.E.Gawith, P.G.R.Smith, M.Kaczmarek, A.Dyadyusha.
Applied Physics B, Vol.81, pp.1-4, 2005

Physical observation of single step UV-written integrated planar Bragg structures and their application as refractive-index sensors.
G.D.Emmerson, C.B.E.Gawith, I.J.G.Sparrow, R.B.Williams, P.G.R.Smith.
Applied Optics Vol.44(24) pp.5042-5045, 2005

B.2 Proceedings

Tunable liquid crystal waveguide devices for filter and sensor applications.
I.J.G.Sparrow, M.Kaczmarek, A.Dyadyusha, G.D.Emmerson, P.G.R.Smith.
Proceedings of SPIE, Liquid Crystals: Optics and Applications. Paper Number: 5947-23, 2005

B.3 International Conferences

Direct grating writing as a characterization technique for direct UV written waveguide structures.
G.D.Emmerson, C.B.E.Gawith, S.P.Watts, I.J.G.Sparrow, V.Albanis, R.B.Williams, P.G.R.Smith, S.G.McMeekin, J.R.Bonar, R.I.Laming.
BGPP 2003, Monterey ,1-3 Sep 2003

Investigation of thermal stability of UV written planar waveguides using direct grating writing.
I.J.G.Sparrow, G.D.Emmerson, C.B.E.Gawith, S.P.Watts, V.Albanis, R.B.Williams, P.G.R.Smith.
CLEO/IQEC 2004 San Francisco 16-21 May 2004, CTuU

All-UV written integrated glass devices including planar Bragg gratings and lasers.
P.G.R.Smith, G.D.Emmerson, C.B.E.Gawith, S.P.Watts, R.B.Williams, D.A.Guilhot, I.J.G.Sparrow, M.F.R.Adikan.
XX International Congress on Glass, (ICGXX) Kyoto 26 Sep - 1 Oct 2004 90026 (Invited)

Integrated Bragg grating sensor applied to detection of phase transitions in liquid crystal and water.
I.J.G.Sparrow, G.D.Emmerson, C.B.E.Gawith, P.G.R.Smith, M.Kaczmarek, A.Dyadyusha.
OFS-17 Bruges 23-27 May 2005 P2-74

Direct UV writing for channel definition on FHD silica-on-silicon.
M.F.R.Adikan, I.J.G.Sparrow, G.D.Emmerson, C.B.E.Gawith, P.Poopalan, W.Y.Chong, T.Subramaniam, H.Ahmad, P.G.R.Smith.
SIOE '05 Cardiff 21-23 Mar 2005

25GHz tunability of planar Bragg grating using liquid crystal cladding and electric field.
I.J.G.Sparrow, D.A.Sager, C.B.E.Gawith, P.G.R.Smith, G.D.Emmerson, M.Kaczmarek, A.Dyadyusha.
CLEO/QELS 2005 Baltimore 22-27 May 2005 JTuC62

35GHz tunable planar Bragg grating using liquid crystal and electric field.
I.J.G.Sparrow, G.D.Emmerson, P.G.R.Smith, M.Kaczmarek, A.Dyadyusha.
ECIO 2005 Grenoble 6-8 Apr 2005 ThPo1

Planar waveguide water state sensor allowing detection of supercooling.
I.J.G.Sparrow, G.D.Emmerson, P.G.R.Smith.
ECIO 2005 Grenoble 6-8 Apr 2005 ThB3-5

35 GHz tunable planar Bragg grating using nematic liquid crystal overlay.
I.J.G.Sparrow, P.G.R.Smith, G.D.Emmerson, M.Kaczmarek, A.Dyadyusha.
CLEO-Europe 2005 Munich 12-17 June 2005 CI4-3-MON

Small-angle ($<5^\circ$) direct-UV-written crossed-waveguide on silica-on-silicon with potential for power switching applications.
M.F.R.Adikan, I.J.G.Sparrow, C.B.E.Gawith, G.D.Emmerson, H.Ahmad, P.G.R.Smith.
CLEO/IQEC-Pacific Rim 2005 Tokyo 11-15 Jul

Tunable liquid crystal waveguide devices for filter and sensor applications.
M.Kaczmarek, I.J.G.Sparrow, G.D.Emmerson, P.G.R.Smith, A.Dyadyusha.
International Congress on Optics and Optoelectronics, Warsaw 28 Aug - 2 Sep 2005 5947-24

B.4 Magazine Publications

Direct writing of waveguides is a versatile approach to sensor technology.
R.B.Williams, I.J.G.Sparrow
Europhotonics Magazine Dec/Jan 2005 pp.26-27

B.5 Patent Applications

Electrically Tunable Planar Bragg Grating using Liquid Crystal Overlayer
I.J.G.Sparrow, P.G.R.Smith, G.D.Emmerson, M.Kaczmarek, A.Dyadyusha.
United Kingdom Patent Application, No. GB0507012.3